The Hong Kong Polytechnic University

Department of Civil and Environmental Engineering

FREQUENCY-DOMAIN BUFFETING ANALYSIS OF A LONG-SPAN TWIN-BOX-DECK BRIDGE WITH DISTRIBUTED BUFFETING LOADS

Qing ZHU

A thesis submitted in partial fulfillment of the requirements for

the Degree of **Doctor of Philosophy**

November 2014

To my family

for their love and support

CERTIFICATE OF ORIGINALITY

I hereby declare that this thesis is my own work and that, to the best of my knowledge and belief, it reproduces no material previously published or written, nor material that has been accepted for the award of any other degree or diploma, except where due acknowledgement has been made in the text.

___________(Signed)

ZHU Qing (Name of student)

ABSTRACT

Excessive buffeting responses can cause fatigue damage in the structural components and connections of long-span steel bridges. Thus, buffeting analyses that can accurately predict fatigue-related stress responses are important for modern cable-supported bridges. Structure health monitoring systems (SHM) have been installed in a number of long-span cable-supported bridges to monitor and assess bridge performance and safety. The number of sensors in an SHM system is always limited, such that not all of the key structural components can be directly monitored. Therefore, to facilitate the effective assessment of stress-related bridge performance and safety, stress-level buffeting analysis is required so that the responses in all of the important structural components can be directly computed and compared with measured values for verification.

Frequency-domain and time-domain methods have been developed to predict the buffeting-induced responses of bridges. These methods are based on integrated sectional aerodynamic and aeroelastic forces rather than distributed forces on the bridge deck. Disregarding the cross-sectional distribution of buffeting forces may affect the accuracy of computed buffeting-induced stress responses, which will in turn affect comparisons with the measured stresses from SHM systems. Thus, to accurately predict the buffeting-induced fatigue of bridges, it is imperative to take into account the cross-sectional distribution of aerodynamic and aeroelastic forces.

Traditional finite element (FE) models that reduce bridge decks to beam elements

with equivalent sectional properties are insufficient for such dynamic analyses. For a stress-level buffeting analysis, accurate FE models need to be built with detailed geometry using plate/shell/solid elements. Multi-scale modeling methods should be used to reduce the number of degrees-of-freedom (DOF) caused by such detailed modeling. Moreover, due to the uncertainties in models of large civil structures, updating processes are usually needed after the initial establishment of the FE models to improve modeling accuracy. The model updating process of multi-scale FE models requires both global and local measured data to ensure multi-scale accuracy. For long-span bridges, research in this area is limited.

In view of the problems outlined, a practical framework that includes the acquisition of distributed aerodynamic and aeroelastic forces, buffeting analysis with distributed loads, and multi-scale FE modelling and model updating techniques are needed for the accurate prediction of the buffeting responses of a long-span bridge.

In this study, the formulation for distributed aerodynamic forces on the surfaces of a bridge deck is first presented. Wind tunnel pressure tests are conducted to obtain the distributed aerodynamic forces on a sectional twin-box deck model. The cross-sectional distribution of signature-turbulence-induced pressure is investigated by separating the signature turbulence-induced pressure from the measured pressure time histories. The span-wise correlation of aerodynamic pressure on the sectional deck model is also studied.

The results for the cross-sectional and span-wise distributions of aerodynamic pressure provide more detailed information and deeper insight into the fluid-motionless structure interaction in a twin-box bridge deck. Signature turbulence mainly affects the leeward box. For certain locations, the signature-turbulence-induced pressure may be significantly larger than the incident-turbulence-induced pressure. For the incident-turbulence-induced pressure, the span-wise correlation weakens stream-wisely on the windward box, and the span-wise correlation on the leeward box is generally weaker than that on the windward box. For the signature-turbulence-induced pressure, the span-wise correlation is negligible for most parts of the deck except for the windward edge of the leeward box and the leeward edge of the windward box.

A new method to obtain distributed aeroelastic forces by distributing measured sectional aeroelastic forces is proposed. The distribution is based on the quasi-static expression of aeroelastic forces. A frequency-domain buffeting analysis framework with the obtained distributed aerodynamic and aeroelastic forces are developed. A case study is carried out on a segment of a twin-box bridge deck to demonstrate the feasibility of the proposed framework. The results show that the responses computed with distributed buffeting loads on a shell model are different from those computed with the traditional method on a beam model. The displacement responses computed with distributed buffeting loads are slightly smaller than those computed with the traditional method. The section-wise distribution of the stress responses yielded by the proposed method is more concentrated on the windward edge, resulting in a larger maximum stress value. The different boundary conditions on the beam and shell models can also cause significant differences in the computed stress response distribution.

A 3D multi-scale FE model of Stonecutters Bridge in Hong Kong is established. The bridge deck is modelled in detail with shell elements, allowing an accurate stress analysis to be conducted. Each deck segment is condensed into a super-element by the sub-structuring method to reduce the computation time for the subsequent dynamic analysis. The established FE model is updated with the measured modal frequencies only. Validation with measured frequency data shows that the established model is generally consistent with the real bridge in terms of dynamic properties. The computed displacement and stress influence lines are also compared with measured data acquired from load tests. The results show that the established multi-scale model is capable of providing both global and local responses. As it is updated only with modal frequencies, however, the computed displacement and stress responses under a vertical load are not accurate. This indicates the need for multi-scale updating techniques that take into account both the dynamic properties and local responses of the multi-scale model.

A new model updating method for the multi-scale FE model of Stonecutters Bridge is thus proposed. The objective functions of the proposed method include both the modal frequencies and multi-scale (displacement and stress) influence lines. The response surface method is adopted to simplify the optimisation problem in the model updating. The results show that the differences between the measured and computed modal frequencies and between the measured and computed multi-scale influence lines are all reduced with the proposed model updating method. A comparison of the additional measured modal frequencies and influence lines with the corresponding computed results further confirms the high quality of the proposed model updating method.

The proposed buffeting analysis framework is then applied to the updated multi-scale model of Stonecutters Bridge. The buffeting responses of the bridge for two wind directions associated with two terrains and three attack angles are investigated. The displacement, acceleration and stress responses of the bridge under distributed buffeting loads are presented. The mean wind from the S-W direction with larger mean wind speed induces larger mean responses of the bridge deck. The mean wind-induced stresses are concentrated on the windward edge of the bridge deck. In terms of the total buffeting responses, turbulent wind from the N-E direction with larger turbulence intensity induces larger responses. The total wind-induced stresses are smaller in the mid-span than in the quarter-span, and the largest longitudinal stress occurs on the windward edge of the bridge deck. For different attack angles, the initial attack angle of -3^{o} leads to the largest lateral and vertical buffeting responses among the three given angles of attack.

To further evaluate the effects of the proposed framework, a traditional buffeting analysis is performed on a spine-beam model of Stonecutters Bridge. The results of the buffeting analysis for the multi-scale model with distributed buffeting loads are compared with those from the analysis of the spine-beam model with sectional forces. The responses at different wind speeds are also investigated to reflect the influence of signature turbulence. The results show that the responses computed with distributed buffeting loads are different from those computed with the traditional method on a beam model. The displacement responses computed with the proposed framework are smaller than those computed with the traditional method. The sectional distribution of the stress responses yielded by the proposed method is more concentrated on the two edges of each box, resulting in a larger maximum stress value. The signature turbulence mainly affects the buffeting responses at low wind speeds.

PUBLICATIONS ARISING FROM THE THESIS

Journal papers

Xiao, X., Xu, Y.L., & **Zhu, Q.** (2014). Multi-scale modeling and model updating of a cable-stayed bridge-Part II: model updating using modal frequencies and influence lines. *Journal of Bridge Engineering* (Accepted).

Zhu, Q., & Xu, Y.L. (2014). Characteristics of distributed aerodynamic forces on a twin-box bridge deck. *Journal of Wind Engineering and Industrial Aerodynamics*, *131*, 31-45.

Zhu, Q., Xu, Y.L., & Xiao, X. (2014). Multi-scale modeling and model updating of a cable-stayed bridge- Part I: modeling and influence line analysis. *Journal of Bridge Engineering* (Accepted).

Zhu, Q., & Xu, Y.L. (2014). A framework for buffeting-induced stress analysis of a twin-box bridge deck in the frequency domain. *Journal of Wind Engineering and Industrial Aerodynamics* (Under review).

Conference papers and presentations

Xu, Y.L., & **Zhu, Q.** (2014). Distributed buffeting forces on the surfaces of a bridge deck. International Wind Engineering Symposium, 12 March 2014, Taipei, Taiwan (Invited Lecture), 23-24.

Xu, Y.L., & **Zhu, Q.** (2014). Frequency-domain buffeting analysis of a twin-box-deck bridge with distributed buffeting loads. The 2nd Workshop on Wind-induced Disaster Mitigation of Infrastructure, Beijing Jiaotong University, Beijing, China, 12-14 September 2014 (Invited Lecture).

Zhu, Q., & Xu, Y.L (2012), Structural health monitoring oriented finite element modeling for a long-span cable-stayed bridge. EMI/PMC 2012: 2012 Joint Conference of the Engineering Mechanics Institute and the 11th ASCE Joint Specialty Conference on Probabilistic Mechanics and Structural Reliability, Notre Dame, IN.

ACKNOWLEDGEMENTS

First, I would like to express my sincere gratitude to my chief supervisor, Prof. You-lin Xu. Thanks to him I had the opportunity to pursue my Ph.D. study in The Hong Kong Polytechnic University (PolyU), which is a milestone in my life. He helped me come up with the thesis topic and has been supportive since the day I began working on it. I deeply appreciate his expert guidance and unfailing encouragement throughout these four years.

I would also like to express my profound appreciation to my co-supervisor, Prof. Le-dong Zhu. His formidable knowledge and extraordinary experience in this field inspired me to pursue an academic career. He also provided valuable guidance in the wind tunnel tests of this Ph.D. study.

I am truly grateful to The Hong Kong Polytechnic University for the financial support through my Ph.D. studentship.

I particularly thank the committee members, Prof. Song-ye Zhu from our department, Prof. Ahsan Kareem from University of Notre Dame, and Prof. Chih-chen Chang from Hong Kong University of Science & Technology for attending my oral examination.

My thanks also go to former and current members of Prof. Xu's research groups, and other co-workers in PolyU, Mr. Sheng Zhan, Dr. Zhi-wei Chen, Dr. Xiao-hua Zhang, Dr. Bin Wang, Dr. Liang Hu, Dr. Xiao-liang Meng, Dr. Xiang Xiao, Dr. Jia He, Dr. Chao Li, Dr. Wen-feng Huang, Dr. Qing Huang, Dr. Wen-ai Shen, Dr.

Jin-hua Li, Mr. Yue Zheng, Mr. Feng-yang Wang, Mr. Jing-hua Lin, Mr. Chao-dong Zhang, Miss. Yi-xin Peng, Mr. Jian-fu Lin, Mr. Rong-pan Hu, Mr. Wen-yu He, and Mr. Can-xing Qiu for their warm support and assistance.

I also thank Dr. Isaac Shum and Mr. David H. Y. Leung from The CLP Power Wind/Wave Tunnel Facility for their help in the wind tunnel tests.

Getting through my Ph.D. study required more than academic support, and I have many people to thank for accompanying me over the past four years. I cannot begin to express my gratitude and appreciation for their friendship.

Most importantly, none of this could have happened without my family. My wife, my parents and my parents-in-law have been kind and supportive to me over the all these years. I am forever grateful to them. This thesis stands as a testament to their unconditional love and support.

CONTENT

LIST OF FIGURES

LIST OF TABLES

LIST OF NOTATIONS

a_0	Weighting factors for the shape of influence lines
$a_{0,i}$, $a_{1,i}$, $a_{2,i}$, $a_{3,ij}$	Regression coefficients
a_i^* (i=1~6)	Distributed aerodynamic derivatives
A	i) Root coherence peak value at zero reduced frequency ii) Effective cross sectional area of cable (Eq.(5.1))
A_i^* (i=1~6)	Aerodynamic derivatives
A_i, A_j	Areas that are represented by point i and point j, respectively
$\mathbf{A}_{se}$	Aeroelastic matrix
b_0	Weighting factors for the shape and amplitude of influence lines
B	Deck width;
c_{i1}, c_{i2}	Fitting parameters for incident turbulence induced admittance
c_{s1}, c_{s2}	Fitting parameters for signature turbulence induced admittance
c_{ux}, c_{wx}	Auto-covariance of u and w.

C	Decay factor
$\mathbf{C}$	Structural damping matrix
$\hat{\mathbf{C}}$	Super-element damping matrix
C_D, C_L, C_M	Drag, lift and moment coefficient, respectively
C'_D, C'_L, C'_M	Derivatives of drag, lift and moment coefficient with respect to the angle of incidence, respectively
$\tilde{C}_L$	RMS of the lift coefficient
C_H	Horizontal force coefficient with respect to the structural coordinate system
$\mathrm{Coh}^{1/2}()$	Root coherence function
C_p	Pressure coefficient
$C_{pi}^{D}, C_{pi}^{L}, C_{pi}^{M}$	Drag, lift and moment components of pressure coefficient C_{pi} with respect to the elastic center of the section, respectively
$\mathbf{C}_{se}$	Aeroelastic damping matrix
$\mathbf{C}_{se,i}$	Distributed aeroelastic damping matrix for the surface point i
$\mathbf{C}_{str}$	Structural damping matrix

C_V	Vertical force coefficient with respect to the structural coordinate system
D	Bridge deck depth
$\mathbf{D}$	Diagonal matrix
D_b	Aerodynamic drag force
DAC	Assurance criterion for the shapes of the displacement influence lines
DNO	Difference of amplitude between the measured and calculated displacement influence lines
E	Effective modulus of elasticity of cable (Eq.(5.1))
E_{eq}	Equivalent modulus of elasticity of cable
f	Frequency
f_{jk}	Flexibility coefficient
f_s	Predominant frequency of the signature turbulence induced pressure
$\mathbf{F}$	Nodal force vector

$\hat{\mathbf{F}}$	Super-element force vector
$[F]$	Flexibility matrix
$\mathbf{F}_b$	Aerodynamic force vector
F_D, F_L, F_M	Wind induced drag force, lift force and pitching moment, respectively
$\mathbf{F}_k$	Pseudo-excitation vector
$\mathbf{F}_s$	Static force vector
$\mathbf{F}_{se}$	Aeroelastic force vector
$[F^{\varepsilon}]$	Strain flexibility matrix
g	gravity acceleration (Eq.(5.1))
h	Vertical displacement of bridge deck
$\dot{h}$	Vertical velocity of bridge deck
h_i^* (i=1~6)	Distributed aerodynamic derivatives
$\mathbf{H}(\omega)$	Transfer function matrix;
H_i^* (i=1~6)	Aerodynamic derivatives

I_u, I_w	Horizontal and vertical turbulence intensity, respectively
J	Objective function
$\mathbf{k}j$	stiffness matrix of the *j*th element
K	Reduced frequency
$\mathbf{K}$	Structural stiffness matrix
$\hat{\mathbf{K}}$	Super-element stiffness matrix
K_I, K_S	Predominant reduced frequencies for the incoming and signature turbulence induced aerodynamic forces, respectively
$\mathbf{K}_{se}$	Aeroelastic stiffness matrix
$\mathbf{K}_{se,i}$	Distributed aeroelastic stiffness matrix for the surface point *i*
$\mathbf{K}_{str}$	Structural stiffness matrix
K_Δ	Reduced frequency with respect to the span-wise distance
$K_{\Delta S}$	Reduced frequency for signature turbulence induced force/pressure
$\bar{l}$	Horizontal projected length of the cable
$\mathbf{L}$	Lower triangular matrix

L_b	Aerodynamic lift force
$\mathbf{L}_j$	Differential operator that transforms the element displacement to the element strain (Eq.7.10)
$\mathbf{L}_k$	kth column of $\mathbf{L}$
L_{se}	Aeroelastic lift force
L_{vs}	Vortex induced lift force
L_u, L_w	Along-wind and vertical turbulence integral scale, respectively
$\mathbf{M}$	Structural mass matrix
$\hat{\mathbf{M}}$	Super-element mass matrix
M_b	Aerodynamic pitching moment
M_{se}	Aeroelastic pitching moment
$\mathbf{M}_{str}$	Structural mass matrix
N	i) Total number of wind pressure points on the section where the pressures are measured ii) Total number of nodes in the structure (Eq.(4.26)-(4.27)) iii) Total number of the axles of all the vehicles in the line

(Eq.(6.11))

$\mathbf{N}_j$ Shape function of the jth element

p Lateral displacement of the bridge deck

p_i^* (i=1~6) Distributed aerodynamic derivatives

P Wind pressure

P_I Incident turbulence induced wind pressure

$\{P_k\}$ Unit load vector

P_S Signature turbulence induced wind pressure

r Updating parameters

r_g Global updating parameters

$\mathbf{R}_e$ 6×3 matrix consisting of 0 and 1 that expands a 3-dimensional aeroelastic property matrix into a 6-dimensional matrix with respect to all 6 DOF of a node

$\mathbf{R}_f$ $n \times m$ matrix consisting of 0 and 1, which expands the m-dimensional loading vector into a n-dimensional vector

$R_j(x)$ Displacement response at the j^{th} location of a bridge due to multiple axle loads

ROTX Torsional displacement (Rotation around the x axis)

S_a Auto spectra of parameter a;

S_{ab} Cross spectra of parameter a *and* b;

S_t Strouhal number

SAC Assurance criterion for the shapes of the strain influence lines

SNO Difference of amplitude between the measured and calculated strain influence lines

T Cable force

$\mathbf{T}_j$ Coordinate transfer matrix from global to local coordinates

$[T_\varepsilon]$ Linear transformation matrix from the displacement vector to strain vector

u Along-wind fluctuating wind speed

$\mathbf{u}$ Nodal displacement vector

U Incoming wind speed

$\overline{U}$ Mean wind speed

U_c	Wind speed at the height of the deck level
U_{ref}	Reference wind speed
UY	Lateral displacement
UZ	Vertical displacement
v	Speed of moving vehicle
w	Vertical fluctuating wind speed
x	Longitudinal coordinate
y_i	y coordinate of surface point i
$\mathbf{Y}, \dot{\mathbf{Y}}, \ddot{\mathbf{Y}}$	Nodal displacement, velocity and acceleration vector, respectively
$Y_1(K)$	Aeroelastic stiffness damping parameter at lock-in
$Y_2(K)$	Aeroelastic stiffness parameter at lock-in
$\mathbf{Y}_k$	Pseudo displacement response vector
$\{Y_{Ti}\},\{Y_{Ai}\}$	Measured and calculated displacement influence line vectors, respectively
$Y_{Ti,max}$, $Y_{Ai,max}$,	Measured and calculated amplitudes of the displacement influence

	lines, respectively
z	Height
z_c	Height of the deck level at the middle of the main span of the bridge
z_i	z coordinate of surface point i
α	i) Effective angle of incidence ii) Torsional displacements of bridge deck (Eq.(4.9))
$\dot{\alpha}$	Torsional velocity of bridge deck
α_0	Mean angle of incidence
$\Delta\alpha$	Additional incident angle induced by turbulence or motion
β_i	Angle between pressure P_i and vertical structural vertical axis
β_j (j=1~3)	Weighting factors for different updating objectives
$\Upsilon_{Fi}, \Upsilon_{Di}, \Upsilon_{Si}$	Error between measured and calculated frequencies, displacements and strains, respectively
δ_f, δ_d, δ_s	Tolerance values for three updating indexes, respectively
δ_r	Tolerance for updating parameters

ε	Non-linear aeroelastic damping coefficient at lock-in
$\{\varepsilon\}$	Strain vector
$\{\varepsilon_{Ti}\},\{\varepsilon_{Ai}\}$	Measured and calculated strain influence line vectors, respectively
$\varepsilon_{Ai,max}$, $\varepsilon_{Ti,max}$	Measured and calculated amplitudes of the strain influence lines, respectively
$\zeta_{ij}(x)$	Interpolation coefficient at the i^{th} location for the j^{th} axle load
λ	Modal frequency
ρ	i) Air density ii) Effective density of cable material (Eq.(5.1)) iii) Mass density parameter (Eq.(6.2))
δ_i	Characteristic length on the deck section outline for the aerodynamic pressure P_i
$\boldsymbol{\sigma}_j$	Stress vector of the jth element
$\sigma_{u,}\ \sigma_w$	Standard deviation of horizontal and along-wind and vertical turbulence, respectively
ϕ	Mode shape

χ_{Du} Aerodynamic transfer function between the horizontal fluctuating wind velocity and aerodynamic drag force

χ_{Dw} Aerodynamic transfer function between the vertical fluctuating wind velocity and aerodynamic drag force

χ_{F} Aerodynamic force admittance function

χ_{Lu} Aerodynamic transfer function between the horizontal fluctuating wind velocity and aerodynamic lift force

χ_{Lw} Aerodynamic transfer function between the vertical fluctuating wind velocity and aerodynamic lift force

χ_{Mu} Aerodynamic transfer function between the horizontal fluctuating wind velocity and aerodynamic moment

χ_{Mw} Aerodynamic transfer function between the vertical fluctuating wind velocity and aerodynamic moment

χ_{pui}, χ_{pwi} Aerodynamic pressure admittance functions with respect to the fluctuating wind u and w, respectively

ω Circular frequency of vibration

LIST OF ABBREVIATIONS

3D	Three-dimensional
CMSM	Component mode synthesis method
DOF	Degree of freedom
D-str	Dynamic strain gauge
FE	Finite element
FEM	Finite element method
MAC	Modal assurance criteria
N-E	Northeast
RMS	Root mean square
SHM	Structural health monitoring
STD	Standard deviation
S-W	Southwest
T.I.	Turbulence intensity

CHAPTER 1

INTRODUCTION

1.1 Research motivation

Excessive buffeting responses can cause fatigue damage in the components and connections of long-span steel bridges (Gu et al., 1999; Li, et al., 2002; Xu et al., 2009). Thus, buffeting analyses that can accurately predict fatigue-related stress responses are important for modern cable-supported bridges (Liu et al. 2009). Structure health monitoring (SHM) systems have been installed in a number of long-span cable-supported bridges to monitor and assess bridge performance and safety (Xu and Xia, 2012). The number of sensors in an SHM system is always limited, such that not all of the key structural components can be directly monitored. Therefore, to facilitate the effective assessment of stress-related bridge performance and safety, stress-level buffeting analysis is required so that the responses in all of the important structural components can be directly computed and compared with measured values for verification.

Frequency-domain (e.g. Davenport, 1962; Scanlan & Gade, 1977; Xu et al.2000) and time-domain (e.g. Chen et al., 2000) methods have been developed to predict the buffeting induced responses of bridges. These methods are based on integrated sectional aerodynamic and aeroelastic forces rather than distributed forces on the bridge deck. Disregarding the cross-sectional distribution of buffeting forces may affect the accuracy of computed buffeting-induced stress responses, which will in turn affect comparisons with the measured stresses from SHM systems. Thus, to accurately predict the buffeting-induced fatigue of bridges, it is imperative to take into account the cross-sectional distribution of aerodynamic and aeroelastic forces.

Wind tunnel pressure tests of motionless sectional model have been used in some studies (e.g. Larose, 1997; Larose & Mann, 1998; Hui, 2006). But most of these studies focused on the aerodynamic admittance functions and/or the span-wise correlations of integrated buffeting forces, rather than distributed aerodynamic forces. The characteristics of distributed aerodynamic pressures have not been investigated.

For aeroelastic forces, Liu et al. (2009) proposed a method to distribute lumped aerodynamic forces to nodes of an SHM-oriented FE model and enabled buffeting analysis with consideration of the spatial distribution of both aerodynamic and aeroelastic forces. However, the proposed distribution method was not based on measured data from wind tunnel tests or field measurements, and thus the sectional distribution considered may be inconsistent with the real fluid-structure interaction pattern.

In view of the above, a practical framework to perform buffeting analysis with distributed buffeting loads on a long-span bridge is needed, and the methods to acquire distributed aerodynamic and aeroelastic forces on the bridge deck should be developed. Furthermore, a FE modeling technique that enables accurate strain/stress analyses for all important components and the corresponding model updating approach are required for such a buffeting analysis framework.

Traditional FE models that reduce bridge decks to beam elements with equivalent sectional properties are insufficient for such dynamic analyses. For a stress-level buffeting analysis, accurate FE models need to be built with detailed geometry using plate/shell/solid elements. On the other hand, the computation capacity for such dynamic analyses shall be considered. A number of studies have been conducted to build detailed shell/solid element models for long-span bridges (e.g. Duan et al.， 2011; Fei et al.， 2007), but the large number of degrees-of-freedom (DOF) resulting from such fine modeling can cause difficulties in dynamic analysis as well as model updating.

Multi-scale modeling methods have been used to build FE models for long-span bridges with affordable number of DOF. Li et al. (2001) adopted the two-step analysis strategy of building a simplified global FE model for the entire structure and a detailed local FE model for the region of interest. The structural analysis of the global model was conducted first to extract the results for the location of interest as the outer boundary conditions on the local model for further analyses. Nevertheless, the inherent difficulties in accurately modeling the complicated boundary conditions may lead to significant errors in a dynamic analysis. McCune et al. (2000) proposed a mixed dimensional coupling FE method that allows the shell/solid element model of the regions of interest to be incorporated into the simplified global beam element model through multi-dimensional constraint equations. This method has improved the modeling accuracy of the connections between the detailed local models and the less-refined parts of the global model. Only a small number of regions of interest, however, can be chosen when building such multi-scale models.

Sub-structuring method has been used in recent years to include both global and local information of a long-span bridge in a single FE model (e.g. Ding et al., 2010; Kong et al., 2012). The sub-structuring method has an advantage in modeling box decks of long-span bridges because it allows the geometry of all the plates and even the stiffeners in the whole deck to be retained in substructures of segments while the global solution only handles the selected master DOF. Besides, it is particularly efficient in dealing with structures with repetitive sub-structures such as the box-deck of a long-span bridge.

Due to the uncertainties of large civil structures, model updating processes are usually needed after the initial establishment of FE models to ensure modeling accuracy (e.g. Friswell 1995; Brownjohn et al. 2011). For the entire FE model of a long-span bridge, the choice of model updating methods is limited because of the high computation demand of the updating algorithms. Sensitivity-based model updating with modal frequencies and mode shapes (using model assurance criteria (MAC) values) are often used in this situation. Nevertheless how the dynamic-property-based updating procedures affect the accuracy of the multi-scale responses of the multi-scale models has not been studied yet.

To ensure the multi-scale accuracy of multi-scale FE models, the model updating process needs to use both global and local measured data. Because it is very difficult, if not impossible, to measure mode shapes or their derivatives with enough accuracy to consider local behaviours of a long-span cable-stayed bridge, a FE updating method for a long-span bridge using both dynamic characteristics and static responses may be a wise solution, but the research in this area is limited.

In view of the problems outlined, a practical framework that includes the acquisition of distributed aerodynamic and aeroelastic forces, buffeting analysis with distributed loads, and multi-scale FE modeling and model updating techniques are needed for the accurate prediction of the buffeting responses of a long-span bridge.

1.2 Research objectives

This thesis focuses on the buffeting analysis of a long-span twin-box-deck bridge with distributed buffeting loads in the frequency domain. The major objectives are as follows:

1. To formularize distributed aerodynamic forces on the surface of a bridge deck. To separate incident and signature turbulence effects in the distributed aerodynamic forces. To identify aerodynamic characteristics including pressure coefficients, pressure admittances and span-wise pressure coherence through wind tunnel tests.

2. To formulate the spectral matrix of distributed aerodynamic forces based on the acquired aerodynamic characteristics. To estimate distributed aeroelastic forces by distributing the measured sectional aeroelastic forces. To propose a frequency-domain buffeting-induced stress analysis framework based on the obtained distributed buffeting forces.

3. To establish a multi-scale FE model for a long-span cable-stayed bridge with twin-box deck that allow for accurate dynamic stress analysis in the bridge deck.

To develop a model updating method for the established multi-scale FE model that can effectively improve the accuracy of both simulated displacement and stress responses.

4. To apply the proposed frequency-domain buffeting-induced stress analysis framework on the multi-scale FE model for dynamic displacement and stress responses with field wind data.

5. To compare the responses computed using the proposed buffeting analysis framework and those computed using the sectional-force-based method on a spine beam model. To further investigate the signature turbulence effects on the buffeting-induced responses.

1.3 Assumptions and limitations

The development and application of the buffeting analysis framework proposed by this study are subject to the following assumptions and limitations:

1. It is assumed that the wind turbulence is a stationary random process. The length scales of the turbulence is sufficiently larger than the chord-wise dimension of the bridge deck so that the secondary span-wise flow and redistribution of pressures can be neglected and therefore the pressures on any section of the span are only due to the wind incident on that section.

2. It is assumed that the mean wind speed is sufficiently larger than the turbulence speed so that the non-linear effects of turbulence can be ignored.

3. It is assumed that the wind-induced dynamic responses are small enough so that the non-linear effects of bridge motion can be ignored. As a result, the results of this study are not applicable in the vicinity of any aerodynamic or aeroelastic instability, or when the vortex shedding induced lock-in phenomenon occurs.

4. In the simulation of the wind forces and wind-induced bridge responses, only wind perpendicular to the longitudinal axis of the bridge deck is considered, and the effect of yaw wind is neglected.

5. Based on the assumption that the coupled effects of incident and signature turbulence can be neglected, the total buffeting-induced responses are obtained by the superposition of incident and signature turbulence induced responses.

6. Although the number of master nodes in the multi-scale model is limited for computation efficiency, it is assumed in the buffeting analyses that this number is large enough so that the area corresponding to each node is small and that the wind loads in the small area represented by each point can be considered uniform.

1.4 Outline of the thesis

This thesis covers a variety of research topics to achieve the aforementioned objectives. It is divided into 9 chapters and is organized as follows.

Chapter 1 introduces the motivation for this study and states its objectives, assumptions and limitations.

Chapter 2 contains an extensive literature review on relevant topics. The wind induced loads and their characteristics on a long-span bridge are reviewed first. The current status of buffeting analyses in both frequency and time domain are then reviewed. The limitations of the cross-sectional-force-based buffeting framework are highlighted. The FE modeling of long-span bridges is introduced in brief and the studies on multi-scale modeling of long-span bridges are reviewed. Finally, the status of multi-scale model updating research and some related techniques are reviewed.

Chapter 3 presented the wind tunnel pressure test results of distributed aerodynamic forces on a sectional twin-box deck model. The formulation for distributed aerodynamic forces on the surfaces of a bridge deck is first presented. By separating the signature turbulence induced pressure from the measured pressure time-histories, the cross-sectional distribution of signature turbulence effects is investigated. The span-wise correlation of aerodynamic pressure on the sectional deck model is also studied.

Chapter 4 proposes a buffeting analysis framework with the distributed buffeting loads. Within this framework, the formation of the spectral matrix of distributed aerodynamic loads is introduced and a new method to obtain distributed aeroelastic forces by distributing the measured sectional aeroelastic forces is proposed. The distribution is based on the quasi-static expression of self-excited forces. A case study on a segment of a twin-box deck is carried out to validate the proposed framework.

Chapter 5 introduces the establishment of a 3D multi-scale FE model of the

Stonecutters Bridge. The bridge deck is modeled in detail with shell elements, and therefore accurate stress analysis is enabled. Each deck segment was condensed into a super-element by the sub-structuring method to reduce computation time for the subsequent dynamic analysis. The established FE model is updated with the measured modal frequencies only. How the traditional dynamic-property-based updating affects the accuracy of the multi-scale responses of the bridge is also investigated. The need for multi-scale updating techniques that take into account both dynamic properties and local responses of the multi-scale model is highlighted.

Chapter 6 presented a new model updating method for the multi-scale FE model of the Stonecutters Bridge. The objective functions of the proposed method for model updating include both modal frequencies and multi-scale (displacement and stress) influence lines. The response surface method is adopted to simplify the optimisation problem involving in the model updating. The proposed method can effectively improve the accuracy of simulated displacement and stress responses.

Chapter 7 presents the buffeting analysis with distributed wind loads of the Stonecutters Bridge. The proposed buffeting analysis framework is applied on the multi-scale FE model of the Stonecutters Bridge. Two wind directions associated with two terrains are considered in the analyses.

Chapter 8 compares the results of buffeting analyses on the multi-scale model with distributed wind forces with the analyses on a beam model with integrated forces. The responses at different wind speeds are presented to reflect the influence of signature turbulence.

Chapter 9 summarizes the contributions, findings, and conclusions of this study. Limitations of this study are discussed and some recommendations for future study are provided.

CHAPTER 2

LITERATURE REVIEW

2.1 Wind-induced loads on long-span bridges

There are several mechanisms that can excite dynamic responses in the decks of long-span bridges. Wind-induced vibration is an important source of loads on bridge structures. Wind-induced loads include mean wind forces, aeroelastic forces and aerodynamic forces.

2.1.1 Mean wind forces

In a typical 2-D analysis, mean wind forces can be split into three parts: the lift force, the drag force and the pitching moment. The lift force equals the integral of the wind pressure on the section in the across-wind direction, the drag force equals the integral of the wind pressure in the along-wind direction and the pithing moment is the torsion with respect to the centroid of the section, which equals the total resultant wind force times a moment distance.

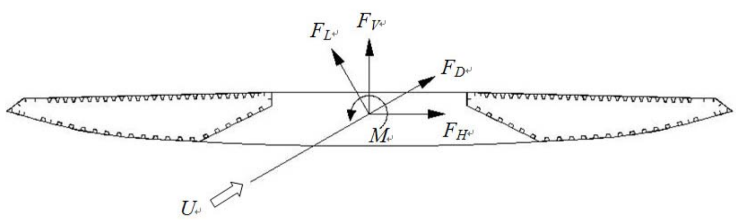

Figure 2.1 Mean wind load in wind coordinate system and structural coordinate system

In a certain wind flow field, it is conventionally assumed that the mean wind force acting on sections with the same shape is proportional to their size. Therefore, three non-dimensional mean wind force coefficients, C_D, C_L and C_M in the wind coordinate system and C_H, C_V and C_M in the structural coordinate system, are introduced to depict the characteristics of the section shapes. Mean wind force coefficients can usually be obtained from either wind tunnel tests or computational fluid dynamics simulations. With these coefficients, the mean wind load on bridge decks, towers and cables can be calculated according to their section shape.

The mean wind forces on a long-span bridge may cause the aerostatic instability of the bridge. The aerostatic instability of long-span bridges usually occurs in a pattern of lateral-torsional divergence. Boonyapinyo et al. (1994) and Nagai et al. (1998) investigated the aerostatic instability of long-span cable-stayed bridges. Cheng et al. (2002) and Zhang et al. (2002) investigated this phenomenon in long-span suspension bridges. The results from these studies show that nonlinear aerostatic instability largely results from the coupling effect of displacement-dependent mean wind loads and the geometric nonlinearity of long-span bridges.

2.1.2. Aeroelastic forces and aerodynamic derivatives

Aeroelastic forces resulting from the fluid-structure interaction of the mean wind flow and deck motion are the main cause of flutter instability. These forces also comprise a large part of the buffeting loads on a bridge deck. For a 2-D situation, the aeroelastic forces can be written as

$$L_{se} = \frac{\partial L_{se}}{\partial \dot{h}} \dot{h} + \frac{\partial L_{se}}{\partial \dot{\alpha}} \dot{\alpha} + \frac{\partial L_{se}}{\partial h} h + \frac{\partial L_{se}}{\partial \alpha} \alpha$$
$$M_{se} = \frac{\partial M_{se}}{\partial \dot{\alpha}} \dot{\alpha} + \frac{\partial M_{se}}{\partial \dot{h}} \dot{h} + \frac{\partial M_{se}}{\partial \alpha} \alpha + \frac{\partial M_{se}}{\partial h} h \tag{2.1}$$

where L_{se} and M_{se} are the aeroelastic lift force and pitching moment, respectively; and h and α are the vertical and torsional displacement of the deck, respectively.

Scanlan & Tomko (1971) introduced aerodynamic derivatives (H_i^*, A_i^* (i=1~4)) to express the aeroelastic forces as:

$$L_{se} = \frac{1}{2}\rho U^2 B \left[K H_1^* \frac{\dot{h}}{U} + K H_2^* \frac{B\dot{\alpha}}{U} + K^2 H_3^* \alpha + K^2 H_4^* \frac{h}{B} \right]$$
$$M_{se} = \frac{1}{2}\rho U^2 B^2 \left[K A_1^* \frac{\dot{h}}{U} + K A_2^* \frac{B\dot{\alpha}}{U} + K^2 A_3^* \alpha + K^2 A_4^* \frac{h}{B} \right] \tag{2.2}$$

where ρ is the air density; U is the mean wind velocity; B is the bridge deck width; K is the reduced frequency; and ω is the circular frequency of vibration. When the aerodynamic derivatives are determined, the aeroelastic forces acting on the structure become linear functions of structural displacement and velocity (Agar, 1991).

Although Scanlan's convention is the most commonly used in practice, there are other types of expressions for aeroelastic forces. Theodorsen and Mutchler (1935) gave the theoretical expressions for the aeroelastic lift force and pitching moment on a flat plate airfoil subject to sinusoidal motions. Quasi-static expressions of aerodynamic derivatives and their relationship between Scanlan's aerodynamic derivatives have also been studied (Zasso, 1996; Scanlan, 2000b; Tubino, 2005).

A simplified 2-D flutter analysis can be performed on real bridges with 2-D aeroelastic forces if it is assumed that only the first-order vertical and torsional modes participate in the coupled flutter. Nevertheless, the flutter of a real bridge may involve many modes. Much research has been conducted on the 3-D coupled flutter analysis of long-span cable-supported bridges in the frequency domain (e.g., Namini et al., 1992; Beith, 1998; Ding et al., 2004). Flutter analysis in the time domain has also been investigated (Chen et al., 2000).

2.1.3 Aerodynamic forces and aerodynamic admittances

The buffeting of a long-span bridge is a random vibration caused by fluctuating winds that appear at a wide range of wind speeds. In the wind resistance design of a long-span bridge, the buffeting responses are normally dominant in determining the sizes of the structural members. When a bridge is immersed in a turbulent wind field, it will be subjected to the dynamic wind forces caused by fluctuating wind speeds, or aerodynamic forces. In addition to aerodynamic forces, the aeroelastic forces induced by wind-structure interactions are important for predicting the buffeting response of long suspension bridges due to the additional energy injected into the oscillating structure by the aeroelastic forces. To predict the buffeting responses, the aerodynamic forces resulting from turbulent winds and the aeroelastic forces due to wind-bridge interactions should both be taken into account. The formulation for 2-D aeroelastic forces was introduced in the previous subsection; the formulation for aerodynamic forces is introduced in this subsection.

Under a quasi-steady assumption, aerodynamic forces can conventionally be expressed as

$$
\begin{aligned}
L_b(t) &= \frac{1}{2}\rho U^2 B\left[C_L(\alpha_0)\cdot\left(\frac{2u(t)}{U}\right)+\left(C_L'(\alpha_0)+C_D(\alpha_0)\right)\cdot\frac{w(t)}{U}\right] \\
D_b(t) &= \frac{1}{2}\rho U^2 B\left[C_D(\alpha_0)\cdot\left(\frac{2u(t)}{U}\right)+C_D'(\alpha_0)\cdot\frac{w(t)}{U}\right] \\
M_b(t) &= \frac{1}{2}\rho U^2 B\left[C_M(\alpha_0)\cdot\left(\frac{2u(t)}{U}\right)+C_M'(\alpha_0)\cdot\frac{w(t)}{U}\right]
\end{aligned}
\tag{2.3}
$$

where L_b, D_b and M_b are the aerodynamic lift force, drag force and pitching moment, respectively; u and w are the horizontal and vertical turbulent components of the incoming wind, respectively; and C_L', C_D' and C_M' are the derivatives of the aerodynamic coefficients with respect to the angle of incidence.

Davenport (1962) used 6 aerodynamic admittances to represent the ratios of the aerodynamic forces in fluctuating flows to their quasi-steady values. The aerodynamic admittances are used for two main reasons: First, because the aerodynamic forces show a dependence on frequency; and second because '*aerodynamic forces on a cross section are generated not by the velocity at a point in the flow but by that over some finite region of the flow surrounding the cross section*' (Davenport, 1962). After the modification with aerodynamic admittances, the aerodynamic forces can be expressed as

$$
\begin{aligned}
L_b &= \frac{1}{2}\rho \bar{U}^2 B\left[2C_L\chi_{Lu}\frac{u}{\bar{U}}+(C_L^{'}+C_D)\chi_{Lw}\frac{w}{\bar{U}}\right] \\
D_b &= \frac{1}{2}\rho \bar{U}^2 B\left[2C_D\chi_{Du}\frac{u}{\bar{U}}+C_D^{'}\chi_{Dw}\frac{w}{\bar{U}}\right] \\
M_b &= \frac{1}{2}\rho \bar{U}^2 B^2\left[2C_M\chi_{Mu}\frac{u}{\bar{U}}+C_M^{'}\chi_{Mw}\frac{w}{\bar{U}}\right]
\end{aligned}
\tag{2.4}
$$

where χ_{Lu}, χ_{Lw}, χ_{Du}, χ_{Dw}, χ_{Mu}, χ_{Mw} are the aerodynamic admittance functions, which are functions of the reduced frequency and dependent on the geometrical configuration of the cross section of the bridge deck.

The conventional approach is to compare the measured wind spectra and buffeting force spectra to obtain the empirical aerodynamic admittance functions:

$$\begin{aligned}
\chi_{Lu}(K) &= \frac{4}{\rho^2 U^2 B^2}\cdot\frac{S_{L_b L_b}(x,K)}{S_{uu}(x,K)} & \chi_{Lw}(K) &= \frac{4}{\rho^2 U^2 B^2}\cdot\frac{S_{L_b L_b}(x,K)}{S_{ww}(x,K)} \\
\chi_{Du}(K) &= \frac{4}{\rho^2 U^2 B^2}\cdot\frac{S_{D_b D_b}(x,K)}{S_{uu}(x,K)} & \chi_{Du}(K) &= \frac{4}{\rho^2 U^2 B^2}\cdot\frac{S_{D_b D_b}(x,K)}{S_{ww}(x,K)} \\
\chi_{Mu}(K) &= \frac{4}{\rho^2 U^2 B^4}\cdot\frac{S_{M_b M_b}(x,K)}{S_{uu}(x,K)} & \chi_{Mu}(K) &= \frac{4}{\rho^2 U^2 B^4}\cdot\frac{S_{M_b M_b}(x,K)}{S_{ww}(x,K)}
\end{aligned} \tag{2.5}$$

Some studies have measured aerodynamic admittances on bluff bodies (e.g., Walshe & Wyatt, 1983; Jancauskas & Melbourne, 1986; Kawatani & Kim, 1992; Sankaran & Jancauskas, 1992). When wind tunnel test results are not available, the aerodynamic admittances are usually taken as unity, or Liepmann's approximation of Sears' function (Liepmann, 1952) is used to estimate them.

Under quasi-static assumption, it is also assumed that the forces acting on one strip of the deck are induced by the gusts acting on that strip only, without considering the gusts on the neighbouring strips. This is known as the strip assumption (Larsose, 1998). Under this assumption, the span-wise correlation of the aerodynamic forces should equal the correlation of the turbulence. However, this assumption does not hold for long-span bridges in most circumstances.

Larose (1997) and Larose and Mann (1998) directly measured the aerodynamic admittance and span-wise coherence of aerodynamic forces based on simultaneous measurements of unsteady surface pressures on three chord-wise strips of section models. Hui (2006) investigated the admittance and span-wise coherence of the aerodynamic forces induced from turbulent wind on a twin-box deck by wind tunnel pressure tests on a sectional model with seven pressure-tapped strips. The results of these studies showed that aerodynamic forces usually have a better span-wise correlation than the incoming turbulence.

The analyses in these studies on aerodynamic forces were all based on the integral of pressure, that is, integrated aerodynamic forces, rather than distributed pressure. The distribution of aerodynamic pressure on bridge decks has seldom been investigated.

2.1.4 Signature turbulence effects

Signature turbulence is the turbulence produced by the structure itself in the flow, even if the incoming flow is perfectly smooth. Aerodynamic forces actually result from both incoming turbulence and signature turbulence. Singh (1997) explained the relationship between signature turbulence and vortex shedding: '*excitation due to signature turbulence includes all wake-induced excitations and not just those associated with critical velocities (vortex shedding)*'.

Few studies have been conducted on the effects of signature turbulence. Zhu et al. (2009) investigated the signature turbulence effects on aerodynamic admittances with and without buffeting responses. The results of their study showed that signature turbulence has a significant influence on buffeting responses only at low wind speeds for a twin-box bridge deck. It should be noted that most other buffeting analyses of long-span bridges have focused on single-box decks, where the signature turbulence effects may be smaller.

2.1.5 Vortex shedding induced forces

In fluid dynamics, vortex-induced vibrations are motions induced by the vortex shedding of the flow (Sarpkaya, 1979; Bearman, 1984).

On bridges, vortex-induced vibrations are important sources of fatigue damage that usually occur on girders or cables. The occurrence of such vibrations means that the amplitude of the vibration must be restrained under a certain limit in bridge design.

A widely used empirical model of vortex-induced force is (Simiu & Scanlan, 1996)

$$L_{VS}(t)=\frac{1}{2}\rho U^2 D\left[Y_1(K)\left(1-\varepsilon\frac{h^2}{D^2}\right)\frac{\dot{h}}{U}+Y_2(K)\frac{h}{D}+\tilde{C}_L(K)\sin(\omega_n t+\phi)\right] \qquad (2.6)$$

where ω_n is the circular lock-in frequency; D is the bridge deck depth; Y_1 and ε are the two aeroelastic damping parameters; Y_2 is the aeroelastic stiffness parameter; and $\tilde{C}_L$ is the root mean squares (RMS) of the lift coefficient. These are all functions of reduced frequency K at lock-in. The aeroelastic damping parameters, Y_2 and $\tilde{C}_L$ are usually ignored as they have negligible effects on the response. Y_1 and ε are functions of the Scruton number and can be extracted from wind tunnel observations of steady-state amplitudes of models at lock-in.

It can be seen from Eq.(2.6) that the vortex-induced force contains both aeroelastic and aerodynamic components.

Studies of spring-mounted rigid cylinders have shown that the span-wise correlation of vortex-induced forces increases with amplitude (Wilkinson, 1981) and decreases with turbulence intensity (Novak & Tanaka, 1975).

2.1.6 Distributed wind induced loads

Distributed aerodynamic pressure time histories can be obtained from pressure tests of a motionless sectional model. Larose (1997) and Larose and Mann (1998) directly measured the aerodynamic admittance and span-wise coherence of aerodynamic forces based on the simultaneous measurements of unsteady surface pressures on three chord-wise strips of section models. Hui (2006) investigated the admittance and span-wise coherence of the aerodynamic forces induced from turbulent wind on a twin-box deck by wind tunnel pressure tests of the sectional model with seven pressure-tapped strips. However, the analyses in these studies were all based on the integral of pressure, or integrated aerodynamic forces, rather than distributed pressure.

For aeroelastic forces, Liu et al. (2009) proposed a method to distribute lumped aerodynamic forces to nodes of an SHM-oriented FE model and enabled buffeting analysis with consideration of the spatial distribution of both aerodynamic and aeroelastic forces. However, the proposed distribution method was not based on measured data from wind tunnel tests or field measurements, and thus the sectional distribution considered may be inconsistent with the real fluid-structure interaction pattern.

Argentini et al. (2012) obtained distributed aerodynamic admittance and derivatives with a forced-vibration pressure test of a sectional model. Their study showed that expressions for buffeting loads may have the advantages of providing more information about the phenomenology of fluid-structure interactions, leading to a unified description of aeroelastic and aerodynamic forces. However, due to the complicated experiment devices required and the inherent difficulty with the accurate identification of aerodynamic forces using the forced-vibration technique, this method is not widely applicable at present.

2.1.7 The quasi-steady and quasi-static assumptions

The quasi-steady hypothesis assumes that the size of the deck section is small compared with the length scales of turbulence components. As a result, the aerodynamic force around the deck can be considered as fully correlated (Davenport, 1962). The aerodynamic admittances measure the ratios of the aerodynamic forces to their quasi-steady values. The quasi-static assumption assumes that the aerodynamic/aeroelastic force on the deck depends on the instantaneous relative motion between deck and the flow (Tubino, 2005). Due to the overlapping in the concept of these two assumptions, the theory developed under them is often referred to as the quasi-steady theory (e.g. Wu & Kareem, 2013a).

In the modeling of the aeroelastic forces, the weakness of quasi-steady theory is that it cannot take account of the fluid memory effects (Wu & Kareem, 2013a; Wu et al., 2013). Unsteady parameters, such as the aerodynamic admittance and derivatives, are therefore introduced to overcome this shortcoming. Nevertheless, the commonly used linear analysis framework with these unsteady parameters cannot take account of the nonlinearity (Wu & Kareem, 2013a). Many studies have been conducted to improve the modeling schemes for wind forces (e.g. Diana et al. 2010; Wu & Kareem, 2013b).

2.2 Buffeting analysis of long-span bridges

2.2.1 Buffeting analysis in the frequency domain

The main purpose of buffeting analysis is to calculate the dynamic responses of a bridge under both aeroelastic and aerodynamic forces. It can be conducted in either the frequency domain (e.g., Davenport, 1962; Scanlan, 1978; Jain, 1996) or the time domain (e.g., Bucher & Lin, 1988; Xiang et al., 1995; Chen et al., 2000b).

Davenport (1961; 1962) first introduced aerodynamic admittance into buffeting analysis. Scanlan (Scanlan & Gade 1977; Scanlan, 1978) proposed a basic multi-mode buffeting analysis framework of long-span bridges that incorporated aeroelastic forces. The governing equation of motion of a bridge excited by fluctuating winds with respect to the static equilibrium position can be given by (Xu, 2013)

$$\mathbf{M}\ddot{\mathbf{Y}} + \mathbf{C}\dot{\mathbf{Y}} + \mathbf{K}\mathbf{Y} = \mathbf{F}_{se} + \mathbf{F}_{b} + \mathbf{F}_{s} \tag{2.7}$$

the subscripts se, b, and s represent the aeroelastic forces, aerodynamic forces and mean wind forces, respectively; $\mathbf{Y}$, $\dot{\mathbf{Y}}$, and $\ddot{\mathbf{Y}}$ are the nodal displacement, velocity and acceleration vector, respectively; $\mathbf{M}$, $\mathbf{C}$ and $\mathbf{K}$ are the structural mass, damping and stiffness matrix, respectively.

Mean wind responses are usually dealt with separately in buffeting analysis.

Aeroelastic forces can be expressed as aeroelastic property matrices. The governing equation of motion of the bridge as a whole can therefore be written as

$$\mathbf{M\ddot{Y}} + \mathbf{C\dot{Y}} + \mathbf{KY} - \boldsymbol{\omega}^2\mathbf{A}_{se}\mathbf{Y} = \mathbf{F}_b \tag{2.8}$$

where $\mathbf{A}_{se}$ is the aeroelastic matrix of the structure.

This governing equation can be solved in the frequency domain.

During the early stages of research on buffeting analysis, the coupling effects between modes were neglected. However, Matsumoto et al. (1994) pointed out that aerodynamic coupling is important in predicting buffeting responses at high wind velocities. Jain et al. (1996) used the mode-superposition method in a buffeting analysis to take account of the inter-mode coupling effect. Since then, much research has been carried out on the buffeting analysis of long-span bridges with multi-mode coupling effects (e.g., Katsuchi et al., 1999; Chen et al., 2000a).

The computational load of the traditional mode-superposition method is heavy for long-span bridges. Xu et al. (1998) adopted the pseudo-excitation method for a buffeting analysis to reduce the computation load. Zhu and Xu (Zhu & Xu, 2005; Xu & Zhu, 2005) investigated the buffeting responses of a long-span bridge under skew winds with an FE-based buffeting analysis framework and the pseudo-excitation method.

2.2.2 Buffeting analysis in the time domain

The dynamic responses of a long-span bridge induced by both aeroelastic and aerodynamic forces can also be computed in the time domain. Compared with the frequency domain approach, time domain analysis offers the benefit of capturing the effects of nonlinearities of both structural and aerodynamic origins and also the influence of non-stationary features in the approaching wind in the analysis (Chen et al., 2000b).

Lin et al. (1983) expressed the aeroelastic forces per unit length in terms of convolution integrals in the time domain. As the aerodynamic derivatives are normally obtained from wind tunnel tests at discrete values of the reduced frequency, approximate expressions are needed to express them as continuous functions of the reduced frequency for time domain analysis (Roger, 1977). Similarly, the buffeting forces per unit length can be expressed in terms of convolution integrals involving aerodynamic impulse functions, which are associated with indicial aerodynamic functions (Scanlan, 1984) and fluctuating wind velocities (Chen et al., 2000b). The solution to the equation of motion in the time domain can be obtained with the Newmark-beta method. As the aeroelastic forces are dependent on motion, iteration is needed for each time-step until a certain convergence criterion is satisfied.

To conduct a buffeting analysis in the time domain, the wind field must be simulated, which is generally represented by turbulence wind components. The simulation of wind field can be achieved by either spectral representation or digital filtering method (Kareem, 2008).

The spectral representation methods appear to be most popular because they are fast and conceptually straightforward (e.g. Shinozuka & Jan, 1972; Deodatis, 1996; Yang et al., 1997). The Cholesky decomposition of the cross power spectral density matrix has been widely used in the spectral representation methods (e.g. Shinozuka & Jan, 1972). Li and Kareem (1995) introduced stochastic decomposition of the cross power spectral density matrix for the simulation of stationary random processes. Stochastic decomposition allows a relatively small number of modes to be involved in the simulation. Typical digital filtering methods use autoregressive–moving-average (ARMA) models to describe the stationary stochastic process in terms with two polynomials, one for the auto-regression and the second for the moving average (e.g. Samaras et al., 1985; Li & Kareem, 1990). The ARMA representation uses weighted recursive relations that connect the random quantity being simulated at successive time increments.

Indicial aerodynamic functions or aerodynamic impulse functions need to be transformed from aerodynamic derivatives and admittances measured from wind tunnel tests. Aerodynamic derivatives, admittances and wind spectra are all naturally frequency-domain functions. As a result, although the time-domain approach can capture structural and aerodynamic nonlinear effects, the frequency-domain approach still has a certain advantage in practice (Scanlan, 1993).

2.3 Finite element modeling for long-span bridges

2.3.1 Spine-beam model

The spine-beam model is an analytical model of a bridge in which the girder is represented by a series of beam elements. The spine-beam model is widely used in the FE modeling of long-span bridges because it is effective for capturing the dynamic characteristics and global structural behaviour of a bridge.

In the spine-beam model, the deck is usually modeled as a central beam (the spine beam) with equivalent cross-sectional properties. In the case of composite sections, the areas are converted to the area of one material according to a modular ratio. The neutral axes and moments of inertia about the vertical and transverse axes are determined in a similar way. The calculation of the torsional stiffness of the deck section should consider both pure and warping torsional constants (Wilson & Liu, 1991). The mass moment of inertia of the deck should include the mass moments of all of the members according to their distances to the centroid of the section.

In a spine-beam model, the other components of the bridge are modeled with beam or truss elements. Towers and piers are usually modeled with beam elements based on their geometric and material properties.

Constraints, usually spring elements, rigid links or direct coupling of nodal displacements, are necessary to connect different parts of the model together and to enforce certain types of rigid body behaviour. For example, rigid links are usually used to connect the spine beam with cables. Appropriate constraints are needed for the nodes of the deck, bearings and tower at their connections to restrain their motions in different directions.

Spine-beam models have been widely used for the dynamic analysis of long-span bridges (e.g., Wilson & Gravelle, 1991) because of their efficiency. Most of the current FE-based buffeting analyses of long-span bridges also use spine-beam models (e.g., Ding, et al., 2002; Xu & Zhu, 2005).

2.3.2 Multi-scale modeling

In practice, a large civil structure such as a long-span bridge is often modeled using the FE method for static and dynamic analyses at a global level. Stress concentration, crack initiation and propagation, fatigue and fracture are local phenomena that are often not represented in global structural models. However, many types of defects are locally generated and may evolve into global structural damage and possibly cause structural failure. A number of studies have been conducted to build detailed shell/solid element models for long-span bridges to capture their local performance. Fei et al. (2007) modeled the Tsing Ma Bridge tower with solid elements except for the steel trusses. More than 4000 solid elements were used in the tower model. Duan et al. (2011) used shell elements to model the deck plates of the Tsing Ma Bridge and solid elements to model the towers. The established bridge model contains 1.2 million DOF.

The large number of DOF resulting from such fine modeling can cause difficulties in dynamic analysis and model updating. Thus, the multi-scale modeling of large civil structures using different scales of elements has recently attracted increasing attention in structural engineering. Multi-scale modeling in structural engineering mainly aims to simultaneously provide both global and local structural information for a comprehensive assessment of structural safety. A typical multi-scale FE model of a long-span bridge contains a global model together with a few local models.

Li et al. (2001) adopted the two-step analysis strategy of building a simplified global FE model for the entire structure and a detailed local FE model for the region of interest. The structural analysis of the global model was conducted first to extract the results for the location of interest as the outer boundary conditions on the local model for further analyses. Nevertheless, the inherent difficulties in accurately modeling the complicated boundary conditions may lead to significant errors in a dynamic analysis. McCune et al. (2000) proposed a mixed dimensional coupling FE method that allows the shell/solid element model of the regions of interest to be incorporated into the simplified global beam element model through multi-dimensional constraint equations. The mixed dimensional coupling method has been applied to the multi-scale modeling of truss structures to connect detail models of joints with beam-element models of the truss (Li et al., 2009; Chan et al., 2009). This method has improved the modeling accuracy of the connections between the detailed local models and the less-refined parts of the global model. Only a small number of regions of interest, however, can be chosen when building such multi-scale models.

The sub-structuring method has also been used in recent years to include both global and local information on a long-span bridge in a single FE model. Ding et al. (2010) established a multi-scale FE model for the Runyang cable-stayed bridge. The local model of a deck segment was built with detailed geometry, whereas the other deck segments were simulated with equivalent orthotropic surface plates. The local models of all of the deck segments were then condensed and assembled into a global structure. The established model was used for damage detection with modal indices. Kong et al. (2012) condensed all of the deck segments of a long-span cable-stayed bridge except for the steel-concrete joint, which was the main focus of the study, to reduce the total number of DOF in the FE model. The dynamic responses of displacement and acceleration induced by vehicles were then calculated with the model.

The FE models established by these studies are all multi-scale models that are capable of providing both global and local responses. The sub-structuring method has an advantage in the modeling of the box decks of long-span bridges because it allows the geometry of all of the plates in the deck – and even the stiffeners – to be retained in substructures of segments, whereas the global solution handles only selected master DOF.

2.3.3 Sub-structuring method

The sub-structuring method uses matrix reduction to reduce the system matrices to a smaller set of DOF. By reducing the system matrices, the sub-structuring reduces the computation time, allowing a solution to very large problems to be found with limited computer resources.

For a large-scale structure such as a long-span bridge, the global structure can be divided into sub-structures. With the sub-structuring method, these sub-structures can be condensed into super-elements that contain only a limited number of master DOF and then assembled to represent the properties of the global structure. With smaller matrices to handle, analyses performed on the global structure are easier and more manageable. This method is particularly efficient when the substructures are identical (Garvey & Penny, 1994). For a structure with repeated patterns, such as the box deck of a long-span bridge, segments with the same geometry can be represented by one super-element, thereby saving a significant amount of computation time.

The sub-structuring method was developed in the 1960s. Guyan (1965) proposed the static condensation method to reduce the size of the stiffness and mass matrices. All of the structural complexity is preserved in the reduced stiffness matrix with this approach, but the reduced mass matrix is not accurate. The eigenvalue-eigenvector solution with the reduced property matrices is close but not exact. However, this method is still widely used due to its simplicity.

The component mode synthesis method (CMSM) is another method that has been widely used to reduce the property matrices of sub-structures. With the CMSM, only a few lowest modes of the sub-structures are retained for efficiency. A key issue with the CMSM is the determination of the modes of the sub-structures. Hurty (1965) and Craig and Bampton (1968) proposed the CMSM with fixed-interface conditions. MacNeal (1971) proposed the CMSM with free-interface conditions. The CMSM is particularly efficient at solving eigen-solutions and eigen-sensitivities (e.g., Heo & Ehmann, 1991; Lallemand, 1999).

Except for the modeling of large-scale structures, sub-structuring techniques have also gained growing attention in model updating and system identification of civil structures (e.g. Weng et al., 2011; Shi & Chang, 2011).

2.4 Model updating for long-span bridges

2.4.1 Model updating with dynamic properties only

Due to the uncertainties in models of large civil structures, model updating processes are usually needed after the initial establishment of the FE model to ensure modeling accuracy (e.g., Friswell, 1995; Brownjohn et al., 2011).

The choice of model updating methods for the entire FE model of a long-span bridge is limited because of the high computation demand of the updating algorithms. Sensitivity-based model updating with modal frequencies and mode shapes (using model assurance criteria (MAC) values) are often used in this situation (e.g., Jaishi et al., 2003; Ren et al., 2004). Mode shapes are difficult to identify accurately from field measurement data of long-span bridges because the number of sensors on such bridges is always limited and errors are often involved in the identification of the mode shapes from field measurement data. Measured modal frequencies are the most convenient updating objectives for long-span bridges, but may be affected by ambient temperature change (Catbas & Aktan, 2002).

FE models are an assembly of individual FEs, each of which is defined by its design parameters, such as its geometry or material properties.

Due to the discretized nature of FE models, iterative methods that work with a parameterized FE model, the 'error model', and introduce changes to a pre-defined number of design parameters on an elemental basis are widely used in FE model updating. The updating of the parameters is usually based on sensitivity analyses of selected parameters, and such methods are thus referred to as 'sensitivity-based model updating methods' (Friswell et al., 1995).

2.4.2 Model updating with dynamic properties and static responses

Static-based model updating is often used for short- and medium-span bridge structures (e.g., Chajes et al., 1997; Enevoldsen et al., 2002). Nevertheless, static-based model updating is seldom used in long-span cable-supported bridges, although static tests are often conducted on these bridges. Static tests and data processing are less complicated, and static measurements are usually more accurate than dynamic measurements. Static responses such as displacements and strains can thus be taken as promising objectives for model updating (Ren et al., 2011). Furthermore, static stress/strain responses can reflect the local behaviour of the structure (Wang et al., 2013). The scale factor between the mass and stiffness can also be considered by adding static responses to the model updating objectives.

In view of these developments, an FE updating method for long-span bridges that uses both dynamic characteristics and static responses may be a wise solution, but research in this area is limited.

2.4.3 Model updating of multi-scale FE models

A number of studies have been conducted to establish multi-scale models of long-span bridges (e.g., Chan et al., 2009; Li et al., 2009; Liu et al., 2009; Wang et al., 2013). However, model updating techniques for multi-scale FE models of large structures are still under investigation (Catbas et al., 2007; Wang et al., 2013).

Catbas et al. (2007) updated the FE model of a long-span bridge that was modeled with shell and beam elements by using identified dynamic properties together with static stress responses. The global and local updating were conducted separately. Schlune et al. (2009) used manual tuning and nonlinear optimisation to update the FE model of a long-span arch bridge. Modal frequencies and multiple static responses were included in the objective functions. Wang et al. (2013) developed a concurrent multi-objective optimisation method for updating multi-scale models of long-span bridges in which static displacement and stress are considered together with the modal frequency and mode shape. However, there are two deficiencies in using mode shapes in model updating. First, it is difficult to obtain accurate mode shapes for a large-scale structure due to the limited number of sensors (Ren et al., 2011). Second, large errors are often involved in the identification of mode shapes from field measurement data. Displacement and strain influence lines can be obtained more easily and accurately from field tests than mode shapes. Recently, the features of influence lines have begun to draw attention in bridge engineering. Zaurin and Catbas (2010) measured the influence lines of a four-span bridge using a fusion of video imaging and sensing data.

To ensure the multi-scale accuracy of multi-scale FE models, the model updating process needs to use both global and local measured data. Chan et al. (2009) updated a local model of truss joints with the nominal stress acquired from static tests. Wang et al. (2013) proposed a multi-objective optimisation technique and updated the refined segment model with global modal frequencies, MAC, static displacements and hot-spot stresses. The local updating processes in these studies were all applied only to a small portion of the entire FE model.

2.4.4 Response surface method

As mentioned, the traditional sensitivity-based updating method requires iterative FE analyses of the model. For a large FE model, such as a multi-scale model of a long-span bridge, the updating process consumes excessive computation time. One solution to this problem is to replace the FE model with an approximate meta-model that is more efficient in computation.

The response surface is one of the commonly used meta-models. Response surface methodology was originally used as an experimental design approach to determine the experimental factors that produce the best set of responses (Khuri & Cornell, 1996; Myers & Montgomery, 2002). This method has typically been used to help analysts or test engineers to quickly and efficiently explore a design space.

The response surface method has used in the model updating of FE models since the late 1990s (Doebling et al., 1999). Once the response surface of a model has been constructed, the FE model updating process can be performed with the response surface rather than the entire FE model. The use of this method in the field of damage detection has also been explored (Faravelli & Casciati, 2004; Rutherford et al., 2005).

Ren and Chen (2010) used the response surface method to update the model of a bridge. The objective function in the study was the residuals between the analytical and measured natural frequencies. Ren et al. (2011) updated a continuous box girder bridge model based on the measured static responses. Both studies showed that the response surface method remarkably improved the efficiency of the FE model updating process.

CHAPTER 3

CHARACTERISTICS OF DISTRIBUTED AERODYNAMIC FORCES ON A TWIN-BOX BRIDGE DECK

3.1 Introduction

As reviewed in Chapter 2, the disregard of the cross-sectional distribution of aerodynamic forces in traditional buffeting analyses may have a considerable impact on the accuracy of computed buffeting-induced stress responses. Although many studies have been performed on the pressure tests of sectional motionless bridge deck models, most of these studies focused on the aerodynamic admittance functions and/or the span-wise correlations of integrated aerodynamic forces rather than distributed aerodynamic pressures.

This chapter focuses on the characteristics of distributed aerodynamic forces on the surfaces of a bridge deck as a first-step towards a framework for buffeting-induced stress analysis. In this chapter, the formulation for distributed aerodynamic forces on the surfaces of a bridge deck is first derived based on the quasi-steady theory. The characteristics of distributed aerodynamic forces, such as distributed force coefficients, pressure admittances and span-wise pressure coherences, are introduced in the formulation. In consideration of different characteristics of incident and signature turbulences, the empirical mode decomposition (EMD) method is then adopted to separate their effects on the distributed aerodynamic forces. Wind tunnel pressure tests of a sectional motionless bridge deck model were conducted to identify the characteristics of distributed aerodynamic forces on the surfaces of the Stonecutters cable-stayed bridge with a twin-box bridge deck as a case study.

3.2 Distributed aerodynamic forces on a bridge deck

3.2.1 Formulation of distributed quasi-steady aerodynamic forces

Aerodynamic forces on a bridge deck result from wind pressures acting on the surfaces of the bridge deck. The distribution of aerodynamic forces can thus be represented by pressure distribution. Based on the quasi-steady assumption, wind pressure on a surface point of a motionless bridge deck section can be expressed as:

$$P_i(t) = \frac{1}{2}\rho\left[\left(\bar{U} + u(t)\right)^2 + w(t)^2\right] \cdot C_{pi}(\alpha_0 + \Delta\alpha) \tag{3.1}$$

where $P_i(t)$ is the time-history of wind pressure on the ith surface point of the bridge deck section; ρ is the density of air; $\bar{U}$ is the mean speed of the incoming wind flow; u and w are the longitudinal and vertical turbulence component, respectively; C_{pi} is the pressure coefficient of the ith surface point and is defined in the structural coordinates; α_0 is the mean angle of incidence; and $\Delta\alpha$ is the additional angle of incidence caused by turbulence. The definitions of structural coordinates, wind axes and angles of incidence can be found in Figure 3.1.

Because $\Delta\alpha$ is a comparatively small angle and u is much smaller than $\overline{U}$ for a normal wind resistance design, it can be assumed that

$$\Delta\alpha \approx \tan(\alpha) = \frac{w(t)}{\bar{U} + u(t)} \approx \frac{w(t)}{\bar{U}} \tag{3.2}$$

and therefore

$$C_{pi}(\alpha_0 + \Delta\alpha) \approx C_{pi}(\alpha_0) + C_{pi}^{'}(\alpha_0) \cdot \Delta\alpha \approx C_{pi}(\alpha_0) + C_{pi}^{'}(\alpha_0) \cdot \frac{w(t)}{\bar{U}} \tag{3.3}$$

where C'_{pi}=dC_{pi}/dα is the derivative of pressure coefficient with respect to the angle of incidence.

Substituting Eq.(3) into Eq.(1) and neglecting quadratic terms of $u(t)$ and $w(t)$ yields

$$P_i(t) = \frac{1}{2}\rho\bar{U}^2 \cdot C_{pi}(\alpha_0) + \frac{1}{2}\rho\bar{U}^2 \cdot \left[2C_{pi}(\alpha_0) \cdot \frac{u(t)}{\bar{U}} + C_{pi}^{'}(\alpha_0) \cdot \frac{w(t)}{\bar{U}} \right] \tag{3.4}$$

The first part of the right side of Eq.(4) is the static pressure, which has been well studied. Thus, aerodynamic pressure can be expressed as

$$P_{i.b}(t) = \frac{1}{2}\rho\bar{U}^2 \cdot \left[2C_{pi}(\alpha_0) \cdot \frac{u(t)}{\bar{U}} + C_{pi}^{'}(\alpha_0) \cdot \frac{w(t)}{\bar{U}} \right] \tag{3.5}$$

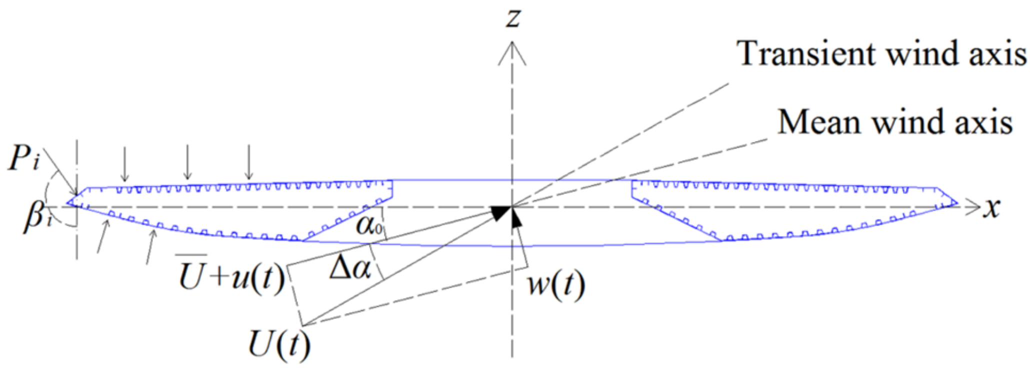

Figure 3.1 Wind coordinates and wind pressure on section outline

Since the quasi-steady assumption does not hold for most wind pressures acting on a bridge deck, the aerodynamic admittance function of wind pressure, which is similar to the aerodynamic admittance functions of integrated aerodynamic forces, should be introduced into Eq.(3.5). Therefore, the aerodynamic pressure can be expressed as

$$P_{i.b}(t) = \frac{1}{2}\rho\bar{U}^2 \cdot \left[2C_{pi}(\alpha_0)\cdot\chi_{pui}\cdot\frac{u(t)}{\bar{U}} + C_{pi}^{'}(\alpha_0)\cdot\chi_{pwi}\cdot\frac{w(t)}{\bar{U}} \right] \tag{3.6}$$

where χ_{pui} and χ_{pwi} are the aerodynamic pressure admittance functions of the fluctuating pressure at the *i*th surface point of the bridge deck with respect to the fluctuating wind u and w, respectively. The pressure admittance functions are the functions of reduced frequency and dependent on the geometrical configuration of the cross section of the bridge deck as well as their locations on the deck surface.

3.2.2. Relationships between distributed and integrated aerodynamic forces

In this subsection, the aerodynamic lift force is taken as an example to show the relationships between distributed aerodynamic pressures and traditionally-used integrated aerodynamic forces.

The aerodynamic lift force per unit length can be calculated as the integration of the distributed aerodynamic pressures on the same section as

$$F_{L,b}(t)=\sum_{i=1}^{N}P_{i,b}(t)\cdot\cos\left(\beta_i+\alpha_0\right)\cdot\delta_i \tag{3.7}$$

where $F_{L,b}$ is the aerodynamic lift force; β_i is the angle between pressure and vertical structural axis z (see Fig. 1); δ_i is the characteristic length on the deck section outline for the aerodynamic pressure $P_{i,b}$; and N is the total number of wind pressure points on the section where the pressures are measured.

Substituting Eq.(3.6) into Eq.(3.7) yields

$$F_{L,b}(t)=\frac{1}{2}\rho\bar{U}^2\cdot\sum_{i=1}^{N}\left[\left(2C_{pi}\left(\alpha_0\right)\cdot\chi_{Pu_i}\frac{u(t)}{\bar{U}}+C_{pi}^{'}(\alpha_0)\cdot\chi_{Pw_i}\frac{w(t)}{\bar{U}}\right)\cdot\cos\left(\beta_i+\alpha_0\right)\cdot\delta_i\right] \tag{3.8}$$

The relationship between the integrated aerodynamic lift coefficient C_L and the pressure coefficients C_{pi} can be derived based on the mean wind lift and the mean wind pressures as

$$C_L(\alpha_0)\cdot B=\sum_{i=1}^{N}C_{Pi}(\alpha)\cdot\cos\left(\beta_i+\alpha_0\right)\cdot\delta_i \tag{3.9}$$

where B is the deck width as a reference length.

Let us define the distributed lift coefficient C_{Li} and drag coefficient C_{Di} in wind coordinates for wind pressure at the ith surface point as

$$C_{Li}(\alpha_0) = C_{Pi}(\alpha_0)\cdot\cos\left(\beta_i + \alpha_0\right)\cdot\delta_i \tag{3.10}$$

$$C_{Di}(\alpha_0) = C_{Pi}(\alpha_0)\cdot\sin\left(\beta_i + \alpha_0\right)\cdot\delta_i \tag{3.11}$$

Eq.(3.8) can then be rewritten as

$$F_{L,b}(t) = \frac{1}{2}\rho\bar{U}^2\cdot\sum_{i=1}^{N}\left\{2C_{Li}(\alpha_0)\cdot\chi_{Pu_i}\frac{u(t)}{\bar{U}} + \left[C_{Li}^{'}(\alpha_0) + C_{Di}(\alpha_0)\right]\cdot\chi_{Pw_i}\frac{w(t)}{\bar{U}}\right\} \tag{3.12}$$

The aerodynamic lift force acting on a bridge deck section is traditionally expressed as

$$F_{L,b}(t) = \frac{1}{2}\rho\bar{U}^2 B\left[2C_L\chi_{Lu}\frac{u(t)}{\bar{U}} + (C_L^{'} + C_D)\chi_{Lw}\frac{w(t)}{\bar{U}}\right] \tag{3.13}$$

where χ_{Lu} and χ_{Lw} are the aerodynamic admittance functions of the integrated aerodynamic lift force with respect to the fluctuating wind u and w, respectively.

The comparison Eq.(3.12) with Eq.(3.13) gives us the relationships between the integrated force admittance functions and the pressure admittance functions.

$$\chi_{Lu} = \frac{\sum_{i=1}^{N}\chi_{Pui}\cdot C_{Li}(\alpha_0)}{B\cdot C_L(\alpha_0)},\quad \chi_{Lw} = \frac{\sum_{i=1}^{N}\chi_{Pwi}\cdot\left[C_{Li}'(\alpha_0) + C_{Di}(\alpha_0)\right]}{B\cdot\left[C_L^{'}(\alpha_0) + C_D(\alpha_0)\right]} \tag{3.14}$$

Eq.(3.14) shows that the integrated force admittance is the average of the corresponding pressure admittances weighed by the distributed aerodynamic coefficients in wind coordinates, indicating that the information on the non-uniform cross-sectional distribution of pressure admittances is lost in this averaging process. The pressure admittance and its distribution, on the other hand, will provide more information on wind effects on a bridge deck.

3.2.3. Identification of pressure admittance

The auto-spectrum of aerodynamic pressure can be obtained based on Eq.(3.6) through Fourier transformation and by ignoring the cross-spectrum between the turbulence components *u* and *w* (Larose, 1999).

$$S_{Pi}(\omega) = \frac{1}{4}\rho^2 \bar{U}^2 \cdot \left[4C_{pi}^2 \cdot \left|\chi_{pui}\right|^2 \cdot S_u(\omega) + C_{pi}^{'\,2} \cdot \left|\chi_{pwi}\right|^2 \cdot S_w(\omega) \right] \tag{3.15}$$

where $S_{Pi}(\omega)$ is the auto-spectrum of aerodynamic pressure; $S_u(\omega)$ and $S_w(\omega)$ are the auto-spectra of turbulence components *u* and *w* respectively; and $|\quad|$ is the operation of module. Due to the practical difficulty in the identification of aerodynamic admittances, it is assumed that the equivalent aerodynamic pressure admittance $\chi_{pi} = \chi_{pui} = \chi_{pwi}$, and the square of the module of the equivalent aerodynamic pressure admittance can then be expressed as

$$\left|\chi_{P_i}(\omega)\right|^2 = \frac{S_{Cp_i}(\omega) \cdot \bar{U}^2}{4C_{pi}^2(\alpha_0) \cdot \dfrac{S_u(\omega)}{\bar{U}^2} + C_{pi}^{'2}(\alpha_0) \cdot \dfrac{S_w(\omega)}{\bar{U}^2}} \tag{3.16}$$

where $S_{Cpi}(\omega)=4S_{pi}(\omega)/\rho^2\,\bar{U}^2B^2$ denotes the normalized auto-spectrum of the *i*th pressure coefficient C_{pi}.

The aerodynamic pressure admittance functions directly identified from the measured wind and pressure time histories based on Eq.(3.16) often involves high frequency peaks due to signature turbulence, which is the turbulence produced by the structure itself in the flow even if the incoming flow is perfectly smooth. Such pressure admittance functions, which are difficult to be fitted with rational functions, cause difficulty in buffeting analysis (Zhu et al. 2009). In this study, a decomposition method is proposed in Section 3.7 to decompose measured pressure time-histories into incident and signature turbulence induced components. Because signature turbulence effects (high frequency) are largely separated from incident turbulence effects (low frequency), the admittance functions can be identified for them separately assuming these two parts are uncorrelated.

Suppose a pressure time-history is decomposed into incident and signature turbulence induced components as

$$P_{i.b}(t) = P_{I,i}(t) + P_{S,i}(t) \tag{3.17}$$

where $P_{I,i}$ and $P_{S,i}$ are the incident turbulence induced component and signature turbulence induced component, respectively.

The admittance function of each component can be identified from its corresponding time-history as

$$\left|\chi_{P_{I,i}}(\omega)\right|^2 = \frac{S_{Cp_{I,i}}(\omega)\cdot\bar{U}^2}{4C_{pi}^2(\alpha_0)\cdot\frac{S_u(\omega)}{\bar{U}^2} + C_{pi}^{'2}(\alpha_0)\cdot\frac{S_w(\omega)}{\bar{U}^2}} \tag{3.18}$$

$$\left|\chi_{P_{S,i}}(\omega)\right|^2 = \frac{S_{Cp_{S,i}}(\omega)\cdot \bar{U}^2}{4C_{pi}^2(\alpha_0)\cdot \frac{S_u(\omega)}{\bar{U}^2} + C_{pi}'^2(\alpha_0)\cdot \frac{S_w(\omega)}{\bar{U}^2}} \tag{3.19}$$

where $\chi_{pI,i}$ and $\chi_{pS,i}$ are the admittance functions of incident and signature components respectively; $S_{CpI,i}(\omega)=4S_{pI,i}(\omega)/\rho^2\bar{U}^2B^2$ and $S_{CpS,i}(\omega)=4S_{pS,i}(\omega)/\rho^2\bar{U}^2B^2$ denote the non-dimensional auto-spectrum of $P_{I,i}$ and $P_{S,i}$ respectively.

3.2.4. Span-wise coherence function of pressure

Span-wise coherence function of aerodynamic pressures can commonly be defined and calculated as

$$\mathrm{Coh}_{\alpha_1\alpha_2}^{1/2}(K_\Delta) = \frac{\left|S_{\alpha_1\alpha_2}^{cr}(K_\Delta)\right|}{\sqrt{S_{\alpha_1}(K_\Delta)S_{\alpha_2}(K_\Delta)}} \tag{3.20}$$

where $\mathrm{Coh}^{1/2}(K_\Delta)$ is the root coherence function; α_1 and α_2 can be turbulence components, aerodynamic forces or pressures; $K_\Delta=f\Delta/U$ is the reduced frequency with respect to the span-wise distance Δ between α_1 and α_2; $S^{cr}(K_\Delta)$ is the cross-spectrum between α_1 and α_2; $S_{\alpha1}$ and $S_{\alpha2}$ are the auto-spectrum of α_1 and α_2 respectively.

The root coherence function is conventionally fitted with an exponential decay function (Davenport, 1961). The root coherence function can be fitted as

$$Coh_{\alpha_1\alpha_2}^{1/2}(K_\Delta) == A\cdot e^{-CK_\Delta} \tag{3.21}$$

where A is the root coherence peak value at zero reduced frequency, which is adopted to cater for the situation where the root coherence is not equal to 1 when K_Δ is 0 (Hui, 2006); and C is the decay factor.

After the decomposition of a pressure time-history into the two parts, the span-wise coherence of incident turbulence component can be directly calculated by Eq.(3.20) and fitted by Eq.(3.21). Unlike the incident turbulence component, the peak value of span-wise coherence of signature turbulence component appears at the predominant signature frequency, which is not zero, of the deck section. As a result, the shape of span-wise coherence function of signature component varies with Δ (see the discussion in Section 3.5). To avoid this problem, the span-wise root coherence of signature turbulence induced pressure is presented with a new reduced frequency $K_{\Delta S}$ defined as

$$K_{\Delta S} = \frac{|f - f_s|\Delta}{U} \tag{3.22}$$

where f_s is the predominant frequency of the signature turbulence induced pressure.

The new reduced frequency $K_{\Delta S}$ is then used instead of K_Δ so that the peak value of the root coherence function occurs at zero reduced frequency and the root coherence value decays exponentially with the increase of the new reduced frequency.

In summary, the span-wise coherence functions of incident and signature pressure components can be calculated as

$$\mathrm{Coh}^{1/2}_{P_{I,1}P_{I,2}}(K_{\Delta}) = \frac{\left| S^{cr}_{P_{I,1}P_{I,2}}(K_{\Delta}) \right|}{\sqrt{S_{P_{I,1}P_{I,1}}(K_{\Delta}) S_{P_{I,2}P_{I,2}}(K_{\Delta})}} \tag{3.23}$$

$$\mathrm{Coh}^{1/2}_{P_{S,1}P_{S,2}}(K_{\Delta S}) = \frac{\left| S^{cr}_{P_{S,1}P_{S,2}}(K_{\Delta S}) \right|}{\sqrt{S_{P_{S,1}P_{S,1}}(K_{\Delta S}) S_{P_{S,2}P_{S,2}}(K_{\Delta S})}} \tag{3.24}$$

Both Eq.(3.23) and Eq.(3.24) can be fitted with exponential decay functions.

3.3 Sectional bridge deck model and wind tunnel tests

3.3.1 Stonecutters Bridge and its pressure-tapped sectional deck model

Stonecutters Bridge is a two cable-plane cable-stayed bridge with a twin-box deck carrying dual 3-lane highway traffic. The bridge is currently the world's third longest cable-stayed bridge with a main span of 1018m. The typical cross section of the bridge deck in the main span is shown in Figure 3.2.

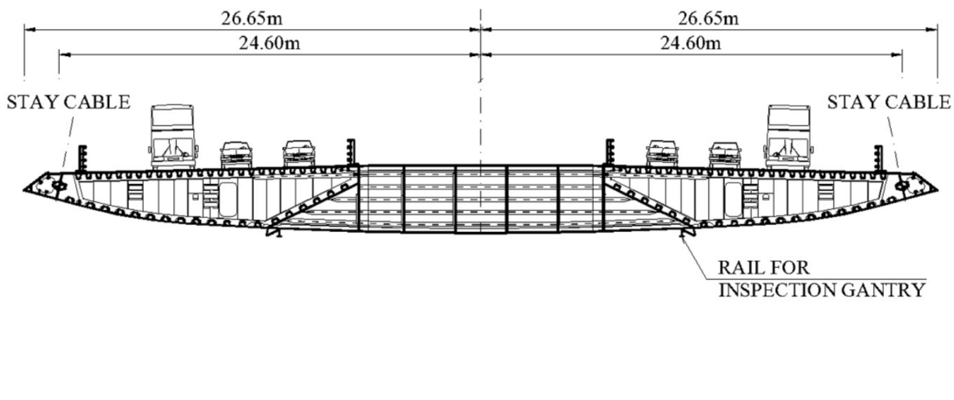

Figure 3.2 Typical cross section of bridge deck in main span

All pressure measurements were conducted on a motionless sectional deck model which represents the typical deck geometry of Stonecutters Bridge. The model was 3m in length with a length scale of 1:80 (see Figure 3.3a). The 1 m central portion of the model was installed with 7 pressure-tapped acrylic strips to measure time-histories of surface pressures. The strips were spaced at 1/8, 1/4, 1/2, 1, 2 and 4 times the chord length of a single box, which is 0.244m, to investigate the span-wise correlation of aerodynamic pressures. Each strip was fitted with 64 pressure taps distributed around the twin-box deck. Locations of the pressure taps are shown in Figure 3.3b with the coordinate systems of aerodynamic forces. The pressure taps on the windward box are denoted with numbers 101 to 132 and the pressure taps on the leeward box are denoted with 201 to 232.

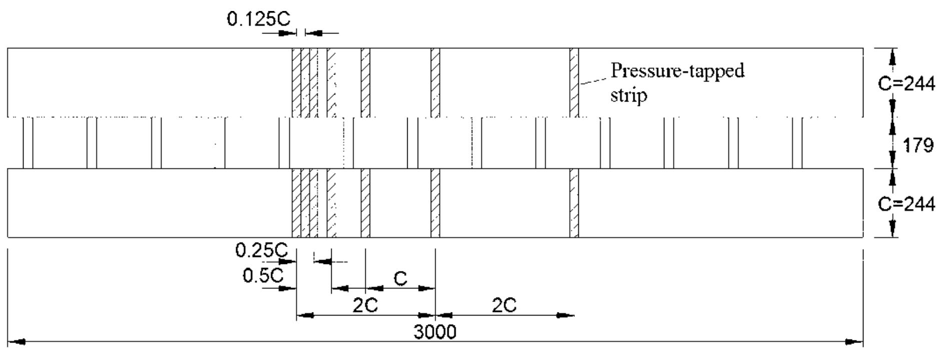

(a) Position of pressure-tapped strips (Unit: mm)

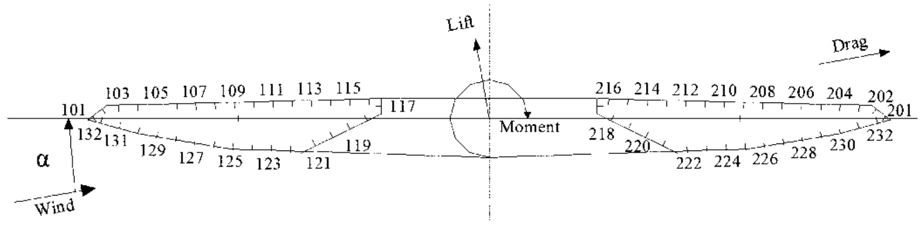

(b) Position of pressure taps

Figure 3.3 Positions of the pressure strips and taps

3.1.2. Simulation of turbulent wind flow field

Turbulent wind flow fields were simulated with horizontal and vertical fences at 8.5m upstream of the model. Two turbulent flow fields with different turbulence intensities (T.I.) were simulated as shown in Figure 3.4: one represents an open ocean fetch and the other an over-land fetch.

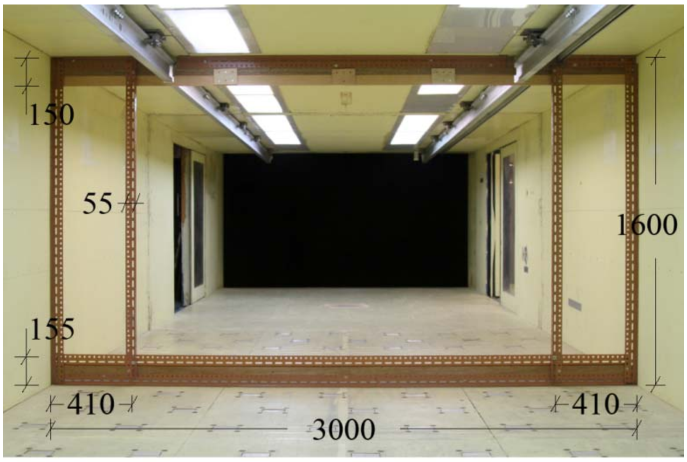

(a) Open ocean fetch (T.I. =6%)

(b) Over-land fetch (T.I. =14%)

Figure 3.4 Wind tunnel simulation of turbulent wind fields (unit: mm)

3.1.3. Wind tunnel pressure tests

Figure 3.5 shows the pressure-tapped sectional model mounted in the wind tunnel and the locations of pitot tube and cobra probe which were used to calibrate mean wind speed and record transient 3D turbulences, respectively. The model was further stabilized with guy wires to avoid vibration. Pressure tests were conducted in two types of turbulent wind flow fields at wind speed of 15m/s with -3º, 0º and +3º angles of incidence for the time-histories of aerodynamic pressures induced by turbulent wind. Additional tests were conducted in smooth flow field at wind speed of 15m/s with ±5º, ±4º, ±3º, ±2º, ±1º and 0º angles of incidence for mean aerodynamic coefficients and their derivatives with respect to angle of incidence. The time-histories of aerodynamic pressures from totally 448 pressure-taps were acquired and collated. The time-histories of aerodynamic forces could also be obtained by integration of the pressure. The time histories of 3-D wind speeds were recorded by cobra probes simultaneously with the pressure measurements.

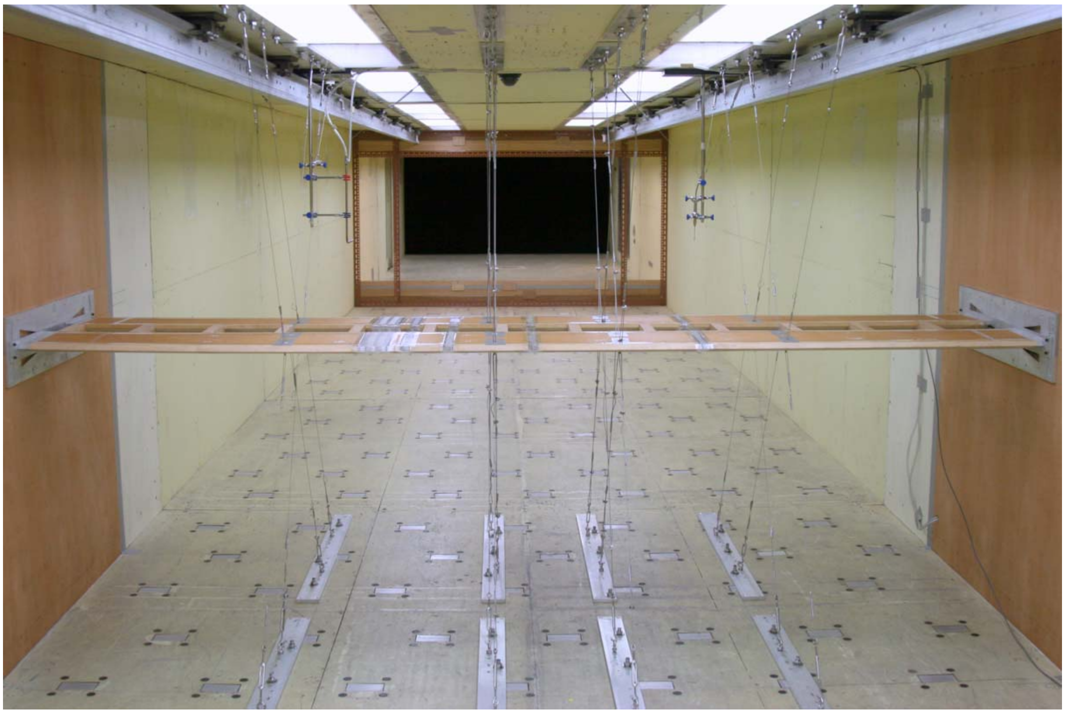

Figure 3.5 Sectional deck model in the wind tunnel

3.4 Characteristics of simulated turbulent field

Two turbulent flow fields with different turbulence intensities (T.I.) were simulated to represent the open ocean fetch and the over-land fetch respectively. Measured turbulence intensity is defined as

$$I_u = \frac{\sigma_u}{\bar{U}} = \frac{\sqrt{\overline{u^2}}}{\bar{U}}; \quad I_w = \frac{\sigma_w}{\bar{U}} = \frac{\sqrt{\overline{w^2}}}{\bar{U}} \tag{3.25}$$

where σ_u and σ_w are the standard deviation of u and w respectively.

The vertical fluctuation is usually more dominant in buffeting analysis so the two turbulence fields are denoted by the vertical turbulence intensity as T.I=6% and

T.I=14%. The integral length scales listed in Table 3.1 are estimated by using Equation (3.26) with the assumption that the vortex patterns do not change as wind sweeps them leeward.

$$
\begin{aligned}
L_{ux} &= \bar{U}\int_0^t c_{ux}(\tau)d\tau, \quad c_{ux}(\tau) = \frac{1}{T}\int_0^T [u(t)\cdot u(t+\tau)]dt / \sigma_u^2 \\
L_{wx} &= \bar{U}\int_0^t c_{wx}(\tau)d\tau, \quad c_{wx}(\tau) = \frac{1}{T}\int_0^T [w(t)\cdot w(t+\tau)]dt / \sigma_w^2
\end{aligned}
\tag{3.26}
$$

where L_{ux} and L_{wx} are the integral length scales of u and w in the longitudinal direction; c_{ux} and c_{wx} are the auto-covariance of u and w.

Table 3.1 Measured turbulence intensities and integral length scales

Flow field	I_u (%)	I_w (%)	L_{ux} (m)	L_{wx} (m)
T.I=6%	7	6	0.325	0.175
T.I=14%	17	14	0.375	0.175

Figure 3.6 shows the auto-spectra of turbulent components u and w. For the convenience of comparison between the force and pressure spectra, the turbulence spectra are presented with respect to the reduced frequency $K=fB/\overline{U}$. The auto-spectra indicate that the energy of turbulence is mainly concentrates in the reduced frequency range from 0.0 to 0.6.

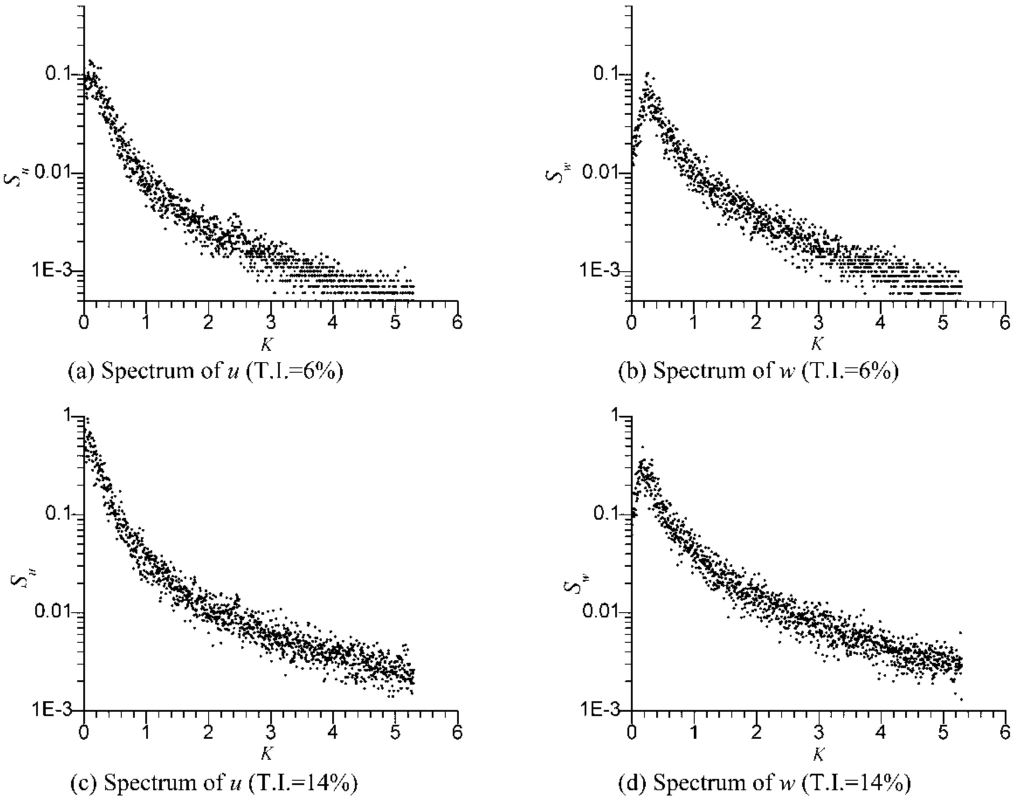

Figure 3.6 Auto-spectra of turbulent components u and w

Figure 3.7 shows the measured and fitted span-wise root coherence of turbulence components u and w with 6% turbulence intensity. The root coherences presented combines 5 groups of coherence data which are obtained for the span-wise distance Δ of 1/8, 1/4, 1/2, 1, and 2 times the chord length of a single box respectively (so as other root coherence figures presented in this chapter). The root coherence of turbulence can be fitted quite well with exponential decay curves.

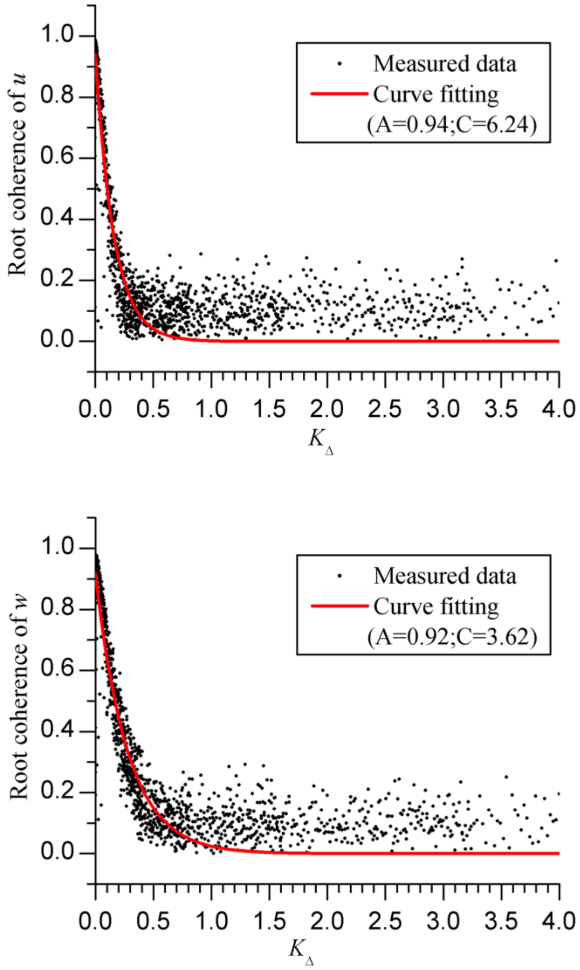

Figure 3.7 Span-wise root coherence of turbulence (T.I.=6%)

3.5 Characteristics of integrated aerodynamic forces

Mean aerodynamic force coefficients and their derivatives with respect to angle of incidence are calculated for integrated aerodynamic forces on the sectional model, and the results are listed in Table 3.2. The aerodynamic admittances of the integrated buffeting forces (drag, lift and pitching moment) are depicted in Figure 3.8a~c and Figure 3.9. Figure 3.8 a~c show the aerodynamic admittances of the integrated buffeting forces with angle of incidence of 0º for the two turbulence fields. Figure 3.8d compares the power spectrum density (PSD) functions of the lift force in the turbulent flow with those in the smooth flow at different wind speeds. Figure 3.9 shows the aerodynamic admittance of the integrated forces with -3º, 0º and +3º angle of incidence for the low turbulent field of 6% turbulence intensity.

Table 3.2 Mean aerodynamic force coefficients and their derivatives

α	C_D	C_L	C_M	C'_D	C'_L	C'_M
-3º	0.0458	-0.2704	-0.0044	-0.1386	4.0027	0.6524
0º	0.0426	-0.1003	0.0295	-0.0490	2.8741	0.8643
+3º	0.0484	0.1038	0.0703	0.2553	3.4827	1.2044

As shown in Figure 3.8 and Figure 3.9, all the force spectra and aerodynamic admittances have two notable peaks. One peak appears at the reduced frequency around 0.3, which is consistent with the spectral peak of vertical turbulence component *w*. The other peak appears at a reduced frequency about 3.95 for a 15m/s wind and about 3.16 for a 12m/s wind in the smooth flow. The proportionality of reduced frequency and wind speed indicates that this peak results from the predominant vortex shedding frequency or, in another word, the predominant signature turbulence frequency of the deck section. The Strouhal number St as defined in Equation (3.27) of the deck is estimated around 0.26. The number is generally consistent with the study carried out by Kwok et al. (2012).

$$\mathrm{St} = \frac{fD}{U} \tag{3.27}$$

where *D* is the depth of the section.

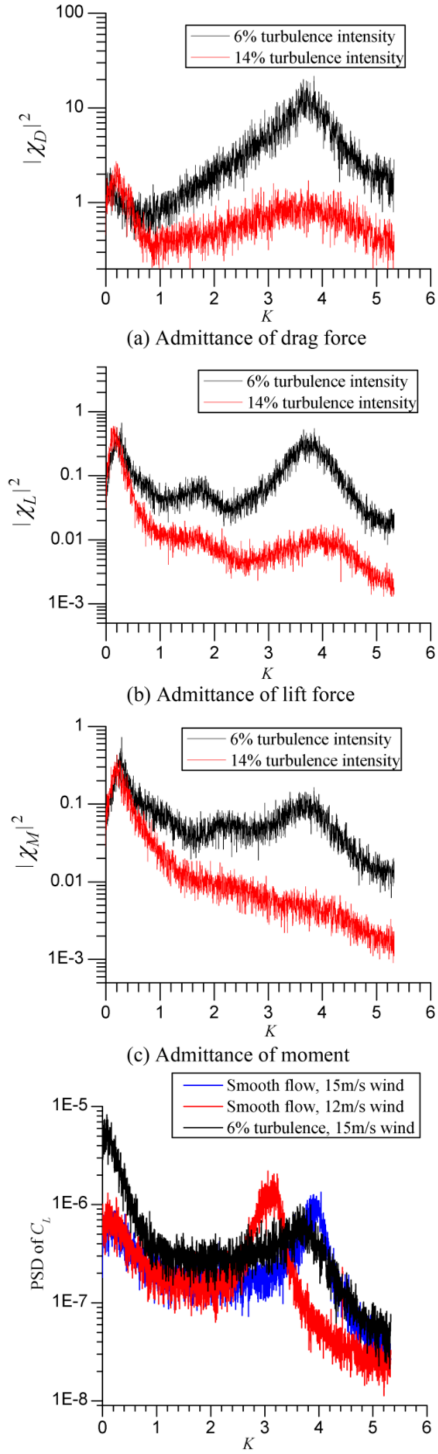

(a) Admittance of drag force

(b) Admittance of lift force

(c) Admittance of moment

(d) PSD of lift force

Figure 3.8 Aerodynamic admittance and PSD of integrated forces in different flow fields with 0° angle of incidence

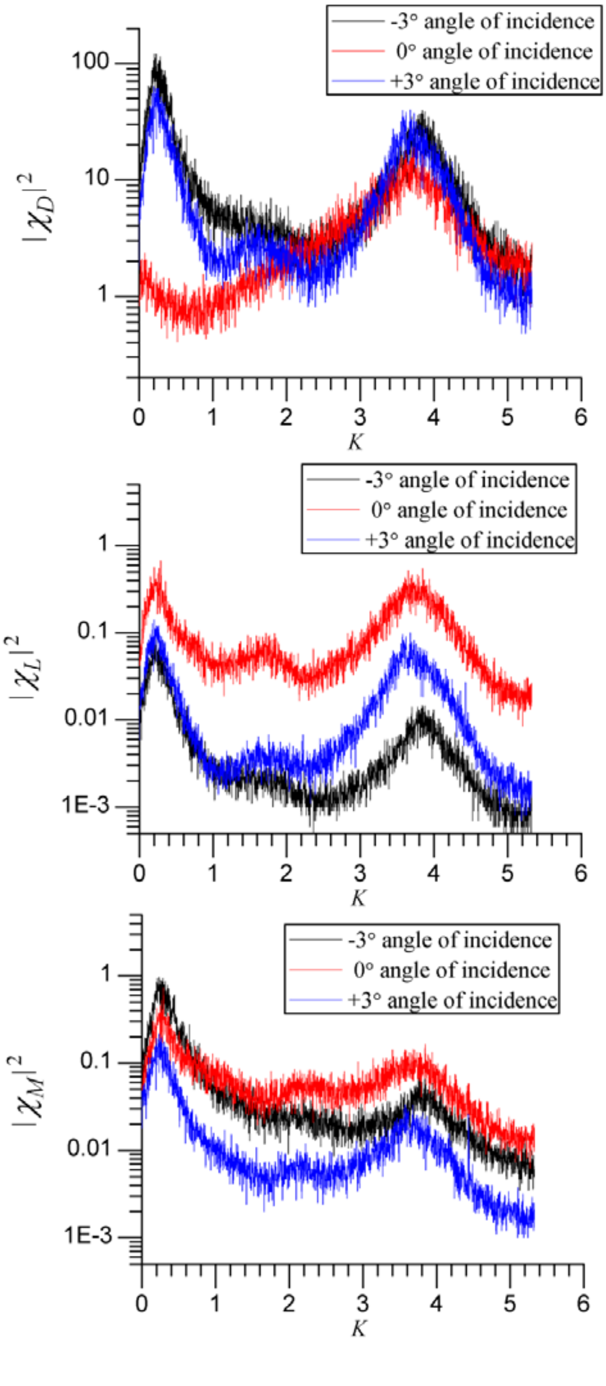

Figure 3.9 Aerodynamic admittance of integrated forces with different angles of incidence (T.I=6%)

As shown in Figure 3.8, the signature turbulence peak of turbulent flow is slightly smaller than that of smooth flow. This may attribute to the interference by the incoming turbulence.

It should be noted that the vortex shedding of such a complicated twin-box section should yield more than one signature frequencies. As shown in Figure 3.8 and Figure 3.9, smaller peaks appear within the reduced frequency range from 1.6 to 2.4 and probably represent some minor signature turbulences. In this study, only the predominant signature turbulence frequency is taken into consideration in the subsequent analysis to simplify the problem.

As shown in Figure 3.8, the signature turbulence has a significant influence on the buffeting forces at high reduced frequency, and such influence is larger with lower turbulence intensity. It can be seen that the signature turbulence effect can be separated from the incident turbulence effect in the frequency domain as the latter mainly dominates the low reduced frequency range. This provides a possibility of analyzing the two types of turbulence effects separately. Besides, the fact that signature turbulence mainly affects high reduced frequency range suggests that its influence is more critical at low wind speed.

Figure 3.10 shows the span-wise root coherence of integrated buffeting forces. As mentioned above, the signature turbulence effect on the deck section has a fixed predominant reduced frequency $K=fB/\overline{U}$ around 4, which should also be the reduced frequency of the signature turbulence coherence peak regardless of the span-wise distance Δ. As a result, when multi-groups of measured coherence are presented with respect to $K_\Delta=f\Delta/\overline{U}$ in the same figure, multiple signature turbulence peaks appear. The multi-peak coherence is difficult to be fitted with either the conventionally used exponential decay function or other simple rational functions. This phenomenon further justifies the need to separately the analysis of incident and signature turbulence induced pressures. The decomposition of these two types of effects on buffeting pressures is introduced in Section 3.7.

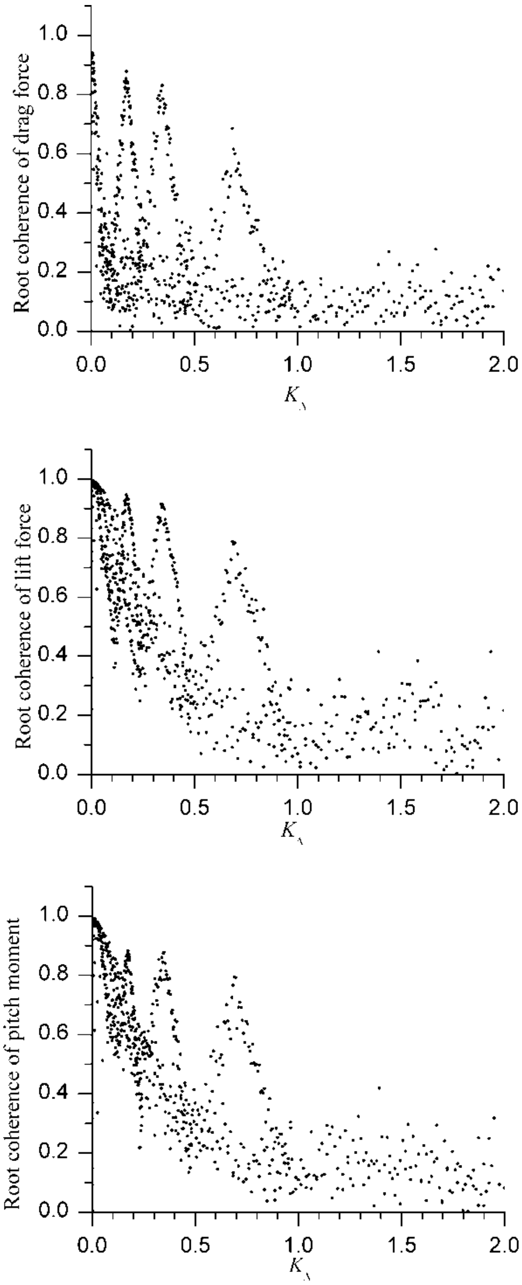

Figure 3.10 Span-wise root coherence of integrated buffeting forces (T.I.=6%)

3.6 Distribution of mean and RMS value of pressure

Figure 3.11 shows the cross-sectional distribution of mean pressure coefficients. Most of the pressure taps yield negative pressure coefficients. The Largest negative pressure coefficients occur on windward corners of both windward and leeward boxes at -3°, 0° and +3° angle of incidence. This indicates the flow separates at these locations. Positive pressures occur at pressure taps 101, 102 and 217, which contribute the largest part to mean drag force. The cross-sectional distribution of C_p of this deck section has also been studied by Kwok et al. (2012). The results are generally consistent with this study.

Figure 3.12 shows the derivatives of pressure coefficients with respect to angle of incidence, which are the quasi-steady multiplier on the turbulence component w. The derivatives were calculated by central difference method. It can be seen from the comparison of Figure 3.11 with Figure 3.12 that the value of C'_p is much larger than the value of $2C_p$, which is the quasi-steady multiplier on the turbulence component u. This fact indicates that the vertical turbulence w has a much larger impact on the buffeting forces than the longitudinal turbulence u. As a result, Figure 3.12 largely represents the quasi-steady cross-sectional distribution of the buffeting forces. Figure 3.12 also indicates that from a quasi-steady point of view, the buffeting forces on the windward box are larger than those on the leeward box.

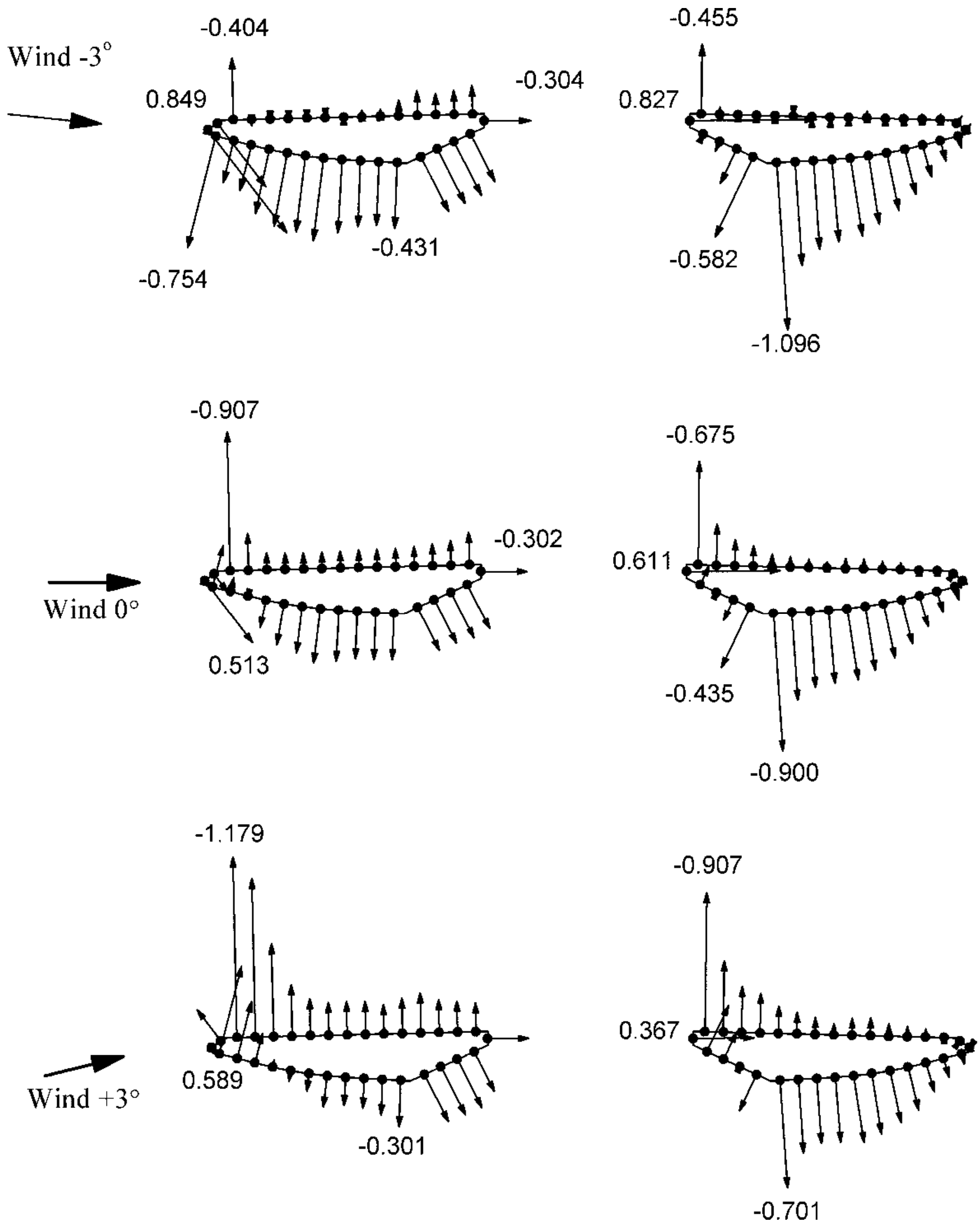

Figure 3.11 Distribution of mean pressure coefficients C_p

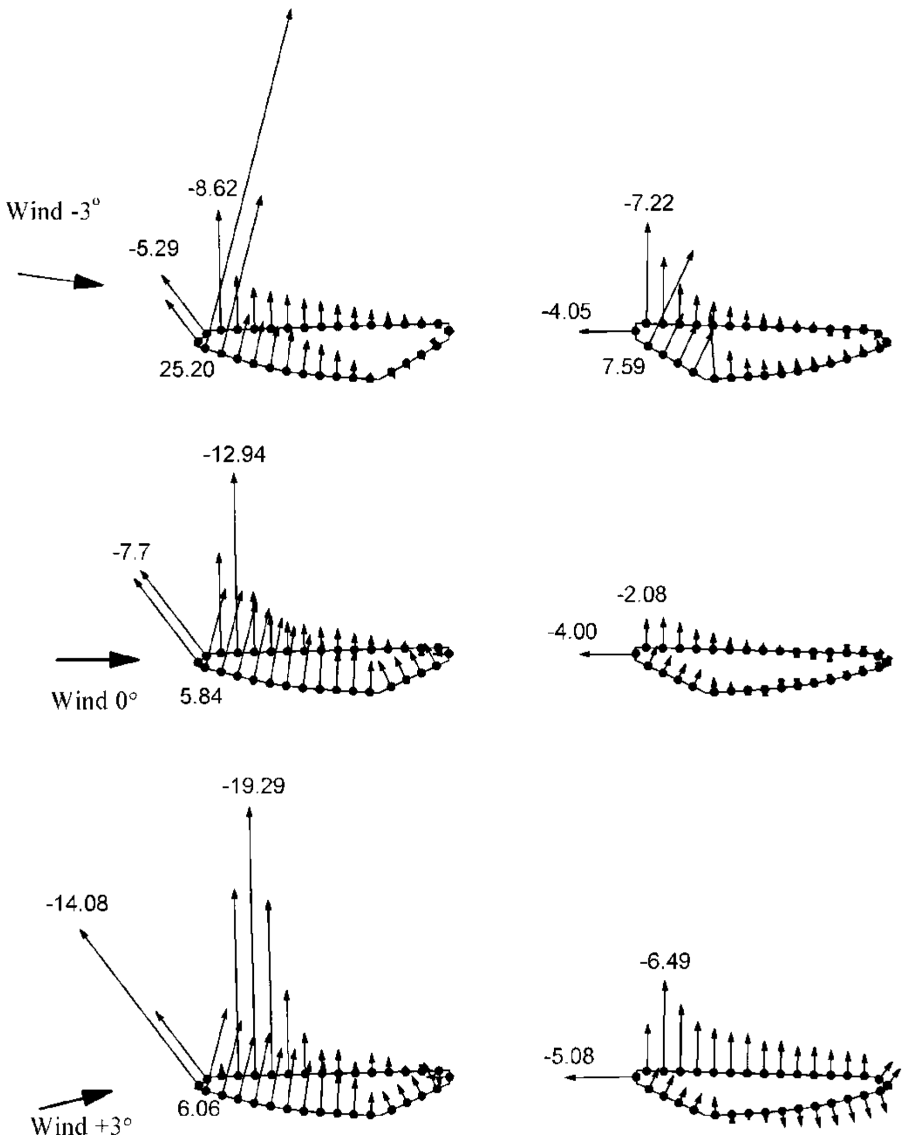

Figure 3.12 Distribution of derivatives of mean pressure coefficients C'_p

Figure 3.13 depicts the root mean square (RMS) value of instantaneous pressure coefficients C_p and shows the general cross-sectional distribution of fluctuating pressure. Although it can be concluded that the windward box bears a larger fluctuating forces, the difference between the fluctuating pressure acting on windward and leeward boxes is not as large as suggested by Figure 3.12. This is mainly because that the quasi-steady theory does not hold in this case where signature turbulence effect is strong. The results indicate that the cross-sectional distribution of buffeting pressure is not uniform, and the exact distribution can hardly be estimated by quasi-steady aerodynamic coefficients. It is necessary to investigate the fluid-structure interaction in terms of the cross-sectional distribution of buffeting pressure. The cross-sectional distributions of C_p and RMS of C_p of this deck section have also been studied by Kwok et al. (2012). The results are generally consistent with this study.

3.7 Decomposition of buffeting pressure time-series

Like the spectra of buffeting forces, the spectra of buffeting pressures also have signature turbulence peaks. The span-wise coherences of buffeting pressures also have multiple signature turbulence peaks. To further investigate the cross-sectional distribution of signature turbulence effects, the empirical mode decomposition (EMD) method (Huang et. al., 1998; Xu and Chen, 2004; Chang & Poon, 2010) is employed to decompose each fluctuating pressure time-history into incident turbulence and signature turbulence induced parts. Firstly, a pressure time-history is decomposed by EMD into several intrinsic mode functions (IMFs). Then, the IMFs representing the low frequency incident turbulence effect and high frequency signature turbulence effect are added up respectively to form two time-histories: one mainly caused by incident wind turbulence and the other by signature turbulence.

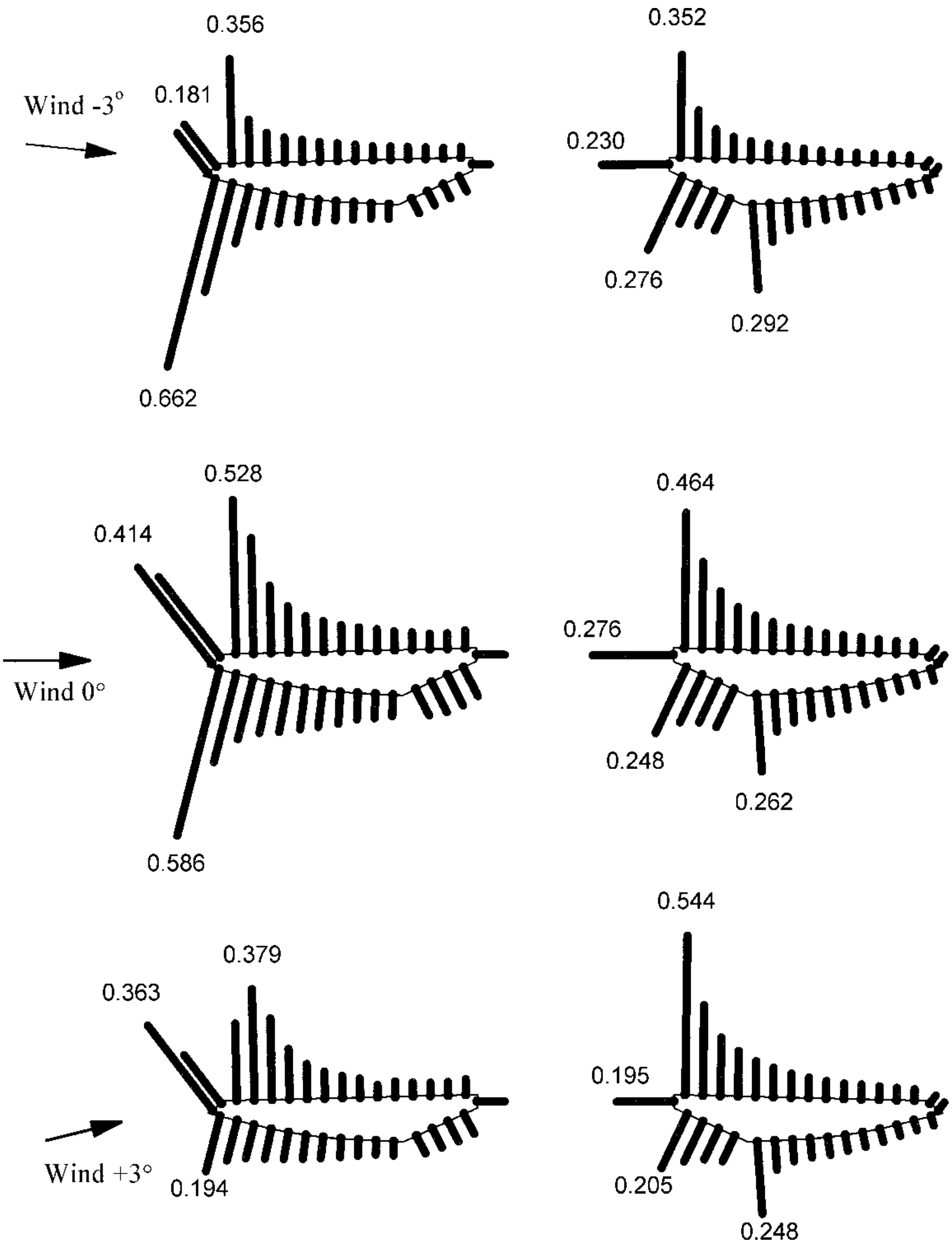

Figure 3.13 Distribution of the RMS values of the measured instantaneous pressure coefficients (T.I.=6%)

Figure 3.14, Figure 3.15 and Figure 3.16 give an example of the decomposition of a pressure time-history. Figure 3.14 shows the power spectral density (PSD) functions of a measured pressure time-history and its first 6 IMFs after EMD. As shown in Figure 3.14, the first decomposed IMF can largely represent the predominant signature turbulence component in the pressure. The second and third IMFs probably represent other minor signature turbulence components. Therefore, the first three IMFs can be added up to represent the signature turbulence induced component of the pressure in this case. The fourth to fifteenth IMFs generally fall into the frequency range of incident turbulence (the seventh to fifteens IMFs have comparatively smaller values and therefore are not depicted in Figure 3.14). Therefore, they were added up to represent the incident turbulence induced component of the pressure. Figure 3.15 depicts the time-histories of the original and decomposed pressure time histories. Figure 3.16 shows the PSDs of the original and decomposed pressures. It should be noted that the original incident component as shown in Figure 3.15 contains the mean pressure while in the following analyses the mean values were removed from all the time-histories.

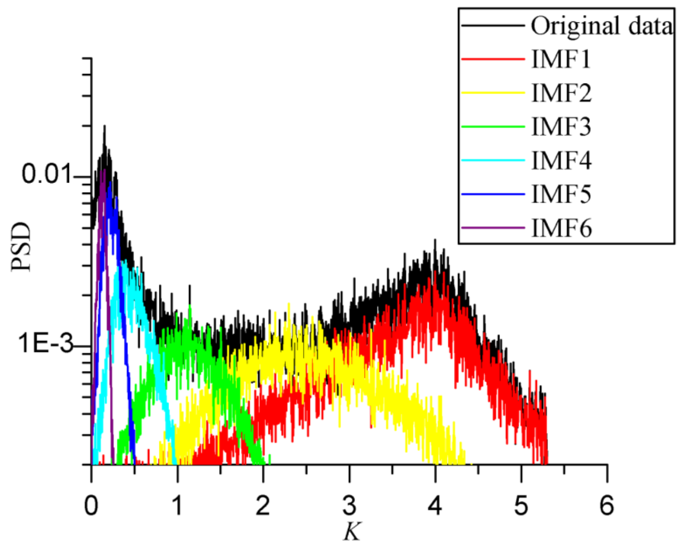

Figure 3.14 EMD results of a pressure time-history

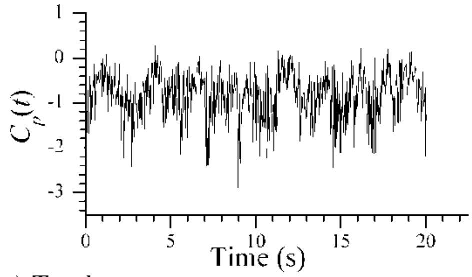

(a) Total pressure

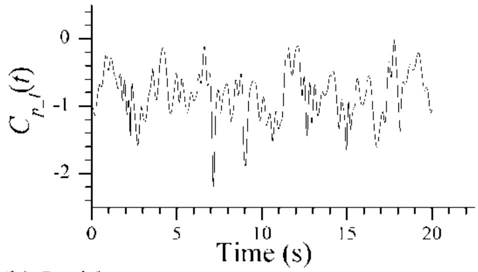

(b) Incident component

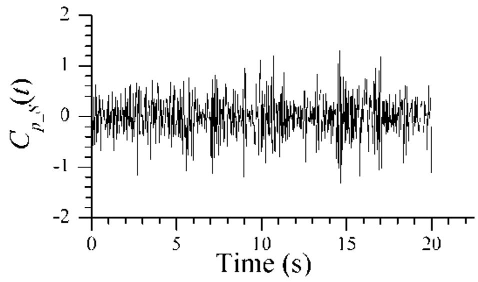

(c) Signature component

Figure 3.15 Decomposition of a pressure time-history in time domain

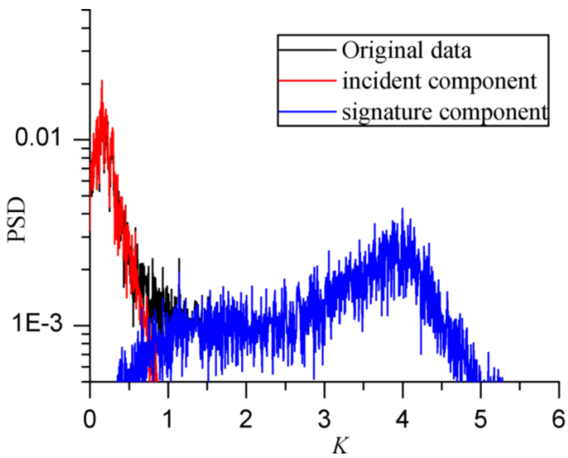

Figure 3.16 PSD of a pressure time-history and its components after decomposition

3.8 Distribution of aerodynamic pressure admittances

After the decomposition of pressure time-histories, aerodynamic pressure admittances are calculated for incident and signature turbulence induced pressures respectively by using the method presented in Subsection 3.2.3. Then, each pressure admittance function can be fitted with a rational equation as

$$\left|\chi_P(K)\right|^2 = \frac{c_{i1}}{1 + c_{i2} \cdot (K - K_I)^2} + \frac{c_{s1}}{1 + c_{s2} \cdot (K - K_s)^2} \tag{3.28}$$

where K_I and K_S are the predominant reduced frequencies for incident and signature admittances respectively; $c_{i(1\sim2)}$ and $c_{s(1\sim2)}$ are the fitting parameters for incident and signature admittance respectively. The first part of the equivalent admittance function represents the incident admittance while the second part represents the signature admittance.

Equation (3.28) is a modified version of the admittance functions proposed by Zhu (2009) to fit the aerodynamic admittance with signature turbulence effect. Figure 3.17 shows an example of measured and fitted pressure admittances. In the identified pressure admittance, the predominant signature turbulence component is more apparent. The curve fitting result is satisfactory.

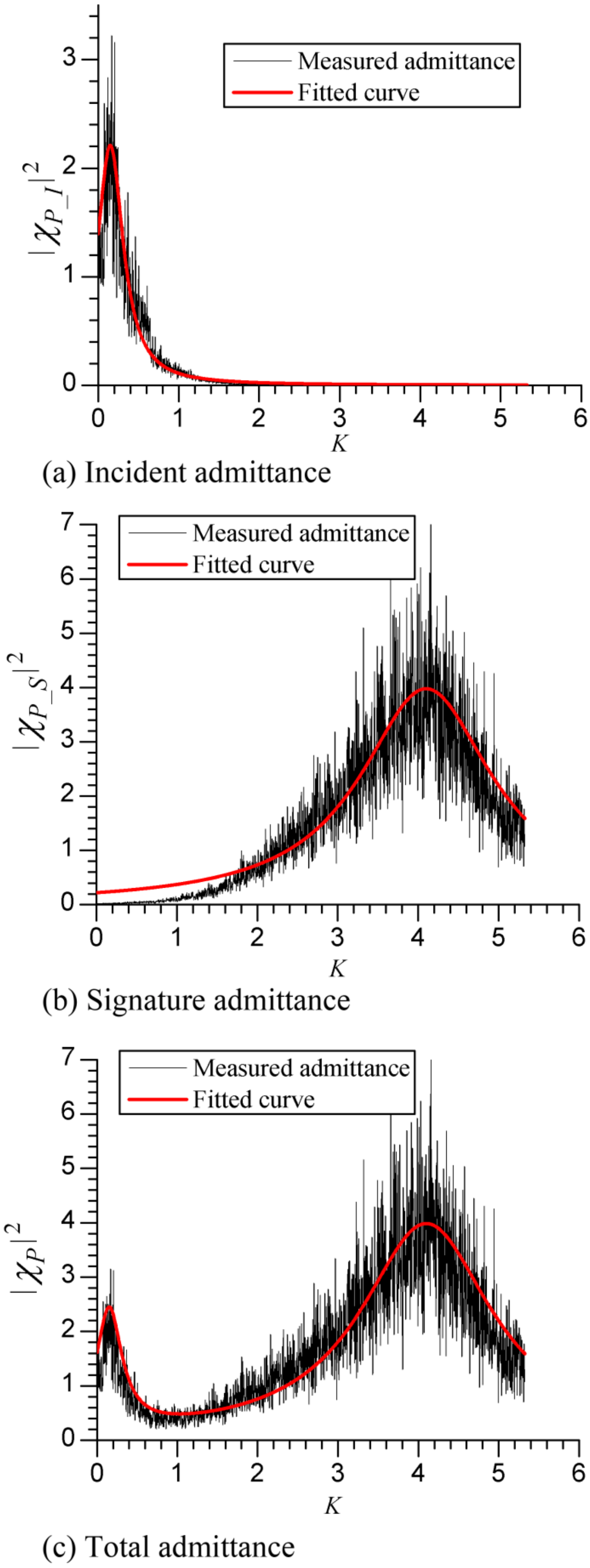

Figure 3.17 An example of measured and fitted pressure admittances

After fitting the identified pressure admittance of each pressure tap, the cross-sectional distribution of c_{i1}, which reflects the distribution of incident admittance peak value, can be obtained. The results are illustrated in Figure 3.18. The distribution patterns of c_{i1} are very similar in the two turbulence field at 0º angle of incidence. The incident admittance peak value varies markedly along the section outline. c_{i1} values larger than 1 indicate that the incident turbulence effect is larger than that estimated with the quasi-steady assumption. At 0º angle of incidence, c_{i1} value is less than 1 on the windward box for most locations except the locations of pressure taps 115 and 132. On the leeward box, the value is larger than 1 for most locations. The incident admittance significantly deviates from the quasi-steady assumption on the leeward edge of the leeward box. The peak admittance values reach up to more than 10 at the locations of pressure taps 203 and 204. The cross-sectional distribution patterns of c_{i1} at -3º and +3º angles of incidence are different from that at 0º angle of incidence. This is particular true for the leeward box. At -3º angle of incidence, large values locate at pressure taps 203 and 204. At +3º angle of incidence, the largest c_{i1} value is only around 2.6 locating at the windward edge of the deck plate.

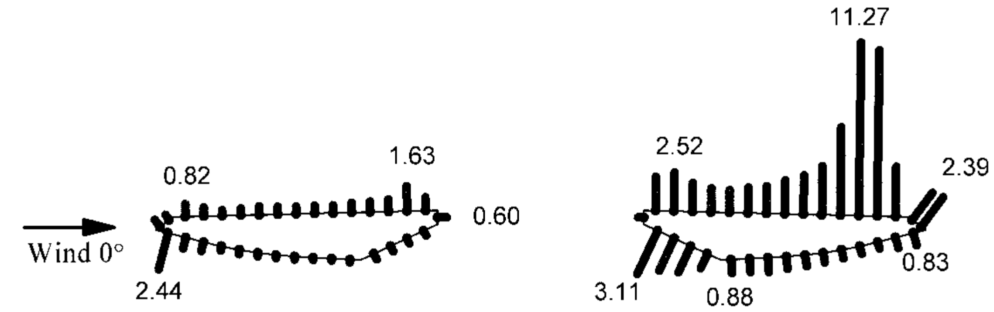

(a) T.I. =14%, α_0= 0°

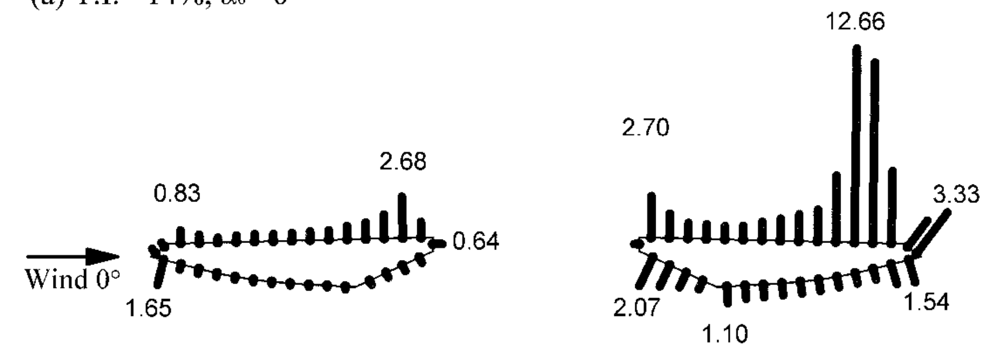

(b) T.I. =6%, α_0= 0°

(c) T.I. =6%, α_0= -3°

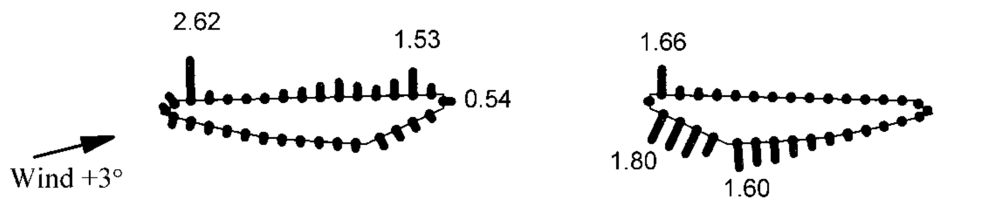

(d) T.I. =6%, α_0= +3°

Figure 3.18 Cross-sectional distribution of the incident admittance peak value

The ratio c_{s1}/c_{i1} between the frequency-domain peak values of incident and signature turbulence induced pressures can give information about the proportion of signature turbulence effect on buffeting pressure. The cross-sectional distributions of c_{s1}/c_{i1} are depicted in Figure 3.19 for different turbulence fields and different angles of incidence. The comparison of the results from different turbulence fields shows that the signature turbulence effect is significantly larger when turbulent intensity is lower, but the cross-sectional distribution pattern of signature turbulence effect is generally alike for different turbulent intensities at 0º angle of incidence. Signature turbulence mainly affects wind pressures on the leeward box. At 0º angle of incidence, for certain locations, the frequency-domain peak value of signature turbulence induced pressure may reach up to about 12 times the value of incident turbulence induced pressure at a turbulent intensity of 6% or 3 times the value of incident turbulence induced pressure at a turbulent intensity of 14%. The ratio can reach up to around 60 at -3º and +3º angles of incidence. These results indicate that signature turbulence effect is somehow negligible for most parts of the windward box but important for the leeward box. Besides, the cross-sectional distribution patterns of signature turbulence effect vary significantly with different angles of incidence.

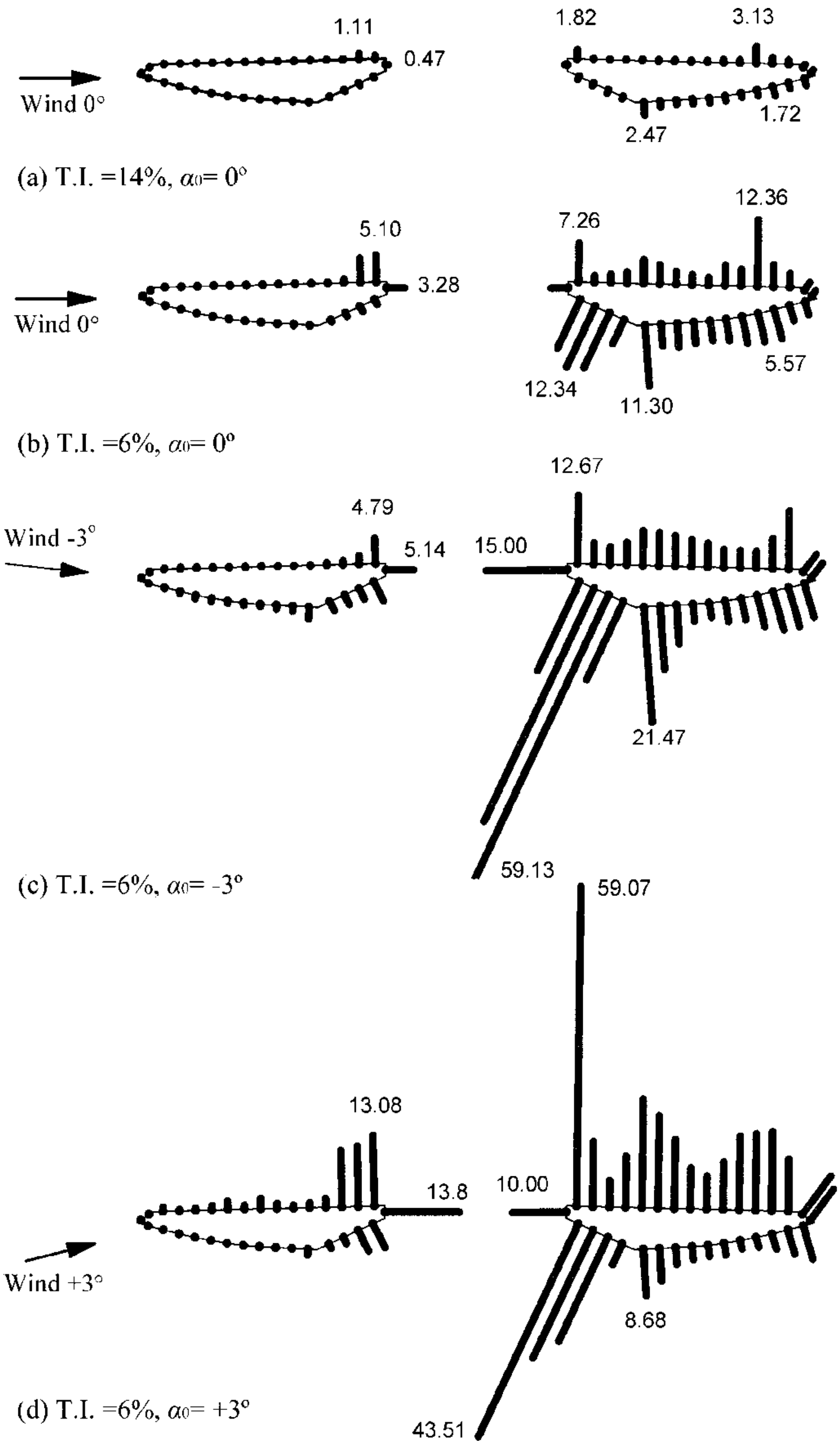

Figure 3.19 Ratio between frequency-domain peak values of incident and signature turbulence induced pressures

3.9 Span-wise pressure coherence

After the decomposition of pressure time-histories, the root coherence of incident and signature turbulence induced pressures can be identified from test data. Figure 3.20 shows an example of measured and fitted root coherence of 7 buffeting pressures that lie on the same line parallel to the deck axis. A total of 64 root coherence functions similar to Figure 3.20 are obtained for either signature turbulence or incident turbulence. The cross-sectional distribution of fitted coherence coefficients of incident turbulence induced pressure at 0º angle of incidence with 6% turbulence intensity is shown in Figure 3.21. The root coherence peak value at zero reduced frequency is approximately 1 for most of the locations. The peak value decreases to about 0.6 at the location of pressure tap 121 and the location around pressure tap 209. The decay factor increases stream-wisely from about 6 to about 11 on the windward box which shows a stream-wise decline trend of pressure correlation. The pressure correlation is weaker in the leeward box and the distribution pattern is not as obvious as the windward one. The decay factors on the leeward box fluctuate from around 9 to around 12.

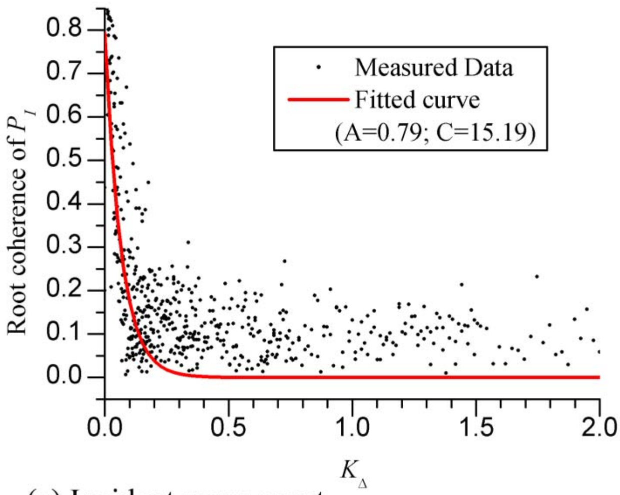

(a) Incident component

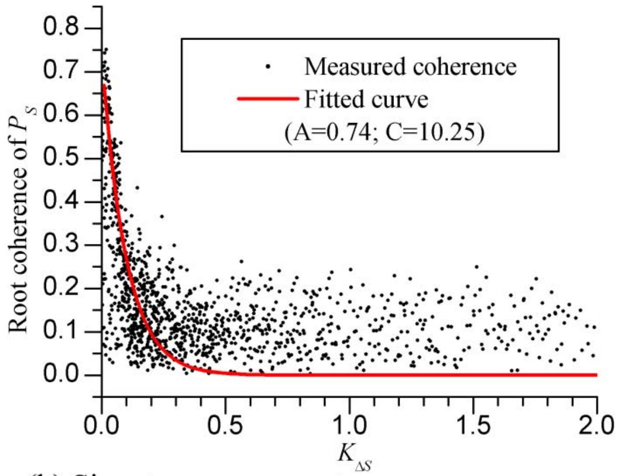

(b) Signature component

Figure 3.20 An example of measured and fitted root coherences of buffeting pressure

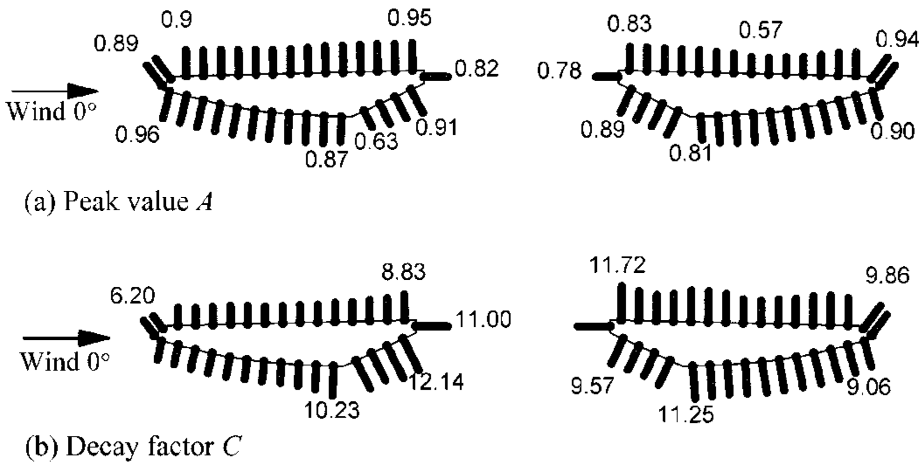

Figure 3.21 Span-wise coherence coefficients of incident turbulence induced pressures (T.I.= 6%)

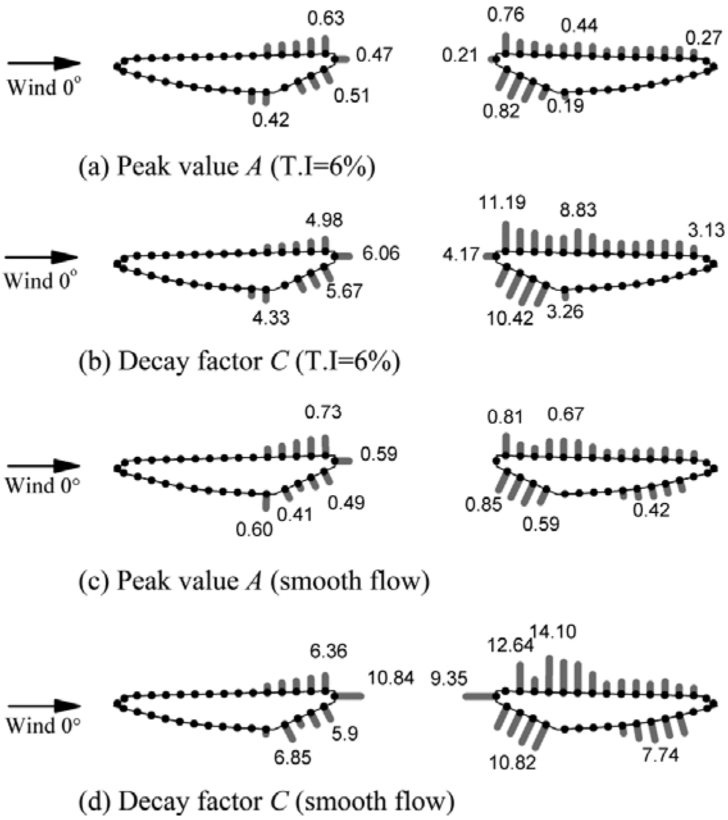

Figure 3.22 Span-wise coherence coefficients of signature turbulence induced pressures

To avoid multiple peaks in coherence function, the span-wise root coherence of signature turbulence induced pressure is presented with a reduced frequency $K_{\Delta S}$. An example of measured and fitted root coherence of signature turbulence induced pressure is given in Figure 3.20b. Figure 3.22 illustrates the cross-sectional distribution of fitted coherence coefficients of signature turbulence induced pressure. Because the signature turbulence effects on the windward box and some parts of the leeward box are marginal, the coherence coefficients are hardly identifiable on these locations. The coherence coefficients for the rest locations are presented in Figure 3.22. It can be seen that signature turbulence induced pressure has a similar correlation distribution pattern in both turbulent and smooth wind flow. The correlation is only slightly stronger in the smooth flow. Signature turbulence induced pressure has much weaker correlation than incident turbulence induced pressure. Its correlation is negligible on most of the locations except the windward edge of the leeward box and the leeward edge of the windward box. The result suggests that the flow separation on the windward box is the main cause of the predominant signature turbulence.

3.10 Summary

The formulation for distributed aerodynamic forces (aerodynamic pressure) on the surfaces of a bridge deck is presented in this chapter based on the quasi-steady theory. Wind tunnel pressure tests were conducted on the motionless pressure-tapped sectional deck model of Stonecutters Bridge with a twin-box deck. By separating the signature turbulence induced pressure from the measured pressure time-histories, the cross-sectional distribution of signature turbulence effects was investigated. The results show that signature turbulence mainly affects the leeward box. For certain locations, the signature turbulence induced pressure may be significantly larger than that of incident turbulence induced pressure. In view of the results from this study, signature turbulence induced forces are important for certain parts of the deck section, where a considerable signature turbulence effect on local aerodynamic responses exists.

The span-wise correlation of aerodynamic pressure on the sectional deck model was also studied. For the incident turbulence induced pressure, the span-wise correlation weakens stream-wisely on the windward box, and the span-wise correlation on the leeward box is generally weaker than that on the windward box. For the signature turbulence induced pressure, the span-wise correlation is negligible for most parts of the deck except the windward edge of the leeward box and the leeward edge of the windward box.

The cross-sectional and span-wise distributions of aerodynamic pressures provide more detailed information and deeper insight into the fluid-motionless structure interaction on the twin-box bridge deck. With the method proposed by this study, the incident and signature turbulence induced pressures can be separated from the measured pressure time-histories. Their admittances and span-wise coherences can be fitted with rational equations separately. As a result, the distributed aerodynamic forces can be represented by rational equations in the frequency domain for buffeting analysis.

The identification of the characteristics of distributed aerodynamic forces on the surfaces of a bridge deck is a first-step towards a framework for buffeting-induced stress analysis. In the next chapter, the formulation of the cross-spectra matrix of distributed aerodynamic forces will be introduced based on the results of this chapter. The entire framework for buffeting-induced stress analysis in the frequency domain will also be proposed in the next chapter with a method to estimate distributed aeroelastic forces over a bridge deck.

CHAPTER 4

A FRAMEWORK FOR BUFFETING-INDUCED STRESS ANALYSIS OF A TWIN-BOX BRIDGE DECK IN THE FREQUENCY DOMAIN

4.1 Introduction

Traditional buffeting analyses methods are all based on integrated sectional aerodynamic and aeroelastic forces rather than distributed forces over the surface of the bridge deck. The disregard of the cross-sectional distribution of the wind loads shall affect the accuracy of predicted buffeting-induced stress responses. Thus, to accurately predict the buffeting-induced stresses of bridges, it is imperative to develop a new framework that can take account of the cross-sectional distribution of aerodynamic and aeroelastic forces.

This chapter proposes a practical framework to perform buffeting-induced stress analysis of a bridge deck with distributed aerodynamic and aeroelastic forces. The aerodynamic pressure admittances and span-wise coherences identified from pressure tests of a motionless sectional model and described in Chapter 3 are used in this Chapter. The cross-spectra matrix of distributed aerodynamic forces is further formulated based on the measurement results in Chapter 3. The distributed aeroelastic forces are acquired based on the quasi-static assumption and the sectional aeroelastic forces.

The traditional buffeting analysis is usually performed on a spine-beam model of the bridge deck, whereas the proposed method is applied to multi-scale FE models or detailed shell/solid FE models to obtain accurate stress responses. Due to the large number of degrees-of-freedom (DOF) involved in either the multi-scale or detailed FE model of an entire bridge, only a segment of detailed FE model of a twin-box bridge deck is employed as a case study to demonstrate the feasibility of the proposed method.

4.2 Distribution of aerodynamic forces

The governing equation of a coupled wind-bridge system under distributed buffeting forces can be written as

$$\mathbf{M}\ddot{\mathbf{Y}} + \mathbf{C}\dot{\mathbf{Y}} + \mathbf{K}\mathbf{Y} = \mathbf{R}_f\mathbf{F}_b \tag{4.1}$$

where **M**, **C** and **K** are the $n \times n$ mass, damping and stiffness matrices, respectively, of the wind-bridge system based on the detailed FE bridge model (see Figure 4.1); **Y** is the displacement vector of n dimension; $\mathbf{F}_b$ is the aerodynamic force vector of m dimension; $\mathbf{R}_f$ is the $n \times m$ matrix consisting of 0 and 1, which expands the m-dimensional loading vector into a n-dimensional vector; and a dot represents the first-order derivative with respect to time.

The overall system property matrices are the sum of structural property matrices and aeroelastic property matrices as

$$\mathbf{M} = \mathbf{M}_{str} \tag{4.2}$$

$$\mathbf{C} = \mathbf{C}_{str} + \mathbf{C}_{se} \tag{4.3}$$

$$\mathbf{K} = \mathbf{K}_{str} + \mathbf{K}_{se} \tag{4.4}$$

where $\mathbf{M}_{str}$, $\mathbf{C}_{str}$ and $\mathbf{K}_{str}$ are the $n \times n$ structural mass, damping and stiffness matrices, respectively; $\mathbf{C}_{se}$ and $\mathbf{K}_{se}$ are the $n \times n$ aeroelastic damping and stiffness matrices, respectively.

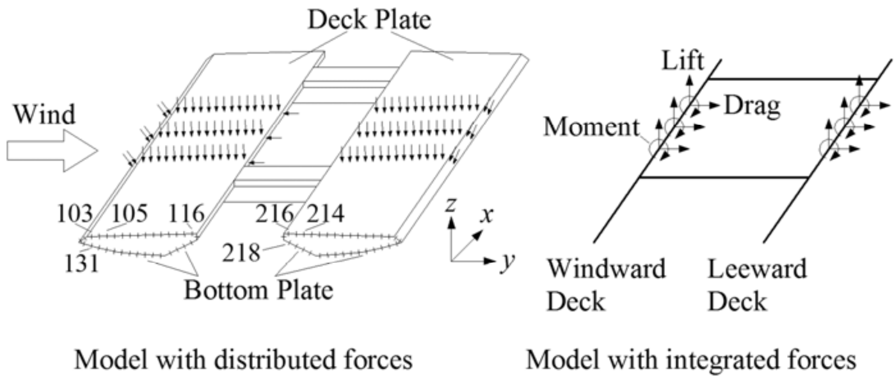

Figure 4.1 Two types of modeling for a segment of the twin-box deck

For an accurate stress analysis of the shell-element FE model of a bridge deck, the matrices **M**, **C** and **K** should include all nodes of the model, so do the matrices $\mathbf{C}_{se}$ and $\mathbf{K}_{se}$. $\mathbf{F}_b$ should also include the aerodynamic forces on all the nodes. The two key issues in the frequency-domain buffeting-induced stress analysis with distributed forces are therefore the formulation of the distributed aeroelastic property matrices and the cross-spectral density matrix of distributed aerodynamic forces. The formulation of the spectral density matrix of distributed aerodynamic forces is presented in this section while the distributed aeroelastic property with be discussed in the next section.

To determine the cross-spectral density matrix of distributed aerodynamic forces, three aerodynamic properties should be obtained: pressure coefficients; pressure admittance functions; and the coherence functions of pressures. The pressure coefficients can be naturally obtained from the wind pressure test of a motionless deck model. The method to identify pressure admittance functions and span-wise pressure coherence functions have been proposed in Chapter 3.

The aerodynamic admittance and span-wise root coherence of the aerodynamic pressure can be identified from wind tunnel pressure tests and fitted with rational functions. Nevertheless, the cross-spectra of the pressures on the deck surface cannot be fully represented only by span-wise coherence functions. The chord-wise correlation of aerodynamic forces, which has not been discussed in any literature, should also be taken into account in the total cross-spectral matrix. However, the consideration of a full 3D correlation of aerodynamic forces over the entire surface of the bridge deck in the computation is difficult and time consuming. To simplify the problem, the surface of both the windward and leeward boxes is divided into a deck plate and a bottom plate, and the entire surface of a twin-box deck is thus divided into 4 plates as shown in Figure 4.1. The following assumptions are then adopted.

(1) The correlation of aerodynamic pressures between the deck plate and the bottom plate is negligible.

(2) The correlation of aerodynamic pressures between the windward and leeward deck is negligible

(3) The span-wise correlation of aerodynamic pressures on each plate is considered line by line (see Figure 4.2). The correlation of the aerodynamic pressures on each line is represented by its own decay function.

(4) For each plate, the chord-wise correlation of aerodynamic pressures is assumed to be only related to the chord-wise distance of pressures. Thus, only one chord-wise correlation function is required for each plate.

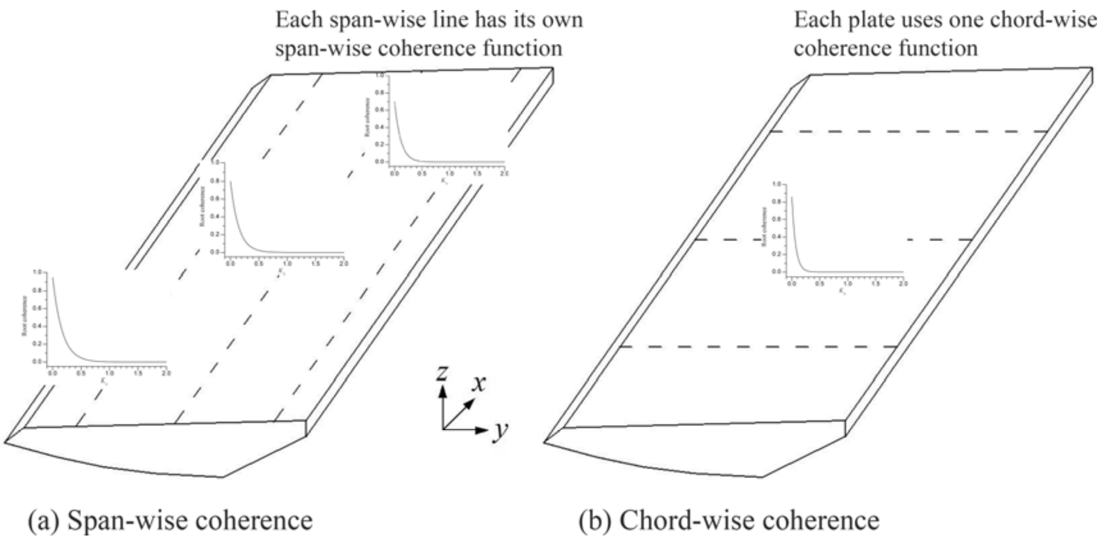

Figure 4.2 Span-wise and chord-wise coherence

As a result of the above simplification, the aerodynamic forces of each plate can be dealt with separately. For each plate, the cross-spectrum of any pair of pressures can then be written as

$$S_{P_{b,(i,r)}P_{b,(j,s)}}(\omega)=\left(\mathrm{Coh}_{x,i}^{1/2}(\Delta x(r,s))\cdot\mathrm{Coh}_{y}^{1/2}(\Delta y(i,j))S_{P_{b,i}}(\omega)S_{P_{b,j}}(\omega)\right)^{1/2} \tag{4.5}$$

where i and j represent the locations of the two pressure points on the section; r and s represent the longitudinal location of the pressure point; Δx and Δy represents the span-wise and chord-wise distance, respectively.

The spectral density matrix of distributed aerodynamic forces $S_{F_b F_b}(\omega)$ can be assembled using the pressure spectral density function computed by Eq.(4.5) and multiplied by the area on the deck surface. The number of pressure points shall be large enough so that the area corresponding to each point is small and that the pressure distribution in the small area represented by each point can be considered uniform.

$$S_{F_{b,(i,r)}F_{b,(j,s)}}(\omega) = \left(\mathrm{Coh}_{x,i}^{1/2}(\Delta x(r,s)) \cdot \mathrm{Coh}_{y}^{1/2}(\Delta y(i,j)) S_{P_{b,i}}(\omega) S_{P_{b,j}}(\omega)\right)^{1/2} A_i A_j \quad (4.6)$$

where A_i and A_j are the areas that are represented by point i and point j, respectively.

Every function on the right side of Eq.(4.6) can be represented by a rational function so that the cross-spectra of any pair of aerodynamic pressures can be simulated with rational functions. The measured chord-wise root coherences of the four plates are shown in Figure 4.3 and Figure 4.4. The chord-wise root coherence of each plate can be fitted with

$$Coh_y^{1/2}(\Delta y) = A \cdot e^{-C\frac{f \cdot \Delta y}{\bar{U}}} \quad (4.7)$$

where A is the root coherence peak value at zero frequency; C is the decay factor.

Some examples of the measured and simulated cross-spectra are presented in Figure

4.5. These examples include four kinds of scenarios on both windward and leeward box: (a) auto-spectrum (i=j and r=s), (b) span-wise cross-spectrum (i=j and $r\neq s$), (c) chord-wise cross-spectrum ($i\neq j$ and r=s), and (d) diagonal cross-spectrum (($i\neq j$ and $r\neq s$)). Simulated cross-spectra show good agreement with the measured data in all four kinds of scenarios and both boxes. It is also shown that the chord-wise correlation is remarkably weaker than the span-wise correlation. This result suggests a possibility to neglect the chord-wise and diagonal cross-spectra of aerodynamic pressures, which further simplifies the problem.

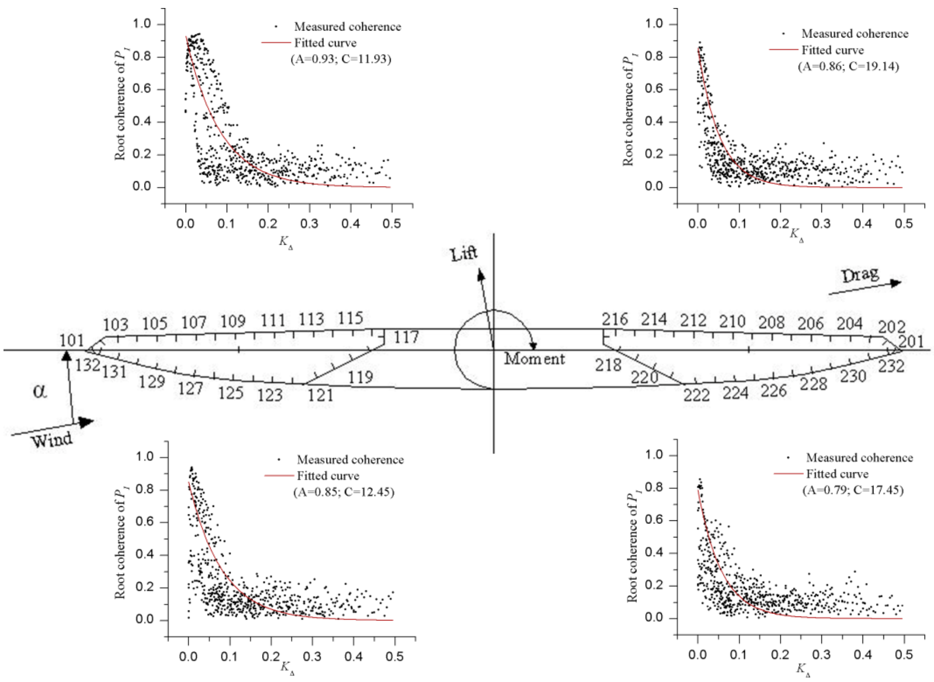

Figure 4.3 Chord-wise root coherence of incident turbulence induced pressure

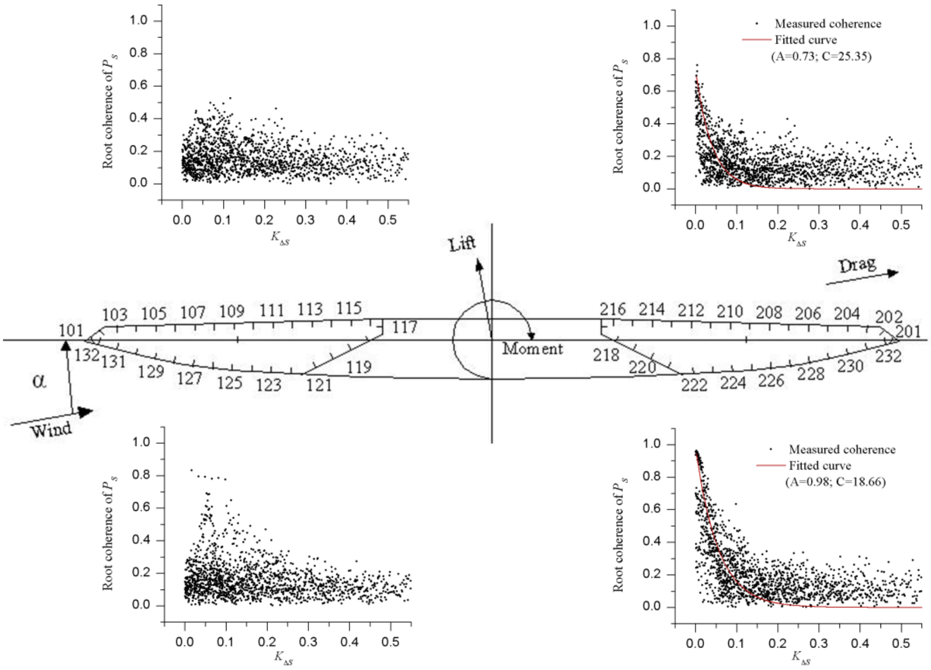

Figure 4.4 Chord-wise root coherence of signature turbulence induced pressure

Figure 4.6 shows the measured cross-spectrum of tap 103 and 131, which largely represents the two points with the strongest pressure correlation between the deck and bottom plates. Figure 4.7 shows the measured cross-spectrum of tap 116 and 216, which represents the two points with the strongest pressure correlation between the windward and leeward boxes. The cross-spectra of these two cases are smaller than the chord-wise cross-spectra presented before. This fact supports the assumption that the correlation between the four plates can be neglected.

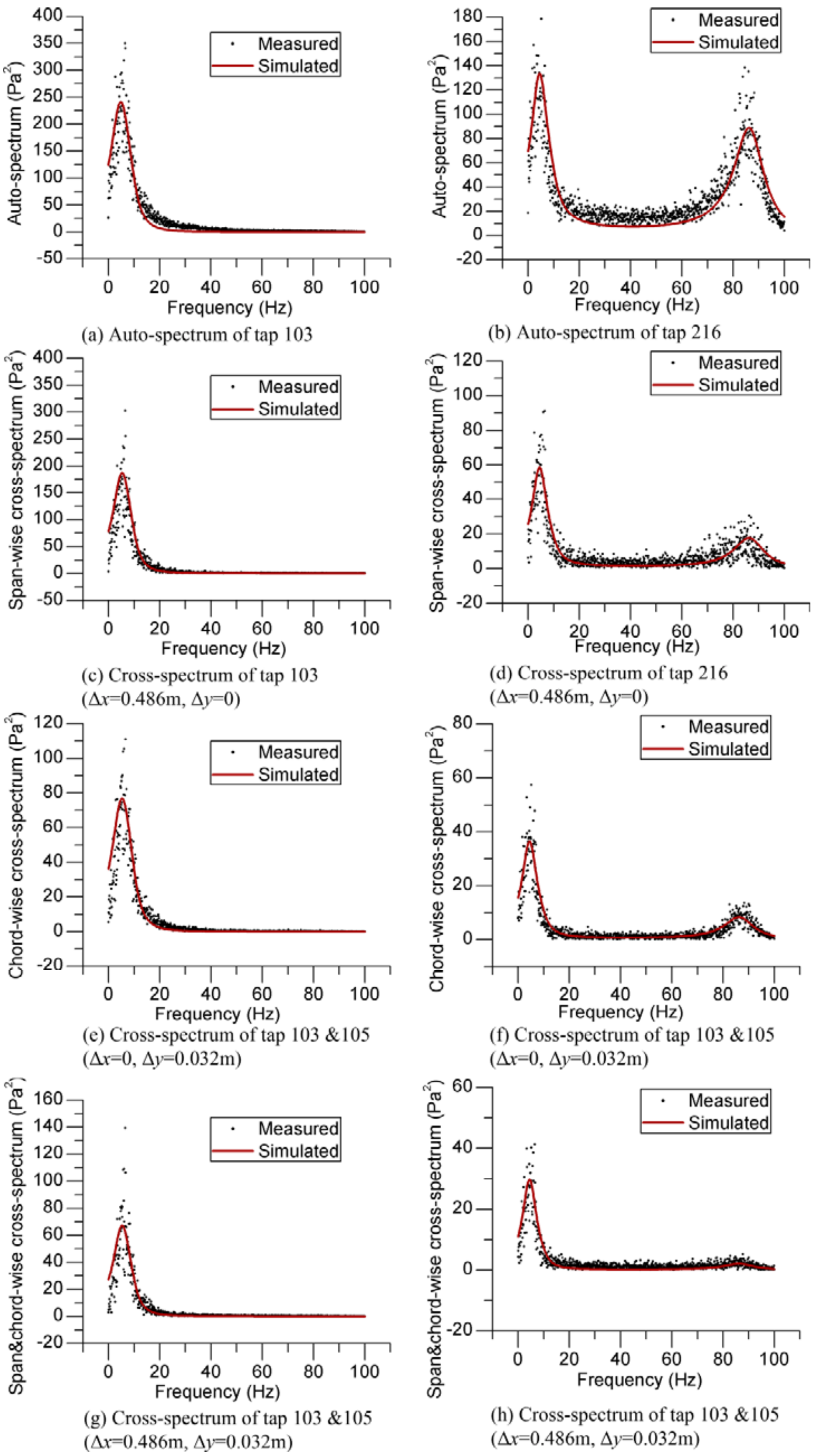

(a) Auto-spectrum of tap 103

(b) Auto-spectrum of tap 216

(c) Cross-spectrum of tap 103 (Δx=0.486m, Δy=0)

(d) Cross-spectrum of tap 216 (Δx=0.486m, Δy=0)

(e) Cross-spectrum of tap 103 &105 (Δx=0, Δy=0.032m)

(f) Cross-spectrum of tap 103 &105 (Δx=0, Δy=0.032m)

(g) Cross-spectrum of tap 103 &105 (Δx=0.486m, Δy=0.032m)

(h) Cross-spectrum of tap 103 &105 (Δx=0.486m, Δy=0.032m)

Figure 4.5 Examples of measured and simulated cross-spectra of pressures

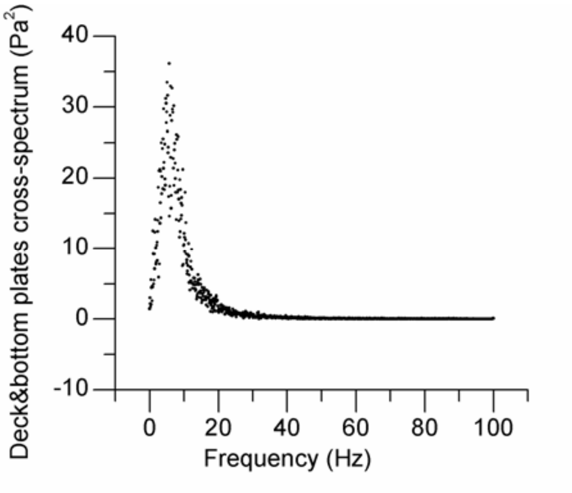

Figure 4.6 Strongest pressure correlation between the deck and bottom plates

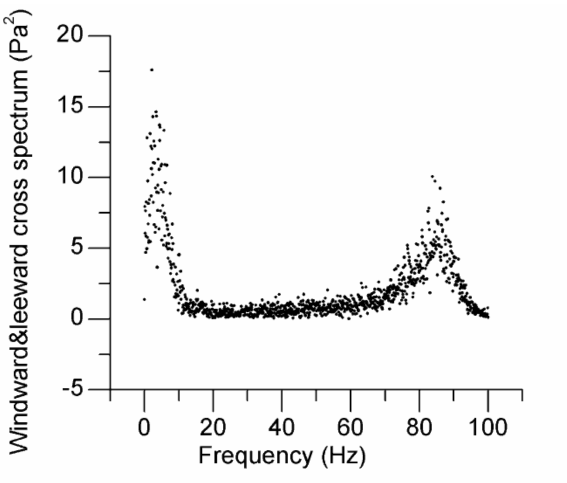

Figure 4.7 Strongest pressure correlation between the windward and leeward boxes

4.3 Distribution of aeroelastic forces

In principle, aeroelastic pressures on a bridge deck can be obtained from pressure tests of an oscillating deck model. However, the research on the identification of distributed aeroelastic forces as well as the associated stiffness and damping matrices from wind tunnel tests is very limited, and so no distributed aeroelastic forces are available at this stage. An alternative to obtain the distributed aeroelastic forces is to find a reasonable way to distribute the sectional aeroelastic forces measured from the traditional wind tunnel tests. This distribution method can be achieved based on the quasi-static expression of aeroelastic forces as described below.

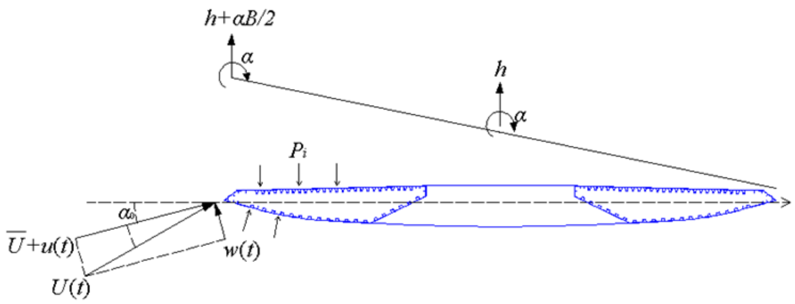

Figure 4. 8 A 2D oscillating deck section

As shown in Figure 4. 8, the wind pressure on a surface point of a vibrating 2D bridge deck section can be expressed as

$$P_i(t) = \frac{1}{2}\rho\left[\left(\bar{U} + u(t)\right)^2 + w(t)^2\right] \cdot C_{pi}(\alpha_0 + \Delta\alpha) \tag{4.8}$$

where the relative transient incidence angle $\Delta\alpha$ can be expressed as

$$\Delta\alpha \approx \frac{w}{\bar{U}} - \frac{\dot{h}}{\bar{U}} - \frac{\dot{\alpha} \cdot B}{2\bar{U}} + \alpha \tag{4.9}$$

where h and α are the vertical and torsional displacement of the entire deck section, respectively; and a dot represents the first-order derivative with respect to time.

By substituting Eq.(4.9) into Eq.(4.8) and considering the first-order Taylor expansion of the pressure coefficient, Eq.(4.8) can be expanded as

$$P_i = \frac{1}{2}\rho\bar{U}^2 \cdot C_{pi}(\alpha_0) + \frac{1}{2}\rho\bar{U}^2 \cdot \left[2C_{pi}(\alpha_0)\cdot\frac{u}{\bar{U}} + C_{pi}^{'}(\alpha_0)\cdot\frac{w}{\bar{U}}\right] + \frac{1}{2}\rho\bar{U}B\cdot\left[-C_{pi}^{'}(\alpha_0)\cdot\dot{h} - \frac{1}{2}C_{pi}^{'}(\alpha_0)\cdot\dot{\alpha}\cdot B + C_{pi}^{'}(\alpha_0)\cdot\bar{U}\cdot\alpha\right] \tag{4.10}$$

The first and second parts of the right side of Eq.(4.10) are the static pressure and buffeting pressure, respectively. The third part is actually the aeroelastic pressure.

$$P_{se,i} = \frac{1}{2}\rho\bar{U}B\cdot\left[-C_{pi}^{'}(\alpha_0)\cdot\dot{h} - \frac{1}{2}C_{pi}^{'}(\alpha_0)\cdot\dot{\alpha} + C_{pi}^{'}(\alpha_0)\cdot\alpha\right] \tag{4.11}$$

The 3D quasi-static aeroelastic pressure acting on a surface point of a vibrating bridge deck section can be derived in a similar way. With respect to the structural coordinate, the 3D quasi-static aeroelastic forces on a surface point of a vibrating bridge deck can be expressed as

$$\mathbf{F}_{se,i}(t) = -\mathbf{C}_{se,i}\cdot\dot{\mathbf{q}} - \mathbf{K}_{se,i}\cdot\mathbf{q} \tag{4.12}$$

$$\mathrm{C}_{se,i} = \frac{1}{2}\rho\bar{U}B\cdot\begin{bmatrix} 2C_{pi}^{D} & \left(C_{pi}^{\prime D} - C_{pi}^{L}\right) & -B\left(C_{pi}^{\prime D} - C_{pi}^{L}\right) \\ 2C_{pi}^{L} & \left(C_{pi}^{\prime L} + C_{pi}^{D}\right) & -B\left(C_{pi}^{\prime L} + C_{pi}^{D}\right) \\ 2BC_{pi}^{M} & BC_{pi}^{\prime M} & -B^2C_{pi}^{\prime M} \end{bmatrix} \tag{4.13}$$

$$\mathbf{K}_{se,i} = \frac{1}{2}\rho\bar{U}^2B\cdot\begin{bmatrix} 0 & 0 & C_{pi}^{\prime D} \\ 0 & 0 & C_{pi}^{\prime L} \\ 0 & 0 & BC_{pi}^{\prime M} \end{bmatrix} \tag{4.14}$$

$$\mathbf{q} = [p \;\; h \;\; a]^{\mathrm{T}} \tag{4.15}$$

where $\mathbf{C}_{se,i}$ and $\mathbf{K}_{se,i}$ are the aeroelastic damping and stiffness matrix for the surface point i; p, h and α are the lateral, vertical and torsional displacement of the centroid of the deck section, respectively; C_{pi}^{D}, C_{pi}^{L} and C_{pi}^{M} are the three components of pressure coefficient C_{pi} with respect to the elastic center of the section and can be obtained by

$$\begin{aligned} C_{Pi}^{L} &= C_{Pi} \cdot \cos\left(\beta_i + \alpha_0\right) \cdot \delta_i \\ C_{Pi}^{D} &= C_{Pi} \cdot \sin\left(\beta_i + \alpha_0\right) \cdot \delta_i \\ C_{Pi}^{M} &= C_{Pi} \cdot \left(\cos\beta_i \cdot y_i - \sin\beta_i \cdot z_i\right) \cdot \delta_i \end{aligned} \tag{4.16}$$

where β_i is the angle between the vertical axis of the deck section and the pressure direction which is perpendicular to the surface outline; y_i and z_i are the coordinates of the surface point in the structural axis; and δ_i is the certain length on the section outline that is represented by the point i.

These three coefficients have the relationship with integrated aerodynamic force coefficients as

$$C_L \cdot B = \sum_{i=1}^{m} C_{Pi}^{L} \quad C_D \cdot B = \sum_{i=1}^{m} C_{Pi}^{D} \quad C_M \cdot B^2 = \sum_{i=1}^{m} C_{Pi}^{M} \tag{4.17}$$

In reality, the quasi-static assumption does not hold. The aerodynamic derivatives of wind pressure, which is similar to the aerodynamic derivatives of integrated sectional forces, should be introduced into Eq.(4.13) and Eq.(4.14). Therefore, the distributed aeroelastic property matrices can be expressed as (Tubino, 2005)

$$\mathrm{C}_{se,i} = \frac{1}{2}\rho\bar{U}B\cdot\begin{bmatrix} 2C_{pi}^{D}p_1^* & \left(C_{pi}'^{D}-C_{pi}^{L}\right)p_5^* & -B\left(C_{pi}'^{D}-C_{pi}^{L}\right)p_2^* \\ 2C_{pi}^{L}h_5^* & \left(C_{pi}'^{L}+C_{pi}^{D}\right)h_1^* & -B\left(C_{pi}'^{L}+C_{pi}^{D}\right)h_2^* \\ 2BC_{pi}^{M}a_5^* & BC_{pi}'^{M}a_1^* & -B^2C_{pi}'^{M}a_2^* \end{bmatrix} \tag{4.18}$$

$$\mathbf{K}_{se,i} = \frac{1}{2}\rho\bar{U}^2B\cdot\begin{bmatrix} 0 & 0 & C_{pi}'^{D}p_3^* \\ 0 & 0 & C_{pi}'^{L}h_3^* \\ 0 & 0 & BC_{pi}'^{M}a_3^* \end{bmatrix} \tag{4.19}$$

where h_i^*, a_i^* and p_i^* (i=1,2,3,5) are the distributed aerodynamic derivatives.

It was found that the span-wise coherence of aeroelastic forces are close to unity in sectional model tests (e.g. Haan, 2000), but no research has been conducted to investigate the chord-wise correlation of aeroelastic forces. It is assumed in this study that the compensation for non-quasi-static effects (i.e. the distributed aerodynamic derivatives) is uniform along the section outline. As a result, the sum of the distributed aeroelastic forces with respect to the sectional elastic center can be performed in conjunction with Eq.(4.17), yielding the following equation for aeroelastic forces on the entire section.

$$\mathbf{F}_{se} = -\mathbf{C}_{se}\cdot\dot{\mathbf{q}} - \mathbf{K}_{se}\cdot\mathbf{q} \tag{4.20}$$

$$\mathbf{C}_{se} = \frac{1}{2}\rho\bar{U}B\cdot\begin{bmatrix} 2C_Dp_1^* & (C_D'-C_L)p_5^* & -B\left(C_D'-C_L\right)p_2^* \\ 2C_Lh_5^* & (C_L'+C_D)h_1^* & -B\left(C_L'+C_D\right)h_2^* \\ 2BC_Ma_5^* & BC_M'a_1^* & -B^2C_M'a_2^* \end{bmatrix} \tag{4.21}$$

$$\mathbf{K}_{se} = \frac{1}{2}\rho \bar{U}^2 B \cdot \begin{bmatrix} 0 & 0 & C'_D p_3^* \\ 0 & 0 & C'_L h_3^* \\ 0 & 0 & BC'_M a_3^* \end{bmatrix} \tag{4.22}$$

On the other hand, the aeroelastic damping and stiffness matrices are conventionally expressed by aerodynamic derivatives in the Scanlan's convention as

$$\tilde{\mathbf{C}}_{se} = \frac{1}{2}\rho \bar{U} B \cdot \begin{bmatrix} KP_1^* & KP_5^* & KBP_2^* \\ KH_5^* & KH_1^* & KBH_2^* \\ KBA_5^* & KBA_1^* & KB^2 A_2^* \end{bmatrix} \tag{4.23}$$

$$\tilde{\mathbf{K}}_{se} = \frac{1}{2}\rho \bar{U}^2 B \cdot \begin{bmatrix} \frac{K^2}{B} P_4^* & \frac{K^2}{B} P_6^* & K^2 P_3^* \\ \frac{K^2}{B} H_6^* & \frac{K^2}{B} H_4^* & K^2 H_3^* \\ K^2 A_6^* & K^2 A_4^* & K^2 BA_3^* \end{bmatrix} \tag{4.24}$$

By comparing Eqs.(4.21) and (4.22) with Eqs.(4.23) and(4.24), the distributed aerodynamic derivatives h_i^*, a_i^* and p_i^* (i=1,2,3,5) can be derived from the conventional Scanlan aerodynamic derivatives. The distributed aeroelastic forces and the associated aeroelastic damping and stiffness matrices can be obtained in terms of the conventional sectional aerodynamic derivatives and the measured pressure coefficients.

$$
\begin{aligned}
&p_1^* = \frac{KP_1^*}{2C_D}, \quad p_2^* = \frac{KP_2^*}{-(C_D^{'} - C_L)}, \quad p_3^* = \frac{K^2 P_3^*}{C_D^{'}}, \quad p_5^* = \frac{KP_5^*}{(C_D^{'} - C_L)} \\
&h_1^* = \frac{KH_1^*}{C_L^{'} + C_D}, \quad h_2^* = \frac{KH_2^*}{C_L^{'} + C_D}, \quad h_3^* = \frac{K^2 H_3^*}{C_L^{'}}, \quad h_5^* = \frac{KH_5^*}{2C_L} \\
&a_1^* = \frac{KA_1^*}{C_M^{'}}, \quad a_2^* = \frac{KA_2^*}{-C_M^{'}}, \quad a_3^* = \frac{K^2 A_3^*}{C_M^{'}}, \quad a_5^* = \frac{KA_5^*}{2C_M},
\end{aligned}
\tag{4.25}
$$

4.4 Buffeting analysis with distributed forces

The distributed aeroelastic stiffness and damping matrices established in the last subsection and expressed by Eq.(4.18) and Eq.(4.19) can be assembled into the total aeroelastic stiffness and damping matrices as

$$
\mathbf{C}_{se} = \begin{bmatrix} \mathbf{R}_e \mathbf{C}_{se,1} & & & \\ & \mathbf{R}_e \mathbf{C}_{se,2} & & \\ & & \ddots & \\ & & & \mathbf{R}_e \mathbf{C}_{se,N} \end{bmatrix} \tag{4.26}
$$

$$
\mathbf{K}_{se} = \begin{bmatrix} \mathbf{R}_e \mathbf{K}_{se,1} & & & \\ & \mathbf{R}_e \mathbf{K}_{se,2} & & \\ & & \ddots & \\ & & & \mathbf{R}_e \mathbf{K}_{se,N} \end{bmatrix} \tag{4.27}
$$

where $\mathbf{R}_e$ is the 6×3 matrix consisting of 0 and 1, which expands a 3-dimensional aeroelastic property matrix into a 6-dimensional matrix with respect to all 6 DOF of a node; and N is the number of nodes.

In consideration that a large number of DOF are involved in the buffeting-induced stress analysis, a computationally efficient algorithm shall be used to find the solution of Eq.(4.1). The pseudo-excitation method (Lin, 1992; Xu et. al., 1998) is selected in this study.

By assuming that the spectral density matrix of the aerodynamic forces, $\mathbf{S}_{F_b F_b}(\omega)$, is a Hermitian matrix (a matrix with complex entries that is equal to its own conjugate transpose), it can be decomposed as

$$\mathbf{S}_{F_b F_b}(\omega) = \mathbf{L}\,\mathrm{D}\,\mathbf{L}^* = \sum_{k=1}^{m} d_{kk}\mathbf{L}_k\mathbf{L}_k^* \tag{4.28}$$

where **L** is the lower triangular matrix; **D** is the diagonal matrix; $\mathbf{L}_k$ is the kth column of **L**; d_{kk} is the kth diagonal element of **D**; and * denotes the conjugate transpose of a matrix.

Based on the decomposition, a series of harmonic pseudo-excitation vectors can be constituted as

$$\mathbf{F}_k = \mathbf{L}_k \exp(i\omega t) \quad (k = 1, 2, \cdots, m) \tag{4.29}$$

For each pseudo-excitation vector, a pseudo displacement response vector can be computed through a harmonic analysis as

$$\mathbf{Y}_k = \mathbf{H}(\omega)\mathbf{R}_f\mathbf{F}_k \tag{4.30}$$

where H(ω) is the frequency-domain transfer function between the loading and displacement response.

The corresponding velocity and acceleration responses are

$$\dot{\mathbf{Y}}_k = i\omega\mathbf{H}(\omega)\mathbf{R}_f\mathbf{F}_k \tag{4.31}$$

$$\ddot{\mathbf{Y}}_k = -\omega^2\mathbf{H}(\omega)\mathbf{R}_f\mathbf{F}_k \tag{4.32}$$

It can be readily proved that the spectral density matrix of the system displacement response can be obtained by

$$\mathbf{S}_{YY}(\omega) = \sum_{k=1}^{m} d_{kk}\mathbf{Y}_k\mathbf{Y}_k^* \tag{4.33}$$

The standard deviation of displacement can therefore be obtained as

$$\mathbf{E}(Y^2) = \int_0^{\omega}\mathbf{S}_{YY}(\omega)\mathrm{d}\omega \tag{4.34}$$

The standard deviations of velocity and acceleration can be computed in the same way.

4.5 A case study

A case study is performed to demonstrate the feasibility and advantage of the proposed method and to examine the accuracy of the corresponding computer program at the same time. The structural modeling and stress analysis of this study are performed using a commercial software ANSYS. Nevertheless, the aeroelastic properties shall be added to each node of the structural FE model using a stiffness/damping matrix element MATRIX27 (Hua and Chen, 2008; Wang et al., 2014).

As mentioned in Introduction, the proposed method can be applied to a shell/solid FE model to obtain accurate stress responses. Due to the large number of DOF involved in the shell/solid FE model of the entire bridge, it is not practical to apply this method directly on such a detailed model of the entire bridge. Only a segment of detailed FE model of a twin-box bridge deck, as shown in Figure 4.9, is employed as a case study. The two ends of the segment are fixed and the cross-section of the segment comes from the steel deck of a real long-span cable-stayed bridge. The results obtained from the proposed method on a shell FE model are finally compared with the results produced by the traditional force-based buffeting analysis on a beam model with equivalent sectional properties.

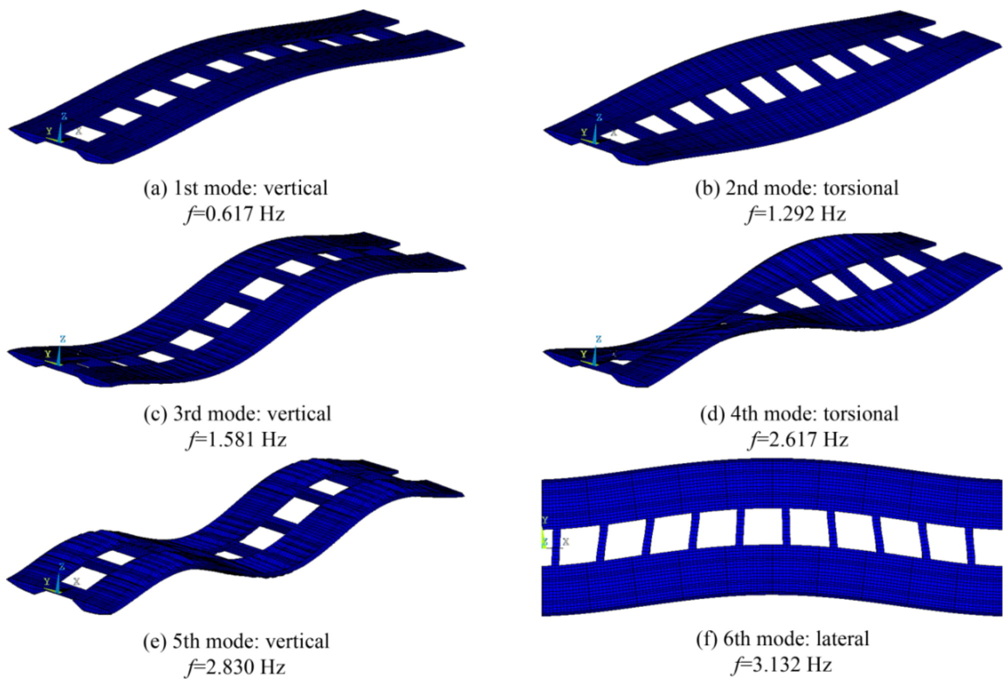

Figure 4.9 First 6 modal frequencies and mode shapes of the segment

The first six modal frequencies and mode shapes of the deck segment are shown in Figure 4.9. These six modes, with frequencies ranging from 0.617Hz to 3.132Hz, include the first 3 vertical bending modes, the first 2 torsional modes and the first lateral bending mode. The mean wind speed is taken as 55m/s and the angle of incidence is taken as 0°. The structural damping is assumed to be Rayleigh damping and the damping ratio for all modes of vibration is assumed to be 0.36%. This damping ratio is a design value that conforms to the requirement of Design Rules for Aerodynamic Effects on Bridges (2001).

For the shell-element FE model, the characteristics of the distributed aerodynamic forces, including the aerodynamic pressure coefficients, pressure admittances and the coherence functions pressures, are all obtained from the wind tunnel pressure tests on the motionless sectional model as introduced in Chapter 3. The characteristics of the distributed aeroelastic stiffness and damping are obtained by distributing the aerodynamic derivatives of sectional aeroelastic forces that can be found in the work of Hui and Ding (2006).

For the traditional beam-element FE model, the characteristics of sectional aerodynamic forces can be obtained by integration of the pressures. The aerodynamic derivatives of sectional aeroelastic forces are directly used.

To enable a direct comparison with the beam model, the lateral and vertical displacements of the shell model were calculated as the mean displacement of all nodes, and the torsional displacement of the shell model were calculated using the vertical displacements of the two nodes on the windward and leeward edges and the distance between the two node. Fig. 10 shows the comparison of the standard deviation of displacement responses computed from the beam model and the shell model. The displacement responses computed with distributed buffeting loads are slightly smaller than those computed with the traditional method. This difference may attribute to the more comprehensive consideration on the correlation of buffeting forces in the shell model. The general agreement of displacement responses between the two models shows that the buffeting-induced stress analysis framework proposed in this chapter can also produce similar results with the traditional buffeting analysis method in terms of displacements.

Figure 4.11 shows the section-wise distribution of the standard deviation of longitudinal stress responses in the mid-span section. The longitudinal stress responses on the beam model are calculated using nodal forces and moments based on the rigid section assumption, whereas the stress responses on the shell model are directly computed using the FE analysis software. It can be seen that in the beam model, the stress on the outline of each box linearly increases with the distance from its centroid. The maximum dynamic stress appears at the leeward edge of the windward box. In the shell model, the distribution of the stress responses is more concentrated on the two edges of both boxes. In the windward box, the maximum dynamic stress occurs on the windward edge of the deck plate with a value slightly larger than the beam model. In the leeward box, the maximum dynamic stress also occurs on the windward edge of the deck plate and its value is about 60% larger than the beam model. The larger maximum stress responses in the shell model may largely attribute to the fact that the shell model can capture more local modes of vibration.

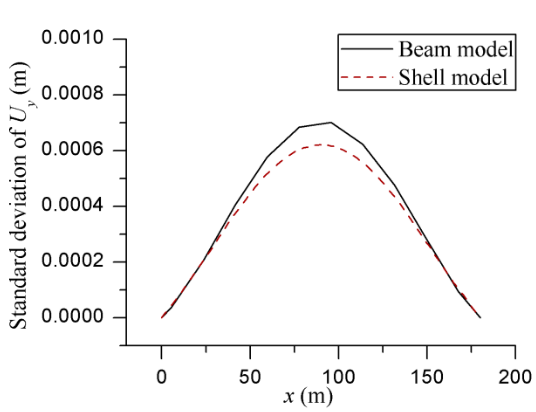

(a) Standard deviation of lateral displacement (windward box)

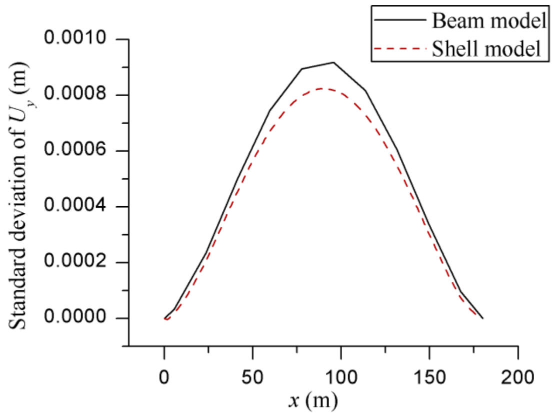

(b) Standard deviation of lateral displacement (leeward box)

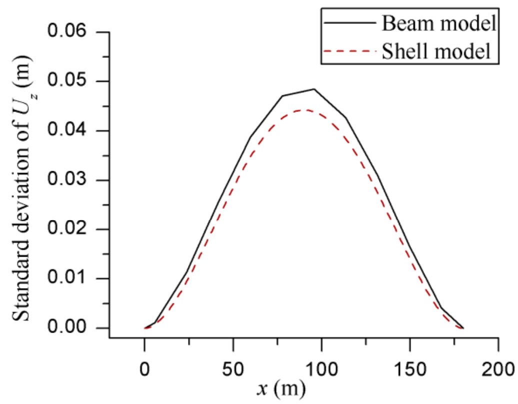

(c) Standard deviation of vertical displacement (windward box)

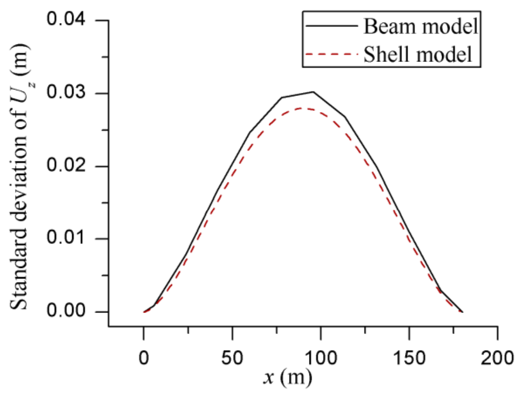

(d) Standard deviation of vertical displacement (leeward box)

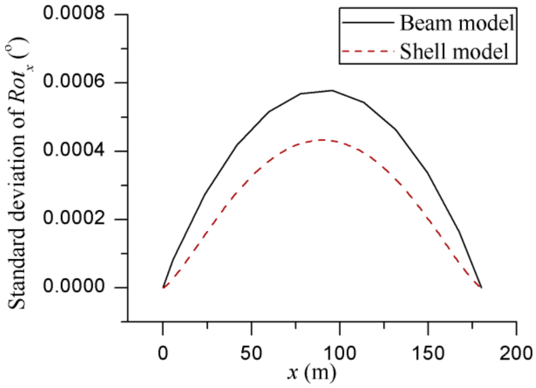

(e) Standard deviation of torsional displacement (windward box)

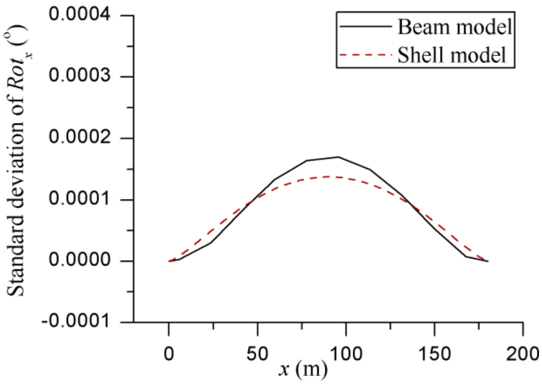

(f) Standard deviation of torsional displacement (leeward box)

Figure 4.10 Standard deviation of displacement responses of the segment

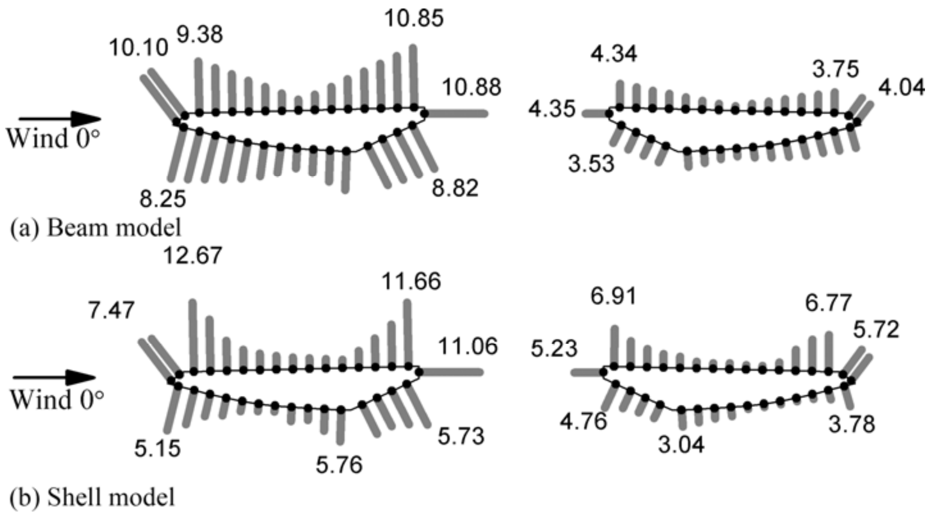

Figure 4.11 Section-wise distribution of the standard deviation of longitudinal stress response (mid-span)

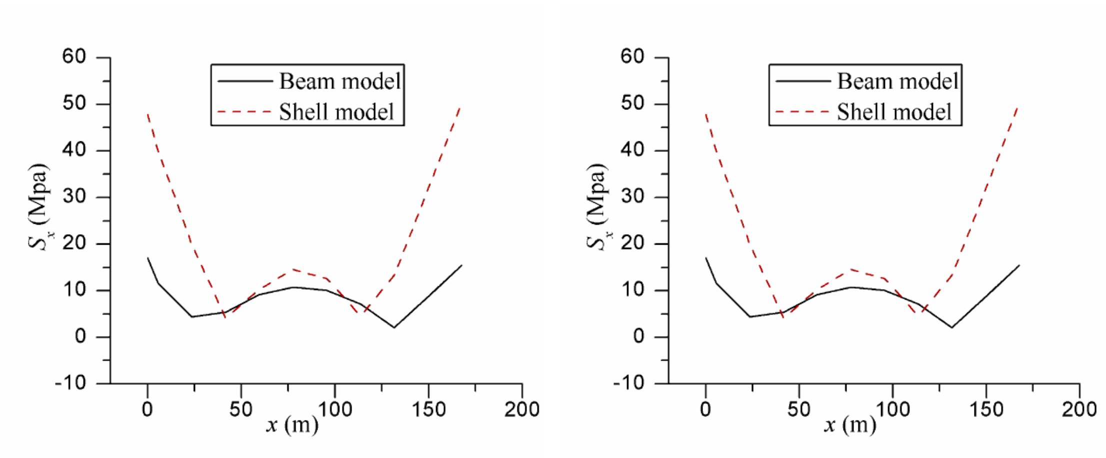

(a) Windward edge of the windward box (b) Windward edge of the leeward box

Figure 4.12 Span-wise distribution of the standard deviation of longitudinal stress response

Figure 4.12 depicts the span-wise distribution of the standard deviation of longitudinal stress responses. Figure 4.12a shows the stress on the windward edge of the windward box, and Figure 4.12b shows the stress on the windward edge of the leeward box. The stress responses yielded by the shell model is much larger than those obtained from the beam model near both ends of the model. This largely results from the different boundary conditions result from the two different types of models: the beam model is actually fixed on both ends on the centroid of the section while the shell model is fixed on all the nodes of the section at both ends. This may be a special phenomenon due to the setting of this case study and probably will not occur in the real bridge. But this phenomenon suggests that the different boundary condition due to these two types of models can cause significant difference in the local stress distribution.

4.6 Summary

A new framework for buffeting-induced stress analysis that can take account of the section-wise distribution of aerodynamic forces on a bridge deck has been developed in this Chapter. Within this framework, the formation of the cross-spectral matrix of distributed aerodynamic forces has been given and the chord-wise correlation of the aerodynamic forces of a twin-box deck has been discussed. A new method to obtain distributed aeroelastic stiffness and damping by distributing the measured sectional aeroelastic properties has been proposed. With the distributed aerodynamic and aeroelastic forces, buffeting analysis has been carried out on a segment of the shell-element model of a twin-box bridge deck. The results show that the responses computed with distributed buffeting loads on the shell model can be different from those computed with the traditional method on a beam model. The displacement responses computed with distributed buffeting loads are slightly smaller than those computed with the traditional method probably because the proposed method more comprehensively considered the correlation of buffeting loads. The section-wise distribution of the dynamic stress responses predicted by the proposed method is more concentrated on the edges for both boxes, resulting in larger maximum stress response. The different boundary conditions due to the two different types of models can also cause significant differences in the computed stress response distribution.

Due to the large computation effort required for the shell-element deck model, the proposed framework was only performed on a segment of the deck model in this Chapter. The modal frequencies of the deck segment are much higher than a real long-span bridge. For the framework to be applied to the full model of Stonecutters Bridge, multi-scale modeling techniques need to be employed so that the total number of DOF of the full model is affordable for computation while the detailed geometry of the twin-box deck can be retained. The establishment of such a multi-scale model of Stonecutters Bridge will be presented in Chapter 5.

CHAPTER 5

MULTI-SCALE MODELING FOR A LONG-SPAN CABLE-STAYED BRIDGE

5.1 Introduction

As reviewed in Chapter 2, traditional FE models that reduce bridge decks to beam elements with equivalent sectional properties are insufficient for a stress-level buffeting analysis, accurate FE models need to be built with detailed geometry using plate/shell/solid elements. The framework for buffeting induced stress analyses in the frequency domain has been proposed in Chapter 4, however, it is very difficult to apply this framework on a detailed FE model of a long-span bridge due to the large computation effort required. Multi-scale modeling techniques are therefore needed to reduce the total number of DOF of the model while the detailed geometry of concerned parts can be retained.

This chapter aims at developing a multi-scale modeling strategy for long-span cable-supported bridges with box decks. With this strategy, multi-scale responses including displacements and stresses in the entire bridge deck can be analyzed with the established multi-scale FE model and compared with those measured by the SHM system. In this regard, a 3-D multi-scale FE model is established in this Chapter for Stonecutters Bridge, which is the third longest cable-stayed bridge in the world. All segments of the twin-box deck are modeled with shell elements in detailed geometry according to the as-built drawings so that stress/strain responses in the bridge girder can be directly computed. The sub-structuring method, which is especially useful in dealing with structures with repetitive geometry like a twin-box deck, is adopted to reduce the number of DOF. The entire main span of the bridge is modeled in the same resolution so that there is no need to pick the concerned regions beforehand. The FE model is then updated with modal frequencies only. After the traditional model updating process, the displacement and stress due to moving trucks are calculated and compared with the measured data.

5.2 Stonecutters Bridge and its SHM system

Stonecutters Bridge (see Figure 5.1) is currently the world's third longest cable-stayed bridge which has a total length of 1596 m and a main span of 1018m. The deck of Stonecutters Bridge is made of steel in the main span. The two side spans are generally in concrete with the transition of 49.74m steel deck from the bridge tower to the concrete deck in the side span. The concrete side spans act as anchor structures balancing the weight and load on the main span. The bridge deck consists of streamlined separated twin-box deck (see Figure 3.2) supported by stay cables every 18m in the main span at the outer edges of the deck and supported by stay cables and piers in the side spans. At the location of the stay cables in the main span, the twin boxes are interconnected by cross girders. The height of the two towers is nearly 300m, measured from the base to the top of the towers. The bridge tower is of single column with a reinforced concrete structure from the base level to level +175m and then a composite steel and concrete structure. The stay cables are anchored in a steel box inside the concrete structure within the height from level +175m to level +293m. The towers are founded on piled foundations.

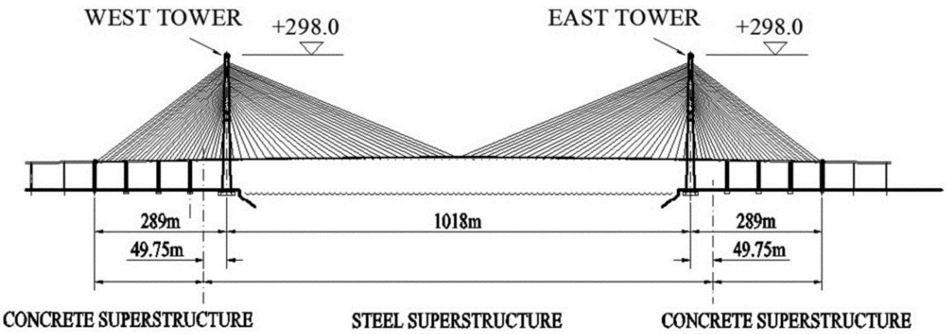

Figure 5.1 Configuration of Stonecutters Bridge

A Structural Health Monitoring and Safety Evaluation System has been deployed for monitoring and evaluating Stonecutters Bridge under in-service condition (Wong 2007). The system is composed of 1571 sensors in 15 different types, namely anemometers, barometers, hygrometers, temperature sensors, corrosion cells, accelerometers, dynamic weigh–in-motion stations, video cameras, dynamic strain gauges, static strain gauges, GPSs, tilt-meters, bearing sensors, buffer sensors and tension-magnetic sensors. The measured natural frequencies and the data from the GPSs and dynamic strain gauges are used in this study to validate the established multi-scale model.

5.3 Multi-scale modeling of the bridge

5.3.1 Modeling of steel deck with sub-structuring method

The bridge is a twin-box deck configuration consisting of two separated longitudinal boxes linked by cross-girders. The steel deck is stayed by the cables with 18m intervals at the outer edge of the deck boxes. Most of the strain gauges of the SHM system are embedded in the steel deck. Therefore, the main focus of this modeling work is the bridge deck.

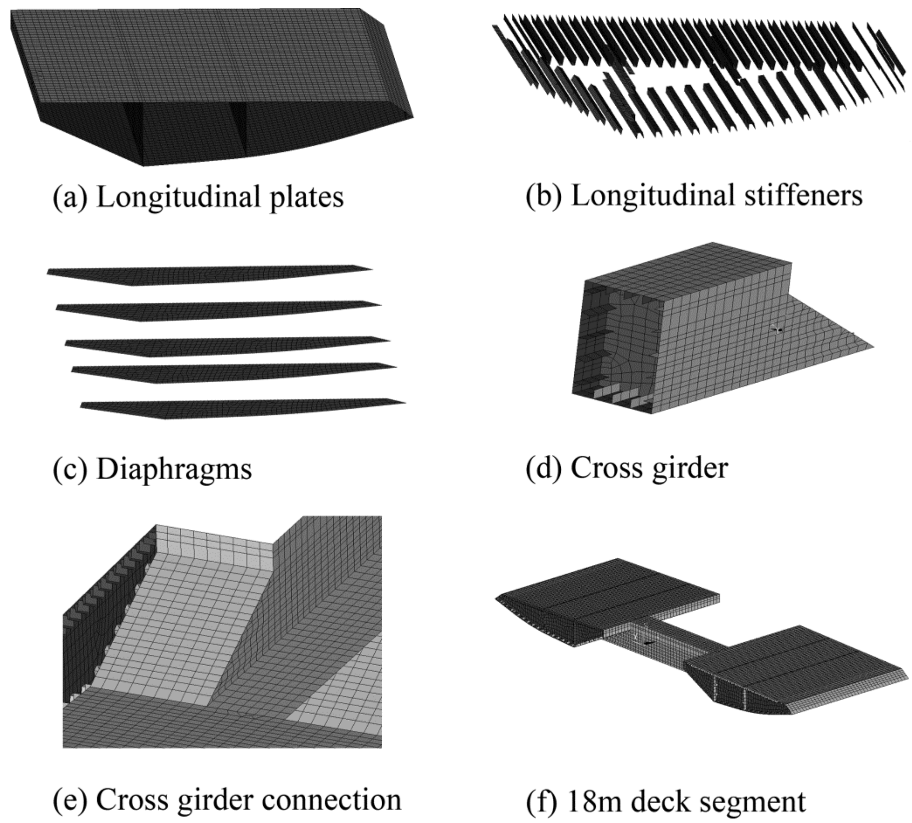

Figure 5.2 FE Model of a typical steel deck segment

The steel deck of Stonecutters Bridge consists of 65 segments. In this study, each segment was modeled with shell elements according to the as-built drawings. Figure 5.2 illustrates the modeling procedure of all the structural components in a typical steel segment. Firstly, the 2D section shape of the longitudinal girder with all the steel plates, webs, troughs and stiffeners was formed with lines. Only T-shape stiffeners were simplified into I-shape for simplification with an equivalent section moment of inertia. Secondly, the section with lines was stretched into the 3-D general geometry of the longitudinal girder. Thirdly, diaphragms were added to the longitudinal girder geometry, and the areas of diaphragms were intersected with the areas of plates and webs but not connected with the areas of troughs and stiffeners. Fourthly, the geometry of the cross girder was formed in a similar way as the longitudinal girder. The longitudinal girders and cross girders were connected by intersecting the areas at the interface (see Figure 5.2e). The material properties were assigned to the components of the deck accordingly and the geometry was meshed into a FE model afterwards.

After the establishment of the shell element models for steel segments, each segment model needs to be condensed into a super-element with the sub-structuring method. Before the procedure, the master nodes should be chosen properly, which should accommodate the connections with other components and all the external forces that may be applied to the model in the subsequent structural analysis. The static reduction method is used in the sub-structuring analysis of this study. The static results yielded by this model are accurate but the dynamic accuracy depends on the choice of master nodes. Thus, mass distribution should also be considered in choosing the master nodes. The selected master nodes in a typical steel segment are shown in Figure 5.3.

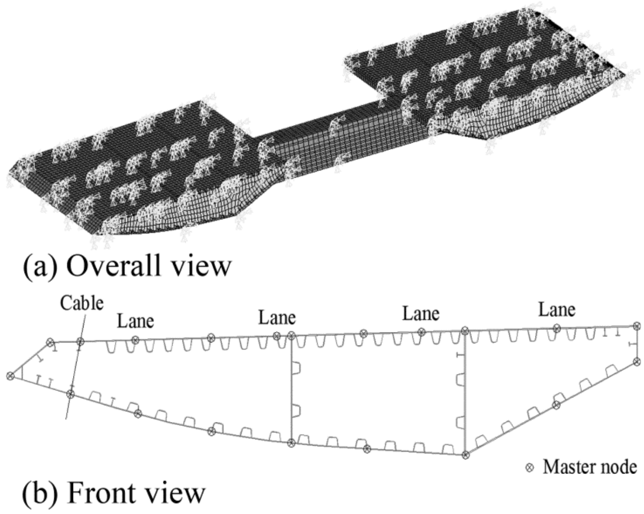

Figure 5.3 Selected master DOF in a steel segment section

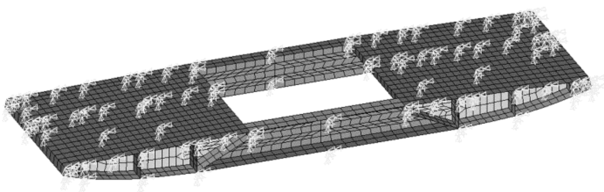

Figure 5.4 FE model of a typical concrete segment

First, in the section-wise plan, the geometry characteristic nodes were selected as master nodes. The geometry characteristic nodes include all the nodes at the corners where deck plates and webs meet. Second, the nodes at cable anchors were selected as master nodes and the nodes at the location of vehicle lanes were also selected so that vehicle loads can be applied on these nodes. Some other nodes were selected to make the distribution of the master nodes in the box girder generally even. The selection of the master nodes in the cross-section of a single box is shown in Figure 5.3b. The nodes at the middle of the top and bottom plates of the cross girder were also selected as master nodes. In the longitudinal direction of the bridge deck, 4 sections were considered for the selection of master nodes for a typical 18m segment (as shown in Figure 5.3a). The detailed locations of the sections are shown in this figure. Two sections are at the two ends of the segment, and the other two are the one crossing the center line of the cross girder and the one crossing the 4th diaphragm, respectively, where the mass of the segment is relatively more concentrated.

The total numbers of the nodes and DOF in the initial and condensed models are listed in Table 5.1. The selection of master nodes and DOF is actually a task to keep a balance between simulation accuracy and computation time. A typical 18m steel segment model contains nearly 150,000 DOF. After sub-structuring, the model is condensed into a super-element with less than 1,000 DOF. With the selection method adopted by this study, the established model of the bridge contains about 75,000 DOF. It is comfortable to conduct dynamic analyses of such FE models with an ordinary personal computer. Theoretically, all the nodes at the connections of segments should be chosen as master nodes in order to maintain simulation accuracy at the connections. This will, however, result in as many as 10 times the number of master DOF in the current model. Therefore, the simulation accuracy at the connections was traded for less computation time without affecting the accuracy for the locations away from the connections.

After forming the super-element for each steel segment, the segments were mounted according to the ideal deck alignment in the global model. Adjacent segments were connected by coupling the corresponding master DOF.

Table 5.1 Numbers of nodes and DOF in the initial and condensed multi-scale models

	NO. of total nodes	NO. of master nodes	NO. of total DOF	NO. of master DOF
Segment connection section	500	42	3,000	252
One 18m steel segment	24,000	164	144,000	984
Entire steel deck	1,496,308	10,142	8,977,848	60,852
Entire model	1,596,247	12569	9,577,482	75,414

5.3.2 Modeling of concrete decks with sub-structuring method

Most of the side spans of the bridge are in concrete. The concrete deck is divided into 14 segments in either the east or west side span. Each segment was modeled with shell elements first and then condensed into a super-element. The FE model of a typical concrete segment is shown in Figure 5.4. The modeling and the selection of master nodes in the concrete decks are similar to those in the steel deck except that the concrete decks were modeled in lower resolution because they are not the main concern of this study. The shell element model of a 15m long typical concrete segment contains about 18,000 DOF. After sub-structuring, the super-element generated contains about 550 master DOF. After forming the super-element for each concrete segment, the segments were mounted according to the ideal deck alignment in the global model. Adjacent segments were connected by coupling the corresponding master DOF. The concrete decks were connected to the steel deck in the same way at their transitions.

5.3.3 Modeling of composite bridge towers

Each tower was composed of a reinforced concrete leg built on a massive reinforced concrete foundation, with the upper part covered by stainless steel skin. No attempt was made to directly monitor the strain/stress of the tower, and the tower was thus modeled with beam elements as shown in Figure 5.5. The bridge tower is of single column with a reinforced concrete structure from the base level to level +175m. This concrete part was modeled as beam elements with equivalent properties calculated based on the cross sections. The concrete towers above level +175m are covered by 20 mm-thick stainless steel skins. Each segment of the composite tower is modeled by two separated and parallel beam elements of different material and section properties. The DOF of stainless steel elements and concrete elements were coupled at the corresponding nodes.

5.3.4 Modeling of piers and pier shafts

The two back spans on the west side and the east side are supported by a total of eight piers. The piers are connected to the concrete deck by pier shafts. All the piers and pier shafts were modeled with beam elements and their properties were calculated based on the cross sections. The models of the piers and piers shafts are shown in Figure 5.6.

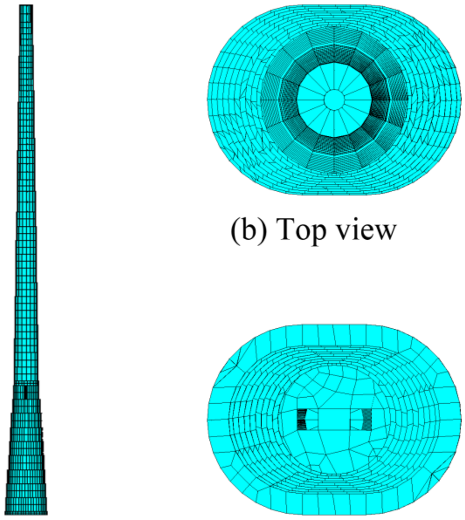

(b) Top view

(a) Front view (c) Bottom view

Figure 5.5 FE model of the bridge towers

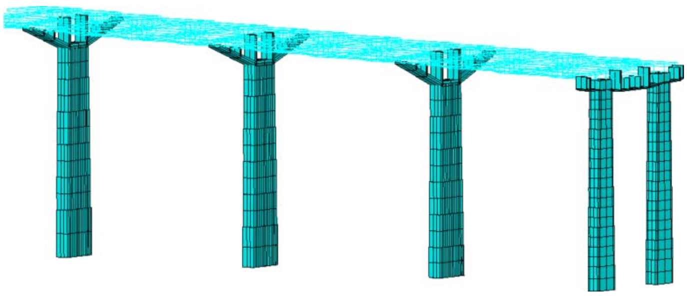

Figure 5.6 FE model of piers and pier shafts

5.3.5 Modeling of stay cables

The cable system of Stonecutters Bridge consists of 112 pairs of stay cables. The cables are composed of different numbers of steel wires. Each stay cable was modeled by one truss element (tension-only). The cable forces were measured and the initial stresses were calculated accordingly and assigned to the elements. The sag effect of a cable element was considered by using the equivalent elastic modulus to replace the actual modulus of the cable. The equivalent elastic modulus is calculated by

$$E_{eq} = \frac{E}{1 + \frac{(\rho A g \bar{l})^2 AE}{12T^3}} \tag{5.1}$$

where E_{eq} is the equivalent modulus of elasticity; E is the effective modulus of elasticity of cable; ρ is the effective density; g the gravity acceleration; $\bar{l}$ is the horizontal projected length of the cable; A the effective cross sectional area; and T is the mean cable tension. In this work, the initial cable elastic modulus is calculated by Eq.(5.1), taking the measured cable force as T. The cables were connected to the decks by sharing nodes and connected to the towers by rigid arms.

5.3.6 Modeling of external tendons

The external pre-stressing steel tendons of the concrete bridge deck were modeled with pre-stressed beam elements. 18 sets of the pre-stressed tendons at the east back span and 18 sets of the pre-stressed tendons at the west back span were modeled. The profiles of tendons were modeled in the concrete bridge decks according to the as-built drawings. The control points of each tendon were anchored to the adjacent concrete deck node with rigid beams (see Figure 5.7).

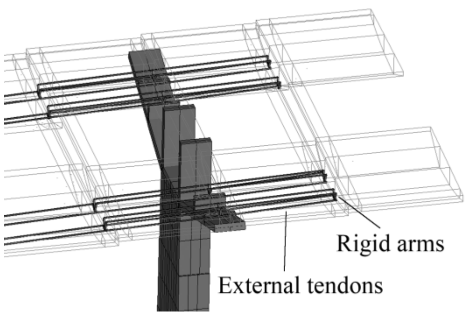

Figure 5.7 Model of external tendons

5.3.7 Modeling of boundaries and connections

The tower and pier bases were modeled as fixed supports, i.e. all DOF were restrained at the supports. Stay cables were connected to the towers by rigid beams at their anchorages at the towers. The bridge deck was stayed by sharing nodes with the cables at the anchorages on deck. The bridge deck and towers are connected by hydraulic buffers in the longitudinal direction. The hydraulic buffers were modeled by spring elements. The horizontal bearings were modeled by coupling the lateral DOF of the corresponding nodes of the tower and decks, i.e. the lateral displacements of the tower and the deck were constrained together at the connections. The modeling details of the deck-to-tower connections are shown in Figure 5.8. The piers and concrete decks were connected with pier shafts. The pier shafts were connected to the concrete decks by sharing nodes. The multi-scale FE model of Stonecutters Bridge, established using commercial software ANSYS, is shown in Figure 5.9.

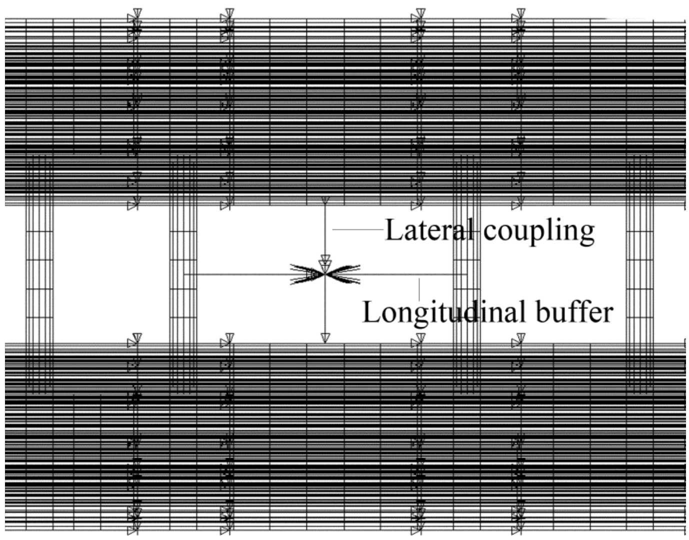

Figure 5.8 Modeling of tower-deck connections

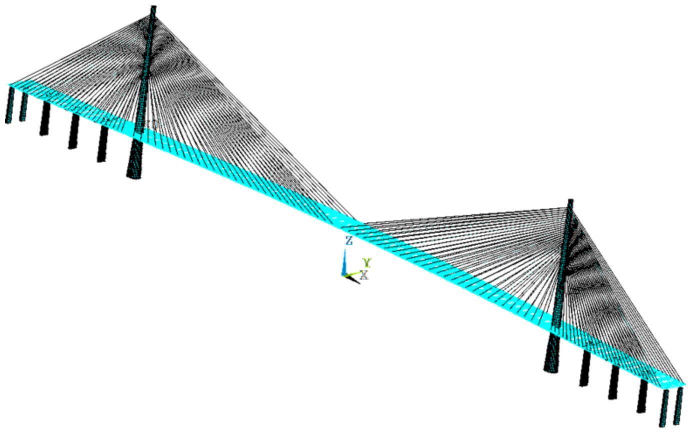

Figure 5.9 The established FE model of Stonecutters Bridge

5.4 Model updating with modal frequencies

In the analysis of cable structures, serious attention should be paid to the appropriate modeling of initial tension (or initial stress) of cables because the geometrical stiffness of the bridge due to initial stresses of cables will considerably affect the results of static and dynamic analyses. In this study, the initial stresses of cables were first calculated by the measured as-built cable forces and then adjusted to match the deck alignment under dead loads with the target configuration of as-built drawings. The adjustment of deck alignment was performed with the geometric non-linear effects and the modal analyses in the updating procedures were performed on the static equilibrium established with non-linear effects.

To ensure the accuracy of the subsequent dynamic analyses using the multi-scale FE model, the established model was updated with reference to the first 10 measured modal frequencies. The updating process was carried out with the sensitivity-based optimization method to minimize the following objective function:

$$J(r_g) = \sum_i w_{\lambda,i} \left[\lambda_i^A(r_g) - \lambda_i^E \right]^2 \tag{5.2}$$

where λ denotes the modal frequency; *i* denotes the number of modes of the global structure; *A* denotes the analytical results; *E* denotes the experiment or measured results; *w* denotes the weighting factor; and r_g denotes the global parameters for updating. In this study, the same weight factor is applied for the concerned modal frequencies.

The selection of parameters is important in sensitivity-based model updating. Not only must the uncertainties in the modeling be parameterized but the objective function must also be sensitive to the chosen parameters. The decision depends on mathematical calculation as well as engineering insights. Computation efforts also need to be considered in the selection because large numbers of iterations are usually needed in the model updating process. Besides, epistemic uncertainty resulting from limited number of sensors can cause multiple solutions to the updating process (Franco et al., 2006). In view of this problem, a limited number of updating parameters are usually selected in the updating of a long span bridge to avoid excessive number of solutions.

FE models can never be exactly the same as the real structures they represent. The differences lie in geometry, material properties, boundary conditions and continuity conditions. Due to the characteristics of FE models, all these uncertainties and inaccuracies are usually considered by updating the stiffness and mass of the components through changing the material properties of elements in the model updating process. The finite element model of Stonecutters Bridge can be divided into several categories: the towers, the cables, the piers, the concrete decks and the steel deck. The towers and piers were modeled by the equivalent beam method and miscellaneous components were not considered in the modeling. Besides, the effect of the internal tendons on the material properties, i.e. the stiffness and density, is merely a rough estimate. The girders were modeled with detailed geometry but secondary components attaching on the girders, such as pavements and railings, were not modeled. Besides, the girders were modeled with the sub-structuring method and the sub-structures were connected through master nodes only. Although the authors had carefully chosen the location of the master nodes to avoid the reduction of stiffness of the connections, but it seems inevitable that this technique will slightly weaken the stiffness of the entire girders. In the modeling, additional mass was added to the deck plates of each segment so that its total weight matches the on-site measurement. However, the additional stiffness contribution of these components and the uncertainties of the manually added mass still need to be considered in the updating process. The uncertainties in the equivalent elastic modulus method used to model the stay cables should also be considered in updating.

A total of 9 parameters were selected and updated after removing low sensitivity parameters. All the selected updating parameters and their initial and updated values are listed in Table 5.2. Due to the aforementioned uncertainties, several frequencies associated with vibration modes of the girders were found to be about 10% lower than the measured results. This magnitude of difference in natural frequencies of a long-span cable-stayed bridge seems to be acceptable for a FE model before updating. Therefore, the change limit of the stiffness was set to be 20% in view of the known deficiencies. Since the change of stiffness in the FE model is often realized through the change of the modulus of steel, the modulus of steel was finally pushed to the bound of +20%.

Table 5.2 Updated structural parameters

Parameter No.	Descriptions	Initial values	Change after updating
1	Elastic modulus of steel longitudinal girder material	2.0e11 N/m^2	+20.0%
2	Elastic modulus of steel cross girder material	2.0e11 N/m^2	+18.2%
3	Elastic modulus of concrete longitudinal girder material	3.55e10 N/m^2	+6.2%
4	Elastic modulus of tower concrete	3.60e10 N/m^2	-20.0%
5	Elastic modulus of cables	varied	+12.4%
6	Density of longitudinal steel girder material	7850 kg/m^3	-20.0%
7	Density of concrete longitudinal girder material	2550 kg/m^3	-6.3%
8	Density of tower concrete	2500 kg/m^3	+20.0%
9	Stiffness of longitudinal buffer	7.115e+07N/m	+20%

The comparison of measured and computed modal frequencies is presented in Table 5.3. It shows that the differences between measured and computed modal frequencies are reduced after the model updating. The lowest natural frequency of 0.161 Hz corresponds to the first lateral bending mode in which the motion of the bridge deck is almost symmetric in the main span. The second lateral mode dominated by the bridge deck is almost asymmetric in the main span at a natural frequency of 0.4125 Hz. The first two natural frequencies in the lateral bending modes dominated by the bridge deck are well separated. Following the first lateral mode of the bridge deck is the two lateral modes dominated by the bridge towers. At the natural frequency of 0.2126 Hz, two towers move in opposite directions whereas at the natural frequency of 0.2167Hz, the two towers move in the same direction. The early occurrence of tower modes indicates that the single column tower used in the bridge is quite slender. The first vertical vibration mode dominated by the bridge deck is almost symmetric in the main span at a natural frequency of 0.2104 Hz. The second vertical vibration mode dominated by the bridge deck is almost asymmetric in the main span at a natural frequency of 0.2632 Hz. The first two natural frequencies in the vertical modes of vibration are relatively close. The first torsional vibration mode dominated by the bridge deck is almost symmetric in the main span at a natural frequency of 0.4586 Hz. The 1st order mode shapes of lateral, vertical and torsional mode of the deck and the 1st order mode shape of the towers are presented in Figure 5.10.

Table 5.3 Comparison of modal frequencies

Mode NO.	Measured (Hz)	Multi-scale model			Mode shape description
		Initial (Hz)	updated (Hz)	Diff*	
1	0.1613	0.1411	0.1662	3.01%	symmetric lateral, deck
2	0.2104	0.2078	0.2174	3.33%	symmetric vertical, deck
3	0.2126	0.2613	0.2150	1.13%	asymmetric lateral, tower
4	0.2167	0.2624	0.2220	2.46%	symmetric lateral, tower
5	0.2632	0.2414	0.2607	-0.95%	asymmetric vertical, deck
6	0.3268	0.3232	0.3234	-1.04%	longitudinal, piers and towers; vertical, deck
7	0.3340	0.3162	0.3385	1.35%	symmetric vertical, deck
8	0.3952	0.3400	0.3927	-0.64%	asymmetric lateral, deck
9	0.4125	0.3649	0.3984	-3.41%	asymmetric vertical, deck
10	0.4586	0.4435	0.4498	-1.92%	symmetric torsional, deck

*Diff refers to the difference between the updated and measured frequency.

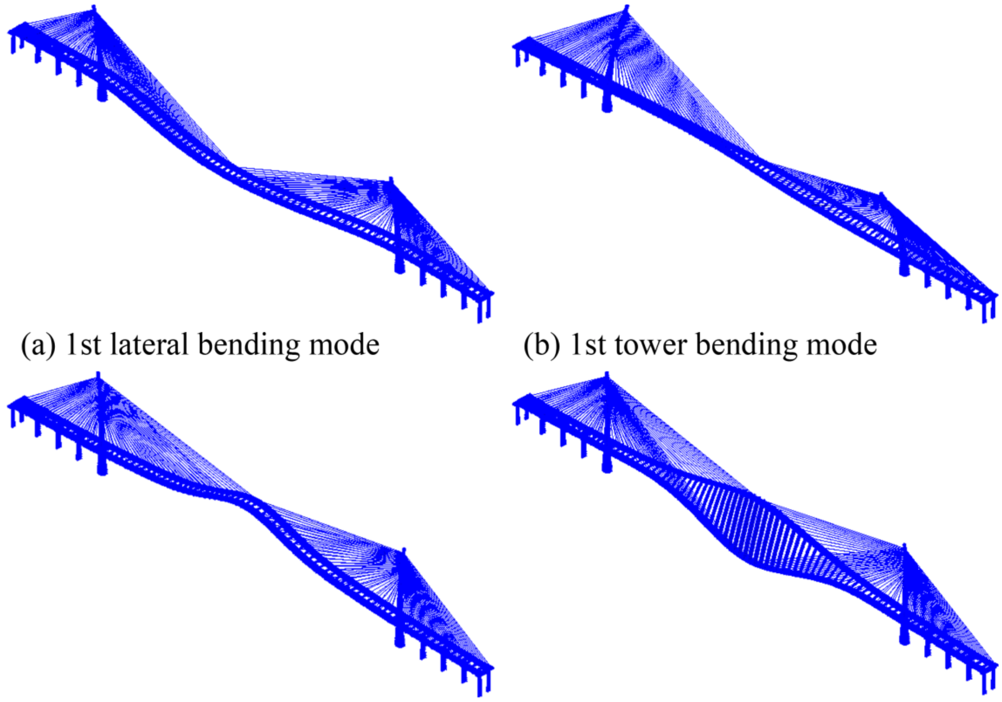

(a) 1st lateral bending mode (b) 1st tower bending mode

(c) 1st vertical bending mode (d) 1st torsional mode

Figure 5.10 1st order mode shapes of lateral, vertical, torsional deck modes and tower modes

5.5 Influence line analysis

Load tests were carried out before the bridge opened to traffic. The displacements and stresses due to moving trucks were recorded by GPSs and strain gauges of the monitoring system during the tests. Comparison between the test data and simulation results with the initial and updated FE model is conducted and the results are presented in Figure 5.11 and Figure 5.12.

Figure 5.11 depicts the vertical displacement of the bridge deck at the middle of the main span due to moving trucks for two cases. The comparison shows that the maximum displacement simulated by the initial model is about 15% larger than the test result. The analytical results of displacement were slightly changed by the model updating process. Nevertheless, the simulation results deviate a little further from the test result after the model updating with measured frequencies. The global updating has increased the stiffness of the deck but it has also reduced the stiffness of the towers. This may account for the deviation of the maximum displacement after model updating and also suggests that the model updating with only the modal frequencies may not improve the accuracy of simulated static displacement responses.

Figure 5.12 depicts the stress recorded by a stress gauge on the deck plate in a steel segment near the middle of the main span for the same cases as the displacements. The comparison shows that the maximum stress simulated by the initial model is about 30% smaller than the test results. The stress results before and after the model updating with only the modal frequencies are nearly the same, which indicates again that the model updating with only the modal frequencies may not improve the accuracy of simulated local responses. A thorough comparison of the measured and computed displacement and stress influence lines can be found in the next chapter.

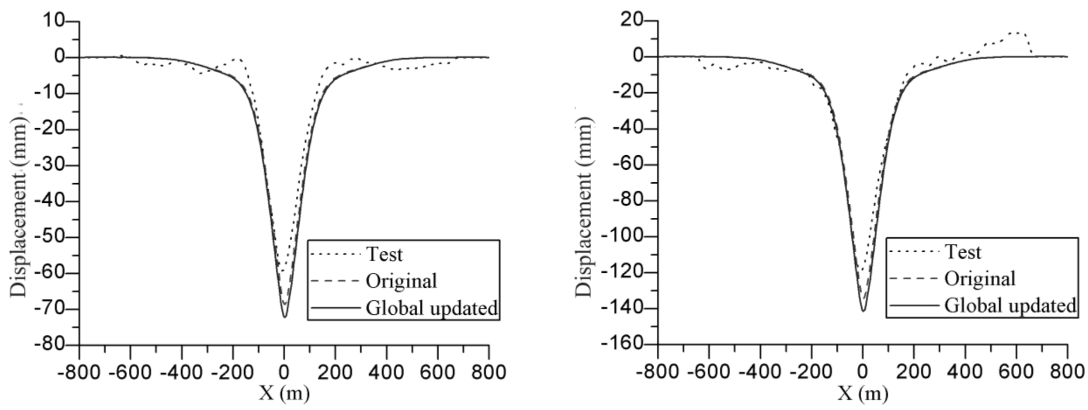

(a) Case A (b) Case B

Figure 5.11 Comparison of computed and measured displacements

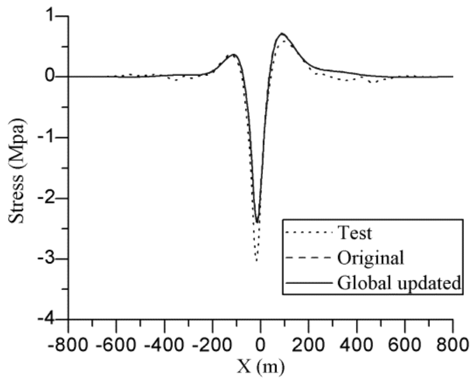

(a) Case A

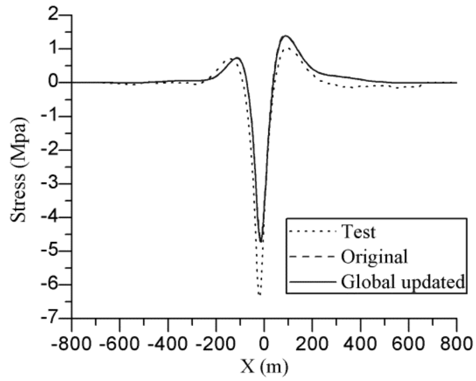

(b) Case B

Figure 5.12 Comparison of computed and measured stresses

5.6 Summary

A 3D multi-scale FE model of Stonecutters Bridge was established in this chapter. All superstructure, substructure, connections and boundary conditions of the bridge were properly modeled. In the FE model, the bridge deck was modeled in detail with shell elements, and therefore accurate stress analysis is enabled. Each deck segment was condensed into a super-element by the sub-structuring method to reduce computation time for the subsequent dynamic analysis. The total number of DOF in the global structure, including all the DOF of normal elements and master DOF of super-elements, amounts to about 75,000. With the multi-scale modeling strategy proposed in this chapter, the entire main span of the bridge can be modeled in detail and the same resolution using shell elements so that all the stress-level responses in the bridge deck can be directly computed and then compared with the measured data from the SHM system. Meanwhile, the total number of DOF in the resulting entire bridge model is suitable for dynamic analyses.

This chapter also investigates how the traditional dynamic-property-based updating affects the accuracy of the multi-scale responses of the bridge. The established FE model was updated with the measured modal frequencies only. Validation with measured frequency data shows that the established model was generally consistent with the real bridge in terms of dynamic properties. The computed displacement and stress influence lines were also compared with the measured data acquired from load tests. The results show that the established multi-scale model is capable of providing both global and local responses. Being updated only with modal frequencies, however, the computed displacement and stress responses under vertical load are not accurate. Updating the model with only modal frequencies cannot improve the accuracy of simulated displacement and stress responses. This indicates a need for multi-scale updating techniques that take into account both dynamic properties and local responses of the multi-scale model, which will be discussed in the next chapter by using the combination of modal frequencies and multi-scale influence lines to update the multi-scale model.

CHAPTER 6

MULTI-SCALE MODEL UPDATING FOR A CABLE-STAYED BRIDGE USING MODAL FREQUENCIES AND INFLUENCE LINES

6.1 Introduction

Chapter 5 has established a substructure-based multi-scale model for Stonecutters Bridge and investigated how the traditional dynamic-property-based updating affects the accuracy of the multi-scale responses of the bridge. The results show that updating the model with only modal frequencies cannot improve the accuracy of simulated displacement and stress responses. This indicates a need for multi-scale updating techniques. As reviewed in Chapter 2, the FE updating method for a long-span bridge using both dynamic characteristics and static responses may be a wise solution.

In view of the above, this chapter presents a new method for updating the multi-scale FE model of a long-span bridge. The method proposes an updating objective function that combines modal frequencies and multi-scale influence lines in order to take into account both dynamic properties and local responses in the updating. This chapter first introduces the proposed method from explaining the relationship between displacement influence lines and mode shapes, and the relationship between strain influence lines and strain mode shapes. The formulation of the multi-scale objective function and the selection of updating parameters are then presented. The proposed model updating method is finally applied to the multi-scale FE model of Stonecutters Bridge, which has been introduced in the last chapter. In light of the large number of DOF of the multi-scale model, the response surface method is adopted in the optimization process to reduce computation time. Finally, the effectiveness of the proposed method is demonstrated by comparison with the measurement data as well as the frequency-only updating technique.

6.2 Advantages of using influence lines in model updating

6.2.1 Review on the model updating based on modal frequencies and mode shapes

Model updating for large-scale structures usually uses iterative methods that work together with a parameterized FE model. The process usually consists of three steps: firstly, a pre-defined number of model parameters are chosen as updating parameters; secondly, the objective functions and constraint conditions are formulated; finally, an optimisation algorithm is performed to minimise the difference between the analytical and measured results from which the updated model parameters are obtained. Structural modal parameters, such as modal frequencies and mode shapes are commonly used for model updating (e.g. Ren et al., 2005).

Modal frequencies can be identified relatively easily form measured structural responses. The relationships between modal frequencies and stiffness matrix and between modal frequencies and mass matrix can be expressed by Eqs. (6.1) and (6.2)

, respectively, in terms of sensitivity coefficients (Zhao & DeWolf, 1999).

$$\frac{\partial \omega_i}{\partial E_{j1}} = \frac{1}{2\omega_i} \{\phi\}_i^T \frac{\partial [K]}{\partial E_{j1}} \{\phi\}_i \tag{6.1}$$

$$\frac{\partial \omega_i}{\partial \rho_{j2}} = -\frac{\omega_i}{2} \{\phi\}_i^T \frac{\partial [M]}{\partial \rho_{j2}} \{\phi\}_i \tag{6.2}$$

$$[K]\{\phi\}_i = \omega_r^2 [M]\{\phi\}_i \tag{6.3}$$

where $\frac{\partial \omega_i}{\partial E_{j1}}$ is the sensitivity coefficient of the *i*th frequency ω_i to the j_1th stiffness parameter E_{j1}; $\frac{\partial \omega_i}{\partial \rho_{j2}}$ is the sensitivity coefficient of the *i*th frequency ω_i to the j_2th mass parameter ρ_{j2}; $\{\phi\}_i$ is the *i*th mode shape of structure; [*K*] and [*M*] are the stiffness and mass matrices of the structure, respectively.

It can be seen from the above equations that the changes in the stiffness and mass matrices with respect to stiffness parameters both will cause changes in modal frequencies. However, from the characteristic equation expressed by Eq.(6.3), it can be seen that no changes will happen if both mass matrix and stiffness matrix change in the same ratio. A similar observation can also be made from the formulation of mode shapes. Consequently, the model updating of a structure based on measured frequencies and mode shapes will neglect the scale factor between mass and stiffness of the bridge structure.

Furthermore, due to the limited number of sensors, it is very difficult, if not impossible, to obtain the accurate mode shapes of a long-span bridge for local structural components. The identification of mode shapes usually involves larger error than the identification of modal frequencies. To overcome the problems mentioned above in the model updating with modal frequencies and mode shapes, a convenient and effective way is to replace mode shapes with static influence lines in the updating objective functions.

6.2.2 Relationship between displacement influence lines and mode shapes

An influence line is defined as the variation of a response (e.g. internal force, displacement or stress) at one location of a bridge structure under a moving unit load. One displacement influence line therefore represents part of the flexibility coefficients in the flexibility matrix of the structure. The moving unit load can be represented by a sequence of unit forces acting on different DOF of the bridge. The unit force moving from DOF i_1 to i_l of a structure of a total of number of n DOF can be expressed as a sequence of load vectors as

$$
\begin{array}{l}
\qquad\qquad\quad \overbrace{\;i_1 \quad i_2 \quad \cdots \quad i_l\;}^{DOF} \\
\{P_1\} = [0 \quad \cdots \quad 1 \quad 0 \quad \cdots \quad 0 \quad \cdots \quad 0]^T \\
\{P_2\} = [0 \quad \cdots \quad 0 \quad 1 \quad \cdots \quad 0 \quad \cdots \quad 0]^T \\
\qquad\qquad\qquad \vdots \\
\{P_l\} = [0 \quad \cdots \quad 0 \quad 0 \quad \cdots \quad 1 \quad \cdots \quad 0]^T
\end{array}
\tag{6.4}
$$

in which i_k (k=1, …, l) is the number of DOF where the unit force acts.

The displacement of the bridge structure under the unit load $\{P_k\}$ (k=1, …, l) can be calculated by

$$\{Y\} = [F]\{P_k\} \tag{6.5}$$

where $\{Y\}$ is the displacement vector of size $n \times 1$ due to $\{P_k\}$; $[F]$ is the flexibility matrix of size $n \times n$; and n is the total number of DOF of the structure.

Assume that the displacement Y_j is the jth element in the displacement vector $\{Y\}$ and that it can be measured by a displacement transducer or GPS. Then, $Y_{jk}=\{F_j\}^T\{P_k\}$, where $\{F_j\}^T$ is the jth row of flexibility matrix $[F]$ and $\{P_k\}$ is the vector with all zero elements except the kth element. As a result, the measured displacement Y_{jk} is actually equal to the flexibility coefficient f_{jk}. The displacement influence line vector $\{Y_{jIL}\}$ at the jth DOF due to the moving unit load can then be formed by the displacements Y_{jk} (k=1 to l) due to the sequence of load vector $\{P_k\}$ (k=1 to l) in Eq.(6.4).

$$\{Y_{jIL}\} = \{Y_{j1}, Y_{j2}, ..., Y_{jl}\} = \{f_{j1}, f_{j2}, ..., f_{jl}\} \tag{6.6}$$

From Eqs.(6.4)~(6.6), it can be found that each element of the displacement influence line is an element of the flexibility matrix $[F]$ of the structure and that the displacement influence line $\{Y_{jIL}\}$ is a sub-vector of the flexibility matrix.

Theoretically, if every displacement influence line of the all DOF is measured with a unit load moving through all DOF of the structure, the whole flexibility matrix can be obtained. It is also noted that the flexibility matrix is the inverse of stiffness matrix, and it is widely used in model updating because of its high sensitivity to the stiffness change in a bridge structure. Furthermore, the flexibility matrix is related to the modal frequencies and mode shapes as expressed by the following equation (Pandey & Biswas; 1994).

$$[F] = [\phi]\left[\frac{1}{\omega^2}\right][\phi]^T = \sum_{j=1}^{r}\frac{1}{\omega_j^2}\{\phi\}_j\{\phi\}_j^T \tag{6.7}$$

It is therefore concluded that displacement influence lines together with modal frequencies can also provide similar information as mode shapes together with modal frequencies.

6.2.3 Relationship between strain influence lines and strain mode shapes

Given a linear transformation matrix $[T_\varepsilon]$ from the displacement vector $\{Y\}$ to strain vector $\{\varepsilon\}$, the following equation can be written.

$$\{\varepsilon\} = [T_\varepsilon]\{Y\} = [T_\varepsilon][F]\{P_k\} = [F^\varepsilon]\{P_k\} \tag{6.8}$$

where $[F^\varepsilon]$ is defined as the strain flexibility matrix of size $m\times n$, and m is the number of elements in the strain vector $\{\varepsilon\}$. Denote the strain ε_j is the jth element in the strain vector $\{\varepsilon\}$, which can be measured by a strain gauge or optical fiber sensor. Then, ε_{jk} $=[F_j^\varepsilon]\{P_K\}$, where $[F_j^\varepsilon]$ is the jth row of strain flexibility matrix $[F^\varepsilon]$. The corresponding strain influence line vector $\{\varepsilon_{jIL}\}$ due to a moving unit force is composed by the measured strain ε_{jk} (k=1~l) under the sequence of the load vector.

$$\{\varepsilon_{jIL}\} = \{\varepsilon_{j1} \quad \varepsilon_{j2} \quad \cdots \quad \varepsilon_{jl}\} = \{f_{j1}^\varepsilon \quad f_{j2}^\varepsilon \quad \cdots f_{jl}^\varepsilon\} \tag{6.9}$$

Clearly, $\{\varepsilon_{jIL}\}$ is a sub-vector of the strain flexibility matrix $[F^{\varepsilon}]$. Theoretically, if every strain influence line of all the concerned elements is measured with a unit load moving through all DOF of the structure, the entire strain flexibility matrix $[F^{\varepsilon}]$ can be obtained. Moreover, the strain flexibility matrix has the relationship with the modal frequencies and mode shapes as follows:

$$\left[F^{\varepsilon}\right]=\left[\phi^{\varepsilon}\right]\left[\frac{1}{\omega^{2}}\right]\left[\phi^{\varepsilon}\right]^{T}=\sum_{j=1}^{r}\frac{1}{\omega_{j}^{2}}\left\{\phi^{\varepsilon}\right\}_{j}\left\{\phi^{\varepsilon}\right\}_{j}^{T} \tag{6.10}$$

The above equation indicates that strain influence lines (strain flexibility matrix) can provide similar information as strain mode shapes. Strain mode shape, which is often obtained by the differentiation of mode shape, is also widely used in the model updating and damage detection due to its high sensitivity to local stiffness changes.

6.2.4 Measurement of displacement and strain influence lines

Since the dynamic amplification effect on stress and displacement responses of a long-span bridge is minimal if a vehicle runs on the bridge at a very low speed (Chen et al., 2011), the static displacement or stress influence line at one location of the bridge can be approximately obtained by the time-domain displacement or stress response of the same location due to the moving vehicle. In fact, a trial static load test which employs pre-weighted trucks running on the bridge at a very low speed is often performed before a long-span bridge is opened to the public, and similar tests can also be periodically scheduled during the service life of bridge. With the aid of a pre-installed structural health monitoring system, the time-domain displacement and strain responses of a bridge under moving trucks can be conveniently obtained.

Static influence lines can be constructed from the measured responses. The relationship between displacement response $R_j(x)$ at the j^{th} location of a bridge due to multiple axle loads and the static displacement influence line is explained by Eq.(6.11).

$$\begin{aligned}
&R_j(x) = \{Y_{jIL}\}\{\Psi(x)\}^T \\
&\{\Psi(x)\}^T = [\Phi(x)]\{A\}^T \\
&\{A\}^T = \{p_1 \quad p_2 \quad \cdots \quad p_N\}_{1\times N}^T \\
&[\Phi(x)] = \begin{bmatrix} \zeta_{11}(x) & \zeta_{12}(x) & \cdots & \zeta_{1N}(x) \\ \zeta_{21}(x) & \zeta_{22}(x) & \cdots & \zeta_{2N}(x) \\ \cdots & \cdots & \cdots & \cdots \\ \zeta_{l1}(x) & \zeta_{l2}(x) & \cdots & \zeta_{lN}(x) \end{bmatrix}
\end{aligned} \tag{6.11}$$

where x is the location of the first axle of the first vehicle along a longitudinal lane and $x=vt$ if all the vehicles run at the same speed v; N is the total number of the axles of all the vehicles in the line; p_i (i=1 to N) is the i^{th} axle load of the vehicle; $\{\Psi(x)\}^T$ is the vector of size $l\times 1$; and $\zeta_{ij}(x)$ is the interpolation coefficient at the i^{th} location for the j^{th} axle load. The relationship between the measured time-domain strain response due to a few moving trucks and the strain influence line can also be obtained in a similar way. By using these relationships, the measured displacement and strain influence lines can be obtained from the measured time-domain displacement and strain responses respectively.

6.3 Objective functions and constraint conditions

The objective function in model updating process is usually defined as an error function between the calculated and measured results. The objective function in term of modal frequency can be defined as

$$\Upsilon_{Fi} = 1 - \omega_{ai} / \omega_{ti} \tag{6.12}$$

where ω_{ai} and ω_{ti} are the calculated and measured frequencies; and Υ_{Fi} represents the error between measured and calculated frequencies.

As mentioned above, each displacement or strain influence line reflects part of the stiffness/flexibility matrix of the structure and can provide a new index for the model updating of a long-span bridge instead of mode shapes or strain mode shapes. Similar to modal assurance criterion (MAC) for each mode shape, two indexes Υ_{Di} and Υ_{Si} are used to represent the error functions between measured and calculated displacement and strain influence lines, respectively.

$$\begin{aligned}
\Upsilon_{Di} &= a_0 DAC_i + b_0 DNO_i^2,\ DAC_i = 1 - \frac{\left(\{Y_{Ai}\}\{Y_{Ti}\}^T\right)^2}{\{Y_{Ai}\}\{Y_{Ai}\}^T \cdot \{Y_{Ti}\}\{Y_{Ti}\}^T},\ DNO_i = 1 - \frac{Y_{Ai,\max}}{Y_{Ti,\max}} \\
\Upsilon_{Si} &= a_0 SAC_i + b_0 SNO_i^2,\ SAC_i = 1 - \frac{\left(\{\varepsilon_{Ai}\}\{\varepsilon_{Ti}\}^T\right)^2}{\{\varepsilon_{Ai}\}\{\varepsilon_{Ai}\}^T \cdot \{\varepsilon_{Ti}\}\{\varepsilon_{Ti}\}^T},\ SNO_i = 1 - \frac{\varepsilon_{Ai,\max}}{\varepsilon_{Ti,\max}}
\end{aligned} \tag{6.13}$$

where $\{Y_{Ti}\}$ and $\{Y_{Ai}\}$ are the measured and calculated displacement influence line vectors at the ith location, respectively; $\{\varepsilon_{Ti}\}$ and $\{\varepsilon_{Ai}\}$ are the measured and calculated strain influence line vectors at the *i*th location, respectively; $Y_{Ai,max}$ and $Y_{Ti,max}$ are the measured and calculated amplitudes of the displacement influence lines; $\varepsilon_{Ai,max}$ and $\varepsilon_{Ti,max}$ are the measured and calculated amplitudes of the strain influence lines. DAC_i and SAC_i are the assurance criterion for the shapes of the displacement and strain influence lines, respectively; DNO_i represents the difference of amplitude between the measured and calculated displacement influence lines; SNO_i represents the difference of amplitude between the measured and calculated strain influence lines; a_0 and b_0 are the weighting factors for the shape and amplitude of influence lines, respectively.

The measured modal frequencies and displacement influence lines reflect the global properties of a long-span bridge, while the strain influence lines reflect the local properties of the long-span bridge. The objective function $J(r)$ for multi-objective model updating should be a function of all the three types of objectives. It should be noted that the three objectives are incommensurable: for example, the unit of model frequency is Hz while the unit of displacement influence line is m. Thus, different weighting factors β_j should be assigned to each objective. As a result, the objective function can be expressed as

$$Min\left(J\left(\mathbf{r}\right)\right) = Min\left(\beta_1 J^1 + \beta_2 J^2 + \beta_3 J^3\right) \tag{6.14}$$

where $\beta_1+\beta_2+\beta_3=1$; J^1, $J^2$and J^3 are the functions with respect to modal frequencies, displacement and strain influence lines, respectively, and they can be expressed as

$$J^1 = \sum_{i=1}^{m}\left(\Upsilon_{Fi}\right)^2, J^2 = \sum_{i=1}^{l}\Upsilon_{Di}, J^3 = \sum_{i=1}^{k}\Upsilon_{Si} \tag{6.15}$$

where m, l and k are the total number of modal frequencies, displacement influence lines and strain influence lines used in the model updating, respectively. During the process of model updating by using the objective function of Eq.(6.14), J^j (j=1~3) must be constrained within a certain region of allowable error as

$$\Upsilon_{Fi} < \delta_f , \Upsilon_{Di} < \delta_d , \Upsilon_{Si} < \delta_s \tag{6.16}$$

where δ_f, δ_d and δ_s are the given value of tolerance for three indexes, respectively.

In order to select reasonable model parameters to be updated, sensitivity analyses should be carried out to select n_p sensitive parameters $\{r\} = \begin{bmatrix} r_1 & r_2 & \cdots & r_{n_p} \end{bmatrix}^T$. In order to maintain the physical meaning of each model parameter in the updating process, the parameters also have to be constrained by certain conditions as

$$\left|1 - r_i^a / r_i^d\right| < \delta_r \tag{6.17}$$

where r_i^a and r_i^d are the calculated and designed values of a model parameter, respectively; and δ_r is the given value of the tolerance.

The objective function Eq.(6.14) and its corresponding constraint equations form a optimization problem for the multi-scale model updating of a long-span bridge.

6.4 Response surface method for model updating of a long-span bridge

Solving the above optimization problem usually requires an iterative process which involves finite element analysis of the model in every step. Such an optimization may be difficult to implement because of the large number of DOF of a detailed multi-scale model of a long-span bridge.

A response surface method provides a simple relationship between the model parameters and objective functions. With the response surface method, the total number of finite element analyses can be considerably reduced in the optimisation process (e.g. Bucher & Bourgund, 1990; Panda & Manohar, 2009; Perotti et al., 2013). In the model updating of structural finite element model, polynomials are often used for constructing response surfaces because the calculations are simple and the resulting function is a closed-form algebraic expression. The following quadratic polynomial response surface model is used in this study.

$$\Upsilon_l = a_0 + \sum_{i=1}^{n_p} a_{1,i} r_i + \sum_{i=1}^{n_p} a_{2,i} r_i^2 + \sum_{i=1}^{n_p} \sum_{j=i}^{n_p} a_{3,ij} r_i r_j \tag{6.18}$$

where Υ_l (l=1 to q) is the lth objective including all Υ_{Fi}, Υ_{Si} and Υ_{Di}; q is the number of objectives; $a_{0,i}$, $a_{1,i}$, $a_{2,i}$ and $a_{3,ij}$ are the regression coefficients.

In addition, as mentioned above, Υ_{Fi} is related to both mass and stiffness parameters, while Υ_{Di} and Υ_{Si} are related to stiffness parameters only. Consequently, the regression coefficients with respect to mass parameters in the response surface model should be zeroes for Υ_{Di} and Υ_{Si}.

With Eq.(6.18), $\{\Upsilon\} = \begin{bmatrix} \Upsilon_1 & \Upsilon_2 & \cdots & \Upsilon_q \end{bmatrix}^T$ can be represented by a series of simple functions of the model parameters $\{r\} = \begin{bmatrix} r_1 & r_2 & \cdots & r_{n_p} \end{bmatrix}^T$. The response surface model can be created by the following steps: 1) FE analyses are carried out for a series of selected model parameters at various sample points; 2) the regression coefficients in Eq.(6.18) are obtained by least-square fitting. After the accuracy of the regressed surface model is verified, the response surface model can be used as a surrogate of the finite element model in model updating.

6.5 Updating the multi-scale model of Stonecutters Bridge

6.5.1 Moving vehicle load tests

Stonecutters Bridge in Hong Kong is a two-cable plane cable-stayed bridge and it is currently the third longest cable-stayed bridge in the world. The bridge has a separated twin-box steel deck at the central span and twin-box concrete decks at two side spans. A SHM system is deployed for monitoring and evaluation of the bridge performance under in-service condition. A large number of sensors including dynamic strain gauges (D-strs) and Global Position Systems (GPSs) are installed in the SHM system. To facilitate an effective assessment of stress-related bridge performance and safety, a multi-scale finite element model with detailed geometry and affordable computation time is established. Accurate stress/strain responses can be obtained with this model. Detailed information on the bridge and its multi-scale finite element model can be found in Chapter 5.

Table 6.1 Weights of test trucks

Truck No.	Cross Weight (ton)	Axle Weight (ton)				
		W1	W2	W3	W4	W5
1	41.68	4.58	7.09	7.09	11.46	11.46
2	40.75	4.48	6.93	6.93	11.21	11.21
3	40.49	4.45	6.88	6.88	11.13	11.13
4	41.89	4.61	7.12	7.12	11.52	11.52
5	41.75	4.59	7.10	7.10	11.48	11.48
6	41.72	4.51	7.09	7.09	11.47	11.47
7	41.01	4.58	6.97	6.97	11.25	11.28
8	41.60	4.52	7.07	7.07	11.44	11.44
9	41.10	4.62	6.99	6.99	11.30	11.30

Before Stonecutters Bridge opened to the public in December, 2009, a series of trial load tests which employs pre-weighted moving trucks were performed. As shown in Figure 6.1, Stonecutters Bridge has eight highway traffic lanes. In the trial load test, nine 13m-long 5-axle trucks, loaded with weighted concrete blocks, were used. Weights of these trucks are in the range from 40.49 tons to 41.89 tons. The axle arrangement and axle load of each truck was measured. Details of the trucks and the weights are shown in Figure 6.2 and Table 6.1.

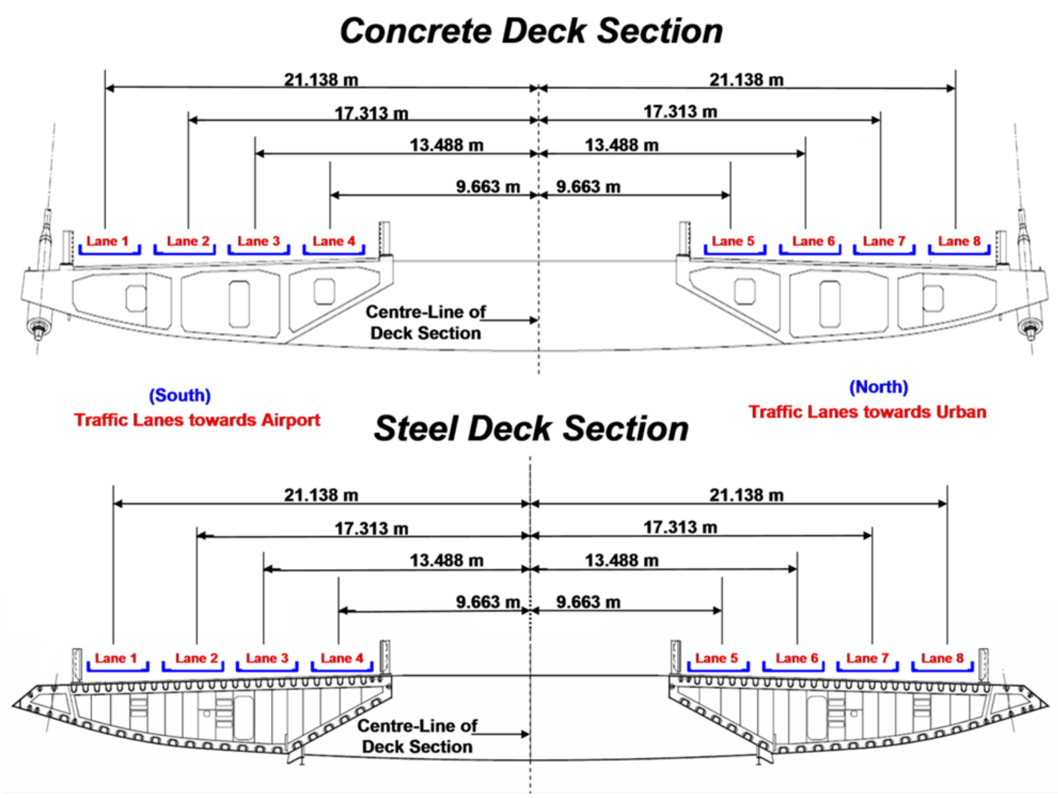

Figure 6.1 Layout of the lanes in Stonecutters Bridge

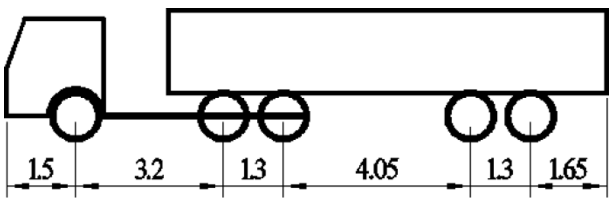

Figure 6.2 Details of a loading truck

Four cases were considered in the load test: one truck on Lane 1 (Case 1); one truck on Lane 8 (Case 2); two trucks on the Lane 1 and 2, respectively (Case 3); two trucks on Lane 7 and 8, respectively (Case 4). The displacement and stress influence lines due to the trucks moving on designated traffic lanes were obtained using the displacement and strain responses measured by GPS receivers and dynamic strain gages in the SHM System.

As shown in Figure 6.3, two GPS receivers (namely GPS01 and GPS08) were installed at the top of the two towers to measure the displacements of the towers at top, and six GPS receivers (namely GPS02 to GPS07) were installed at the outer edges of the bridge deck (located approximately at the quarter and middle of the main span) to measure the displacements of the bridge deck. The real-time data were acquired at a sampling frequency of 20Hz and smoothed with 5-point moving average method. As shown in Figure 6.4, five dynamic strain gauges were installed at the top and bottom deck-plates of Segments Nos.4, 7, 32 and 62 of the south box and four strain gauges were installed at the top and bottom deck-plates of Segment No.17 of the south box. The layout of dynamic strain gages in the north box and the south box is symmetrical about the longitudinal axis of the bridge. These strain gages were used to measure the longitudinal stresses in the bridge deck.

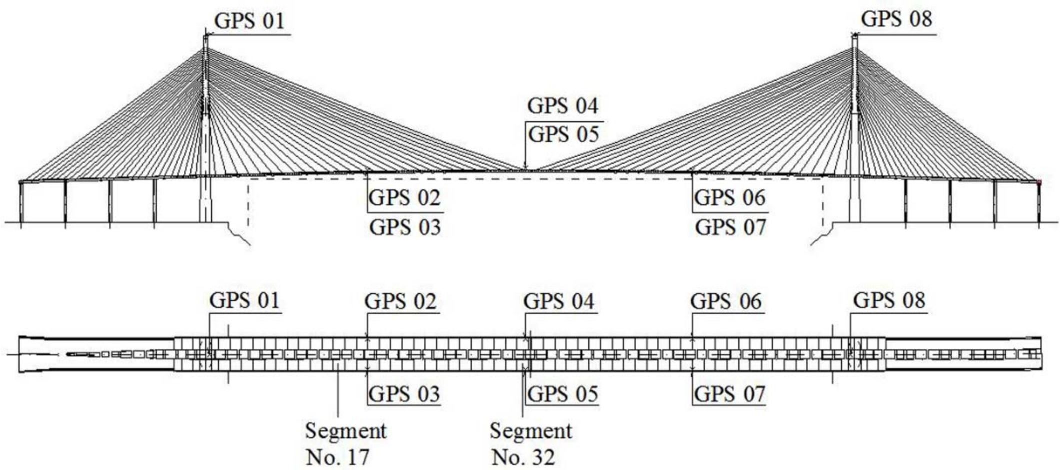

Figure 6.3 GPS locations at Stonecutters Bridge

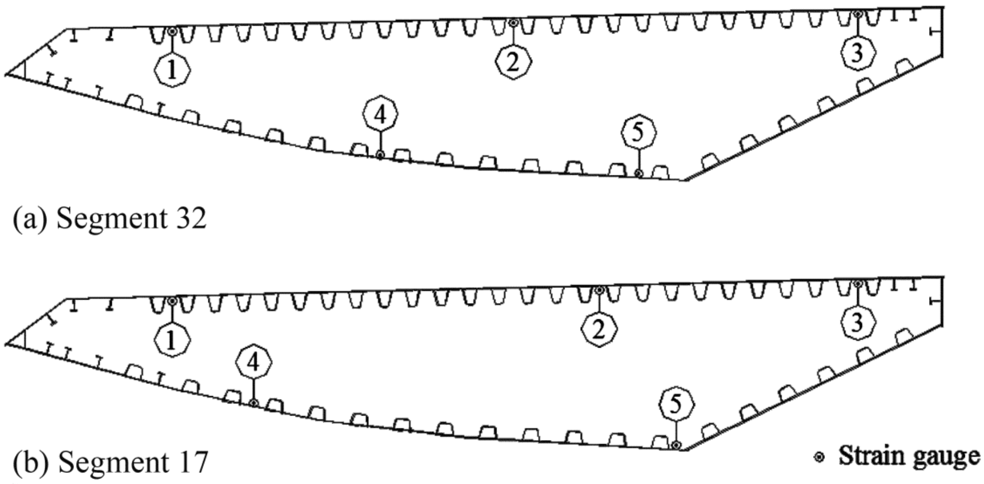

Figure 6.4 Layout of the longitudinal D-Strs at the deck-plates, webs and deck-troughs of longitudinal steel girder

12 measured displacement influence lines and 20 measured stress influence lines acquired from the tests were used in this case study. The description of these influence lines is listed in Table 6.2 and Table 6.3. Some typical displacement and stress influence lines are shown in Figure 6.5 and Figure 6.6. The vertical displacement influence lines of No.1, 3 and 8, and the longitudinal stress influence lines of No.15, 16 and 21 are respectively shown in Figure 6.5 and Figure 6.6 along with those calculated by the initial multi-scale bridge model. As shown in Figure 6.5 and Figure 6.6, the measured and calculated displacement influence lines have similar shapes. However, the differences between the maximum values of measured and calculated influence lines are remarkable.

Table 6.2 Description of vertical displacement influence lines (IL)

Parameter No.	GPS No.	Location of truck/trucks
1	GPS02	Lane 8
2	GPS03	Lane 8

3	GPS04	Lane 8
4	GPS05	Lane 8
5	GPS06	Lane 8
6	GPS07	Lane 8
7	GPS04	Lane 1
8	GPS05	Lane 1
9	GPS04	Lane 7 and Lane 8
10	GPS05	Lane 7 and Lane 8
11	GPS04	Lane 1 and Lane 2
12	GPS05	Lane 1 and Lane 2

Table 6.3 Description of longitudinal stress influence lines (IL)

Parameter No.	Segment No.	Girder	D-Str No.	Location of truck/trucks
13	32	North	D-str1	Lane 8
14	32	North	D-str2	Lane 8
15	32	North	D-str3	Lane 8
16	32	North	D-str4	Lane 8
17	32	North	D-str5	Lane 8
18	32	South	D-str1	Lane 8
19	32	South	D-str2	Lane 8
20	32	South	D-str3	Lane 8
21	32	South	D-str4	Lane 8
22	32	South	D-str5	Lane 8
23	17	North	D-str2	Lane 8
24	17	North	D-str4	Lane 8
25	17	South	D-str1	Lane 8
26	17	South	D-str2	Lane 8
27	17	South	D-str3	Lane 8
28	17	South	D-str4	Lane 8
29	32	North	D-str3	Lane 7 and Lane 8
30	32	North	D-str5	Lane 7 and Lane 8
31	32	South	D-str3	Lane 7 and Lane 8
32	32	South	D-str5	Lane 7 and Lane 8

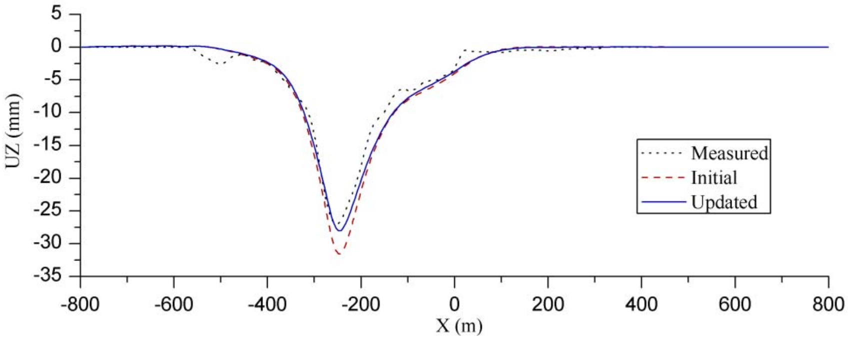

(a)

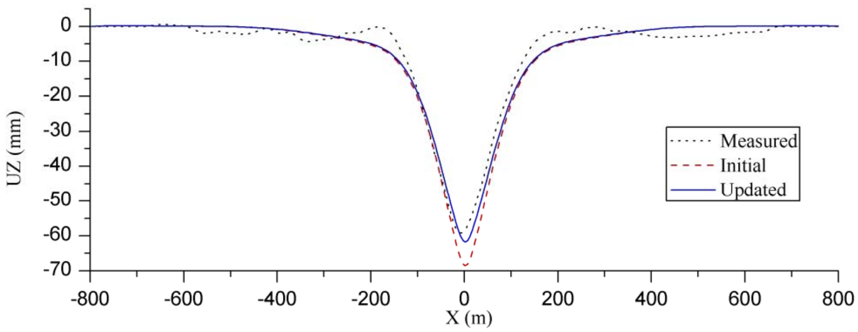

(b)

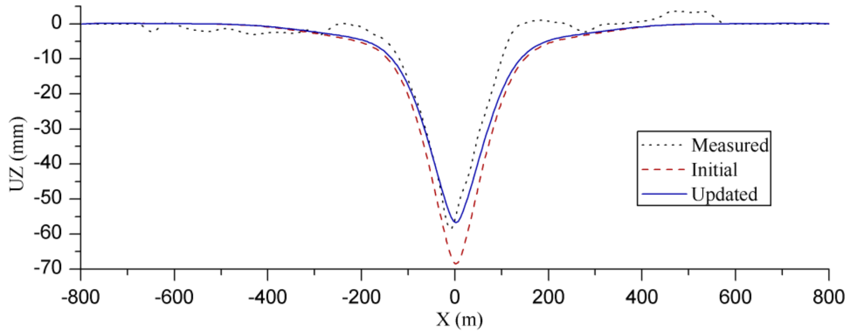

(c)

Figure 6.5 Typical measured displacement IL(the dotted line is measured displacement IL; the dashed and solid line are stress ILs calculated by initial and updated model, respectively; a, b and c represent No.1, 3 and 8 displacement ILs, respectively)

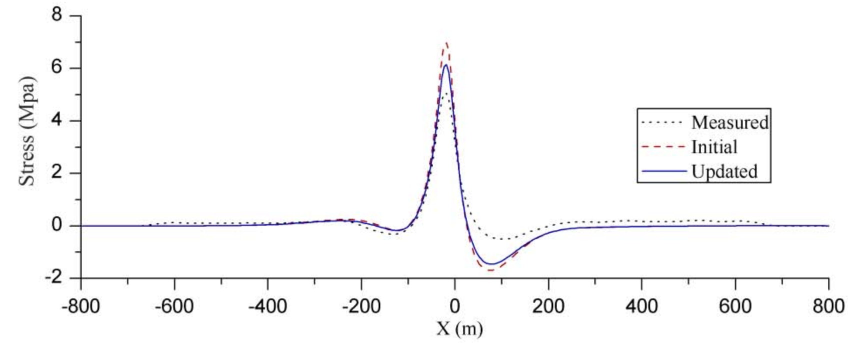

(a)

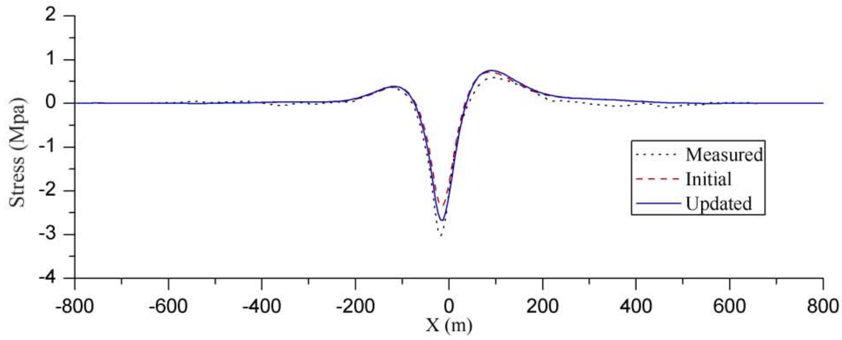

(b)

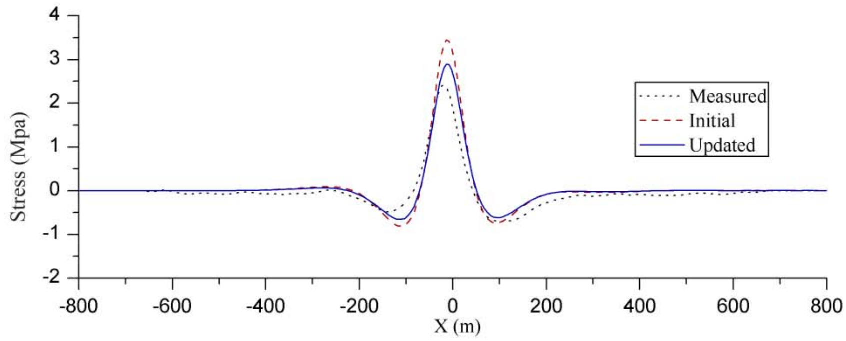

(c)

Figure 6.6 Typical measured stress IL(the dotted line is measured stress IL; the dashed and solid line are stress ILs calculated by initial and updated model, respectively; a, b and c represent No. 16, 15 and 21 stress ILs, respectively) (MPa)

6.5.2 Objectives and parameters in model updating

It can be found from the Chapter 5 that the updating technique using only modal frequencies can ensure the consistency in dynamic properties between the finite element model and the prototype. Nevertheless, the accuracy in predicting static displacement and stress responses may not be improved by such updating process. In view of this, the proposed model updating technique in terms of both modal frequencies and influence lines is applied to update the multi-scale finite element model of Stonecutters Bridge. In the model updating, the first six modal frequencies, the first eight displacement influence lines and the first nine stress influence lines were selected and used to update the model (the number of objectives q=23), and the other measured data could be used for verification of the updated model.

Considering the special feature of the multi-scale model of Stonecutters Bridge, a series of sensitivity analysis was conducted and thirteen sensitive model parameters (n_p=13) were selected, in which nine are stiffness model parameters and four are mass model parameters. The properties of the upper deck plates were considered separately from the other plates in this updating process because the upper deck-plate stresses and bottom deck-plate stresses show opposite trends of deviation from the measured stresses: the simulated upper deck-plate stresses are generally smaller than the measured stresses while the bottom deck-plate stresses are generally larger than the measured stresses. This phenomenon may attribute to uncertainties in additional stiffness and mass contributions made by pavements on the upper deck surface. All the thirteen parameters selected and their initial and updated values are listed in Table 6.4. The tolerances in Eqs. (16 and 17) are set as $\delta_f = 0.1, \delta_d = \delta_s = 0.1$ and $\delta_r = 0.2$, and the weighting factors for the shape and amplitude of influence lines in Eq.(6.13) are set as a_0=0.5 and b_0=0.5.

Table 6.4 Updated model parameters

No.	Description	Initial values	Change after updating
1	Equivalent modulus of elasticity of upper deck plates of steel girder	2.0e11 N/m^2	+20%
2	Equivalent modulus of elasticity of other plates of the steel girder		+14.59%
3	Equivalent mass density of upper deck plates of the steel girder	7850 kg/m^3	-20.00%
4	Equivalent mass density of other plates of the steel girder		-20.00%
5	Equivalent modulus of elasticity of the steel cross girders	2.0e11 N/m2	-12.75%
6	Equivalent modulus of elasticity of upper deck plates of the concrete girder	3.55e10 N/m^2	+9.50%
7	Equivalent modulus of elasticity of other plates of the concrete girder		+10.25%
8	Equivalent modulus of elasticity of the concrete towers	3.60e10 N/m^2	+20%
9	Equivalent mass density of the concrete towers	2500 kg/m^3	+20%
10	Equivalent modulus of elasticity of the tower steel skins	2.0e11 N/m2	+5.69%
11	Equivalent modulus of elasticity of the cables	varied	+3.49%
12	Equivalent mass density of concrete girder	7850 kg/m3	-4.50%
13	Stiffness of the longitudinal buffers	7.115e+07N/m	+20%

It should be noted that the change of each parameter actually reflects the updating of the stiffness or mass of each component group, not the updating in the material property. The change limit of each parameter was set to be 20% in order to maintain physical meaning of the updating process. Some parameters were pushed up to the bound by model updating as in Chapter 5 where due explanations have been given. Most of the parameters show similar trends in the updating as the corresponding parameters updated in Chapter 5 except the elastic moduli of cross-girder steel and tower concrete. The difference between these two updated parameters reflects the influence of influence lines as updating objectives. The elastic moduli of deck plate steel and other plate steel bear different values after model updating. This may improve the matching between analytical and measured stress influence lines.

6.5.3 Response surface model and updated results

A series of data sets were calculated with the selected parameters at various sample points using commercial software ANSYS. Then, the regression coefficient of response surface model in Eq.(6.19) can be obtained by the least-square method. The weighting coefficients for objectives were set as $\beta_1=0.3$, $\beta_2=0.4$, $\beta_3=0.3$ after testing different sets of weighting factors. According to Eqs.(6.14)~(6.18), the mathematic optimization problem for this model updating can be expressed as

$$\begin{aligned}
&Min\left(J\left(\mathbf{r}\right)\right)=Min\left(\beta_1\sum_{i=1}^{6}\left(\Upsilon_{Fi}\right)^2+\beta_2\sum_{i=1}^{8}\Upsilon_{Di}+\beta_3\sum_{i=1}^{9}\Upsilon_{Si}\right)\\
&\Upsilon_{Fi}<0.1,\Upsilon_{Di}<0.1,\Upsilon_{Si}<0.1\\
&\left|1-r_i^a/r_i^d\right|<0.2\\
&\Upsilon_l=\tilde{a}_0+\sum_{i=1}^{p}\tilde{a}_{1,i}r_i+\sum_{i=1}^{p_l}\tilde{a}_{2,i}r_i^2+\sum_{i<j}\sum_{j=1}^{p_l}\tilde{a}_{3,ij}r_ir_j
\end{aligned}\tag{6.19}$$

The optimum solution of the optimization problem in Eq.(6.19) is obtained by the fmincon function in Matlab toolbox which is commonly used to find the minimum of a constrained nonlinear multivariable function. It should be noted that the result of this updating algorithm is probably a local minimum. Theoretically, if a multi-start method is used to run the algorithm with a large number of initial conditions in the domain, at least one initial guess close to the global solution, which should converge to the global minimum, can be obtained. However, for an optimization problem with such heavy computation load, it is impossible to test a large number of initial conditions.

The comparison of measured and updated modal frequencies is presented in Table 6.5, and the comparisons of measured and updated displacement and stress influence lines are shown in Figure 6.5 and Figure 6.6. As mentioned above, the indexes Υ_{Di} and Υ_{Si} reflect the differences between measured and updated displacement and strain influence lines, respectively. The values of the indices Υ_{Di} and Υ_{Si} are presented in Table 6.6.

Table 6.5 The first six modal frequencies before and after model updating

Mode NO.	Measured (Hz)	Initial (Hz)	Updated 1* (Hz)	Updated 2* (Hz)	Diff 1*	Diff 2*
1	0.1613	0.1411	0.1662	0.1598	3.01%	-0.94%
2	0.2104	0.2078	0.2174	0.2121	3.33%	0.80%
3	0.2126	0.2613	0.2150	0.2321	1.13%	9.17%
4	0.2167	0.2624	0.2220	0.2400	2.46%	10.77%
5	0.2632	0.2414	0.2607	0.2481	-0.95%	-5.75%
6	0.3268	0.3232	0.3234	0.3122	-1.04%	-4.48%

* Updated 1 refers to the modal frequency of the model updated with modal frequencies only as presented in Chapter 5; Updated 2 refers to the modal frequency of the model updated with multi-scale updating; Diff is the difference between the updated and measured frequency; the same below.

Table 6.6 Values of indexes Υ_{Di} or Υ_{Si}

NO.	Initial	Updated 1	Updated 2	NO.	Initial	Updated 1	Updated 2
1	0.0156	0.0188	0.0080	14	0.1546	0.1575	0.0399
2	0.0235	0.0285	0.0110	15	0.0632	0.0686	0.0161
3	0.0201	0.0236	0.0092	16	0.0852	0.0894	0.0344
4	0.0165	0.0207	0.0081	17	0.0425	0.0463	0.0348
5	0.0966	0.1039	0.0174	18	0.0659	0.0690	0.0153
6	0.0401	0.0463	0.0142	19	0.0643	0.0687	0.0157
7	0.0432	0.0481	0.0116	20	0.0302	0.0322	0.0133
8	0.0338	0.0374	0.0092	21	0.0950	0.0994	0.0317
13	0.0466	0.0470	0.0321				

It can be found from Table 6.5 that the differences between the measured and computed modal frequencies are reduced after the model updating and that the updated modal frequencies are close to the measured ones. It can be seen from Figure 6.5 and Figure 6.6 that the differences between the measured and computed displacement and stress responses are all reduced after the model updating. As shown in Table 6.6, the values of indexes Υ_{Di} and Υ_{Si} are changed after model updating and they are within the range of the constrained region in Eq.(6.19). The simulated influence lines by the proposed model technique are close to the measurement ones.

For a long-span bridge, the information obtained from the real structure is limited because of incomplete measurement data recorded by a limited number of sensors, and accordingly the solution to the updating is non-unique. In view of this problem, a limited number of updated parameters are usually selected in the updating of a long span bridge to avoid an excessive number of solutions and boundaries are set for the change of the parameters to maintain physical meaning in the updating process.

6.5.4 Further validation

Four modal frequencies, four displacement influence lines and thirteen stress influence lines selected from the measured data were used to compare with the simulated results from the updated model to verify the quality of the updated model. The comparison of measured and computed modal frequencies is presented in Table 6.7, and the comparison of measured and computed displacement and stress influence lines is shown in Figure 6.7 and Figure 6.8. The values of indices Υ_{Di} and Υ_{Si} are presented in Table 6.8. These measured frequencies and influence lines have not been taken as objectives for the above model updating. It can be seen from Figure 6.7 and Figure 6.8 and from Table 6.7 and Table 6.8 that the differences between the measured and computed modal frequencies and influence lines are all reduced after the model updating. These results indicate the good quality of the model updating technique proposed in this study.

Table 6.7 Modal frequencies

Mode NO.	Measured (Hz)	Initial (Hz)	Updated 1 (Hz)	Updated 2 (Hz)	Diff 1	Diff 2
7	0.3340	0.3162	0.3385	0.3247	1.35%	-2.78%
8	0.3952	0.3400	0.3927	0.37867	-0.64%	-4.18%
9	0.4125	0.3649	0.3984	0.37691	-3.41%	-8.63%
10	0.4586	0.4435	0.4498	0.46424	-1.92%	1.23%

Table 6.8 Values of Υ_{Di} or Υ_{Si}

NO.	Initial	Updated 1	Updated 2	NO.	Initial	Updated 1	Updated 2
9	0.0201	0.0244	0.0092	26	0.1361	0.1362	0.0512
10	0.0704	0.0721	0.0113	27	0.0650	0.0685	0.0121
11	0.0491	0.0510	0.0113	28	0.0770	0.0803	0.0361
12	0.0208	0.0238	0.0096	29	0.1130	0.1137	0.0165
22	0.0350	0.0367	0.0312	30	0.0655	0.0679	0.0344
23	0.0860	0.0871	0.0645	31	0.0475	0.0481	0.0134
24	0.1887	0.1905	0.0464	32	0.0503	0.0566	0.0313
25	0.1201	0.1256	0.0542				

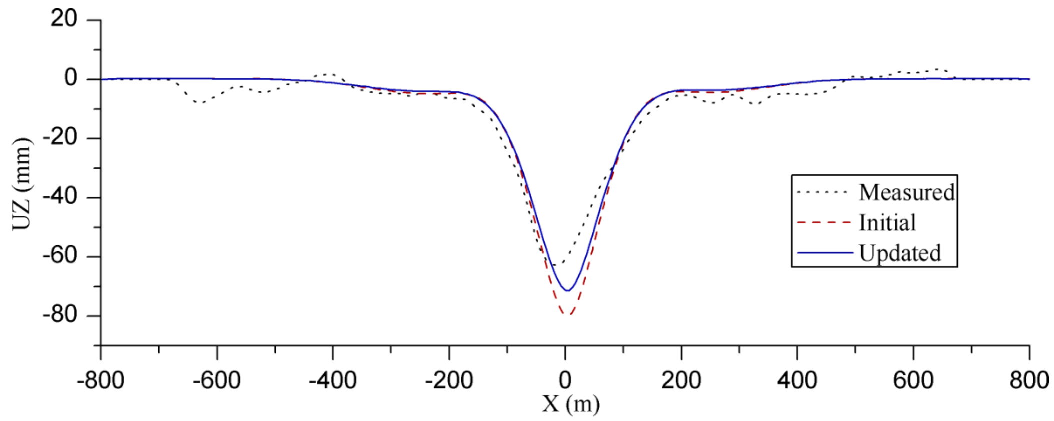

(a)

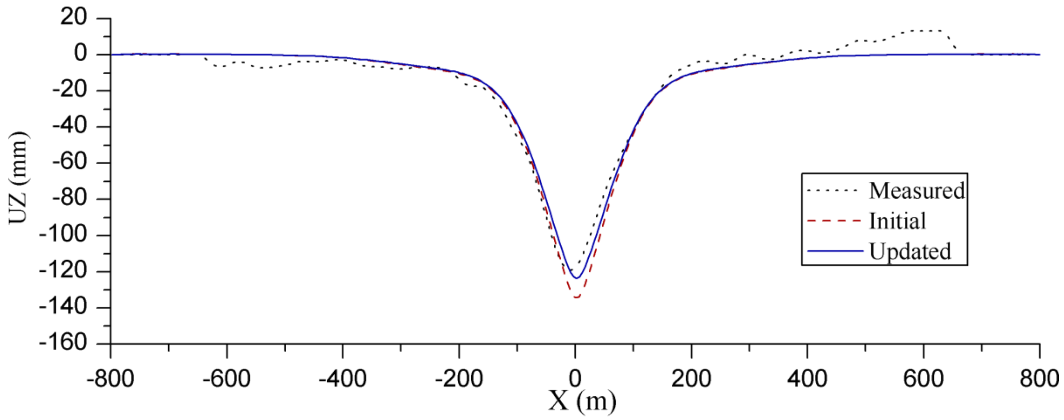

(b)

Figure 6.7 Comparison of measured and calculated displacement IL(the dotted line is measured IL; the dashed and solid line are ILs calculated by the initial and the updated model, respectively; a and b represent No.13 and 14 stress ILs, respectively)

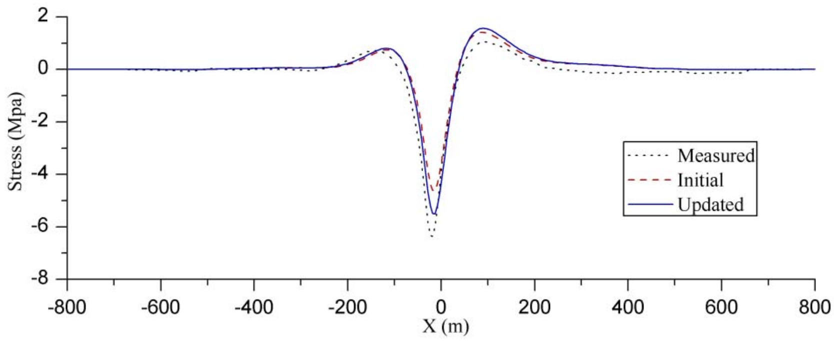

(a)

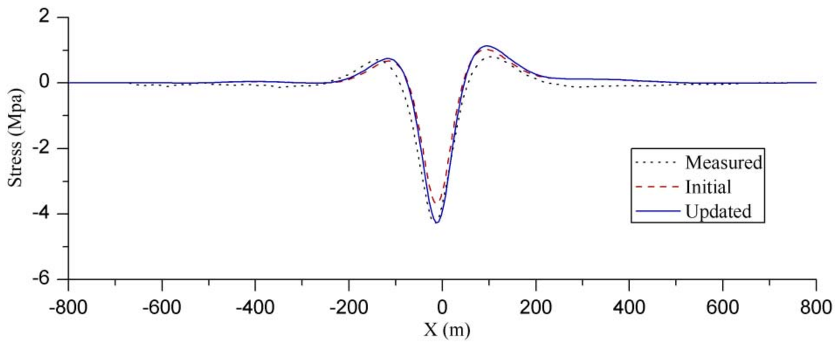

(b)

Figure 6.8 Comparison of measured and calculated stress IL (the dotted line is measured IL; the dashed and solid line are ILs calculated by initial and updated model, respectively; a and b represent No.29 and 31 stress ILs, respectively) (MPa)

6.5.5 Comparison with traditional model updating using modal frequencies

Table 6.5~Table 6.8 also present the objective indices computed from the traditionally updated model, which was updated with modal frequencies only and presented in Chapter 5. In view of the modal frequencies, traditional updating has better results in general. This is not surprising because model updating algorithms aim for global optimization of all the objectives. In the traditional updating, the parameters are optimized for modal frequencies only while in the combined updating presented in this chapter, the change of parameters should consider both frequencies and influence lines at the same time. Interestingly, the combined updating yields better results for the first two modes, which are the 1st order of lateral and vertical deck modes respectively. This may attribute to the possible fact that the part of stiffness matrix represented by influence lines has a better correlation with the lower order deck modes.

In view of displacement and stress influence lines, traditional updated model has a slightly worse match than the initial model with the measured data. Furthermore, the influence of traditional updating on the stress influence lines is negligible. Model updating with only the modal frequencies cannot improve the accuracy of simulated displacement and stress responses. In contrast, combined updating can effectively improve the match between computed and measured displacement and stress influence lines. It should be noted that the improvement in stress results may largely attribute to the separation of the upper deck plate form other plates in the combined updating process because it affects the distribution of stress in the deck. The separation is proposed after an attentive investigation into the comparison of computed and measured stresses as mentioned in Subsection 5.2.

6.6 Summary

This chapter presented a new model updating method for updating the multi-scale finite element model of a long-span bridge. The objective functions of the proposed method for model updating include both modal frequencies and multi-scale influence lines. The relationships between displacement influence lines and mode shapes and between strain influence lines and strain mode shape were discussed. Based on the modal frequencies and influence lines, the objective functions and constraint conditions were formulated. The response surface model of a long-span bridge was established to simplify the optimisation problem involving in the model updating. Finally, the proposed method was applied to Stonecutters Bridge as a case study. The results showed that the differences between the measured and computed modal frequencies and between the measured and computed multi-scale influence lines were all reduced after using the proposed model updating method. The comparison of the additional measured modal frequencies and influence lines with the corresponding computed results further confirms the quality of the proposed model updating method.

In contrast with traditional model updating using modal frequencies only, the proposed method can effectively improve the accuracy of simulated displacement and stress responses. As static responses are as important as dynamic characteristics for long-span bridges and accurate stress responses are a crucial objective of multi-scale models, the proposed method is preferable for the model updating multi-scale models of long-span bridges.

As the multi-scale model has been updated with the displacement and stress responses, the accuracy of the model is ensured. The frequency-domain framework for buffeting induced stress analyses proposed in Chapter 4 can be applied on the multi-scale model of Stonecutters Bridge to obtain displacement and stress responses. In the next chapter, the proposed buffeting analysis framework will be applied on the substructure-based multi-scale model of Stonecutters Bridge. The buffeting induced displacement and stress responses of the bridge will be presented.

CHAPTER 7

BUFFETING ANALYSIS ON STONECUTTERS BRIDGE WITH DISTRIBUTED WIND LOADS

7.1 Introduction

In Chapter 3, the characteristics of distributed aerodynamic forces, such as pressure admittances and span-wise pressure coherences have been identified from wind tunnel pressure tests. In Chapter 4, the distributed aeroelastic stiffness and damping have been obtained with the proposed approximate distribution method. With the cross-spectral matrix of distributed aerodynamic forces and the distributed aeroelastic property matrices, the buffeting analysis framework established in Chapter 4 enables buffeting analysis on a shell-element model of a twin-box bridge deck. Due to the large computation load caused by the fine modeling with shell elements, this framework was applied to a segment of a bridge deck rather than a real long-span bridge. Now that the multi-scale FE model of Stonecutters Bridge has been established in Chapter 5 and updated with multi-scale influence lines in Chapter 6, the number of DOF required to be dealt with has been significantly reduced, thus enabling a buffeting induced stress analysis of Stonecutters Bridge with the proposed framework.

In this chapter, some technique details on applying the proposed buffeting analysis framework on the substructure-based model are first introduced. Then the wind characteristics and the aerodynamic/aeroelastic properties of the bridge components, obtained based on the field measurement and/or wind tunnel tests, are presented. Buffeting analyses on Stonecutters Bridge using distributed loads is then performed with these data and parameters. The displacement and stress responses of the bridge with two wind directions associated with two terrains and three angles of incidence are investigated.

This chapter focuses on the mean wind responses and total buffeting responses of some key locations of the bridge. The maximum values of the displacement and stress responses together with the span-wise and section-wise distribution of these responses are presented in this chapter.

The signature turbulence induced responses are included in the results presented in this chapter. Detailed analyses of the signature turbulence effects on the total responses will be provided in the next chapter. It should be noted that as the aeroelastic effects of the signature turbulence are not fully considered in the proposed framework, the signature turbulence effects may be significantly underestimated at the lock-in or near-flutter wind speed range.

7.2 Buffeting analysis on the substructure-based model using distributed loads

The general framework of the buffeting analysis with distributed buffeting loads has been introduced in Chapter 4. Some modifications on the framework are required so that it can be applied on the substructure-based model with affordable computation load. The procedure of the buffeting analysis on the substructure-based model of Stonecutters Bridge is introduced in this subsection.

Using the sub-structuring method, the DOF in the FE model can be divided into the master DOF and the slave DOF. Then the governing equation of the entire structure can be written as

$$\begin{bmatrix} \mathbf{M}_{mm} & \mathbf{M}_{ms} \\ \mathbf{M}_{sm} & \mathbf{M}_{ss} \end{bmatrix} \begin{Bmatrix} \ddot{\mathbf{u}}_m \\ \ddot{\mathbf{u}}_s \end{Bmatrix} + \begin{bmatrix} \mathbf{C}_{mm} & \mathbf{C}_{ms} \\ \mathbf{C}_{sm} & \mathbf{C}_{ss} \end{bmatrix} \begin{Bmatrix} \dot{\mathbf{u}}_m \\ \dot{\mathbf{u}}_s \end{Bmatrix} + \begin{bmatrix} \mathbf{K}_{mm} & \mathbf{K}_{ms} \\ \mathbf{K}_{sm} & \mathbf{K}_{ss} \end{bmatrix} \begin{Bmatrix} \mathbf{u}_m \\ \mathbf{u}_s \end{Bmatrix} = \begin{Bmatrix} \mathbf{F}_m \\ \mathbf{F}_s \end{Bmatrix} \tag{7.1}$$

where the subscript "*m*" denotes the master DOF and the subscript "*s*" denotes the slave DOF,

Eq.(7.1) can be condensed into a governing equation of the global structure with only master DOF as

$$\hat{\mathbf{M}}\ddot{\mathbf{u}}_m + \hat{\mathbf{C}}\dot{\mathbf{u}}_m + \hat{\mathbf{K}}\mathbf{u}_m = \hat{\mathbf{F}} \tag{7.2}$$

where the "^" denotes superelement property matrices and force vector that only associate with the master DOF; and

$$\hat{\mathbf{K}} = \mathbf{K}_{mm} - \mathbf{K}_{ms}\mathbf{K}_{ss}^{-1}\mathbf{K}_{sm} \tag{7.3}$$

$$\hat{\mathbf{M}} = \mathbf{M}_{mm} - \mathbf{K}_{ms}\mathbf{K}_{ss}^{-1}\mathbf{M}_{sm} - \mathbf{M}_{ms}\mathbf{K}_{ss}^{-1}\mathbf{K}_{sm} + \mathbf{K}_{ms}\mathbf{K}_{ss}^{-1}\mathbf{M}_{ss}\mathbf{K}_{ss}^{-1}\mathbf{K}_{sm} \tag{7.4}$$

$$\hat{\mathbf{C}} = \mathbf{C}_{mm} - \mathbf{K}_{ms}\mathbf{K}_{ss}^{-1}\mathbf{C}_{sm} - \mathbf{C}_{ms}\mathbf{K}_{ss}^{-1}\mathbf{K}_{sm} + \mathbf{K}_{ms}\mathbf{K}_{ss}^{-1}\mathbf{C}_{ss}\mathbf{K}_{ss}^{-1}\mathbf{K}_{sm} \tag{7.5}$$

$$\hat{\mathbf{F}} = \mathbf{F}_m - \mathbf{K}_{ms}\mathbf{K}_{ss}^{-1}\mathbf{F}_s \tag{7.6}$$

The above equations depict the general process of the condensation of sub-structure property matrices and force vectors. In practice, it is usually preferable that the external forces are applied on the master nodes only ($\mathbf{F}_s$=0) so that iterative generations of the sub-structures can be avoided in the analyses of the global structure. In this regard, the aerodynamic and aeroelastic forces should be lumped onto the master nodes and thus the framework proposed in Chapter 4 can be applied to the governing equation of the global structure as

$$\hat{\mathbf{M}}_{str}\ddot{\mathbf{u}}_m + (\hat{\mathbf{C}}_{str} + \hat{\mathbf{C}}_{se})\dot{\mathbf{u}}_m + (\hat{\mathbf{K}}_{str} + \hat{\mathbf{K}}_{se})\mathbf{u}_m = \mathbf{R}_f\hat{\mathbf{F}}_b \tag{7.7}$$

where $\hat{\mathbf{M}}_{str}, \hat{\mathbf{C}}_{str}$ and $\hat{\mathbf{K}}_{str}$ are the condensed structural mass, damping and stiffness matrices that associate only with the master DOF, $\hat{\mathbf{C}}_{se}$ and $\hat{\mathbf{K}}_{se}$ are the lumped aeroelastic damping and stiffness matrix on the master nodes, respectively; $\hat{\mathbf{F}}_b$ is the lumped aerodynamic forces on the master nodes.

The distribution method for aeroelastic property matrices proposed in Chapter 4 allows the sectional aeroelastic property matrices to be distributed to an arbitrary set of nodes on the section outline. This method can be directly used to determine $\hat{\mathbf{C}}_{se}$ and $\hat{\mathbf{K}}_{se}$. These lumped aeroelastic property matrices can be added on to the FE model with stiffness/damping matrix element MATRIX27 in ANSYS (see Figure 7.1). If the number of master nodes is large enough so that the area corresponding to each master node is small and that the pressure distribution in the small area represented by each node can be considered uniform, the cross-spectrum of lumped aerodynamic forces on the master nodes i and j can be computed as

$$S_{\hat{F}_b(i)\hat{F}_b(j)}(\omega) = \left(\mathrm{Coh}_{x,i}^{1/2}(\Delta x(i,j)) \cdot \mathrm{Coh}_{y}^{1/2}(\Delta y(i,j)) S_{P_b,i}(\omega) S_{P_b,j}(\omega)\right)^{1/2} A_i A_j \quad (7.8)$$

where A_i and A_j are the areas that are represented by master nodes i and j, respectively; S_{pi} and S_{pj} can be computed with linear interpolation between two adjacent measured points.

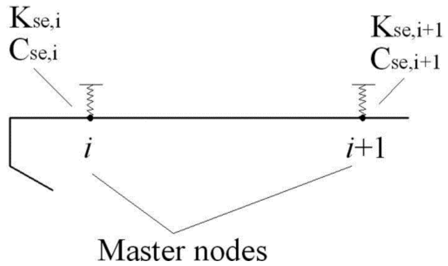

Figure 7.1 Adding aeroelastic properties on to the master nodes

The pseudo excitation method is used to solve the governing equation. For each harmonic pseudo-excitation vector, a pseudo displacement response vector containing results of all master DOF can be computed through harmonic analysis of the global structure. The pseudo displacement responses of the slave DOF in a sub-structure can therefore be obtained in the expansion of the sub-structure as

$$\mathbf{u}_s = \mathbf{K}_{ss}^{-1}\mathbf{F}_s - \mathbf{K}_{ss}^{-1}\mathbf{K}_{sm}\mathbf{u}_m \quad (7.9)$$

The above equation can be derived from Eq.(7.1)~(7.5).

Once the nodal displacement vector of every element is obtained, the element stress vector induced by the elastic deformation without considering the initial strains and stresses can be obtained as

$$\boldsymbol{\sigma}_j = \mathbf{k}_j \mathbf{L}_j \mathbf{N}_j \mathbf{T}_j \mathbf{u}_j \tag{7.10}$$

where $\boldsymbol{\sigma}_j$ is the stress vector of the jth element; $\mathbf{u}_j$ is the nodal displacement vector in the global coordinate; $\mathbf{T}_j$ is the coordinate transfer matrix from global to local coordinates; $\mathbf{N}_j$ is the shape function; $\mathbf{L}_j$ is the differential operator that transforms the element displacement to the element strain; and $\mathbf{k}_j$ denotes the elastic stiffness matrix that represents the stress-strain relationship.

The pseudo stress responses can also be obtained in the expansion process. It should be noted that as the aerodynamic and aeroelastic forces are applied on the master nodes only, the expansion process of each sub-structure is a standard sub-structuring analysis process that can be directly conducted in ANSYS.

The spectral density matrix of the system displacement and stress responses can be computed after harmonic analyses of all pseudo-excitation vectors. And the standard deviations of the displacement and stress responses can then be obtained by integration of the spectral density matrices over the frequency range.

The buffeting analysis process was programmed through APDL (ANSYS Parametric Design Language) and carried out with ANSYS. The flowchart of the analysis is shown in Figure 7.2.

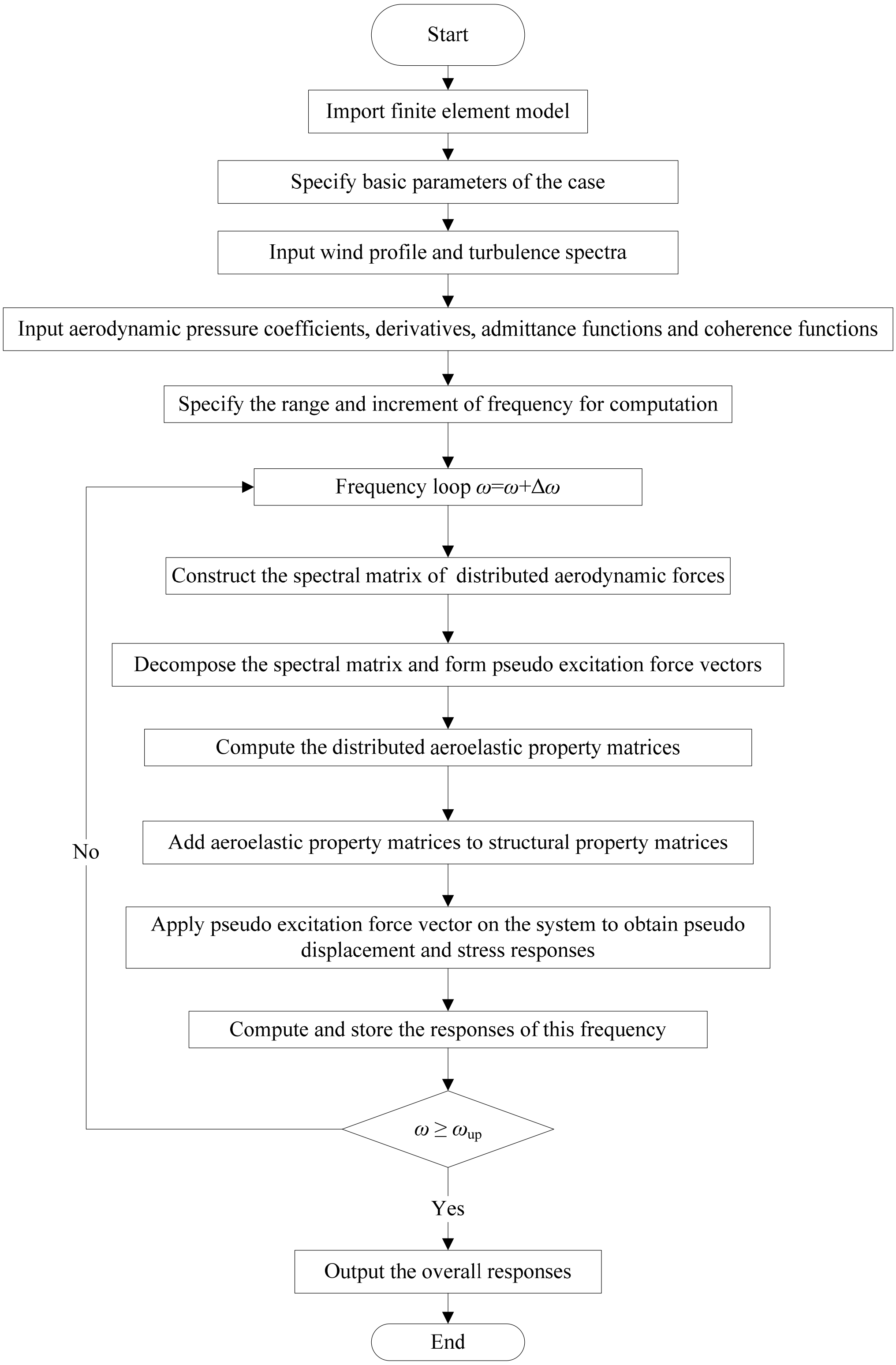

Figure 7.2 Flowchart of the buffeting analysis using distributed wind loads

7.3 Wind characteristics

Stonecutters Bridge is a cable-stayed bridge which spans the Rambler Channel in Hong Kong, connecting Nam Wan Kok, Tsing Yi island and Stonecutters Island. The bridge is surrounded by a complex topography.

In October 2002, a 50 m mast was erected at the site of the bridge to record strong winds and to ascertain wind turbulence parameters for design purpose (Chen et al., 2007). Based on the measured data, the major topographical conditions that may affect wind characteristics at the bridge site are described as follows using 8 cardinal directions (Chen & Xu, 2004).

(a) Wind from the North and North-East of the bridge site: the near field effect may be arising from buildings in Kwai Chung and container port terminals whereas the far field effect may be caused by the mountains of Tai Mo Shan and Grassy Hill at the respective heights of 957 m and 647m.

(b) Wind from the East and North-East of the bridge site: the near field effect may be arising from buildings in Cheung Sha Wan and North Kowloon and container port terminals whereas the far field effect may be induced by the mountains of Beacon Hill, Lion Rock, Tate's Cairn, and Kowloon Peak at the respective heights of 457m, 495m, 577m and 602m.

(c) Wind from the East and South-East of the bridge site: the near field effect may be arising from container port terminals and Stonecutter Island whereas the far field effect may be induced by the mountains of Victoria Peak at a height of 552 m.

(d) Wind from the South and South-East of the bridge site: the near field effect may be arising from the open sea whereas the far field effect may be induced by the mountains of Mount Davis and Victoria Peak at a height of 269m and 552m respectively.

(e) Wind from the South and South-West of the bridge site: the effect of open sea.

(f)Wind from the West and South-West of the bridge site: the near field may be arising from the open sea whereas the far field effect may be induced by Lantau Island.

(g) Wind from the West and North-West of the bridge site: the near field effect may be arising from the mountain of Tsing Yi, at a height of 334m, whereas the far field effect may be generated by the mountains of Fa Peng at north-east of Lantau Island, at a height of 273 m.

(h) Wind from the North and North-West of the bridge site: the near field effect may be arising from the mountain of Tsing Yi whereas the far field effect may be generated by the mountain of Tai Mo Shan.

In summary, according to the near field effect, the terrains from the West to the South-East rotating clockwise can be seen as over-land fetch while those from the South-East to the West rotating in clockwise can be seen as open-sea fetch.

The wind characteristics on the site of Stonecutters Bridge depend on the two wind direction and they are described as follows based on the on-site measurement data.

7.3.1 Mean wind speed profiles

The mean wind speed profile used in this study conforms to the power law:

$$U(z) = U_{ref} \cdot \left(\frac{z}{10}\right)^{\alpha} \tag{7.11}$$

where U_{ref} is defined as the reference wind speed; the exponential factor $\alpha = 0.29$ for the N-E direction (over-land fetch) and $\alpha = 0.19$ for the S-W direction (open-ocean fetch).

When U_{ref} is taken as 37m/s, the formulas for mean wind speed at any height z can be derived as follows:

$$\text{N-E direction:} \qquad U(z) = 46 \cdot \left(\frac{z}{z_C}\right)^{0.29} \tag{7.12}$$

$$\text{S-W direction:} \qquad U(z) = 55 \cdot \left(\frac{z}{z_C}\right)^{0.19} \tag{7.13}$$

where z_c=87.7m is the height of the deck level at the middle of the main span of the bridge and the 10-minute design mean wind speed at the deck level in the S-W direction is 55m/s.

The wind profiles for different reference wind speed can be obtained in the same way.

7.3.2 Turbulence intensities and RMS

According to the Design Memorandum, the turbulence intensity of the along-wind (u), vertical (w) and lateral (v) turbulence components at height z above ground are given by the following expressions:

$$I_i = \frac{\sigma_i}{V_{10}(z)} \tag{7.14}$$

For the along-wind component the following expression can be derived corresponding to the open-ocean fetch.

$$I_u = \frac{\sigma_u}{V_{10}(z)} = 0.175 \cdot \left(\frac{10}{z} \right)^{0.19} \tag{7.15}$$

σ_u is assumed to be constant with height based on I_u equal to 14.5% at 70 m height above sea level inferred from the Waglan Island data reproduced in the review of the Structures Design Manual.

When the wind is approaching from the over-land fetch, the turbulence intensity profile is modified as follows:

$$I_u = \frac{\sigma_u}{V_{10}(z)} = 0.437 \cdot \left(\frac{10}{z} \right)^{0.29} \tag{7.16}$$

It is further assumed that

for the over-land fetch: $\sigma_w = 0.6\sigma_u$ (7.17) for the open-ocean fetch: $\sigma_w = 0.5\sigma_u$ (7.18)

Thus the deck-level over-land fetch deck-level turbulent intensity can be derived as I_u = 0.234, I_w=0.142. And the deck-level open-ocean turbulent intensity can be derived as I_u = 0.116, I_w=0.058. As these two wind fields have been roughly simulated in the wind-tunnel tests introduced in Chapter 3, the aerodynamic admittance and coherence functions of the measured pressure can be directly used in the buffeting analysis.

7.3.3 Turbulence integral scales

Based on the measurement data, the turbulence integral scale, L_u, of the longitudinal turbulence component of wind at the middle point of the main span of the bridge is assumed to be 200m. The integral scale L_w of the vertical turbulence component of wind at the middle point of the main span of the bridge is then given as follows:

$$\frac{L_w}{L_u} = \frac{1}{9} \tag{7.19}$$

7.3.4 Wind power spectra

Based on the turbulence intensity, turbulence integral scale and mean wind speed, the wind power spectra S_{uu} and S_{ww} can be given in terms of the von Karman formulas as

$$\frac{nS_{uu}(n)}{\sigma_u^2} = 4\left(\frac{nL_u}{U(z)}\right)\left[1 + 70.8\left(\frac{nL_u}{U(z)}\right)^2\right]^{-5/6} \tag{7.20}$$

$$\frac{nS_{ww}(n)}{\sigma_w^2} = 4\left(\frac{nL_w}{U(z)}\right)\left[1+755\left(\frac{nL_w}{U(z)}\right)^2\right]\left[1+283\left(\frac{nL_w}{U(z)}\right)^2\right]^{-11/6} \tag{7.21}$$

7.3.5 Computation cases

In view of the wind characteristics presented above, the displacement and stress responses of Stonecutters Bridge with two wind fields associated with two terrains and three angles of incidence are investigated in this chapter. The computation cases are listed in Table 7.1.

Table 7.1 Computation cases of Chapter 7

Case No.	U_c (m/s)	Wind Direction	Attack Angle (^{o})
1	55	S-W	-3
2	55	S-W	0
3	55	S-W	+3
4	46	N-E	-3
5	46	N-E	0
6	46	N-E	+3

7.4 Aerodynamic properties of bridge components

7.4.1 Aerodynamic coefficients of bridge components

The aerodynamic pressure coefficients of the Stonecutters bridge deck at the complete stage without traffic were acquired from wind tunnel pressure tests. The pressure coefficients and their derivatives with respect to the angle of incidence are listed in Table 7.2.

Table 7.2 Pressure coefficients and their derivatives with respect to incidence angle

Tap No.	C_P(-3°)	C_P(0°)	C_P(+3°)	C'_P(-3°)	C'_P(0°)	C'_P(+3°)
101	0.80	0.51	0.08	-3.78	-7.57	-14.08
102	0.49	0.15	-0.26	-5.29	-7.77	-6.09
103	-0.49	-0.91	-1.18	-8.62	-7.22	-0.85
104	0.04	-0.24	-1.04	-3.81	-12.94	-13.43
105	0.00	-0.11	-0.61	-2.97	-4.32	-19.29
106	-0.01	-0.11	-0.34	-2.63	-2.64	-12.55
107	-0.01	-0.11	-0.24	-2.34	-2.11	-6.05
108	-0.02	-0.11	-0.21	-2.07	-1.93	-2.94
109	-0.05	-0.11	-0.22	-1.84	-1.66	-1.67
110	-0.07	-0.12	-0.22	-1.58	-1.51	-1.66
111	-0.08	-0.12	-0.19	-1.33	-1.18	-0.81
112	-0.12	-0.12	-0.23	-1.13	-1.03	-1.38
113	-0.18	-0.13	-0.26	-0.93	-0.68	-1.08
114	-0.16	-0.14	-0.22	-0.73	-0.49	-0.42
115	-0.19	-0.16	-0.20	-0.52	-0.14	0.19
116	-0.23	-0.21	-0.19	-0.30	0.42	1.09
117	-0.33	-0.30	-0.27	-0.35	1.14	1.71
118	-0.36	-0.32	-0.29	-0.07	1.83	2.11
119	-0.40	-0.33	-0.35	-0.35	1.79	1.60
120	-0.40	-0.32	-0.35	-0.41	1.85	1.46
121	-0.41	-0.32	-0.34	-0.49	2.07	1.47
122	-0.43	-0.31	-0.30	0.40	2.20	1.60
123	-0.42	-0.31	-0.23	1.21	2.93	2.56
124	-0.44	-0.31	-0.19	1.82	2.80	2.89
125	-0.48	-0.34	-0.18	2.19	3.49	3.63
126	-0.54	-0.36	-0.20	2.43	3.87	3.57
127	-0.50	-0.31	-0.12	2.93	4.31	4.31
128	-0.47	-0.27	-0.07	3.02	4.76	4.25
129	-0.43	-0.18	0.05	3.08	5.26	5.13
130	-0.28	-0.02	0.20	3.30	5.48	4.72
131	-0.15	0.10	0.38	11.72	6.02	5.49
132	-0.86	0.28	0.59	25.20	5.84	6.06
201	-0.07	-0.02	0.01	0.46	0.18	-1.49
202	-0.07	-0.01	-0.01	0.44	0.19	-1.58
203	-0.05	-0.03	-0.03	0.27	0.14	-1.60
204	-0.05	-0.03	-0.05	-0.05	0.08	-1.75
205	-0.04	-0.05	-0.07	-0.19	-0.03	-1.82
206	-0.03	-0.05	-0.08	-0.45	-0.18	-2.04
207	-0.05	-0.07	-0.12	-0.50	-0.21	-2.00
208	-0.02	-0.07	-0.11	-0.77	-0.41	-2.35
209	-0.01	-0.04	-0.07	-0.99	-0.56	-2.34
210	0.00	-0.06	-0.11	-1.15	-0.73	-2.85
211	0.01	-0.07	-0.14	-1.36	-0.91	-2.90
212	-0.02	-0.08	-0.18	-1.69	-1.18	-3.15

213	-0.02	-0.13	-0.26	-2.12	-1.40	-3.63
214	-0.01	-0.17	-0.30	-2.90	-1.86	-4.78
215	-0.01	-0.27	-0.47	-4.80	-2.19	-6.49
216	-0.34	-0.68	-0.91	-7.22	-2.08	-3.35
217	0.80	0.61	0.40	-4.05	-4.00	-5.08
218	-0.06	0.13	0.33	7.59	1.57	1.63
219	-0.12	0.02	0.20	3.23	1.32	1.61
220	-0.29	-0.15	0.03	3.14	1.25	1.20
221	-0.62	-0.44	-0.26	3.30	1.36	1.27
222	-1.14	-0.90	-0.70	4.77	1.03	1.29
223	-0.70	-0.58	-0.48	1.96	0.64	0.04
224	-0.60	-0.50	-0.43	1.33	0.32	-0.43
225	-0.55	-0.48	-0.43	1.13	0.19	-0.66
226	-0.53	-0.47	-0.44	0.91	-0.03	-1.18
227	-0.46	-0.42	-0.40	0.87	-0.12	-1.23
228	-0.39	-0.37	-0.35	0.81	-0.31	-1.51
229	-0.32	-0.30	-0.29	0.62	-0.24	-1.59
230	-0.23	-0.21	-0.20	0.70	-0.28	-1.70
231	-0.16	-0.14	-0.13	0.67	-0.24	-1.66
232	-0.10	-0.09	-0.07	0.66	-0.23	-1.60

The drag coefficient of the bridge tower is taken as C_D=0.9 along the entire height of the tower. This drag coefficient is normalized by the width of the tower perpendicular to the wind direction. The drag coefficient of the piers is taken as C_D=1.1 and it is also normalized by the actual width of the piers perpendicular to the wind direction. The drag coefficient of the stay cables is taken as C_D=0.8 and it is normalized by the diameter of the stay cables. As the cross sections of the stay cables, towers and piers are symmetric, their aerodynamic lift and moment coefficients for wind perpendicular to the bridge axis are taken as zero. The dynamic effects of wind loading on the towers, piers and cables are neglected in this study.

7.4.2 Aerodynamic derivatives of bridge deck

The aerodynamic derivatives of the Stonecutters bridge deck at the complete stage without traffic were obtained with the section model tests in wind tunnels. Only the derivatives H_i^* and A_i^* (i=1~4) are available, and they are listed in Table 7.3 and plotted in Figure 7.11. Since the derivatives related to the lateral motion of the bridge deck are not available, they are calculated based on the quasi-static theory as

$$\begin{aligned}
&P_1^* = -\frac{1}{K}C_D, \quad P_2^* = \frac{1}{2K}C_D', \quad P_3^* = \frac{1}{2K^2}C_D' \\
&P_5^* = \frac{1}{2K}C_D', \quad H_5^* = \frac{1}{K}C_L, \quad A_5^* = -\frac{1}{K}C_M \\
&P_4^* = P_6^* = H_6^* = A_6^* = 0
\end{aligned} \tag{7.22}$$

This work uses distributed aeroelastic forces based on distributed aeroelastic stiffness and damping matrices, which can be computed with the derivatives introduced above. Details of this technique can be found in Chapter 4. Figure 7.4 and Figure 7.5 give two examples of the distributed aeroelastic damping and stiffness on the section outline. Distributed by this technique, the aeroelastic damping and stiffness are concentrated on the windward region of the deck. The aeroelastic damping and stiffness on the leeward box are very small. Figure 7.6 and Figure 7.7 show the distribution of aeroelastic damping and stiffness on the master nodes.

The aeroelastic properties and the aerodynamic coefficients are assumed to be uniform along the bridge deck in the buffeting analysis.

Table 7.3 Aerodynamic derivatives of the Stonecutters bridge deck

K	H_1^*	H_4^*	A_1^*	A_4^*	H_2^*	H_3^*	A_2^*	A_3^*
0	0.00	0.00	0.00	0.00	0.00	0.00	0.00	0.00
2	-0.41	0.37	0.12	0.01	-0.10	-0.21	-0.13	-0.02
4	-0.57	0.63	0.35	0.16	-0.10	-0.34	-0.22	0.10
6	-0.88	0.40	0.51	0.13	0.00	-0.83	-0.28	0.23
8	-1.33	0.48	0.57	0.06	0.17	-1.59	-0.37	0.41
10	-1.54	0.65	0.72	0.01	0.05	-2.89	-0.50	0.61
12	-2.17	0.36	0.64	-0.10	-0.16	-4.13	-0.61	0.96
14	-1.84	1.16	0.92	0.01	-0.06	1.16	0.92	0.01
16	-2.46	0.82	1.38	0.21	0.09	0.82	1.38	0.21

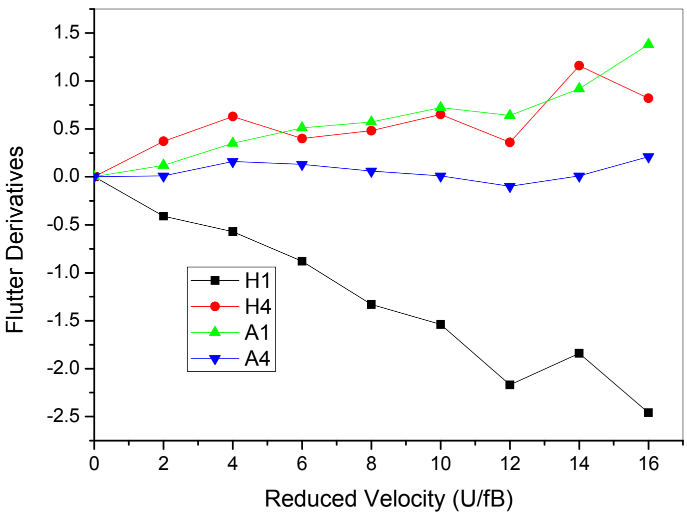

(a) H_1^*, H_4^*, A_1^*, A_4^*

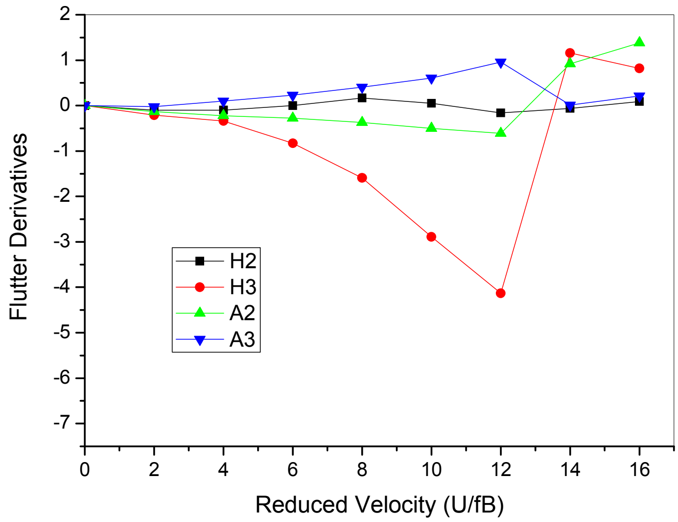

(b) H_2^*, H_3^*, A_2^*, A_3^*

Figure 7.3 Aerodynamic derivatives of the Stonecutters bridge deck at the complete stage

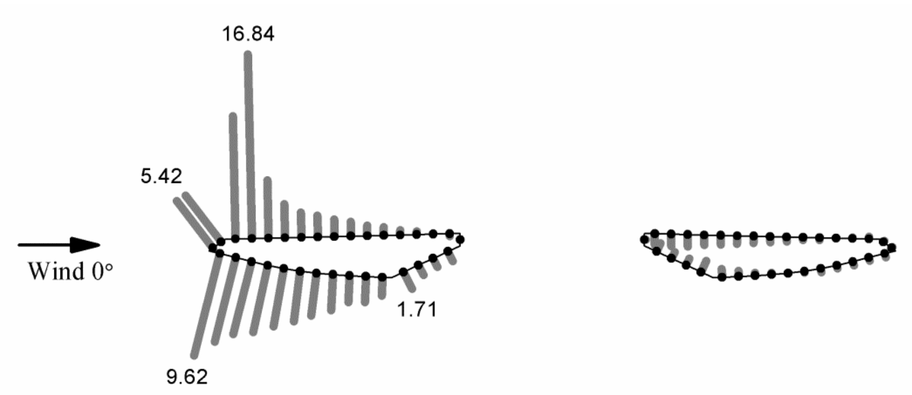

Figure 7.4 Distributed torsional aeroelastic damping on pressure taps at K=10 (N·s/m)

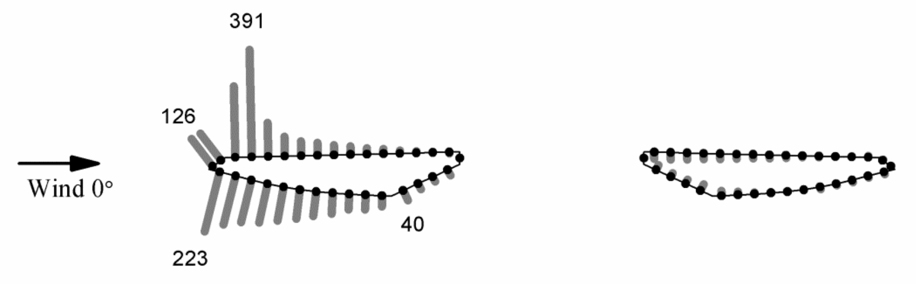

Figure 7.5 Distributed torsional aeroelastic stiffness on pressure taps at K=10 (N·s/m)

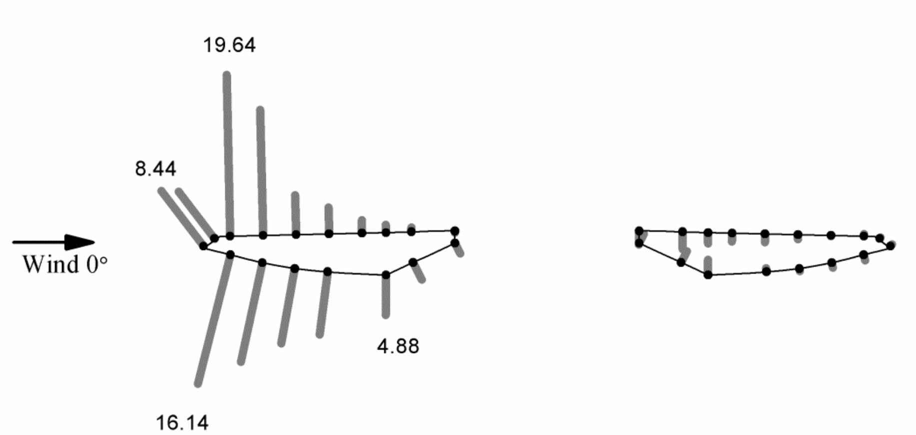

Figure 7.6 Distributed torsional aeroelastic damping on master nodes at K=10 (N·s/m)

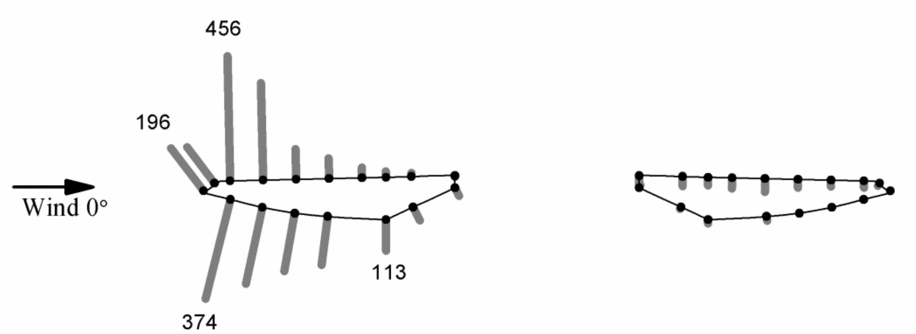

Figure 7.7 Distributed torsional aeroelastic stiffness on master nodes at K=10 (N·s/m)

7.5 Mean wind induced displacements and stresses

Under the action of dynamic wind, there are three major components of wind forces acting on the bridge: the mean wind forces due to mean wind, the aerodynamic forces due to turbulent wind, and the aeroelastic forces due to aeroelastic interaction between bridge motion and the wind. The responses of the bridge are traditionally divided into the responses to mean wind (mean wind responses) and the responses to aerodynamic and aeroelastic forces (buffeting responses). The mean wind responses will be presented in this subsection, while the buffeting responses will be presented in the next subsection.

7.5.1 Mean wind displacement responses

The mean wind responses can be determined through static analyses. Before determining the mean wind responses of the bridge, a geometrically nonlinear static analysis of the bridge, in which only the gravity forces of all bridge components and the initial tension forces of cables are included, is performed to determine a reference position of the bridge at its complete stage. The mean wind responses are then computed with respect to the reference position.

The mean wind load on a bridge component is determined by the aerodynamic coefficients and the mean wind speed at the bridge components and then converted to the relevant nodes of the bridge component in the FE model. The total mean wind load on a stay cable is assigned to its two ends. The mean wind loads on bridge components may be affected by the deformation of the bridge components, i.e. the rotation of the bridge deck may affect the mean wind loads on the bridge deck. Such non-linearity of the mean wind loads is also considered in the determination of mean wind response of the bridge in this study.

The mean wind responses of the complete bridge are then computed for two wind directions and three initial wind angles of attack.

The mean wind displacement responses of the complete bridge are computed and those at the following key locations are presented in this Chapter (see Figure 7.8): (a) at the west end of the west side span (D1); (b) at the east end point of the west side span (D2); (c) at the west quarter-span of the main span (D3); (d) at the mid-span of the main span (D4); (e) at east quarter-span of the main span (D5); (f) at the west end of the east side span (D6); (g) at the east end of the east side span (D7); (h) at the top of the west tower (T1). (i) at the top of the east tower (T2).

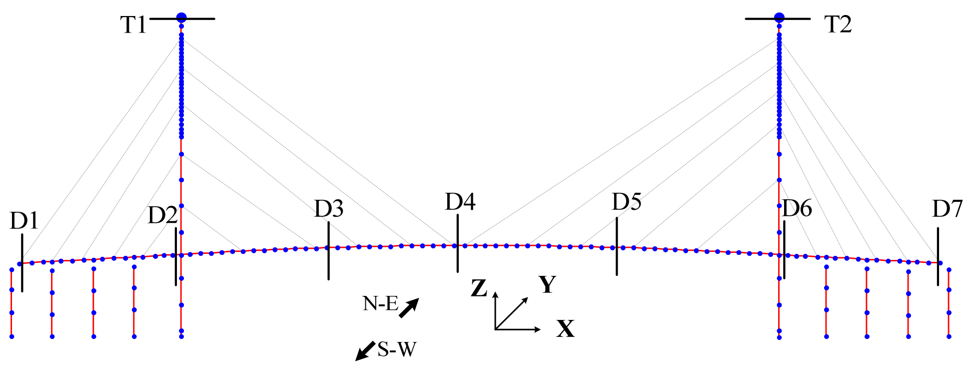

Figure 7.8 The key locations of the Stonecutters Bridge in the computation

Three types of mean displacement responses of the key positions are listed in Table 7.4~Table 7.6, labeled as UY, UZ (displacements along the global Y and Z axes) and ROTX (rotational angles around the global X axis).

As shown in Table 7.4~Table 7.6, the absolute values of the mean displacements are generally larger in Cases 1, 2 and 3 compared with those in Cases 4, 5, and 6 correspondingly. It can be concluded that the mean wind from the S-W direction induces larger mean displacements of the bridge deck than the mean wind from the N-E direction due to the larger wind speed.

Table 7.4 Mean wind displacements UY (m)

Location	Case 1	Case 2	Case 3	Case 4	Case 5	Case 6
D1-windward	0.00E+00	0.00E+00	0.00E+00	0.00E+00	0.00E+00	-1.12E-03
D1-leeward	0.00E+00	0.00E+00	0.00E+00	0.00E+00	0.00E+00	-1.13E-03
D2-windward	4.81E-02	4.73E-02	4.87E-02	-3.79E-02	-3.97E-02	-3.91E-02
D2-leeward	5.06E-02	4.89E-02	4.92E-02	-4.08E-02	-4.04E-02	-3.94E-02
D3-windward	3.72E-01	3.75E-01	3.68E-01	-2.74E-01	-2.65E-01	-2.75E-01
D3-leeward	3.65E-01	3.61E-01	3.79E-01	-2.77E-01	-2.66E-01	-2.75E-01
D4-windward	5.53E-01	5.67E-01	5.47E-01	-4.13E-01	-4.09E-01	-4.11E-01
D4-leeward	5.58E-01	5.62E-01	5.71E-01	-4.01E-01	-3.92E-01	-3.98E-01
D5-windward	3.52E-01	3.47E-01	3.56E-01	-2.58E-01	-2.53E-01	-2.56E-01
D5-leeward	3.47E-01	3.48E-01	3.54E-01	-2.51E-01	-2.49E-01	-2.54E-01
D6-windward	4.86E-02	4.77E-02	4.73E-02	-3.82E-02	-4.00E-02	-4.00E-02
D6-leeward	5.00E-02	4.94E-02	5.00E-02	-4.07E-02	-4.07E-02	-4.06E-02
D7-windward	0.00E+00	1.18E-03	1.14E-03	0.00E+00	-1.15E-03	-1.17E-03
D7-leeward	1.13E-03	1.15E-03	1.16E-03	-1.15E-03	-1.15E-03	-1.15E-03
T1	7.06E-01	7.23E-01	7.19E-01	-6.21E-01	-6.02E-01	-6.20E-01
T2	7.11E-01	7.17E-01	7.45E-01	-6.15E-01	-6.24E-01	-6.36E-01

Table 7.5 Mean wind displacements UZ (m)

Location	Case 1	Case 2	Case 3	Case 4	Case 5	Case 6
D1-windward	-2.30E-03	-1.10E-03	-1.14E-03	-1.09E-03	-1.08E-03	-1.14E-03
D1-leeward	1.20E-03	1.20E-03	9.92E-04	1.02E-03	1.13E-03	1.08E-03
D2-windward	-3.21E-02	-3.73E-02	-4.04E-02	-2.77E-02	-3.28E-02	-3.64E-02
D2-leeward	4.88E-02	5.40E-02	4.73E-02	4.27E-02	4.33E-02	4.34E-02
D3-windward	7.30E-02	2.71E-02	-2.03E-02	4.23E-02	1.02E-02	-2.20E-02
D3-leeward	1.92E-01	1.61E-01	1.14E-01	1.48E-01	1.28E-01	1.00E-01
D4-windward	2.56E-01	1.32E-01	4.04E-02	1.50E-01	8.08E-02	1.79E-02
D4-leeward	3.22E-01	2.63E-01	1.89E-01	2.59E-01	1.96E-01	1.45E-01
D5-windward	6.26E-02	2.17E-02	-2.18E-02	3.57E-02	5.21E-03	-2.72E-02
D5-leeward	1.69E-01	1.35E-01	1.29E-01	1.40E-01	1.04E-01	9.02E-02
D6-windward	-2.97E-02	-3.45E-02	-3.93E-02	-2.79E-02	-3.26E-02	-3.39E-02
D6-leeward	4.84E-02	4.68E-02	5.23E-02	4.00E-02	4.14E-02	3.76E-02
D7-windward	-1.09E-03	-1.14E-03	-1.09E-03	-1.01E-03	-1.09E-03	-1.20E-03
D7-leeward	1.11E-03	1.18E-03	9.98E-04	1.12E-03	1.14E-03	1.13E-03
T1	2.18E-03	1.07E-03	1.03E-03	1.14E-03	1.16E-03	1.10E-03
T2	2.37E-03	1.16E-03	1.15E-03	1.11E-03	1.07E-03	1.13E-03

Table 7.6 Mean wind displacements ROTX ($^{\circ}$)

Location	Case 1	Case 2	Case 3	Case 4	Case 5	Case 6
D1-windward	-2.25E-03	-2.42E-03	-2.42E-03	1.88E-03	1.99E-03	2.01E-03
D1-leeward	-2.11E-03	-2.35E-03	-2.27E-03	1.78E-03	1.98E-03	1.92E-03
D2-windward	-6.22E-02	-6.26E-02	-6.41E-02	5.57E-02	5.73E-02	5.53E-02
D2-leeward	-7.26E-02	-7.10E-02	-7.84E-02	6.09E-02	6.11E-02	6.27E-02
D3-windward	-9.58E-02	-1.12E-01	-1.22E-01	8.65E-02	9.67E-02	1.05E-01
D3-leeward	-9.27E-02	-1.01E-01	-1.21E-01	7.73E-02	9.42E-02	1.01E-01
D4-windward	-7.25E-02	-1.02E-01	-1.31E-01	7.17E-02	8.89E-02	1.04E-01
D4-leeward	-6.50E-02	-9.73E-02	-1.24E-01	6.43E-02	8.86E-02	1.06E-01
D5-windward	-9.27E-02	-1.14E-01	-1.26E-01	8.63E-02	9.38E-02	9.87E-02
D5-leeward	-8.55E-02	-1.05E-01	-1.19E-01	8.09E-02	8.65E-02	9.59E-02
D6-windward	-6.17E-02	-6.41E-02	-6.87E-02	5.35E-02	5.43E-02	5.98E-02
D6-leeward	-7.09E-02	-7.53E-02	-7.82E-02	5.99E-02	6.29E-02	6.58E-02
D7-windward	-1.97E-03	-2.13E-03	-2.15E-03	1.81E-03	1.80E-03	1.92E-03
D7-leeward	-1.81E-03	-1.92E-03	-1.98E-03	1.59E-03	1.74E-03	1.80E-03
T1	-1.73E-01	-1.70E-01	-1.72E-01	1.45E-01	1.54E-01	1.52E-01
T2	-1.76E-01	-1.68E-01	-1.75E-01	1.51E-01	1.47E-01	1.57E-01

The results presented in Table 7.4~Table 7.6 show that the mean displacements of the bridge deck vary with the initial wind angle of incidence. For instance, the vertical mean displacements of the bridge deck in Case 1 are larger than those in Case 2 and Case 3. Among the three given initial angles of attack, the -3° initial angle of incidence leads to the largest vertical mean displacements of the bridge deck. For the lateral mean displacements, the influence of initial angles of attack is very small. The +3° initial angle of incidence leads to the largest absolute torsional displacements of the bridge deck among the three given initial angles of attack.

It is also shown in the results that the absolute maximum of the lateral, vertical and torsional mean displacements of the bridge deck all occur at the middle point of the main span (D4). The values are 0.571m, 0.322m and 0.131° respectively. The absolute maximum of the lateral mean displacement responses of the right tower at its top is

0.745m.

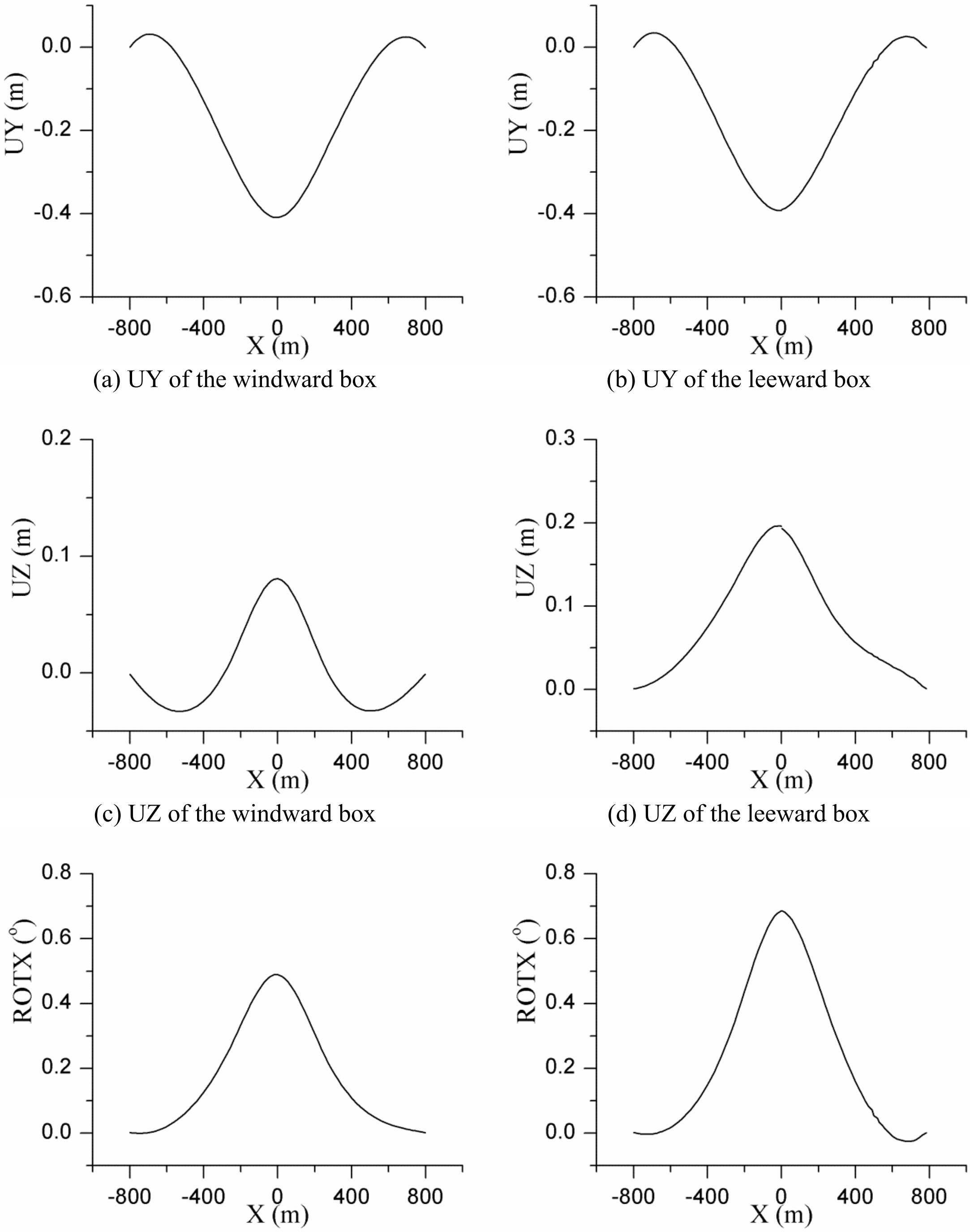

(a) UY of the windward box
(b) UY of the leeward box
(c) UZ of the windward box
(d) UZ of the leeward box
(e) ROTX of the windward box
(f) ROTX of the leeward box

Figure 7.9 Span-wise distribution of mean wind induced displacement (Case 5)

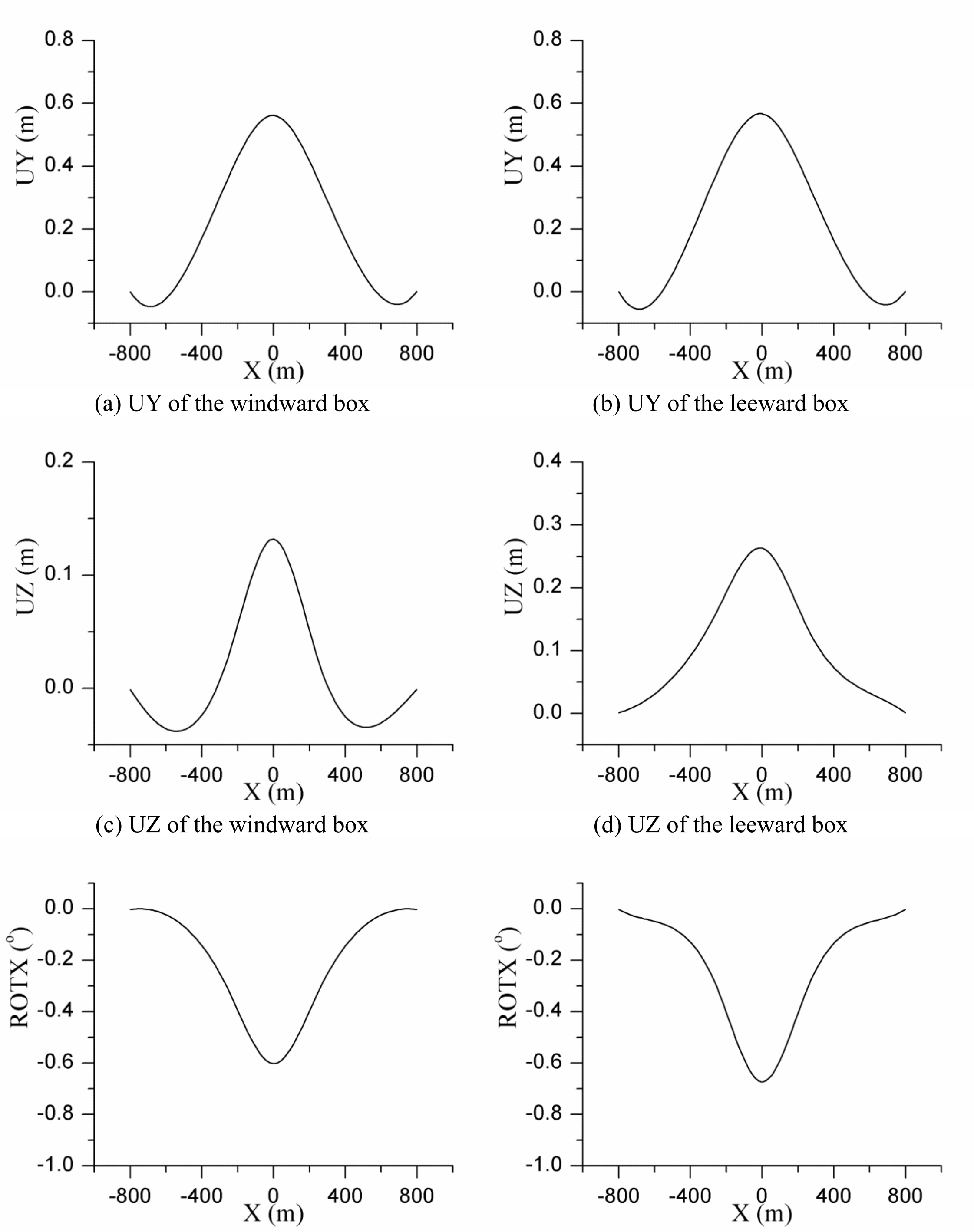

(a) UY of the windward box (b) UY of the leeward box

(c) UZ of the windward box (d) UZ of the leeward box

(e) ROTX of the windward box (f) ROTX of the leeward box

Figure 7.10 Span-wise distribution of mean wind induced displacement (Case 2)

Figure 7.9 and Figure 7.10 depict the span-wise distributions of the mean wind induced lateral, vertical, and torsional displacements in Case 5 and Case 2, respectively. All maximum displacement values occur in the middle of the main span. The lateral displacements of the windward and leeward boxes are almost equal. The vertical displacement of the leeward box is much larger than that of the windward box and their span-wise patterns are different because of the torsion of the deck. The torsional displacement of the leeward box is larger than that of the windward box but they share a similar span-wise distribution pattern.

7.5.2 Mean wind stress responses

As the bridge deck is modeled by shell elements and the buffeting analysis is performed with distributed buffeting loads, the stresses and strains in the components of the bridge deck can be generally captured in this work. Nevertheless, due to the complicated connections and boundary conditions of local components, not all stress/strain results are accurate. Based on the work presented in Chapter 6, it is believed that the longitudinal stresses on the steel deck yielded with this FE model are generally consistent with the measured results. Thus the stress responses of these locations are also presented in this Chapter. Figure 7.11 shows the locations of stress outputs. The output section in Segment 32 is at the same location of D4 in Figure 7.8; and the section in Segment 17 is at the same location of D3.

Table 7.7 lists the mean wind longitudinal stresses of the above mentioned locations. The absolute values of the stresses are generally larger in Cases 1, 2 and 3 compared with those in Cases 4, 5, and 6 correspondingly. It can be concluded that the mean wind from the S-W direction induces larger stresses of the bridge deck than the mean wind from the N-E direction due to larger mean wind speed.

The stress responses in Segment 32 are much larger than those in Segment 17. This is because the mean wind induced moment is much larger in the mid-span than in the quarter-span.

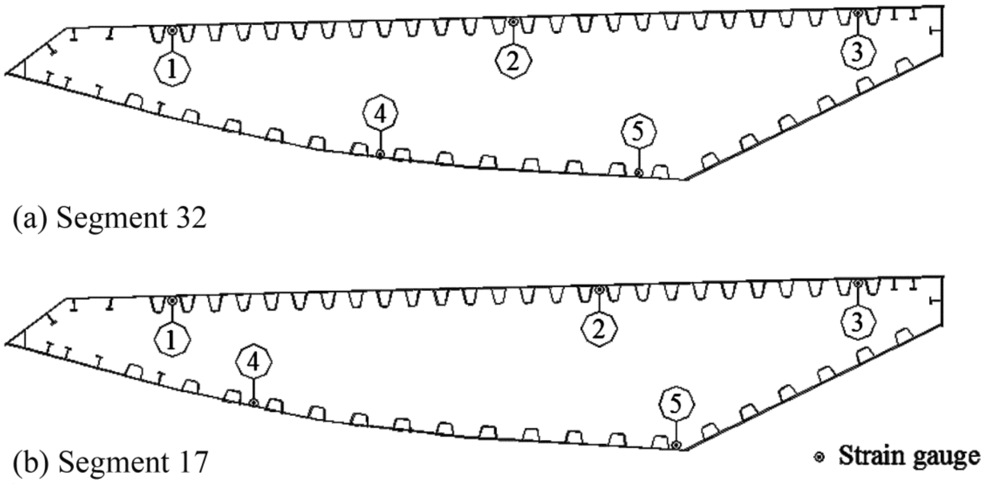

Figure 7.11 The locations of stress outputs

Table 7.7 Mean wind longitudinal stresses SX (MPa)

Segment	Location	Case 1	Case 2	Case 3	Case 4	Case 5	Case 6
32	D-str1-windward	-7.84	-7.43	-7.18	-16.70	-16.70	-17.10
32	D-str1-leeward	23.80	23.70	24.10	4.02	4.20	4.45
32	D-str2-windward	-16.60	-16.60	-16.90	-10.00	-9.98	-10.10
32	D-str2-leeward	13.80	13.80	14.10	11.70	11.70	11.90
32	D-str3-windward	-23.90	-24.20	-24.90	-4.50	-4.36	-4.30
32	D-str3-leeward	5.48	5.55	5.71	18.20	18.00	18.20
32	D-str4-windward	-9.78	-9.85	-10.10	-13.90	-14.20	-14.70
32	D-str4-leeward	21.90	21.50	21.60	7.44	7.33	7.36
32	D-str5-windward	-16.30	-17.00	-18.00	-7.89	-8.27	-8.79
32	D-str5-leeward	14.70	14.10	13.90	14.60	14.20	14.00
17	D-str1-windward	-1.21	-0.29	0.58	-6.41	-5.45	-4.63
17	D-str1-leeward	3.07	3.56	4.10	-3.09	-2.52	-2.03
17	D-str2-windward	-6.63	-5.38	-4.29	-2.71	-1.95	-1.26
17	D-str2-leeward	-2.00	-1.26	-0.58	0.43	0.87	1.30
17	D-str3-windward	-9.72	-8.28	-7.07	-0.60	0.04	0.66
17	D-str3-leeward	-4.89	-4.02	-3.26	2.45	2.81	3.20
17	D-str4-windward	-2.08	-1.09	-0.17	-6.00	-5.05	-4.23
17	D-str4-leeward	2.32	2.88	3.46	-2.65	-2.08	-1.57
17	D-str5-windward	-6.18	-4.91	-3.78	-3.58	-2.73	-1.97
17	D-str5-leeward	-1.39	-0.59	0.16	-0.24	0.29	0.80

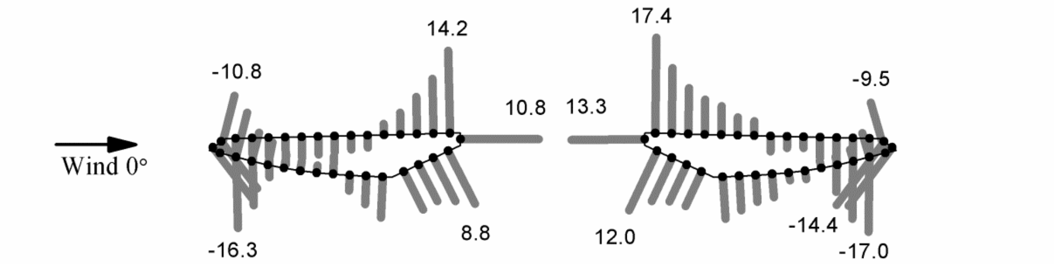

(a) Mid-span

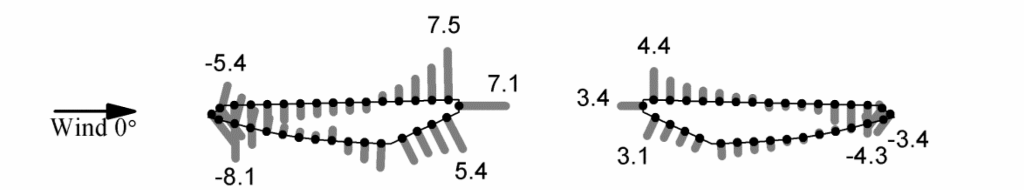

(b) Quarter-span

Figure 7.12 Section-wise distribution of mean wind induced stresses (Case 5) (MPa)

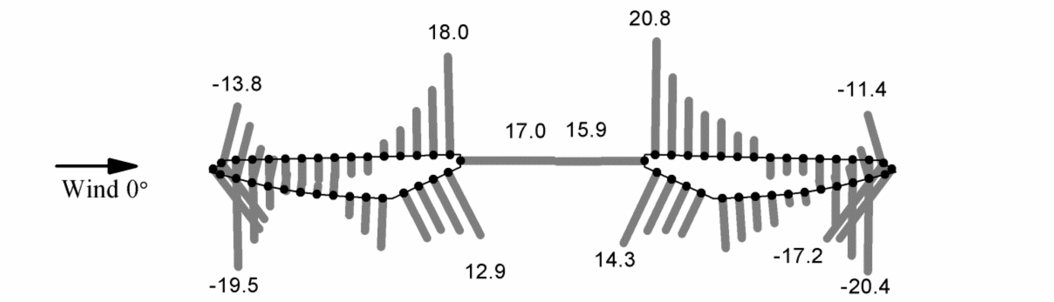

(a) Mid-span

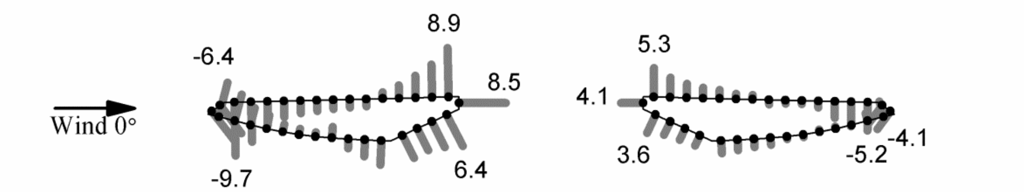

(b) Quarter-span

Figure 7.13 Section-wise distribution of mean wind induced stresses (Case 2) (MPa)

Figure 7.12 and Figure 7.13 plot the section-wise distributions of mean wind induced stresses in Case 5 and Case 2, respectively. As the sizes of the finite elements are very small, only the stress responses values at a series of evenly distributed locations instead of all elements are plotted. The outer edges of the two boxes bear tensile stresses while the inner edges bear compression stresses. Besides, the absolute values of the stresses increase with the distance from the section centroid of each box. Generally speaking, the mean wind induced stresses in the leeward box is larger than those in the windward box.

The stress responses in the quarter-span section are much smaller than those in the mid-span section due to the larger moments in the mid-span. The largest stress responses appear on the mid-span section of due to the wind from the S-W direction. The maximum absolute stress appears at the inner edge of the leeward box and the value is 20.8MPa.

7.6 Total buffeting displacements and stresses

The total buffeting responses of the complete bridge are presented in this subsection. The total wind response then refers to (1) maximum total buffeting responses, i.e., the mean wind response plus the corresponding peak buffeting response (the RMS buffeting response multiplied by a peak factor) and (2) minimum total buffeting responses, i.e., the mean wind response minus the corresponding peak buffeting response. The peak factor of the buffeting response is taken as 3.5 in this study.

The buffeting response analysis is carried out in the frequency domain with the first 50 modes of vibration included. To compute the RMS buffeting responses within the frequency range of interest, a frequency interval about 0.002Hz is used within the range from 0.06 to 1Hz. A damping ratio of 0.36% for all modes of vibration is used.

Both structural and aeroelastic couplings between modes of vibration are naturally retained. Mean wind loads on the bridge towers, piers and cables are taken into consideration in addition to those on the bridge deck whereas the dynamic wind loads are applied only on the bridge deck. The turbulent wind components in the longitudinal and vertical directions are considered in terms of the aerodynamic coefficients, aerodynamic admittance functions, wind spectra, and coherence functions introduced in Section 7.3 and 7.4. The aeroelastic forces are included in terms of aeroelastic stiffness and aeroelastic damping.

7.6.1 Total buffeting displacement responses

For the key location D4-windward (mid-span), its maximum and minimum total buffeting displacements are presented in Table 7.8 and

Table 7.9, respectively.

The influences of different load cases on the total buffeting displacement responses can be observed as follows:

(1) The results in Case 4, 5 and 6 are significantly larger than the results in case 1, 2 and 3. It can be therefore concluded that the wind from N-E produces larger buffeting displacement responses than the wind from S-W due to larger turbulence intensity.

(2) The effects of initial wind angle of incidence on the lateral buffeting response are small. It can be observed that Case 4 corresponds to the largest maximum lateral and vertical displacement, indicating that the -3° initial angle of incidence leads to the

largest lateral and vertical buffeting responses among the three given angles of attack.

(3) It can be seen that the absolute values of the maximum lateral, vertical, and torsional total buffeting displacements of the windward deck at the middle point of the main span are 1.313m, 2.856m and 0.879°, respectively. These values are also the maximum absolute values of the total buffeting responses.

Table 7.8 Maximum total buffeting displacements at D4-windward

Cases	UY (m)	UZ (m)	ROTX (°)
Case 1	2.731E-001	1.820E+000	4.477E-001
Case 2	2.705E-001	1.714E+000	4.206E-001
Case 3	2.687E-001	1.550E+000	3.951E-001
Case 4	1.313E+000	2.856E+000	8.567E-001
Case 5	1.303E+000	2.766E+000	8.664E-001
Case 6	1.311E+000	2.563E+000	8.786E-001

Table 7.9 Minimum total buffeting displacements at D4-windward

Cases	UY (m)	UZ (m)	ROTX (°)
Case 1	-1.235E+000	-1.531E+000	-5.397E-001
Case 2	-1.225E+000	-1.584E+000	-5.567E-001
Case 3	-1.230E+000	-1.564E+000	-5.752E-001
Case 4	-7.812E-001	-2.749E+000	-6.980E-001
Case 5	-7.745E-001	-2.770E+000	-6.774E-001
Case 6	-7.774E-001	-2.663E+000	-6.593E-001

Figure 7.14 and Figure 7.15depict the span-wise distributions of maximum total displacement responses in Case 5 and Case 2, respectively. The largest values of total displacement responses all occur at the middle of the main span. The vertical maximum total displacement of the windward box is slightly larger than that of the leeward box. The lateral and torsional maximum total displacement of the windward

box is slightly smaller than that of the leeward box.

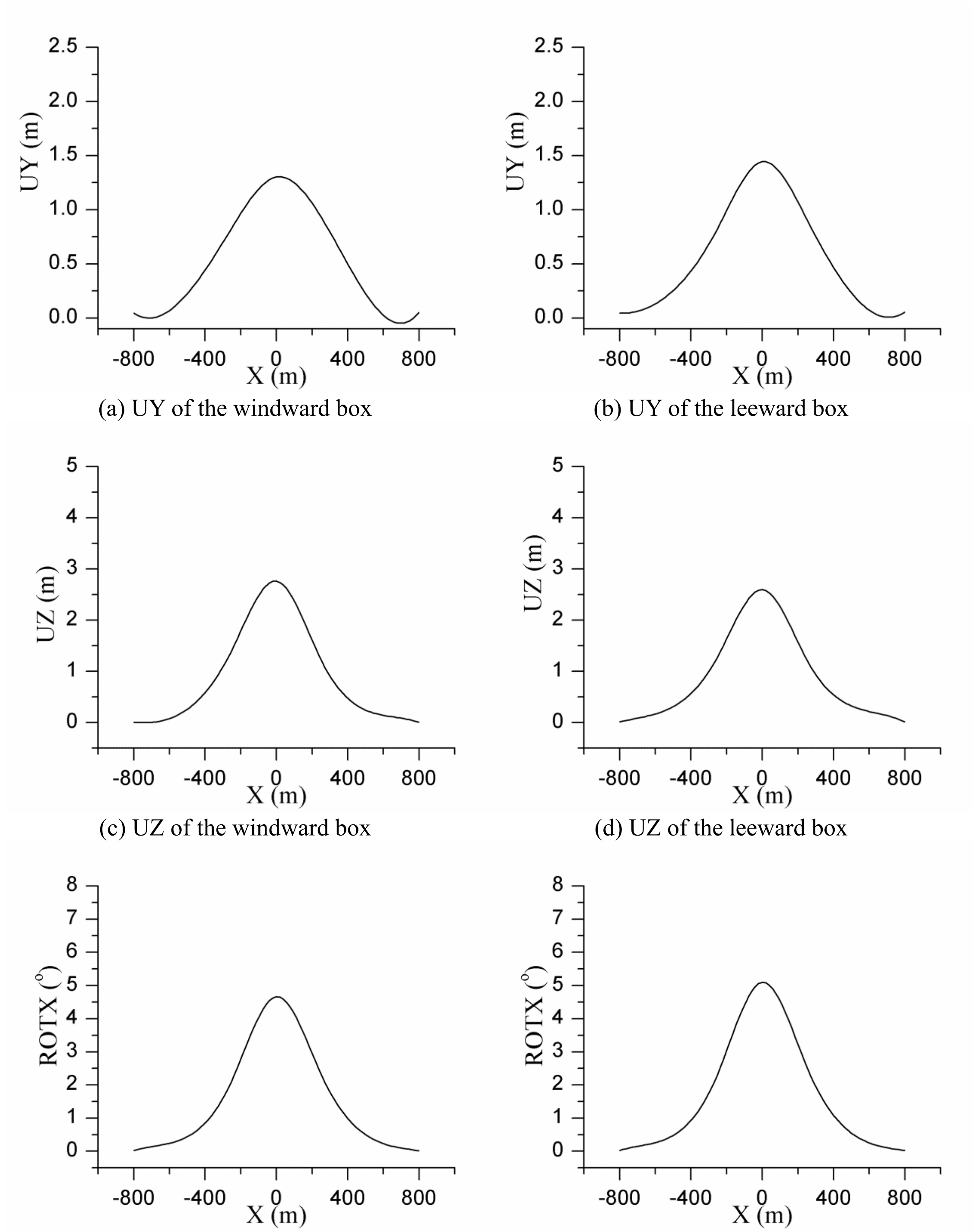

(a) UY of the windward box (b) UY of the leeward box

(c) UZ of the windward box (d) UZ of the leeward box

(e) ROTX of the windward box (f) ROTX of the leeward box

Figure 7.14 Span-wise distribution of maximum total displacement (Case 5)

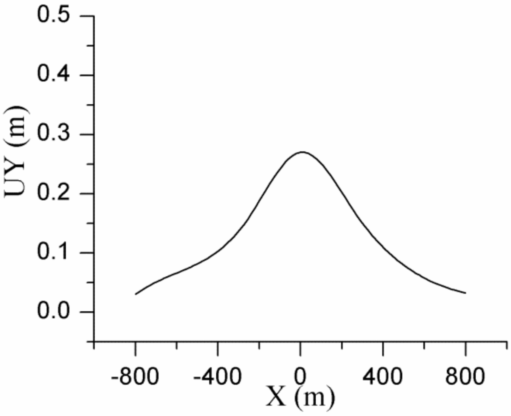

(a) UY of the windward box

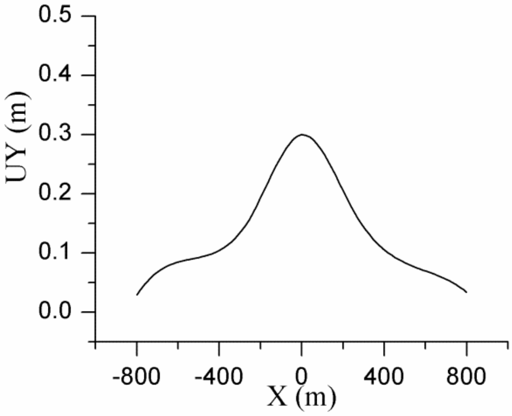

(b) UY of the leeward box

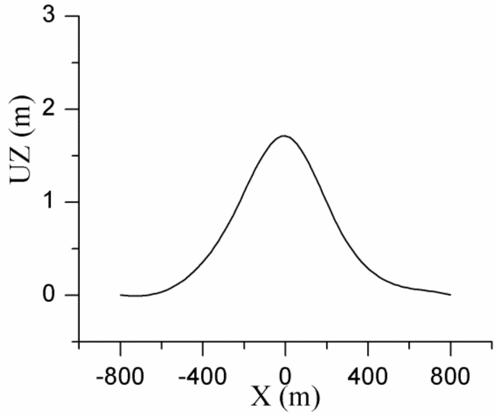

(c) UZ of the windward box

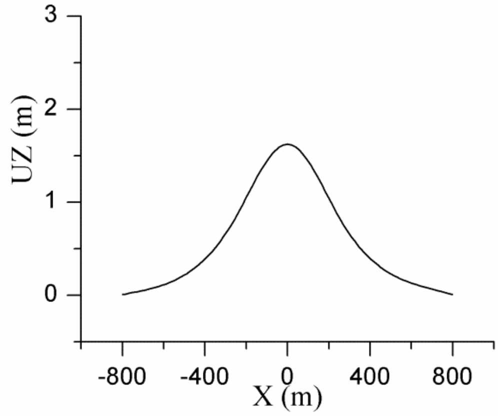

(d) UZ of the leeward box

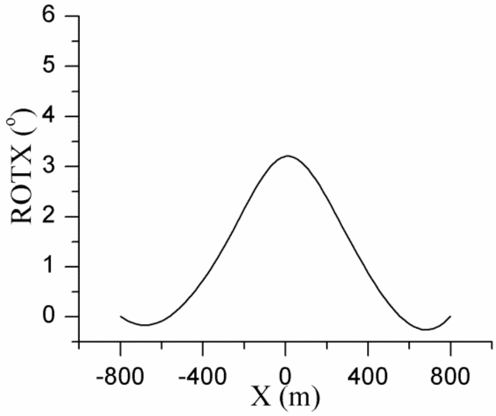

(e) ROTX of the windward box

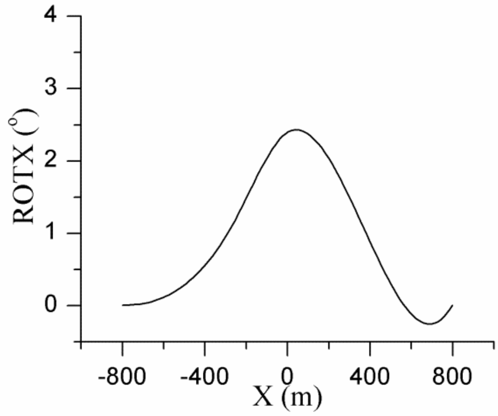

(f) ROTX of the leeward box

Figure 7.15 Span-wise distribution of maximum total displacement (Case 2)

7.6.2 Total buffeting stress responses

Table 7.10 and Table 7.11 list the maximum and minimum total buffeting longitudinal stresses of the stress output locations. The influences of different load cases on the total buffeting stress responses can be observed as follows:

(1) The absolute values of the stresses are generally smaller in Cases 1, 2 and 3 compared with those in Cases 4, 5, and 6 correspondingly. It can be concluded that the wind from N-E produces larger buffeting stress responses than the wind from S-W due to larger turbulence intensity.

(2) Generally speaking, the absolute values of the stresses on Segment 32 are larger than those on Segment 17. The dynamic wind induces larger stresses in the mid-span than the quarter-span.

(3) The D-str No.1 on the windward box gives the largest total buffeting stress in most cases. This is mainly because 1) D-str No.1 locates the farthest away from the centroid of the box section and 2) the largest mean wind pressures occurs on the windward edge of the bridge deck. The largest maximum total longitudinal stress is about 106MPa. The largest minimum total longitudinal stress is about -139MPa.

Figure 7.16 and Figure 7.17 plot the section-wise distributions of maximum total longitudinal stresses in Case 5 and Case 2, respectively. The total buffeting induced longitudinal stresses increase with the distance from the section centroid of each box for both models. The maximum total stresses in the windward box are larger than those in the leeward box. The dynamic longitudinal stress responses in the quarter-span section are much smaller than those in the mid-span section due to the larger dynamic moments in the mid-span. The largest maximum total stress responses appear on the mid-span section due to the wind from the N-E direction. The largest value appears at the inner edge of the windward box and the value is 131MPa.

Table 7.10 Maximum total longitudinal stresses SX (MPa)

Segment	Location	Case 1	Case 2	Case 3	Case 4	Case 5	Case 6
32	D-str1-windward	68.00	59.70	72.10	106.00	105.00	96.20
32	D-str1-leeward	44.40	59.10	80.10	88.20	131.00	128.00
32	D-str2-windward	48.60	34.30	31.70	64.40	63.60	57.70
32	D-str2-leeward	26.70	34.60	44.70	57.40	85.00	83.10
32	D-str3-windward	32.30	13.10	-2.07	29.30	28.80	25.70
32	D-str3-leeward	11.90	14.20	15.10	31.70	46.40	45.90
32	D-str4-windward	40.00	31.90	32.00	47.90	47.60	48.20
32	D-str4-leeward	16.80	31.80	69.40	79.20	72.30	72.10
32	D-str5-windward	5.52	-5.85	-24.50	-25.10	-24.70	-13.80
32	D-str5-leeward	-16.40	-4.99	40.60	54.40	-3.49	0.04
17	D-str1-windward	43.00	59.70	59.60	93.10	92.60	82.70
17	D-str1-leeward	44.50	59.10	40.10	57.60	88.60	84.90
17	D-str2-windward	28.70	30.00	30.70	58.30	58.30	52.00
17	D-str2-leeward	29.60	30.50	20.10	37.10	55.40	52.80
17	D-str3-windward	20.60	13.10	14.20	38.50	38.80	34.50
17	D-str3-leeward	21.10	14.20	8.70	25.40	36.50	34.40
17	D-str4-windward	32.10	44.10	44.20	69.10	68.80	64.20
17	D-str4-leeward	33.50	43.80	37.40	54.80	65.20	62.80
17	D-str5-windward	4.26	-0.16	0.67	5.96	6.27	13.70
17	D-str5-leeward	4.73	0.53	23.20	40.20	3.98	4.47

Table 7.11 Minimum total longitudinal stresses SX (MPa)

Segment	Location	Case 1	Case 2	Case 3	Case 4	Case 5	Case 6
32	D-str1-windward	-83.70	-74.60	-86.50	-139.00	-138.00	-130.00
32	D-str1-leeward	3.20	-11.70	-31.90	-80.20	-123.00	-119.00
32	D-str2-windward	-81.80	-67.50	-65.50	-84.40	-83.60	-77.90
32	D-str2-leeward	0.90	-7.00	-16.50	-34.00	-61.60	-59.30
32	D-str3-windward	-80.10	-61.50	-47.70	-38.30	-37.50	-34.30
32	D-str3-leeward	-0.94	-3.10	-3.68	4.70	-10.40	-9.50
32	D-str4-windward	-59.60	-51.60	-52.20	-75.70	-76.00	-77.60
32	D-str4-leeward	27.00	11.20	-26.20	-64.30	-57.60	-57.40
32	D-str5-windward	-38.10	-28.20	-11.50	9.32	8.16	-3.78
32	D-str5-leeward	45.80	33.20	-12.80	-25.20	31.90	28.00
17	D-str1-windward	-45.40	-60.30	-58.40	-106.00	-104.00	-92.00
17	D-str1-leeward	-38.40	-52.00	-31.90	-63.80	-93.60	-89.00
17	D-str2-windward	-42.00	-40.80	-39.30	-63.70	-62.20	-54.50
17	D-str2--leeward	-33.60	-33.00	-21.30	-36.20	-53.70	-50.20
17	D-str3-windward	-40.00	-29.70	-28.30	-39.70	-38.70	-33.20
17	D-str3-leeward	-30.90	-22.20	-15.20	-20.50	-30.90	-28.00
17	D-str4-windward	-36.30	-46.30	-44.50	-81.10	-78.90	-72.70
17	D-str4-leeward	-28.90	-38.00	-30.50	-60.10	-69.40	-65.90
17	D-str5-windward	-16.60	-9.66	-8.23	-13.10	-11.70	-17.60
17	D-str5-leeward	-7.51	-1.71	-22.90	-40.70	-3.40	-2.87

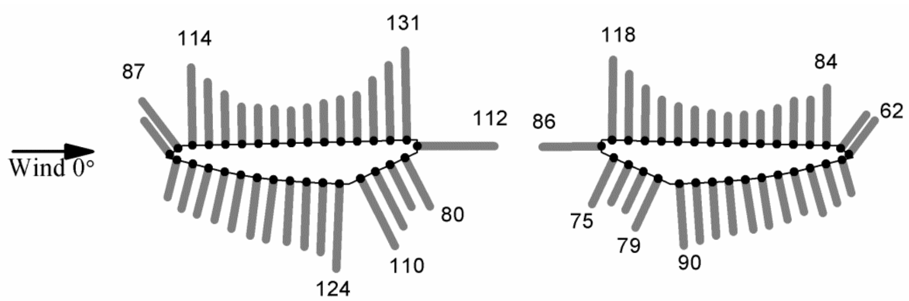

(c) Mid-span

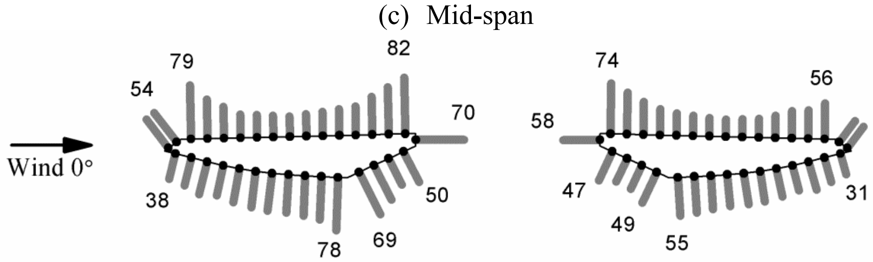

(d) Quarter-span

Figure 7.16 Section-wise distribution of maximum total longitudinal stresses (Case 5) (MPa)

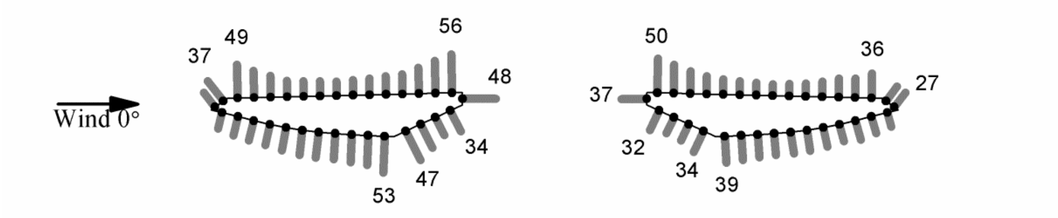

(c) Mid-span

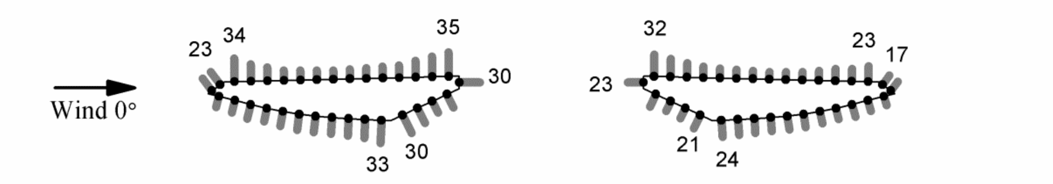

(d) Quarter-span

Figure 7.17 Section-wise distribution of maximum total longitudinal stresses (Case 2) (MPa)

7.7 Summary

This chapter first introduces the technique details on applying the proposed buffeting analysis framework on the substructure-based model of Stonecutters Bridge. Then the wind characteristics and the aerodynamic/aeroelastic properties of the bridge components are presented. Buffeting analyses on Stonecutters Bridge with distributed loads is performed with these data and parameters.

Two wind directions associated with two terrains are considered: one is the open-sea terrain mainly from the S-W direction and the other is the over-land terrain mainly from the N-E direction. The levels of turbulence intensity in terms of wind turbulence standard deviation, 10m/s and 17m/s, are used for these two directions respectively. Three angles of incidence, $\pm 3°$ and 0°, are deliberated in this analysis, resulting in totally 6 cases. The coherence and admittance of buffeting loads are directly acquired from wind tunnel pressure tests. The mean wind responses and total buffeting responses at the critical locations are presented.

The mean wind from the S-W direction induces larger mean displacements and stress responses of the bridge than the mean wind from the N-E direction due to larger mean wind speed. The -3° initial angle of incidence leads to the largest vertical mean displacements of the bridge deck among the three given initial angles of attack. The +3° initial angle of incidence leads to the largest absolute torsional displacements of the bridge deck among the three given initial angles of attack. The stress responses in Segment 32 are much larger than those in Segment 17, indicating that the mean wind induced moment is much larger in the mid-span than in the quarter-span. The absolute values of the stresses increase with the distance from the section centroid of each box. Generally speaking, the mean wind induced stresses in the leeward box is larger than those in the windward box. The largest mean wind longitudinal stress response appear on the mid-span section of due to the wind from the S-W direction. The maximum absolute stress appears at the inner edge of the leeward box and the value is 20.8MPa.

The dynamic wind from the N-E direction induces larger total buffeting displacement and stress responses of the bridge than the dynamic wind from the S-W direction due to larger turbulence intensity. The -3° initial angle of incidence leads to the largest lateral and vertical buffeting responses among the three given angles of attack. Generally speaking, the absolute values of the total buffeting stresses on Segment 32 are larger than those on Segment 17. The dynamic wind induces larger stresses in the mid-span than the quarter-span. The total buffeting induced longitudinal stresses increase with the distance from the section centroid of each box. The maximum total stresses in the windward box are larger than those in the leeward box. The largest maximum total stress responses appear on the mid-span section due to the wind from the N-E direction. The largest value appears at the inner edge of the windward box and the value is 131MPa.

For brevity, only some selected sets of the results are presented in this chapter. Detailed results on mean wind and total buffeting responses for all cases are listed in Appendix A to Appendix E.

This chapter focuses on the mean wind responses and total buffeting responses of some key locations of Stonecutters Bridge. These responses were computed by applying the buffeting analysis framework proposed in this study on the multi-scale FE model. In the next chapter, these results will be compared with responses computed by force-based buffeting analysis method on a spine-beam model.

CHAPTER 8

COMPARING THE PROPOSED AND TRADITIONAL METHODS

8.1 Introduction

As demonstrated in Chapter 7, the buffeting analysis framework proposed in this study is capable of providing both displacement and stress responses with the multi-scale model. The proposed framework considers the sectional distribution of aerodynamic forces, aeroelastic damping and stiffness. The detailed geometry of the deck and the sectional distribution of the material properties are also simulated in the multi-scale model in this framework. Theoretically speaking, the stress responses yielded by this study should be more accurate than those computed using the traditional method.

As the site data from the real bridge's SHM system are not available at the moment, a comparison is made in this chapter between the responses computed using the proposed framework, and those computed using a sectional-force-based method on a spine-beam model to investigate the differences between the two methods. The modeling of the spine-beam model of Stonecutters Bridge and the characteristics of the integrated sectional forces are introduced first. The wind forces on the windward box and on the leeward box of the deck are dealt with separately to enable a better comparison with the pressure-based framework. The mean wind and maximum total buffeting responses are obtained with the spine-beam model. A comparison is made between the results of the two methods.

8.2 Spine-beam model of Stonecutters Bridge

The spine-beam model of Stonecutters Bridge is also established in ANSYS for an effective comparison.

The windward and leeward box decks are modeled as two parallel beams with equivalent cross-sectional properties for both the steel and concrete decks. The cross-sections of the decks are directly imported in the FE beam element as shown in Figure 8.1. The cross-sectional properties can be automatically calculated by the FE software.

The windward and leeward box decks are connected by cross-girders with 18 m intervals in the longitudinal direction. The effective length of the elastic transverse beam is taken as 18.5 m (Ding & Xu, 2004). This length is chosen generally based on the rule that the area of the longitudinal girder at the intersection approximately equals the cross-section area of the cross girder. The sensitivity of the elastic length to the bridge dynamic characteristics was also investigated to determine this value. Thus, each cross girder is modeled in three parts: one elastic beam and two rigid arms (see Figure 8.2). The elastic segment in the middle with a length of 18.5 m represents the actual flexibility of the cross-girder. The elastic beam is connected to the longitudinal girders by two rigid arms (see Figure 8.3).

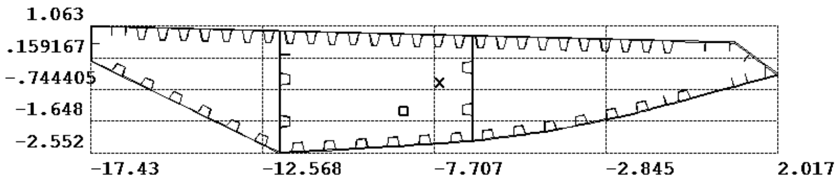

(a) Steel deck section

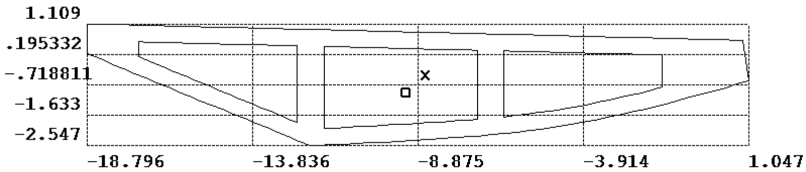

(b) Concrete deck section

Figure 8.1 Steel and concrete deck sections in the spine-beam model

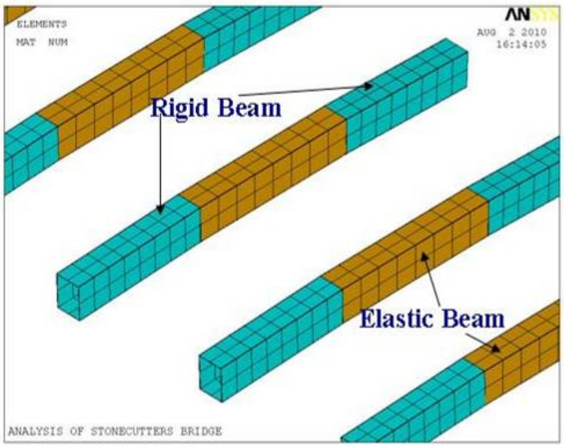

Figure 8.2 Modeling of the cross-girders

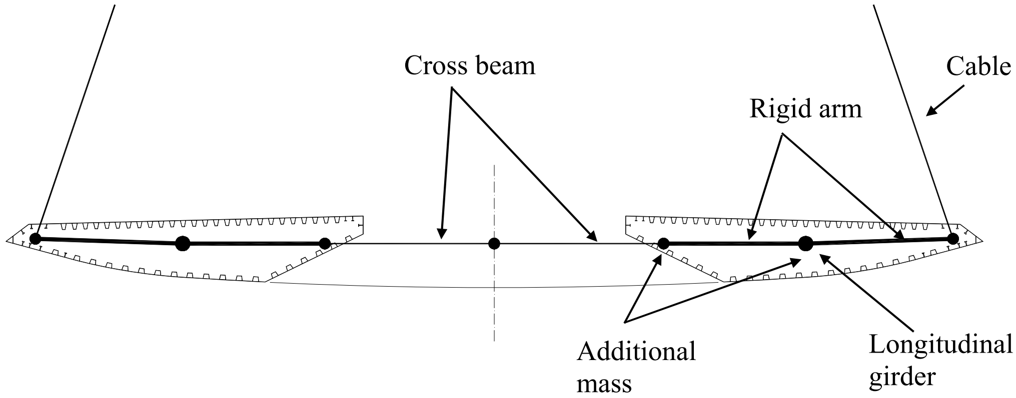

(a) Steel deck

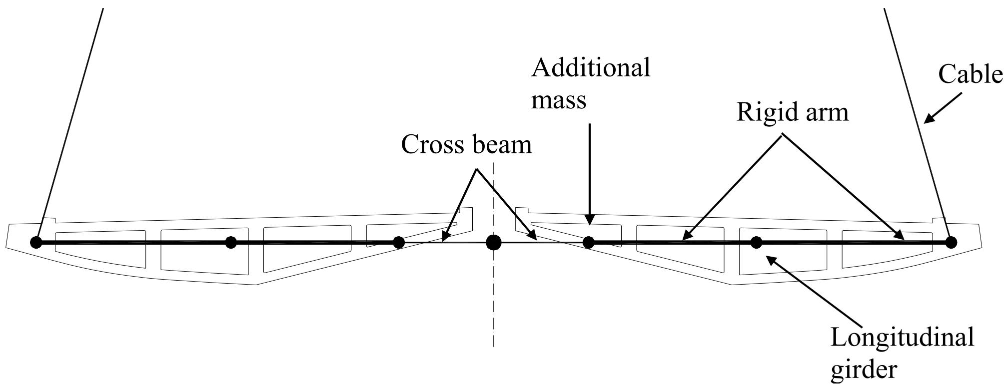

(b) Concrete deck

Figure 8.3 Modeling of the steel and concrete decks

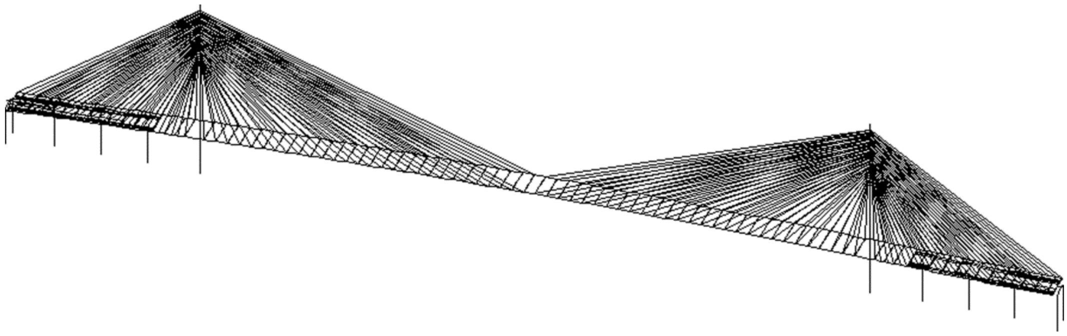

Figure 8.4 Established spine-beam model of Stonecutters Bridge

Additional mass resulting from the secondary components of the deck, including the pavement and the diaphragms, is added to the model with additional mass elements as shown in Figure 8.3.

The modeling of the towers, piers and cables is the same as in the multi-scale model. The cables are connected to the longitudinal girders by rigid arms as shown in Figure 8.3.

The established 3D spine-beam model of Stonecutters Bridge is shown in Figure 8.4.

8.3 Comparison of dynamic properties

The modal frequencies of the first 10 modes of the established spine-beam model are listed and compared with those of the multi-scale model and the real bridge in Table 8.1. The first 10 mode shapes of the two models are consistent, and the differences between the modal frequencies of the two models are small. The maximum difference in the modal frequencies is only about 3%. Moreover, the two models exhibit good consistencies with the real bridge in the case of the modal frequencies.

8.4 Aerodynamic forces on the spine-beam model

The wind forces on the windward and leeward boxes of the deck are dealt with separately to enable a better comparison with the pressure-based framework.

Table 8.1 Modal frequencies of the spine-beam and multi-scale models

Mode NO.	Measured (Hz)	Beam model (Hz)	Multi-scale Model (Hz)	Diff*	Mode shape description
1	0.1613	0.1609	0.1662	-3.19%	symmetric lateral, deck
2	0.2104	0.2121	0.2174	-2.44%	symmetric vertical, deck
3	0.2126	0.2124	0.2150	-1.21%	asymmetric lateral, tower
4	0.2167	0.2185	0.2220	-1.58%	symmetric lateral, tower
5	0.2632	0.2605	0.2607	-0.08%	asymmetric vertical, deck
6	0.3268	0.3274	0.3234	1.24%	longitudinal, piers and towers; vertical, deck
7	0.3340	0.3314	0.3385	-2.10%	symmetric vertical, deck
8	0.3952	0.3993	0.3927	1.68%	asymmetric lateral, deck
9	0.4125	0.391	0.3984	-1.86%	asymmetric vertical, deck
10	0.4586	0.4501	0.4498	0.07%	symmetric torsional, deck

*Diff refers to the frequency difference between the beam and multi-scale models

8.4.1. Mean aerodynamic force coefficients

The aerodynamic force coefficients of the two boxes and their derivatives with respect to the angle of incidence are listed in Table 8.2. The windward box has a larger C_d and smaller absolute values of C_l and C_m than the leeward box. The mean wind-induced pitching moment on the windward box seems negligible. For the derivatives to the angle of incidence, in contrast, the windward box has a smaller absolute value of C'_d and larger values of C'_l and C'_m. As the dynamic responses are usually dominated by the lift force and the pitching moment, the coefficients suggest larger dynamic responses on the windward box than on the leeward box.

Table 8.2 Aerodynamic force coefficients of the two boxes

	C_d	C_l	C_m	C'_d	C'_l	C'_m
Windward box	0.025	-0.031	-0.003	-0.009	2.063	0.834
Leeward box	0.017	-0.070	0.033	-0.040	0.811	0.031

8.4.2 Aerodynamic force admittance functions

The aerodynamic force admittance functions can be fitted with rational functions as

$$|\chi_F(K)|^2 = \frac{c_{i1}}{1 + c_{i2} \cdot (K - K_I)^2} + \frac{c_{s1}}{1 + c_{s2} \cdot (K - K_s)^2} \tag{8.1}$$

The fitting function for the force admittance is the same as that of the pressure admittance, and it considers both the incoming and signature turbulence effects. Table 8.3 and Table 8.4 list the fitting parameters for the aerodynamic force admittances of the N-E and S-W wind directions, respectively. Figure 8.5 and Figure 8.6 plot the measured and fitted aerodynamic force admittances of the N-E and S-W wind directions, respectively.

It can be seen from the fitting parameters and the figures that the windward box bears a much larger aerodynamic lift force than the leeward box, whereas the aerodynamic drag force and pitch moment are smaller on the windward box. The signature turbulence mainly affects the aerodynamic forces on the leeward box. For the N-E wind direction with larger incoming turbulence, the signature turbulence induced aerodynamic forces are small. For the N-E wind direction with smaller incoming turbulence, the signature turbulence effects are important at higher reduced frequencies, as suggested by the force admittance.

Table 8.3 Fitting parameters for the aerodynamic force admittances (N-E wind direction)

	Windward box			Leeward box		
	F_D	F_L	F_M	F_D	F_L	F_M
C_{i1}	0.0032	342	0.536	0.012	39.0	3.29
C_{i2}	24	14	41	22	48	32
C_{s1}	0.0002	5.220	-	0.0058	5.13	1.33
C_{s2}	0.51	0.50	-	0.95	1.7	0.82

Table 8.4 Fitting parameters for the aerodynamic force admittances (S-W wind direction)

	Windward box			Leeward box		
	F_D	F_L	F_M	F_D	F_L	F_M
C_{i1}	0.034	428	0.612	-	25.4	2.15
C_{i2}	81	12	45	-	26	26
C_{s1}	0.0008	32.5	0.024	0.21	195	21.2
C_{s2}	0.14	2.5	0.5	8.3	8.5	8.7

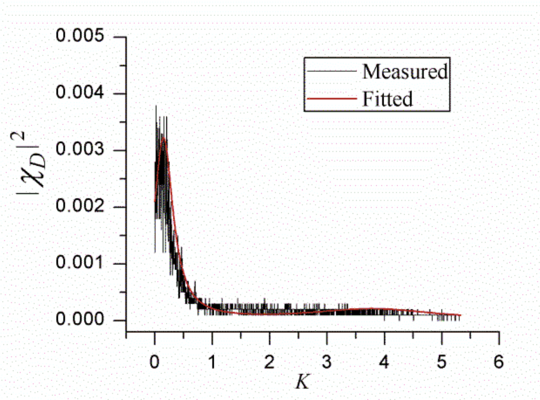

(a) Drag admittance (windward box)

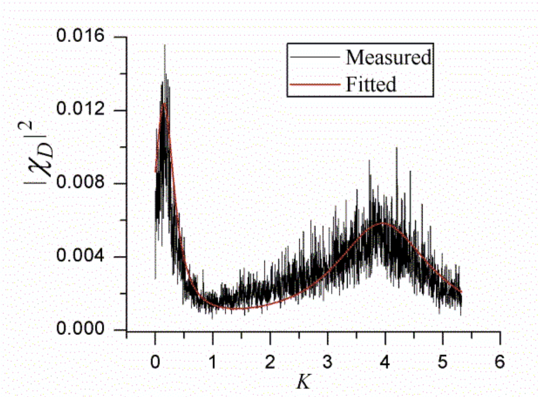

(b) Drag admittance (leeward box)

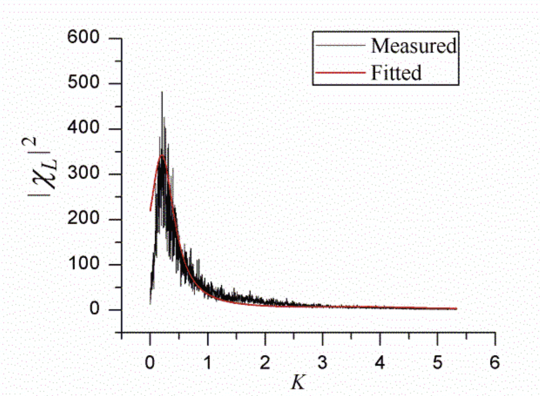

(c) Lift admittance (windward box)

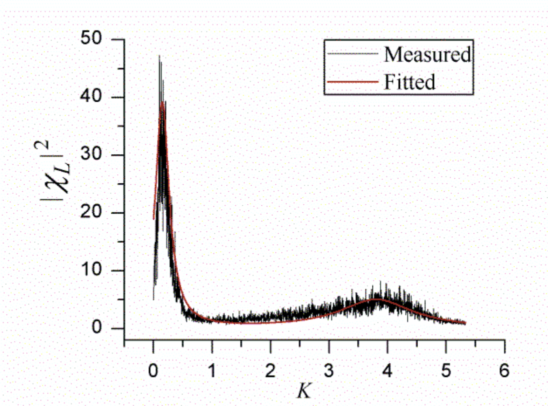

(d) Lift admittance (leeward box)

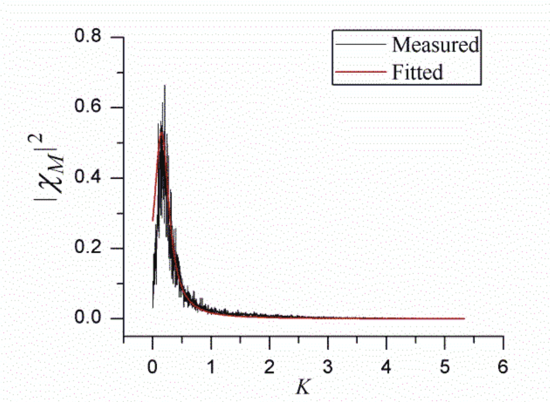

(e) Pitch admittance (windward box)

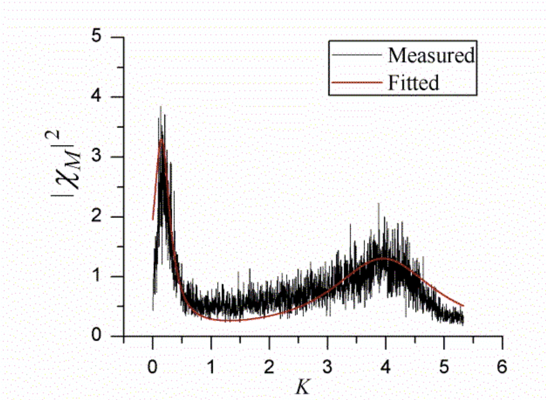

(f) Pitch admittance (leeward box)

Figure 8.5 Measured and fitted aerodynamic force admittance functions (N-E wind direction)

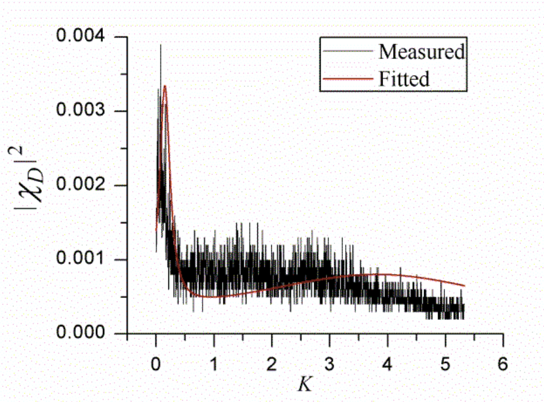

(a) Drag admittance (windward box)

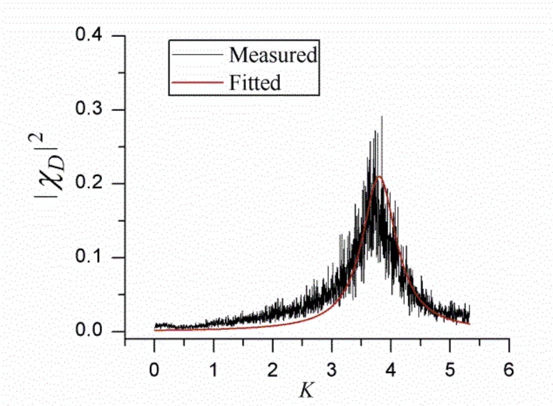

(b) Drag admittance (leeward box)

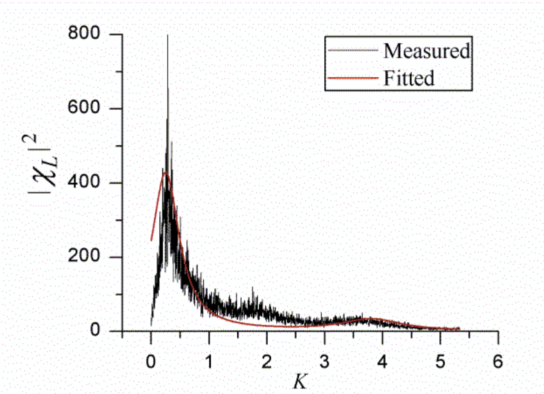

(c) Lift admittance (windward box)

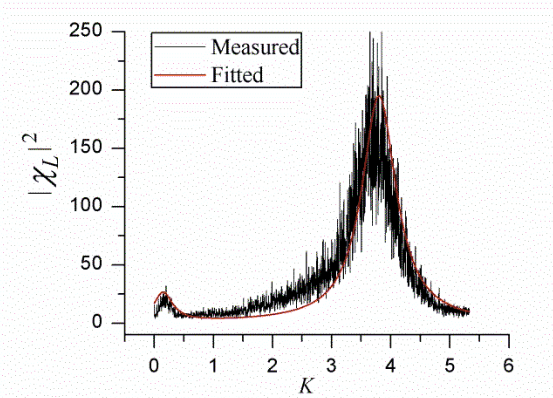

(d) Lift admittance (leeward box)

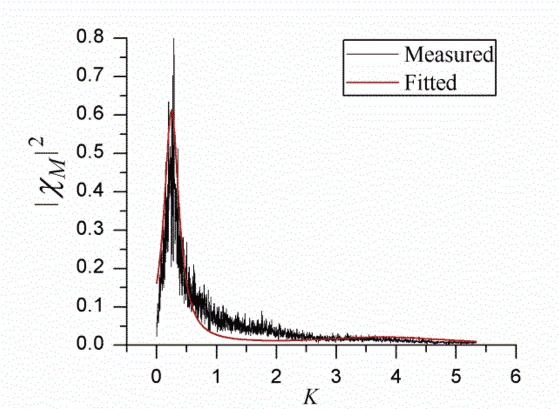

(e) Pitch admittance (windward box)

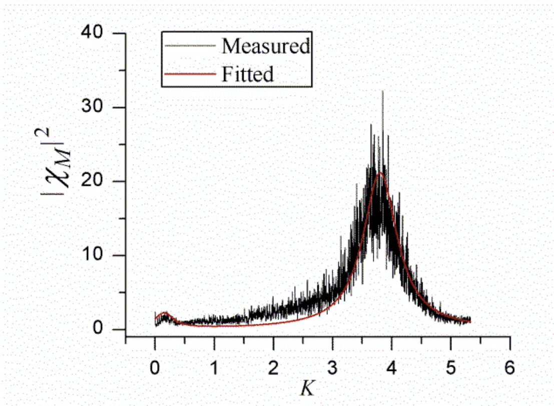

(f) Pitch admittance (leeward box)

Figure 8.6 Measured and fitted aerodynamic force admittance functions (S-W wind direction)

8.5 Comparison of mean wind responses

For an efficient comparison of the results, only the 0° angle of incidence is considered in this chapter. Moreover, to further investigate the signature turbulence effects on the bridge, analyses with different mean wind speeds are conducted. The computation cases in this chapter are listed in Table 8.5.

Table 8.5 Computation cases in Chapter 8

Case No.	U_c (m/s)	Wind Direction	Attack Angle (°)
1	55	S-W	0
2	46	N-E	0
3	45	S-W	0
4	35	S-W	0
5	25	S-W	0
6	15	S-W	0
7	5	S-W	0

8.5.1 Comparison of mean displacement responses

Figure 8.7 and Figure 8.8 compare the mean wind induced displacement of the multi-scale and spine-beam models.

Figure 8.7 shows the displacement responses due to a 46 m/s mean wind speed. The mean wind induced lateral and vertical displacements of the multi-scale model are slightly smaller than those of the spine-beam model. The difference may be because the multi-scale model has a slightly higher lateral and vertical stiffness, judging from its modal frequencies. The mean wind induced torsional displacements of the multi-scale model are slightly larger than those of the spine-beam model. It should be noted that the torsional displacements of the multi-scale model were calculated with the vertical displacements of the two nodes on the windward and leeward edges of each box. Thus, the calculated torsional displacement may be slightly larger than that of the section centroid due to possible local deformation. Generally speaking, the displacement responses of the leeward box are larger than those of the windward box in both models because the lift force and the pitching moment on the leeward box are larger.

Figure 8.8 shows the displacement responses due to a 55 m/s mean wind speed. The results are larger than those reported in Figure 8.7 due to a larger wind speed, but the differences between the displacement responses of the two models show exactly the same trend as that noted in Figure 8.7.

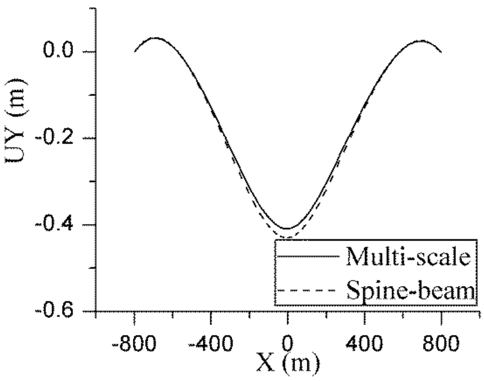

(a) UY of the windward box

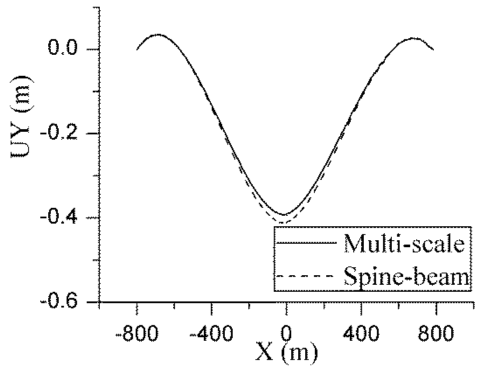

(b) UY of the leeward box

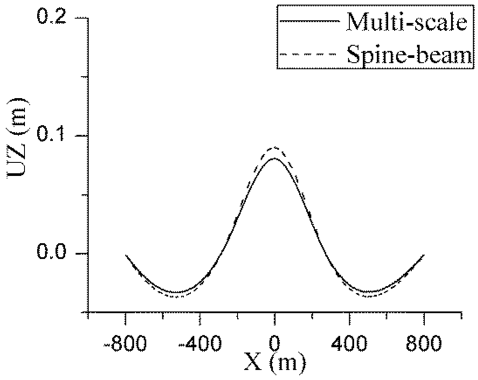

(c) UZ of the windward box

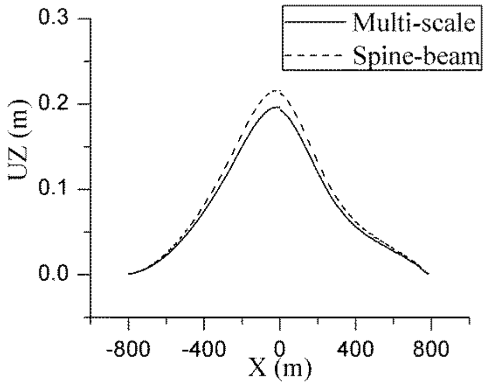

(d) UZ of the leeward box

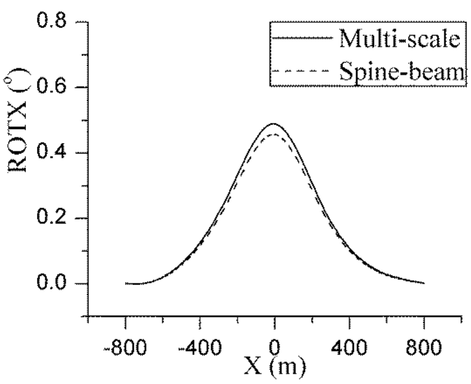

(e) ROTX of the windward box

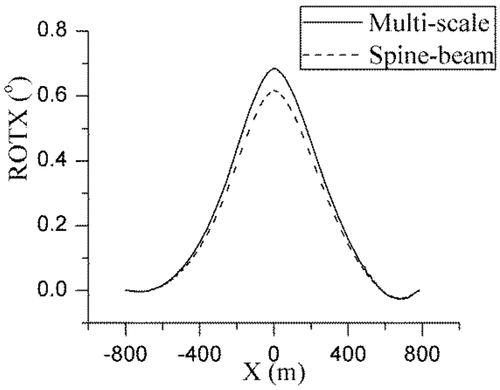

(f) ROTX of the leeward box

Figure 8.7 Mean wind induced displacement (N-E wind direction, U = 46 m/s)

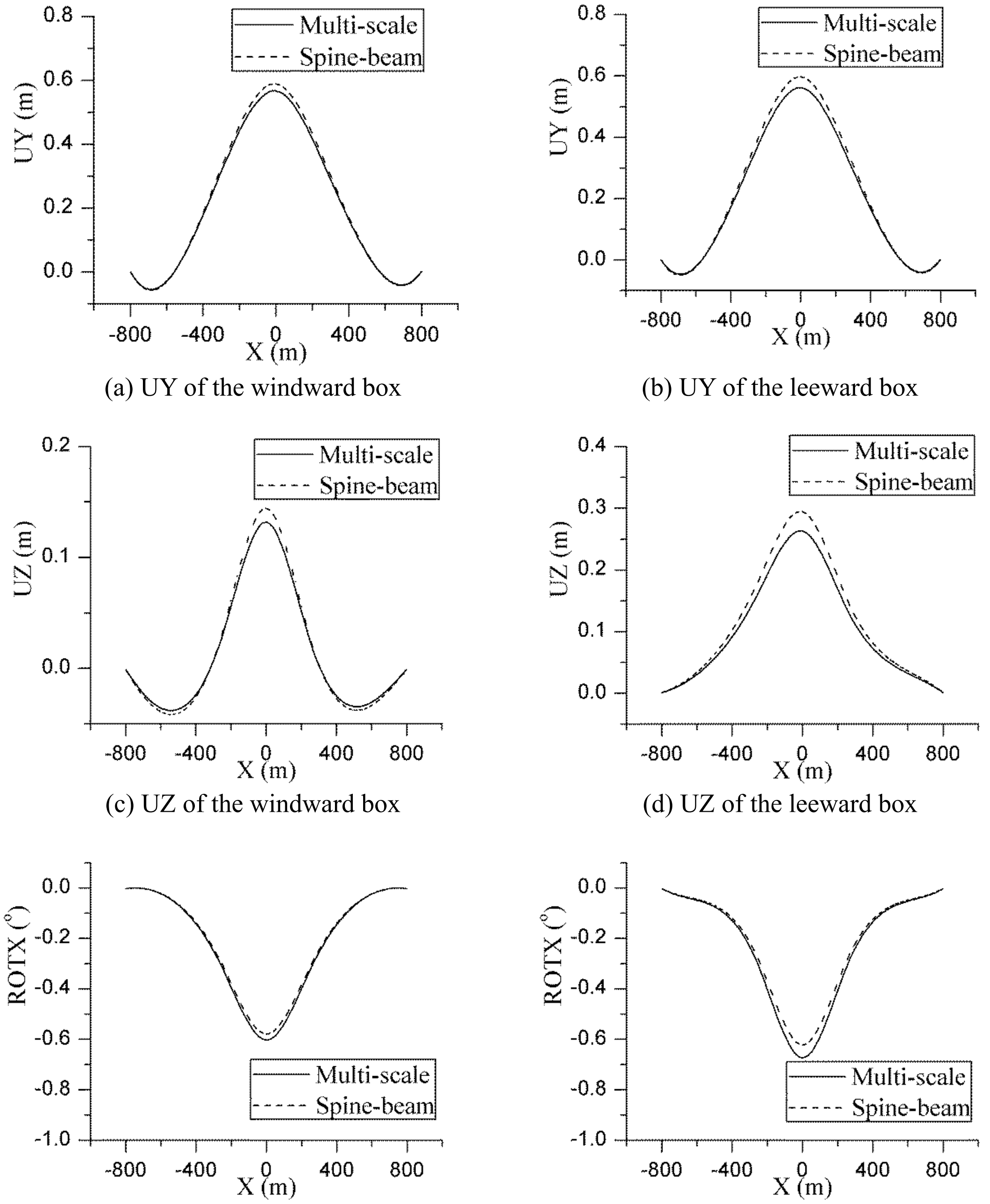

(a) UY of the windward box (b) UY of the leeward box

(c) UZ of the windward box (d) UZ of the leeward box

(e) ROTX of the windward box (f) ROTX of the leeward box

Figure 8.8 Mean wind induced displacement (S-W wind direction, U = 55 m/s)

8.5.2 Comparison of mean stress responses

Figure 8.9 and Figure 8.10 compare the mean wind-induced stress of the multi-scale and spine-beam models.

Figure 8.9 shows the stress responses due to a 46 m/s mean wind speed. For both models, the outer edges of the two boxes bear tensile stresses while the inner edges bear compression stresses. Moreover, the absolute values of the stresses increase with the distance from the section centroid of each box. Generally speaking, the mean wind induced stresses in the leeward box are larger than those in the windward box.

The stress responses in the quarter-span section are much smaller than those in the mid-span section due to the larger moments in the mid-span in both models.

The stress responses of the multi-scale model are much larger than those of the spine-beam model on the edges of both boxes. This difference probably results from the stress concentration induced by the longitudinal-and-cross-girder connections on the inner edge, and the cable-deck connections on the outer edge.

Figure 8.10 shows the stress responses due to a 55 m/s mean wind speed. The results are larger than those reported in Figure 8.9 due to larger wind speed, but the stress responses of the two models show exactly the same trend as that noted in Figure 8.7.

Among all of the cases investigated, the largest stress responses appear on the mid-span section due to the wind from the S-W direction. The maximum absolute stress in the spine-beam model appears at the outer edge of the leeward box with a value of -13.2 MPa. The maximum absolute stress in the multi-scale model appears at the inner edge of the leeward box with a value of 20.8 MPa.

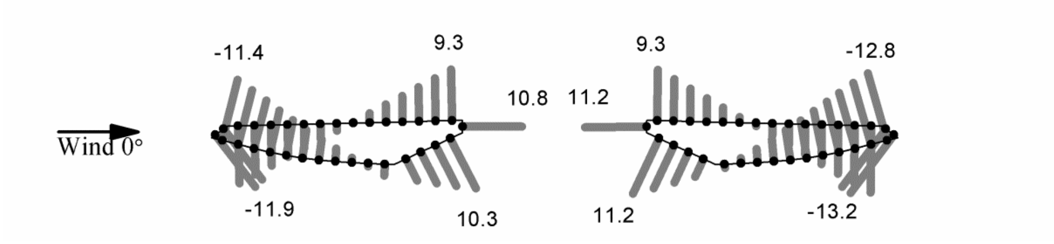

(a) Spine-beam model, mid-span

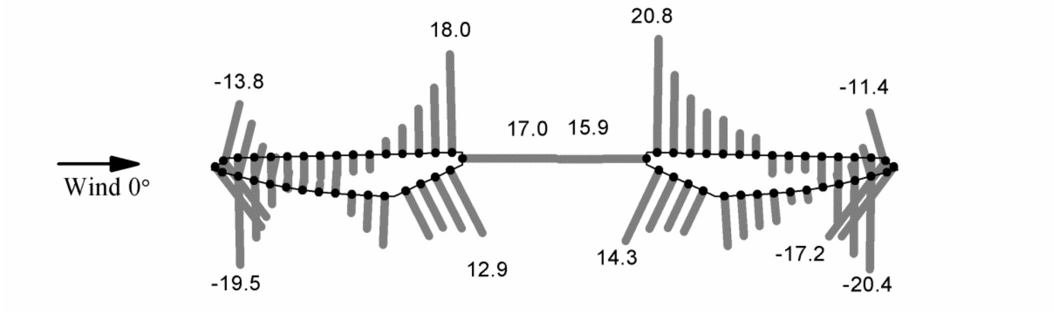

(b) Multi-scale model, mid-span

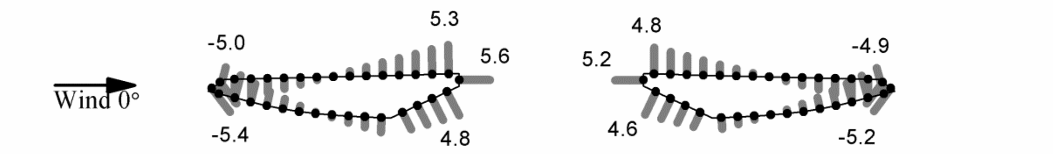

(c) Spine-beam model, quarter-span

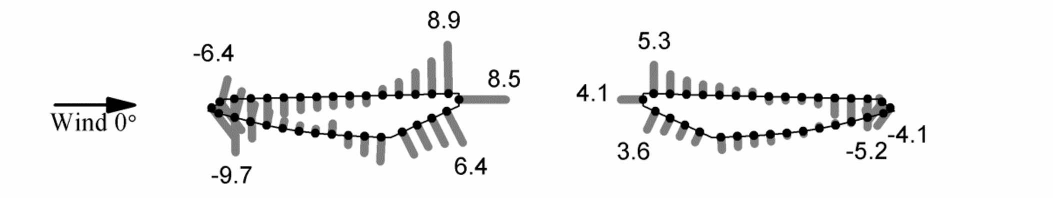

(d) Multi-scale model, quarter-span

Figure 8.9 Mean wind-induced stresses (S-W wind direction, U = 55 m/s) (MPa)

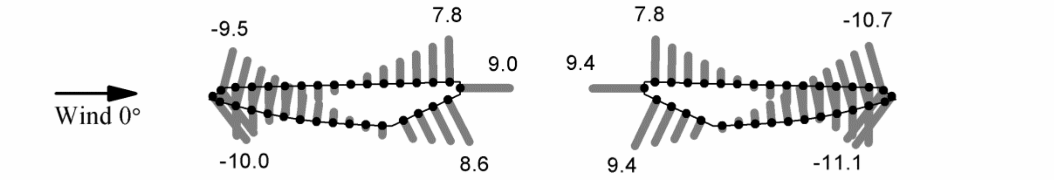

(a) Spine-beam model, mid-span

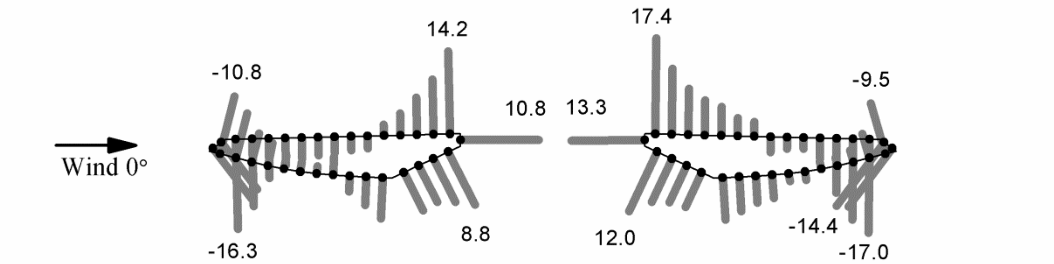

(b) Multi-scale model, mid-span

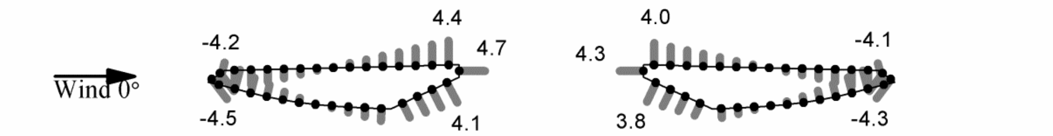

(c) Spine-beam model, quarter-span

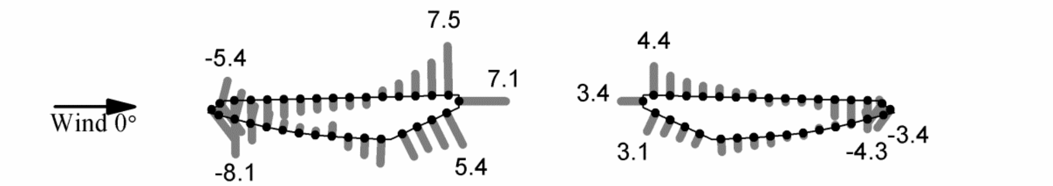

(d) Multi-scale model, quarter-span

Figure 8.10 Mean wind-induced stresses (N-E wind direction, U = 46 m/s) (MPa)

8.6 Comparison of maximum total wind responses

8.6.1 Comparison of maximum total displacement responses

Figure 8.11 and Figure 8.12 compare the maximum total displacement of the multi-scale and spine-beam models. The maximum total buffeting responses are taken as the mean wind response plus the corresponding peak buffeting response (the RMS of the dynamic response multiplied by a peak factor of 3.5).

Figure 8.11 shows the maximum total displacement responses due to the wind from the N-E direction. The maximum total lateral, vertical and torsional displacements of the multi-scale model are all smaller than those of the spine-beam model. This difference may be attributed to the more comprehensive consideration of the correlation of buffeting loads in the proposed framework.

Generally speaking, the displacement responses of the windward box are larger than those of the leeward box in both models due to the larger aerodynamic wind forces acting on the windward box.

Figure 8.12 shows the maximum total displacement responses due to the wind from the S-W direction. The results are smaller than those reported in Figure 8.11 due to smaller turbulence intensity, but the patterns are the same as those noted in Figure 8.11.

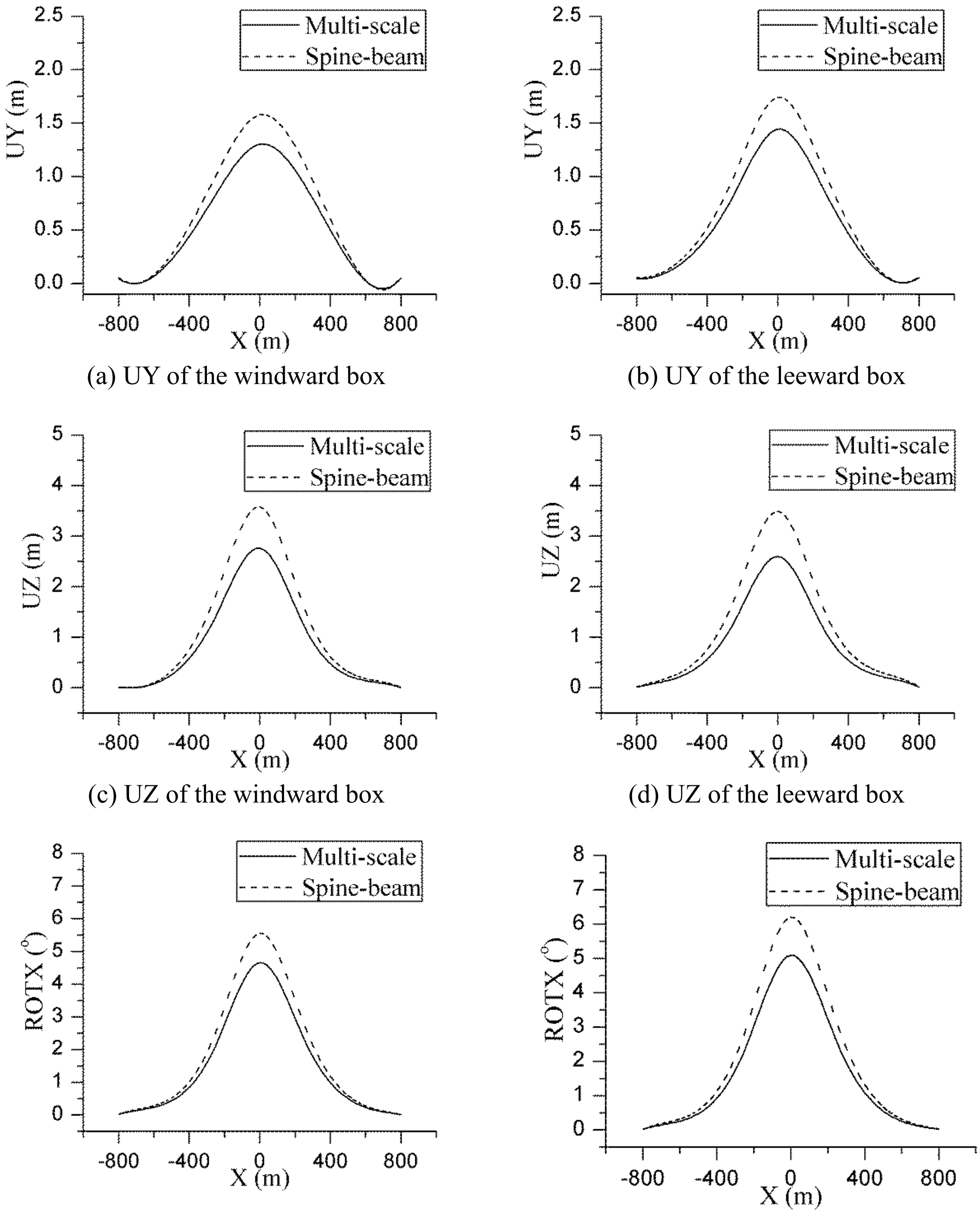

(a) UY of the windward box (b) UY of the leeward box

(c) UZ of the windward box (d) UZ of the leeward box

(e) ROTX of the windward box (f) ROTX of the leeward box

Figure 8.11 Maximum total displacement (N-E wind direction, $U = 46$ m/s)

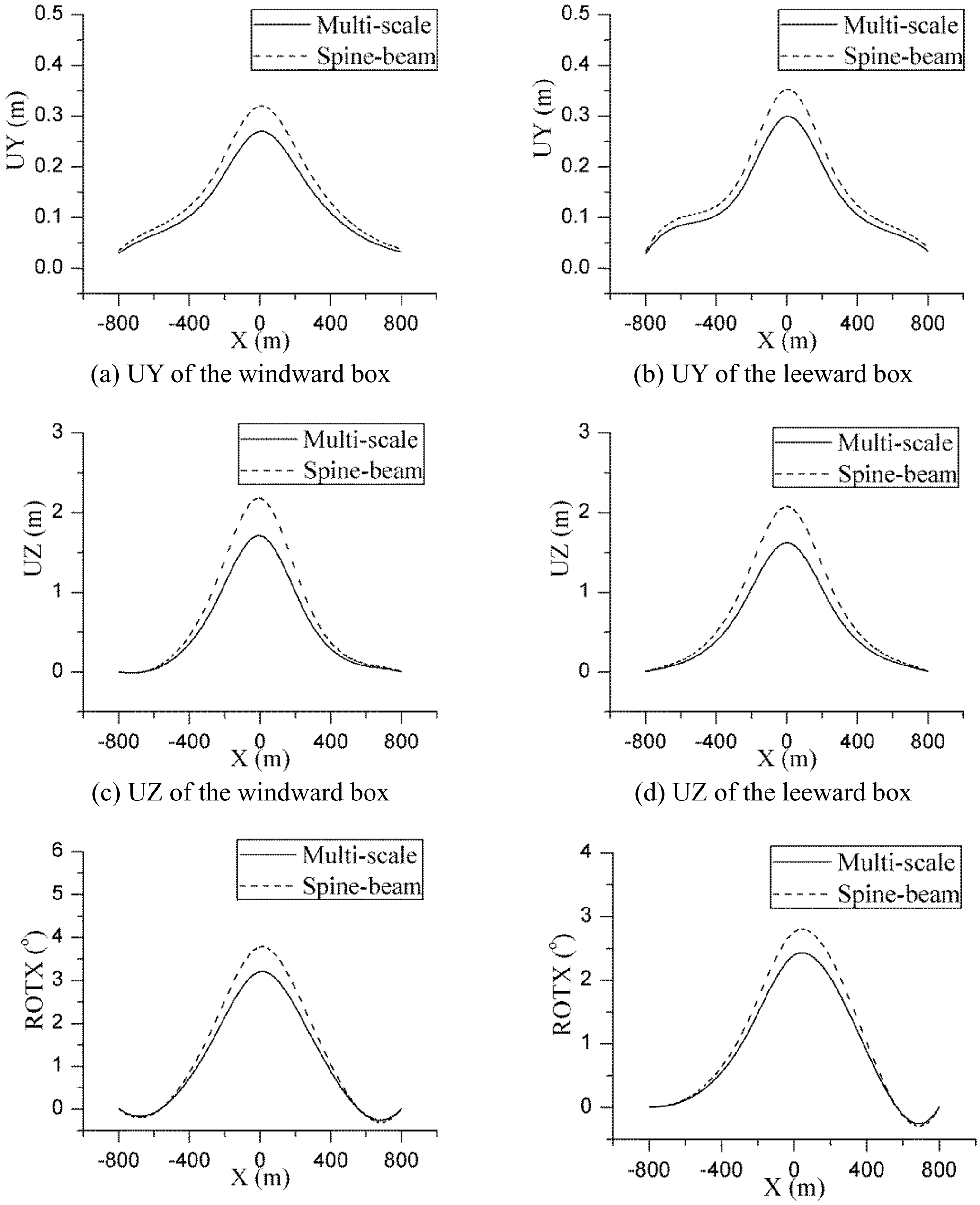

(a) UY of the windward box (b) UY of the leeward box

(c) UZ of the windward box (d) UZ of the leeward box

(e) ROTX of the windward box (f) ROTX of the leeward box

Figure 8.12 Maximum total displacement (S-W wind direction, U = 55 m/s)

8.6.2 Comparison of the maximum total stress responses

Figure 8.13 and Figure 8.14 compare the maximum total stress of the multi-scale and spine-beam models.

Figure 8.13 shows the maximum total stress due to the N-E turbulent wind with a mean speed of 46 m/s. The stresses increase with the distance from the section centroid of each box for both models. The maximum total stresses in the windward box are larger than those in the leeward box.

The dynamic longitudinal stress responses in the quarter-span section are much smaller than those in the mid-span section due to the larger dynamic moments in the mid-span.

The stress responses of the multi-scale model are larger than those of the spine-beam model on the edges of both boxes. This difference is probably due to the stress concentration induced by the longitudinal-and-cross-girder connections on the inner edge, and the cable-deck connections on the outer edge.

Figure 8.14 shows the maximum total stress responses due to the S-W turbulent wind with a mean speed of 55 m/s. The results are much smaller than those in Figure 8.13 due to the smaller turbulence intensity, but the patterns are similar.

Among all of the cases investigated, the largest maximum total stress responses appear on the mid-span section due to the wind from the N-E direction. The largest maximum total stress in the spine-beam model appears at the inner edge of the windward box with a value of 106 MPa. The largest value in the multi-scale model appears at the same location with a value of 131 MPa.

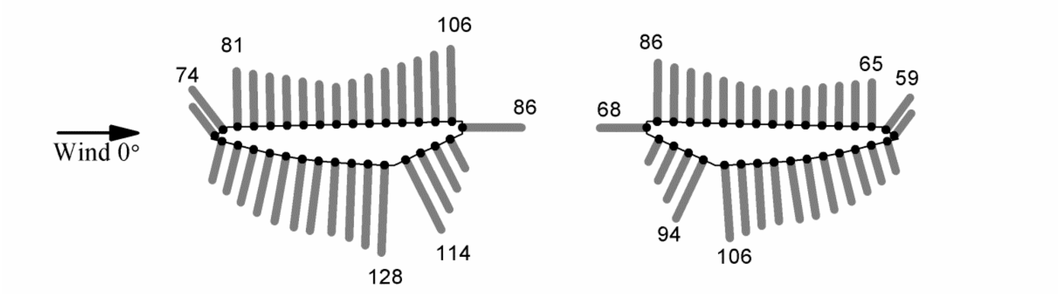

(a) Spine-beam model, mid-span

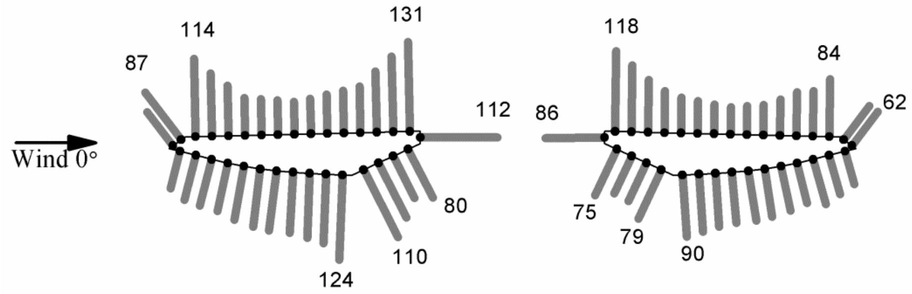

(b) Multi-scale model, mid-span

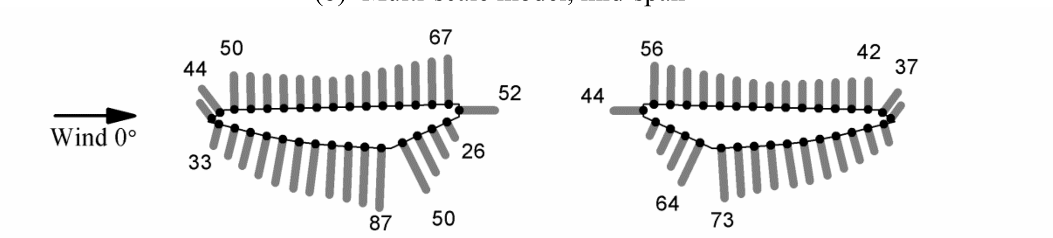

(c) Spine-beam model, quarter-span

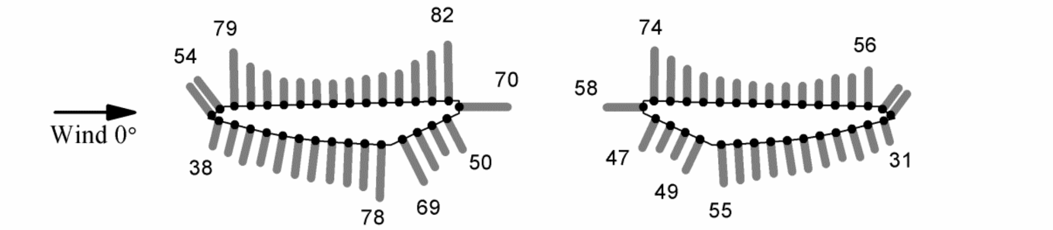

(d) Multi-scale model, quarter-span

Figure 8.13 Maximum total stress (N-E wind direction) (MPa)

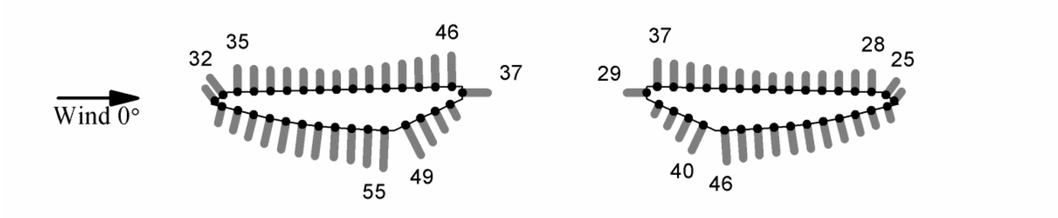

(a) Spine-beam model, mid-span

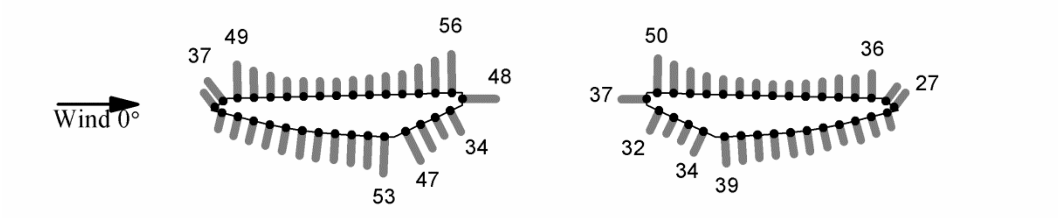

(b) Multi-scale model, mid-span

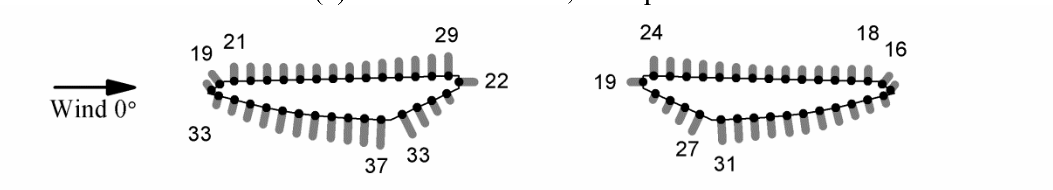

(c) Spine-beam model, quarter-span

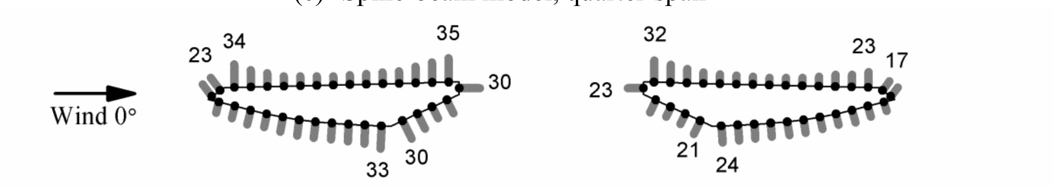

(d) Multi-scale model, quarter-span

Figure 8.14 Maximum total stress (S-W wind direction) (MPa)

8.7 Signature turbulence effects on the dynamic responses

Figure 8.15 shows the incident and signature turbulence induced mid-span displacement STD on the multi-scale model due to the S-W incoming wind at different wind speeds. The results show that, generally speaking, both the incident and signature turbulence induced displacement responses increase with the wind speed. The signature turbulence induced displacement responses are significantly smaller than those induced by the incident turbulence. For high wind speeds, the signature turbulence effects are negligible, but for very low wind speed, such as 5 m/s in this case, the signature turbulence effects may be important.

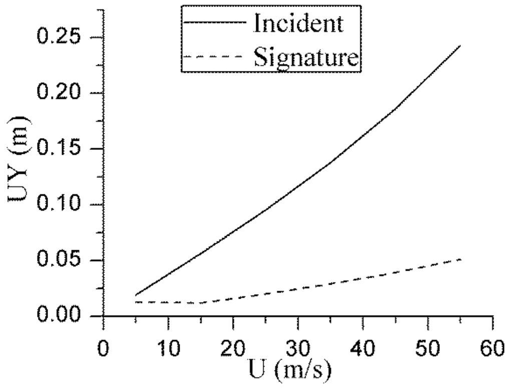

(a) UY

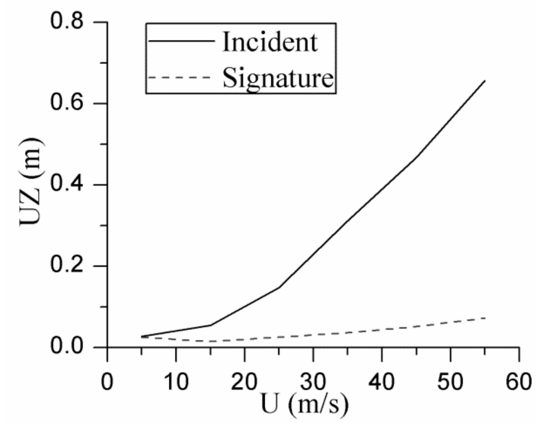

(b) UZ

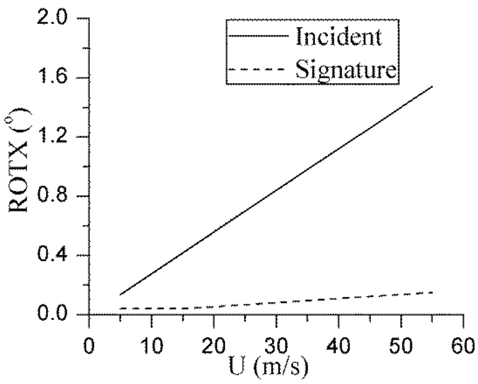

(c) ROTX

Figure 8.15 Signature turbulence effects on the STD of the mid-span displacement response

Figure 8.16 shows the maximum total stress responses in the mid-span section due to the S-W incoming wind at different wind speeds. The maximum stress responses increase with the mean wind speed from 15-55m/s. In this wind speed range, the stress responses on the windward box are larger than those on the leeward box and the stress distribution patterns are similar at all wind speeds. Under a 5 m/s incoming wind, the maximum stress responses are slightly larger than those induced by a 15 m/s incoming wind, because the signature turbulence effects mainly affect the high reduced frequency range; that is, the low wind speed range. Figure 8.16(a) also shows that the signature turbulence effects change the stress distribution pattern, and thus the stress responses on the leeward box are slightly higher than those on the windward box.

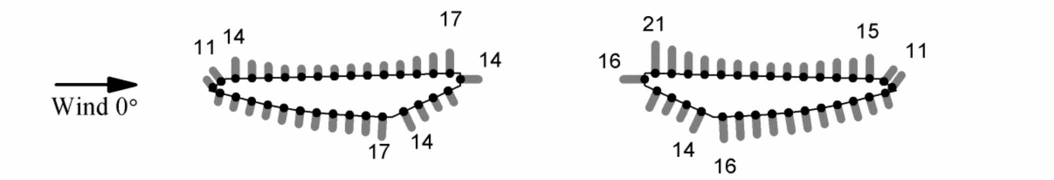

(a) $U = 5$ m/s

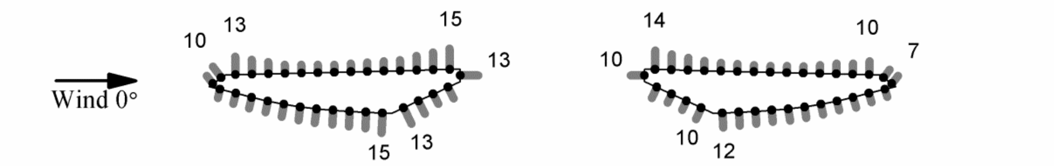

(b) $U = 15$ m/s

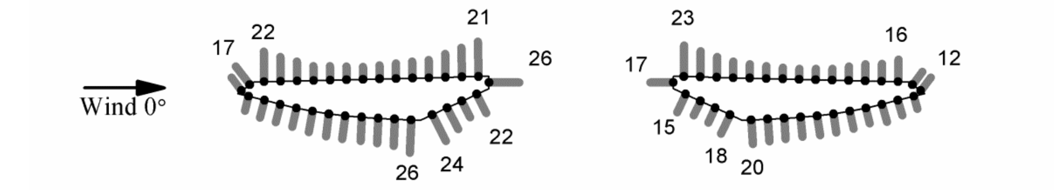

(c) $U = 25$ m/s

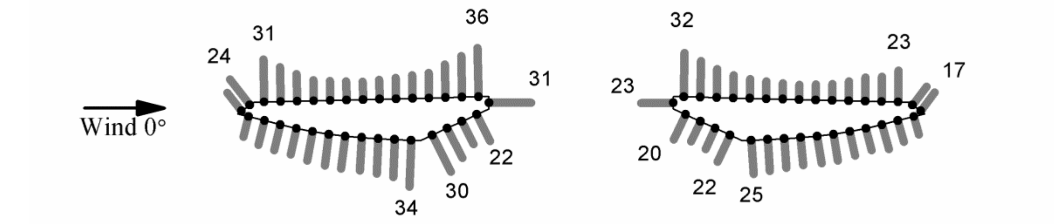

(d) $U = 35$ m/s

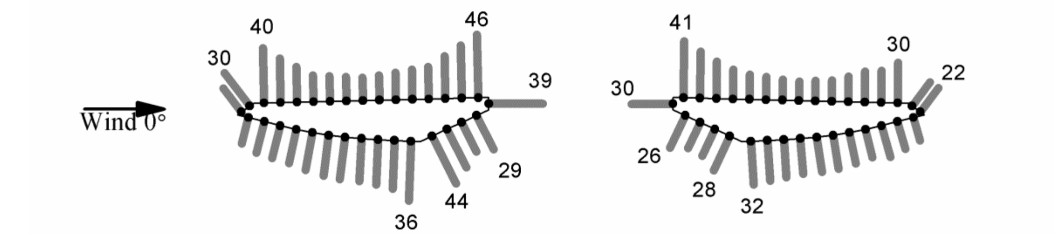

(e) $U = 45$ m/s

Figure 8.16 Maximum total stresses on the mid-span at different wind speeds (S-W wind direction)

8.8 Summary

This chapter compares the responses computed using the proposed buffeting analysis framework, and those computed using a sectional-force-based method on a spine-beam model. The modeling of the spine-beam model of Stonecutters Bridge and the characteristics of the sectional aerodynamic forces are introduced first. Then the wind forces on the windward and leeward boxes of the deck are dealt with separately to enable a better comparison with the pressure-based framework. The mean wind and maximum total buffeting responses are obtained using the spine-beam model. A comparison is made between the results yielded by the two methods in terms of mean wind displacement and stress responses, and maximum total displacement and stress responses.

The mean wind induced lateral and vertical displacements of the multi-scale model are slightly smaller than those of the spine-beam model, probably because the multi-scale model has a slightly higher lateral and vertical stiffness, judging from its modal frequencies. The mean wind-induced torsional displacements of the multi-scale model are slightly larger than those of the spine-beam model. In terms of mean wind induced responses, the displacement responses of the leeward box are larger than those of the windward box because the lift force and the pitching moment on the leeward box are larger.

Regarding the mean wind-induced stress responses of both models, the outer edges of the two boxes bear tensile stresses while the inner edges bear compression stresses. Moreover, the absolute values of the stresses increase with the distance from the section centroid of each box. Generally speaking, the mean wind induced stresses in the leeward box are larger than those in the windward box. The stress responses in the quarter-span section are much smaller than those in the mid-span section due to the larger moments in the mid-span. The mean wind stress responses of the multi-scale model are much larger than those of the spine-beam model on the edges of both boxes. This difference probably results from the stress concentration induced by the longitudinal-and-cross-girder connections on the inner edge, and the cable-deck connections on the outer edge.

The maximum total lateral, vertical and torsional displacements of the multi-scale model are all smaller than those of the spine-beam model. This difference may be attributed to the more comprehensive consideration of the correlation of buffeting loads in the proposed framework. Generally speaking, the displacement responses of the windward box are larger than those of the leeward box due to the larger aerodynamic wind forces acting on the windward box.

The maximum total stresses increase with the distance from the section centroid of each box for both models. The maximum total stresses in the windward box are larger than those in the leeward box. The dynamic stress responses in the quarter-span section are much smaller than those in the mid-span section due to the larger dynamic moments in the mid-span. The stress responses of the multi-scale model are larger than those of the spine-beam model on the edges of both boxes. This difference probably results from the stress concentration induced by the longitudinal-and-cross-girder connections on the inner edge, and the cable-deck connections on the outer edge.

To further investigate the signature turbulence effects on the buffeting responses of the bridge, analyses with different mean wind speeds are conducted.

Generally speaking, both the incident and signature turbulence induced displacement responses increase with the wind speed. The signature turbulence induced displacement responses are significantly smaller than those induced by the incident turbulence. For high wind speeds, the signature turbulence effects are negligible, but for very low wind speed, such as 5 m/s in this case, the signature turbulence effects may be important.

The maximum stress responses increase with the mean wind speed from 15-55m/s. In this wind speed range, the stress responses on the windward box are larger than those on the leeward box and the stress distribution patterns are similar at all wind speeds. Under a 5 m/s incoming wind, when the signature turbulence effects are important, the maximum stress responses are slightly larger than those induced by a 15 m/s incoming wind because the signature turbulence effects mainly affect low wind speed range. In this range, signature turbulence effects not only contribute greatly to the total responses, but also change the stress distribution pattern. Thus, the stress responses on the leeward box are slightly higher than those on the windward box.

CHAPTER 9

CONCLUSIONS AND RECOMMENDATIONS

9.1 Conclusions

This thesis focuses on the frequency-domain buffeting analysis of a long-span twin-box deck bridge with distributed buffeting loads. In particular, this study is devoted to: (1) proposing the formulation of the distributed aerodynamic pressure admittance and identifying the frequency-domain characteristics of the aerodynamic pressure of a twin-box deck from the wind tunnel test; (2) proposing a frequency-domain buffeting-induced stress analysis framework with distributed buffeting loads, including a new method for obtaining distributed aeroelastic forces; (3) establishing the 3D multi-scale FE model of a long-span cable-stayed bridge using the sub-structuring method; (4) updating the multi-scale model with measured modal frequencies and multi-scale influence lines; (5) applying the proposed buffeting analysis framework to the multi-scale model of Stonecutters Bridge to determine dynamic displacement and stress responses; and (6) comparing the results from the proposed framework with those computed using sectional-force-based buffeting analyses on a spine-beam model. The main contributions and conclusions of this study are summarized below.

1. The formulation for the distributed aerodynamic forces (i.e., aerodynamic pressure) on the surfaces of the bridge deck is proposed. The characteristics of the distributed aerodynamic forces, such as pressure admittances and span-wise pressure

coherences, are introduced in the formulation. EMD is then adopted to separate the effects on the distributed aerodynamic forces with consideration of the different characteristics of incident and signature turbulences. Wind tunnel pressure tests are subsequently conducted on the motionless pressure-tapped sectional model of Stonecutters Bridge with a twin-box deck. The cross-sectional distributions of the signature turbulence effects are also investigated. The results show that signature turbulence mainly affects the leeward box. For certain locations, the signature turbulence induced pressures are significantly larger than those induced by the incident turbulence. The span-wise correlation of the aerodynamic pressures is also studied. The span-wise correlation for the incident-turbulence-induced pressure stream-wisely weakens on the windward box, whereas that on the leeward box is generally weaker. The span-wise correlation for the signature-turbulence-induced pressure is negligible for most parts of the deck, except for the windward edge of the leeward box and the leeward edge of the windward box. The cross-sectional and span-wise distributions of the aerodynamic pressures provide more detailed information and deeper insight into the fluid–motionless structure interaction in the twin-box bridge deck. The proposed method is employed to represent the distributed aerodynamic forces using rational equations in the frequency domain for the buffeting analyses.

2. A new framework is developed for the buffeting-induced stress analysis. This framework considers the section-wise distribution of the aerodynamic forces on the bridge deck. Within this framework, the formation of the cross-spectral matrix of distributed aerodynamic forces is given, and the chord-wise correlation of the

aerodynamic forces of the twin-box deck is discussed. A new method for obtaining the distributed aeroelastic stiffness and damping by distributing the measured sectional aeroelastic properties is proposed. Buffeting analysis is conducted on a segment of the shell element model of the twin-box bridge deck using the distributed aerodynamic and aeroelastic forces. The responses computed using the distributed buffeting loads on the shell model differ from those computed using the traditional method on a beam model. The displacement responses computed using the distributed buffeting loads are slightly smaller than those computed using the traditional method probably because the proposed method more comprehensively considers the correlation of buffeting loads. The section-wise distribution of the dynamic stress responses predicted by the proposed method is more concentrated on the edges of both boxes, thus resulting in a large maximum stress response. The different boundary conditions caused by the two different model types also result in significant differences in the computed stress response distribution.

3. A 3D multi-scale FE model of Stonecutters Bridge is established. All superstructure, substructure, connections, and boundary conditions of the bridge are properly modeled. The bridge deck in the FE model is modeled in detail using shell elements. Subsequently, accurate stress analysis is enabled. With the use of the sub-structuring method, each deck segment is condensed into a super element to reduce the computation time for the subsequent dynamic analyses. How the traditional dynamic-property-based updating affects the accuracy of the multi-scale responses of the bridge is likewise investigated. The established FE model is updated with the use of only the measured modal frequencies. Validation using the measured

frequency data shows that the established model is generally consistent with the real bridge in terms of dynamic properties. The computed displacement and stress influence lines are compared with the site data acquired from the load tests. The established multi-scale model is capable of providing both global and local responses. However, the computed displacement and stress responses under vertical load are inaccurate when the update is performed using only modal frequencies. Model updating using only modal frequencies fails to improve the accuracy of the simulated displacement and stress responses. This result indicates a need for multi-scale updating techniques that consider both the dynamic properties and the local responses of the multi-scale model.

4. A new model updating method for the multi-scale FE model of a long-span bridge is proposed. The objective functions of the proposed method include both modal frequencies and multi-scale influence lines. The relationships between the displacement influence lines and the mode shapes, as well as that between the strain influence lines and the strain mode shape, are discussed. The response surface model of a long-span bridge is established to simplify the optimization problem involved in model updating. The proposed method is applied as a case study to the multi-scale model of Stonecutters Bridge. The differences between the measured and the computed modal frequencies, as well as those between the measured and computed multi-scale influence lines, are reduced when the proposed model updating method is used. Comparing the additional measured modal frequencies and influence lines with the corresponding computed results further confirms the quality of the proposed method. Furthermore, the proposed method effectively improves the accuracy of the

simulated displacement and stress responses as opposed to the traditional model updating method that uses only modal frequencies. The proposed method is preferable for model updating multi-scale models of long-span bridges because static responses are as important as the dynamic characteristics for long-span bridges. Moreover, accurate stress responses are a crucial objective of multi-scale models.

5. The details of the technique for applying the proposed buffeting analysis framework on the substructure-based multi-scale model of Stonecutters Bridge are introduced. The wind characteristics and the aerodynamic/aeroelastic properties of the bridge components are presented. Buffeting analyses on Stonecutters Bridge are performed with the distributed loads by employing these data and parameters. The mean wind responses and the total buffeting responses at the critical locations are computed. The mean wind from the S–W direction induces mean displacements and stress responses that are larger than the mean wind from the N–E direction because of the high mean wind speed. Among the three given initial angles of attack, the −3° initial angle of incidence results in the largest vertical mean displacements of the bridge deck. Among the three given initial angles of attack, the +3° initial angle of incidence results in the largest absolute torsional displacements of the bridge deck. The absolute values of the mean wind-induced stresses increase with the distance from the section centroid of each box. The mean wind-induced stresses in the leeward box are larger than those in the windward box. The largest mean wind longitudinal stress response appears on the mid-span section because of the wind from the S–W direction. The maximum absolute stress appears at the inner edge of the leeward box. The dynamic wind from the N–E direction induces larger total

buffeting displacement and stress responses of the bridge than the dynamic wind from the S–W direction because of the high turbulence intensity. Among the three given angles of attack, the −3° initial angle of incidence results in the largest lateral and vertical buffeting responses. The total buffeting-induced longitudinal stresses increase with the distance from the section centroid of each box. The maximum total stresses in the windward box are larger than those in the leeward box. The largest maximum total stress responses appear on the mid-span section because of the wind from N–E direction. The largest value appears at the inner edge of the windward box.

6. The responses computed using the proposed buffeting analysis framework and those computed using the sectional-force-based method on a spine-beam model are compared. The spine-beam modeling of Stonecutters Bridge and the characteristics of the sectional aerodynamic forces are discussed. The mean wind-induced lateral and vertical displacements of the multi-scale model are slightly smaller than those of the spine-beam model. The difference may have resulted from the multi-scale model with slightly higher lateral and vertical stiffness. The mean wind-induced torsional displacements of the multi-scale model are slightly larger than those of the spine-beam model. The mean wind stress responses of the multi-scale model are significantly larger than those of the spine-beam model on the edges of both boxes. This difference probably results from the stress concentration induced by the longitudinal-and-cross-girder connections on the inner edge and the cable-deck connections on the outer edge. The maximum total lateral, vertical, and torsional displacements of the multi-scale model are smaller than those of the spine-beam model. This difference may be attributed to the more comprehensive consideration of

the correlation of buffeting loads by the proposed framework. The stress responses of the multi-scale model are larger than those of the spine-beam model on the edges of both boxes. This difference probably results from the stress concentration induced by the longitudinal-and-cross-girder connections on the inner edge and the cable-deck connections on the outer edge. To investigate further the signature turbulence effects on the buffeting responses of the bridge, analyses with different mean wind speed are conducted. Both the incident- and signature-turbulence-induced responses increase with wind speed. The signature-turbulence-induced displacement responses are significantly smaller than those induced by the incident turbulence. For high wind speeds, the signature turbulence effects are negligible. However, the signature turbulence effects may be important for very low wind speeds (e.g., 5 m/s in this study). Under 5 m/s incoming wind, signature turbulence effects not only contribute significantly to the total responses, but also change the stress distribution pattern. Accordingly, the stress responses on the leeward box are slightly higher than those on the windward box.

9.2 Recommendations for future studies

Although progress has been made in this thesis for the development and application of frequency-domain buffeting analyses of long-span bridges with distributed buffeting loads, several important issues require further studies.

1. The proposed method for obtaining the distributed aeroelastic stiffness and damping by distributing the measured sectional aeroelastic properties is purely based

on the quasi-static assumption and has not been validated with test data. In future studies, wind tunnel pressure tests on oscillating models should be conducted to validate or modify the proposed distribution method. The formulation of the distributed aeroelastic stiffness and damping suggest an identification method for these properties. The direct identification of these properties shall also be investigated in future studies.

2. The aeroelastic effects of the signature turbulence have not been fully considered in the analyses. Therefore, the signature turbulence effects on the responses may be underestimated. The aeroelastic effects of signature turbulence may relate to the vortex-shedding-induced "lock-in" phenomenon, which is not considered in the common buffeting analysis framework. In future studies, the aeroelastic effects of signature turbulences warrant further investigation, especially for long-span bridges with twin-box decks.

3. This study only models the bridge deck in detail with shell elements because of limited computation capacity. Meanwhile, the piers and cables are modeled using line elements. The connections between the deck and the other components are roughly modeled by sharing nodes, which may result in stress concentration at the connections. The connections between each pair of deck segments are modeled by coupling the corresponding DOF of the master nodes, which also causes error in the computed stress responses near the connections. In future studies, a more refined model with detailed modeling of connections should be examined.

4. Only a few updating parameters are chosen in this study because of the limited

site-data availability. Furthermore, these parameters are not really “local.” Consequently, the updated model cannot absolutely ensure the accuracy of local response prediction. The proposed multi-scale updating method still requires some refinement in the near future. Accordingly, the methodology for determining the change bounds of the updating parameters and the weighting factors for different objectives is worth studying.

5. The buffeting analyses in this study are performed on the basis of the substructure-based FE model. The sub-structuring method significantly reduces the number of DOF in the model. However, the method also causes error in the computed dynamic stress responses. A refined local model without condensation is required for the accurate prediction of the maximum stress responses. Moreover, suitable multi-scale connection techniques for incorporating the local model into the global model warrant further study.

APPENDIX A

TABLES OF MEAN WIND RESPONSES

Table A.1 Mean wind displacements UX (m)

Location	Case 1	Case 2	Case 3	Case 4	Case 5	Case 6
D1-windward	-5.769E-03	-5.457E-03	-4.902E-03	-4.504E-03	-4.876E-03	-4.385E-03
D1-leeward	1.723E-03	2.522E-03	2.971E-03	1.678E-03	2.454E-03	2.846E-03
D2-windward	-9.634E-03	-9.339E-03	-9.641E-03	-7.415E-03	-6.766E-03	-6.667E-03
D2-leeward	7.947E-03	7.063E-03	7.887E-03	5.619E-03	5.454E-03	5.868E-03
D3-windward	-2.183E-02	-2.069E-02	-2.081E-02	-1.615E-02	-1.532E-02	-1.464E-02
D3-leeward	2.372E-02	2.007E-02	2.146E-02	1.539E-02	1.479E-02	1.490E-02
D4-windward	-3.456E-04	-3.496E-04	-3.531E-04	-2.618E-04	-2.629E-04	-2.687E-04
D4-leeward	4.240E-04	4.193E-04	4.142E-04	3.093E-04	3.211E-04	3.062E-04
D5-windward	2.114E-02	2.204E-02	2.448E-02	1.692E-02	1.690E-02	1.705E-02
D5-leeward	-2.070E-02	-2.011E-02	-2.432E-02	-1.484E-02	-1.658E-02	-1.484E-02
D6-windward	1.128E-02	1.069E-02	9.637E-03	7.759E-03	7.261E-03	6.405E-03
D6-leeward	-7.916E-03	-8.719E-03	-7.618E-03	-5.224E-03	-5.589E-03	-5.577E-03
D7-windward	6.174E-03	5.398E-03	4.531E-03	4.634E-03	4.532E-03	3.622E-03
D7-leeward	-1.662E-03	-2.565E-03	-3.207E-03	-1.843E-03	-2.358E-03	-2.818E-03
T1	-5.282E-02	-3.289E-02	-2.131E-02	-3.639E-02	-2.303E-02	-1.346E-02
T2	5.143E-02	3.757E-02	1.877E-02	3.221E-02	2.654E-02	1.585E-02

Table A.2 Mean wind displacements UY (m)

Location	Case 1	Case 2	Case 3	Case 4	Case 5	Case 6
D1-windward	-0.000E+0	0.000E+0	0.000E+0	-0.000E+0	-0.000E+0	-1.124E-03
D1-leeward	-0.000E+0	0.000E+0	0.000E+0	-0.000E+0	-0.000E+0	-1.125E-03
D2-windward	4.810E-02	4.730E-02	4.873E-02	-3.794E-02	-3.970E-02	-3.914E-02
D2-leeward	5.064E-02	4.886E-02	4.919E-02	-4.081E-02	-4.040E-02	-3.944E-02
D3-windward	3.715E-01	3.747E-01	3.678E-01	-2.743E-01	-2.648E-01	-2.745E-01
D3-leeward	3.654E-01	3.605E-01	3.793E-01	-2.769E-01	-2.656E-01	-2.745E-01
D4-windward	5.533E-01	5.674E-01	5.471E-01	-4.127E-01	-4.091E-01	-4.105E-01
D4-leeward	5.575E-01	5.618E-01	5.708E-01	-4.014E-01	-3.919E-01	-3.977E-01
D5-windward	3.524E-01	3.471E-01	3.557E-01	-2.578E-01	-2.529E-01	-2.562E-01
D5-leeward	3.466E-01	3.475E-01	3.536E-01	-2.514E-01	-2.488E-01	-2.544E-01
D6-windward	4.855E-02	4.767E-02	4.733E-02	-3.818E-02	-4.004E-02	-4.002E-02
D6-leeward	4.997E-02	4.935E-02	5.000E-02	-4.074E-02	-4.068E-02	-4.055E-02
D7-windward	0.000E+0	1.177E-03	1.141E-03	-0.000E+0	-1.150E-03	-1.167E-03
D7-leeward	1.128E-03	1.153E-03	1.160E-03	-1.149E-03	-1.148E-03	-1.147E-03
T1	7.058E-01	7.230E-01	7.192E-01	-6.207E-01	-6.017E-01	-6.200E-01
T2	7.111E-01	7.170E-01	7.453E-01	-6.152E-01	-6.243E-01	-6.358E-01

Table A.3 Mean wind displacements UZ (m)

Location	Case 1	Case 2	Case 3	Case 4	Case 5	Case 6
D1-windward	-2.296E-03	-1.104E-03	-1.139E-03	-1.094E-03	-1.084E-03	-1.136E-03
D1-leeward	1.203E-03	1.198E-03	9.915E-04	1.024E-03	1.132E-03	1.082E-03
D2-windward	-3.210E-02	-3.730E-02	-4.041E-02	-2.769E-02	-3.284E-02	-3.643E-02
D2-leeward	4.883E-02	5.403E-02	4.730E-02	4.270E-02	4.330E-02	4.341E-02
D3-windward	7.295E-02	2.712E-02	-2.026E-02	4.232E-02	1.017E-02	-2.197E-02
D3-leeward	1.923E-01	1.606E-01	1.139E-01	1.475E-01	1.282E-01	1.001E-01
D4-windward	2.555E-01	1.317E-01	4.039E-02	1.503E-01	8.081E-02	1.789E-02
D4-leeward	3.217E-01	2.628E-01	1.885E-01	2.586E-01	1.960E-01	1.453E-01
D5-windward	6.262E-02	2.172E-02	-2.183E-02	3.567E-02	5.210E-03	-2.717E-02
D5-leeward	1.688E-01	1.347E-01	1.287E-01	1.402E-01	1.037E-01	9.015E-02
D6-windward	-2.969E-02	-3.452E-02	-3.925E-02	-2.785E-02	-3.258E-02	-3.392E-02
D6-leeward	4.838E-02	4.677E-02	5.232E-02	4.002E-02	4.138E-02	3.760E-02
D7-windward	-1.087E-03	-1.137E-03	-1.094E-03	-1.010E-03	-1.091E-03	-1.197E-03
D7-leeward	1.106E-03	1.176E-03	9.979E-04	1.117E-03	1.136E-03	1.132E-03
T1	2.181E-03	1.066E-03	1.029E-03	1.140E-03	1.159E-03	1.095E-03
T2	2.365E-03	1.162E-03	1.149E-03	1.110E-03	1.067E-03	1.131E-03

Table A.4 Mean wind displacements ROTX (^{o})

Location	Case 1	Case 2	Case 3	Case 4	Case 5	Case 6
D1-windward	-2.250E-03	-2.420E-03	-2.421E-03	1.876E-03	1.988E-03	2.007E-03
D1-leeward	-2.111E-03	-2.346E-03	-2.265E-03	1.784E-03	1.984E-03	1.918E-03
D2-windward	-6.219E-02	-6.257E-02	-6.414E-02	5.565E-02	5.726E-02	5.529E-02
D2-leeward	-7.261E-02	-7.102E-02	-7.835E-02	6.093E-02	6.110E-02	6.267E-02
D3-windward	-9.582E-02	-1.122E-01	-1.215E-01	8.651E-02	9.666E-02	1.054E-01
D3-leeward	-9.268E-02	-1.007E-01	-1.211E-01	7.731E-02	9.416E-02	1.014E-01
D4-windward	-7.254E-02	-1.020E-01	-1.312E-01	7.172E-02	8.893E-02	1.043E-01
D4-leeward	-6.501E-02	-9.725E-02	-1.241E-01	6.429E-02	8.864E-02	1.056E-01
D5-windward	-9.271E-02	-1.136E-01	-1.261E-01	8.634E-02	9.378E-02	9.871E-02
D5-leeward	-8.554E-02	-1.047E-01	-1.191E-01	8.089E-02	8.651E-02	9.586E-02
D6-windward	-6.165E-02	-6.411E-02	-6.868E-02	5.350E-02	5.432E-02	5.979E-02
D6-leeward	-7.091E-02	-7.527E-02	-7.820E-02	5.985E-02	6.293E-02	6.576E-02
D7-windward	-1.973E-03	-2.130E-03	-2.148E-03	1.811E-03	1.804E-03	1.919E-03
D7-leeward	-1.806E-03	-1.924E-03	-1.980E-03	1.588E-03	1.735E-03	1.795E-03
T1	-1.728E-01	-1.703E-01	-1.724E-01	1.452E-01	1.537E-01	1.523E-01
T2	-1.764E-01	-1.679E-01	-1.751E-01	1.512E-01	1.474E-01	1.567E-01

Table A.5 Mean wind displacements ROTY (^{o})

Location	Case 1	Case 2	Case 3	Case 4	Case 5	Case 6
D1-windward	2.452E-03	1.770E-03	1.514E-03	1.702E-03	1.537E-03	1.168E-03
D1-leeward	9.445E-04	4.100E-04	-7.651E-05	5.632E-04	1.500E-04	-1.603E-04
D2-windward	-7.105E-03	-4.125E-03	-1.371E-03	-5.105E-03	-2.484E-03	-5.329E-04
D2-leeward	-1.300E-02	-9.537E-03	-6.851E-03	-8.879E-03	-6.511E-03	-4.963E-03
D3-windward	-2.782E-02	-1.860E-02	-9.000E-03	-1.914E-02	-1.193E-02	-6.351E-03
D3-leeward	-2.868E-02	-1.970E-02	-1.245E-02	-1.865E-02	-1.368E-02	-8.032E-03
D4-windward	-1.607E-03	-1.270E-03	-7.835E-04	-1.057E-03	-8.897E-04	-6.822E-04
D4-leeward	-1.436E-03	-1.201E-03	-7.459E-04	-1.038E-03	-7.462E-04	-5.433E-04
D5-windward	2.701E-02	1.773E-02	8.866E-03	1.895E-02	1.252E-02	5.894E-03
D5-leeward	2.532E-02	1.927E-02	1.190E-02	1.969E-02	1.398E-02	8.657E-03
D6-windward	7.758E-03	4.768E-03	1.359E-03	4.789E-03	2.817E-03	5.572E-04
D6-leeward	1.298E-02	9.472E-03	6.423E-03	8.492E-03	6.429E-03	5.152E-03
D7-windward	-2.508E-03	-1.707E-03	-1.288E-03	-1.858E-03	-1.518E-03	-9.659E-04
D7-leeward	-1.094E-03	-3.773E-04	2.288E-04	-6.535E-04	-1.704E-04	3.364E-04
T1	-1.185E-02	-8.351E-03	-4.322E-03	-7.979E-03	-5.921E-03	-3.309E-03
T2	1.207E-02	8.300E-03	5.224E-03	8.106E-03	6.239E-03	3.875E-03

Table A.6 Mean wind displacements ROTZ (^{o})

Location	Case 1	Case 2	Case 3	Case 4	Case 5	Case 6
D1-windward	6.775E-03	7.099E-03	7.084E-03	-5.735E-03	-5.535E-03	-5.780E-03
D1-leeward	6.763E-03	6.605E-03	6.740E-03	-5.454E-03	-5.948E-03	-5.584E-03
D2-windward	1.597E-02	1.579E-02	1.648E-02	-1.251E-02	-1.149E-02	-1.193E-02
D2-leeward	1.603E-02	1.593E-02	1.576E-02	-1.156E-02	-1.128E-02	-1.125E-02
D3-windward	5.041E-02	4.679E-02	4.748E-02	-3.441E-02	-3.558E-02	-3.534E-02
D3-leeward	4.900E-02	4.931E-02	4.802E-02	-3.381E-02	-3.317E-02	-3.589E-02
D4-windward	9.151E-04	8.656E-04	9.979E-04	-6.271E-04	-6.111E-04	-6.147E-04
D4-leeward	9.233E-04	9.289E-04	9.189E-04	-6.110E-04	-6.507E-04	-6.162E-04
D5-windward	-5.337E-02	-4.878E-02	-4.918E-02	3.610E-02	3.597E-02	3.602E-02
D5-leeward	-5.132E-02	-5.244E-02	-4.838E-02	3.719E-02	3.585E-02	3.587E-02
D6-windward	-1.764E-02	-1.726E-02	-1.678E-02	1.248E-02	1.236E-02	1.255E-02
D6-leeward	-1.798E-02	-1.667E-02	-1.583E-02	1.166E-02	1.217E-02	1.219E-02
D7-windward	-7.126E-03	-7.663E-03	-7.736E-03	5.825E-03	6.251E-03	6.304E-03
D7-leeward	-7.218E-03	-7.069E-03	-7.214E-03	6.249E-03	5.951E-03	5.884E-03
T1	-1.594E-03	-1.967E-03	-2.226E-03	1.415E-03	1.631E-03	1.761E-03
T2	1.560E-03	1.965E-03	2.197E-03	-1.365E-03	-1.609E-03	-1.764E-03

Table A.7 Mean wind longitudinal stresses SX (MPa)

Segment	Location	Case 1	Case 2	Case 3	Case 4	Case 5	Case 6
32	D-str1-windward	-7.84E+0	-7.43E+0	-7.18E+0	-1.67E+01	-1.67E+01	-1.71E+01
32	D-str1-leeward	2.38E+01	2.37E+01	2.41E+01	4.02E+0	4.20E+0	4.45E+0
32	D-str2-windward	-1.66E+01	-1.66E+01	-1.69E+01	-1.00E+01	-9.98E+0	-1.01E+01
32	D-str2-leeward	1.38E+01	1.38E+01	1.41E+01	1.17E+01	1.17E+01	1.19E+01
32	D-str3-windward	-2.39E+01	-2.42E+01	-2.49E+01	-4.50E+0	-4.36E+0	-4.30E+0
32	D-str3-leeward	5.48E+0	5.55E+0	5.71E+0	1.82E+01	1.80E+01	1.82E+01
32	D-str4-windward	-9.78E+0	-9.85E+0	-1.01E+01	-1.39E+01	-1.42E+01	-1.47E+01
32	D-str4-leeward	2.19E+01	2.15E+01	2.16E+01	7.44E+0	7.33E+0	7.36E+0
32	D-str5-windward	-1.63E+01	-1.70E+01	-1.80E+01	-7.89E+0	-8.27E+0	-8.79E+0
32	D-str5-leeward	1.47E+01	1.41E+01	1.39E+01	1.46E+01	1.42E+01	1.40E+01
17	D-str1-windward	-1.21E+0	-2.91E-01	5.81E-01	-6.41E+0	-5.45E+0	-4.63E+0
17	D-str1-leeward	3.07E+0	3.56E+0	4.10E+0	-3.09E+0	-2.52E+0	-2.03E+0
17	D-str2-windward	-6.63E+0	-5.38E+0	-4.29E+0	-2.71E+0	-1.95E+0	-1.26E+0
17	D-str2-leeward	-2.00E+0	-1.26E+0	-5.83E-01	4.32E-01	8.69E-01	1.30E+0
17	D-str3-windward	-9.72E+0	-8.28E+0	-7.07E+0	-5.99E-01	4.44E-02	6.58E-01
17	D-str3-leeward	-4.89E+0	-4.02E+0	-3.26E+0	2.45E+0	2.81E+0	3.20E+0
17	D-str4-windward	-2.08E+0	-1.09E+0	-1.69E-01	-6.00E+0	-5.05E+0	-4.23E+0
17	D-str4-leeward	2.32E+0	2.88E+0	3.46E+0	-2.65E+0	-2.08E+0	-1.57E+0
17	D-str5-windward	-6.18E+0	-4.91E+0	-3.78E+0	-3.58E+0	-2.73E+0	-1.97E+0
17	D-str5-leeward	-1.39E+0	-5.89E-01	1.64E-01	-2.43E-01	2.89E-01	8.00E-01

APPENDIX B

TABLES OF BUFFETING RESPONSES

Table B.1 Maximum total buffeting displacements at D1-windward

Cases	UX (m)	UY (m)	UZ (m)	ROTX (^{o})	ROTY (^{o})	ROTZ (^{o})
Case 1	4.883E-02	3.049E-02	6.230E-03	1.164E-02	3.987E-02	3.462E-02
Case 2	4.909E-02	3.049E-02	6.230E-03	1.146E-02	3.997E-02	3.462E-02
Case 3	4.666E-02	2.962E-02	6.230E-03	1.129E-02	3.802E-02	3.455E-02
Case 4	8.366E-02	4.705E-02	1.068E-02	2.361E-02	6.823E-02	3.777E-02
Case 5	8.359E-02	4.617E-02	1.068E-02	2.353E-02	6.814E-02	3.754E-02
Case 6	7.920E-02	4.617E-02	1.068E-02	2.353E-02	6.433E-02	3.731E-02

Table B.2 Minimum total buffeting displacements at D1-windward

Cases	UX (m)	UY (m)	UZ (m)	ROTX (^{o})	ROTY (^{o})	ROTZ (^{o})
Case 1	-5.759E-02	-3.136E-02	-8.815E-03	-1.437E-02	-4.429E-02	-2.440E-02
Case 2	-5.654E-02	-3.136E-02	-8.815E-03	-1.437E-02	-4.334E-02	-2.422E-02
Case 3	-5.313E-02	-3.136E-02	-8.815E-03	-1.437E-02	-4.040E-02	-2.387E-02
Case 4	-8.734E-02	-4.748E-02	-1.234E-02	-1.698E-02	-7.056E-02	-5.533E-02
Case 5	-8.637E-02	-4.659E-02	-1.234E-02	-1.683E-02	-6.961E-02	-5.524E-02
Case 6	-8.148E-02	-4.659E-02	-1.234E-02	-1.676E-02	-6.525E-02	-5.515E-02

Table B.3 Maximum total buffeting displacements at D1-leeward

Cases	UX (m)	UY (m)	UZ (m)	ROTX (^{o})	ROTY (^{o})	ROTZ (^{o})
Case 1	5.429E-02	2.954E-02	9.859E-03	9.274E-03	3.540E-02	4.235E-02
Case 2	5.449E-02	2.954E-02	9.859E-03	9.084E-03	3.557E-02	4.235E-02
Case 3	5.235E-02	2.869E-02	8.962E-03	8.893E-03	3.394E-02	4.226E-02
Case 4	8.526E-02	4.557E-02	1.434E-02	1.817E-02	5.911E-02	4.630E-02
Case 5	8.510E-02	4.473E-02	1.434E-02	1.817E-02	5.895E-02	4.611E-02
Case 6	8.112E-02	4.473E-02	1.434E-02	1.810E-02	5.587E-02	4.573E-02

Table B.4 Minimum total buffeting displacements at D1-leeward

Cases	UX (m)	UY (m)	UZ (m)	ROTX (^{o})	ROTY (^{o})	ROTZ (^{o})
Case 1	-5.122E-02	-3.311E-02	-7.626E-03	-1.227E-02	-4.332E-02	-2.172E-02
Case 2	-4.999E-02	-3.311E-02	-6.779E-03	-1.227E-02	-4.228E-02	-2.157E-02
Case 3	-4.651E-02	-3.311E-02	-6.779E-03	-1.233E-02	-3.925E-02	-2.126E-02
Case 4	-8.227E-02	-5.014E-02	-1.186E-02	-1.487E-02	-7.009E-02	-4.916E-02
Case 5	-8.111E-02	-4.920E-02	-1.186E-02	-1.469E-02	-6.905E-02	-4.909E-02

Table B.5 Maximum total buffeting displacements at D2-windward

Cases	UX (m)	UY (m)	UZ (m)	ROTX (^{o})	ROTY (^{o})	ROTZ (^{o})
Case 1	4.079E-02	8.019E-02	1.445E-01	1.960E-01	9.732E-02	4.802E-02
Case 2	4.079E-02	8.019E-02	1.403E-01	1.929E-01	9.298E-02	4.717E-02
Case 3	3.848E-02	7.932E-02	1.351E-01	1.894E-01	8.472E-02	4.702E-02
Case 4	7.244E-02	2.092E-01	2.420E-01	4.136E-01	1.535E-01	3.517E-02
Case 5	7.208E-02	2.083E-01	2.386E-01	4.138E-01	1.499E-01	3.478E-02
Case 6	6.812E-02	2.083E-01	2.326E-01	4.133E-01	1.392E-01	3.470E-02

Table B.6 Minimum total buffeting displacements at D2-windward

Cases	UX (m)	UY (m)	UZ (m)	ROTX (^{o})	ROTY (^{o})	ROTZ (^{o})
Case 1	-5.791E-02	-1.702E-01	-1.849E-01	-3.601E-01	-1.006E-01	-1.808E-02
Case 2	-5.681E-02	-1.702E-01	-1.874E-01	-3.612E-01	-1.036E-01	-1.799E-02
Case 3	-5.386E-02	-1.702E-01	-1.882E-01	-3.618E-01	-1.010E-01	-1.790E-02
Case 4	-8.297E-02	-1.682E-01	-2.729E-01	-4.137E-01	-1.768E-01	-6.732E-02
Case 5	-8.187E-02	-1.672E-01	-2.745E-01	-4.105E-01	-1.781E-01	-6.633E-02
Case 6	-7.754E-02	-1.663E-01	-2.729E-01	-4.067E-01	-1.702E-01	-6.606E-02

Table B.7 Maximum total buffeting displacements at D2-leeward

Cases	UX (m)	UY (m)	UZ (m)	ROTX (^{o})	ROTY (^{o})	ROTZ (^{o})
Case 1	5.938E-02	9.288E-02	2.080E-01	2.712E-01	8.773E-02	6.715E-02
Case 2	5.921E-02	9.191E-02	2.063E-01	2.671E-01	8.428E-02	6.597E-02
Case 3	5.683E-02	9.094E-02	2.029E-01	2.625E-01	7.733E-02	6.564E-02
Case 4	8.727E-02	2.399E-01	2.952E-01	5.799E-01	1.354E-01	4.999E-02
Case 5	8.693E-02	2.399E-01	2.935E-01	5.800E-01	1.325E-01	4.945E-02
Case 6	8.285E-02	2.390E-01	2.893E-01	5.794E-01	1.233E-01	4.923E-02

Table B.8 Minimum total buffeting displacements at D2-leeward

Cases	UX (m)	UY (m)	UZ (m)	ROTX (^{o})	ROTY (^{o})	ROTZ (^{o})
Case 1	-3.952E-02	-1.587E-01	-1.405E-01	-3.812E-01	-8.624E-02	-1.843E-02
Case 2	-3.896E-02	-1.587E-01	-1.396E-01	-3.821E-01	-8.859E-02	-1.825E-02
Case 3	-3.615E-02	-1.587E-01	-1.378E-01	-3.826E-01	-8.567E-02	-1.816E-02
Case 4	-6.868E-02	-1.570E-01	-2.477E-01	-4.334E-01	-1.568E-01	-6.675E-02
Case 5	-6.809E-02	-1.561E-01	-2.477E-01	-4.301E-01	-1.577E-01	-6.569E-02
Case 6	-6.394E-02	-1.552E-01	-2.441E-01	-4.263E-01	-1.500E-01	-6.542E-02

Table B.9 Maximum total buffeting displacements at D3-windward

Cases	UX (m)	UY (m)	UZ (m)	ROTX (^{o})	ROTY (^{o})	ROTZ (^{o})
Case 1	4.156E-02	1.586E-01	9.102E-01	3.869E-01	4.414E-01	1.862E-01
Case 2	4.122E-02	1.578E-01	8.584E-01	3.723E-01	4.271E-01	1.841E-01
Case 3	3.920E-02	1.578E-01	7.748E-01	3.578E-01	3.940E-01	1.841E-01
Case 4	8.041E-02	8.282E-01	1.426E+0	8.013E-01	7.070E-01	1.434E-01
Case 5	7.979E-02	8.207E-01	1.383E+0	8.079E-01	6.941E-01	1.420E-01
Case 6	7.672E-02	8.248E-01	1.283E+0	8.154E-01	6.480E-01	1.416E-01

Table B.10 Minimum total buffeting displacements at D3-windward

Cases	UX (m)	UY (m)	UZ (m)	ROTX (^{o})	ROTY (^{o})	ROTZ (^{o})
Case 1	-8.007E-02	-7.426E-01	-7.978E-01	-6.150E-01	-3.332E-01	-5.479E-02
Case 2	-7.919E-02	-7.355E-01	-8.273E-01	-6.268E-01	-3.375E-01	-5.425E-02
Case 3	-7.746E-02	-7.390E-01	-8.202E-01	-6.393E-01	-3.239E-01	-5.370E-02
Case 4	-1.054E-01	-4.608E-01	-1.379E+0	-7.277E-01	-5.785E-01	-1.859E-01
Case 5	-1.044E-01	-4.572E-01	-1.393E+0	-7.155E-01	-5.790E-01	-1.841E-01
Case 6	-1.017E-01	-4.590E-01	-1.345E+0	-7.040E-01	-5.496E-01	-1.841E-01

Table B.11 Maximum total buffeting displacements at D3-leeward

Cases	UX (m)	UY (m)	UZ (m)	ROTX (^{o})	ROTY (^{o})	ROTZ (^{o})
Case 1	7.972E-02	1.576E-01	8.570E-01	4.363E-01	4.756E-01	1.812E-01
Case 2	7.896E-02	1.568E-01	8.244E-01	4.180E-01	4.619E-01	1.790E-01
Case 3	7.734E-02	1.568E-01	7.616E-01	3.997E-01	4.271E-01	1.789E-01
Case 4	1.051E-01	8.228E-01	1.288E+0	8.821E-01	7.625E-01	1.393E-01
Case 5	1.042E-01	8.153E-01	1.260E+0	8.905E-01	7.499E-01	1.380E-01
Case 6	1.015E-01	8.195E-01	1.178E+0	8.993E-01	7.002E-01	1.375E-01

Table B.12 Minimum total buffeting displacements at D3-leeward

Cases	UX (m)	UY (m)	UZ (m)	ROTX (^{o})	ROTY (^{o})	ROTZ (^{o})
Case 1	-3.961E-02	-7.913E-01	-5.364E-01	-4.863E-01	-3.189E-01	-5.510E-02
Case 2	-3.925E-02	-7.837E-01	-5.521E-01	-4.973E-01	-3.219E-01	-5.455E-02
Case 3	-3.729E-02	-7.875E-01	-5.340E-01	-5.083E-01	-3.074E-01	-5.400E-02
Case 4	-7.676E-02	-4.910E-01	-1.009E+0	-5.889E-01	-5.541E-01	-1.874E-01
Case 5	-7.619E-02	-4.872E-01	-1.015E+0	-5.778E-01	-5.539E-01	-1.855E-01
Case 6	-7.326E-02	-4.891E-01	-9.666E-01	-5.669E-01	-5.242E-01	-1.854E-01

Table B.13 Maximum total buffeting displacements at D4-windward

Cases	UX (m)	UY (m)	UZ (m)	ROTX (^{o})	ROTY (^{o})	ROTZ (^{o})
Case 1	4.695E-02	2.731E-01	1.820E+0	4.477E-01	6.194E-01	5.318E-02
Case 2	4.642E-02	2.705E-01	1.714E+0	4.206E-01	6.125E-01	5.252E-02
Case 3	4.403E-02	2.687E-01	1.550E+0	3.951E-01	5.753E-01	5.235E-02
Case 4	7.423E-02	1.313E+0	2.856E+0	8.567E-01	1.038E+0	8.135E-02
Case 5	7.350E-02	1.303E+0	2.766E+0	8.664E-01	1.029E+0	8.027E-02
Case 6	6.977E-02	1.311E+0	2.563E+0	8.786E-01	9.682E-01	7.986E-02

Table B.14 Minimum total buffeting displacements at D4-windward

Cases	UX (m)	UY (m)	UZ (m)	ROTX (^{o})	ROTY (^{o})	ROTZ (^{o})
Case 1	-5.504E-02	-1.235E+0	-1.531E+0	-5.397E-01	-6.148E-01	-4.740E-02
Case 2	-5.444E-02	-1.225E+0	-1.584E+0	-5.567E-01	-6.087E-01	-4.671E-02
Case 3	-5.170E-02	-1.230E+0	-1.564E+0	-5.752E-01	-5.723E-01	-4.648E-02
Case 4	-8.632E-02	-7.812E-01	-2.749E+0	-6.980E-01	-1.033E+0	-7.637E-02
Case 5	-8.547E-02	-7.745E-01	-2.770E+0	-6.774E-01	-1.025E+0	-7.538E-02
Case 6	-8.119E-02	-7.774E-01	-2.663E+0	-6.593E-01	-9.646E-01	-7.499E-02

Table B.15 Maximum total buffeting displacements at D4-leeward

Cases	UX (m)	UY (m)	UZ (m)	ROTX (^{o})	ROTY (^{o})	ROTZ (^{o})
Case 1	5.422E-02	3.027E-01	1.702E+0	4.691E-01	5.969E-01	6.205E-02
Case 2	5.382E-02	2.999E-01	1.627E+0	4.395E-01	5.903E-01	6.128E-02
Case 3	5.123E-02	2.979E-01	1.487E+0	4.113E-01	5.543E-01	6.099E-02
Case 4	8.532E-02	1.456E+0	2.661E+0	8.768E-01	9.991E-01	9.487E-02
Case 5	8.480E-02	1.445E+0	2.598E+0	8.870E-01	9.906E-01	9.352E-02
Case 6	8.074E-02	1.453E+0	2.413E+0	8.984E-01	9.314E-01	9.303E-02

Table B.16 Minimum total buffeting displacements at D4-leeward

Cases	UX (m)	UY (m)	UZ (m)	ROTX (^{o})	ROTY (^{o})	ROTZ (^{o})
Case 1	-5.399E-02	-1.109E+0	-1.122E+0	-6.028E-01	-5.689E-01	-6.124E-02
Case 2	-5.358E-02	-1.098E+0	-1.156E+0	-6.227E-01	-5.633E-01	-6.035E-02
Case 3	-5.094E-02	-1.104E+0	-1.119E+0	-6.435E-01	-5.293E-01	-6.006E-02
Case 4	-8.578E-02	-7.012E-01	-2.152E+0	-7.963E-01	-9.546E-01	-9.868E-02
Case 5	-8.526E-02	-6.952E-01	-2.167E+0	-7.716E-01	-9.470E-01	-9.739E-02
Case 6	-8.114E-02	-6.978E-01	-2.058E+0	-7.484E-01	-8.907E-01	-9.690E-02

Table B.17 Maximum total buffeting displacements at D5-windward

Cases	UX (m)	UY (m)	UZ (m)	ROTX (^{o})	ROTY (^{o})	ROTZ (^{o})
Case 1	8.724E-02	1.735E-01	7.834E-01	4.097E-01	3.130E-01	6.231E-02
Case 2	8.625E-02	1.725E-01	7.384E-01	3.957E-01	3.174E-01	6.178E-02
Case 3	8.439E-02	1.725E-01	6.675E-01	3.818E-01	3.049E-01	6.108E-02
Case 4	1.146E-01	9.291E-01	1.228E+0	8.597E-01	5.439E-01	2.127E-01
Case 5	1.135E-01	9.211E-01	1.191E+0	8.668E-01	5.446E-01	2.105E-01
Case 6	1.106E-01	9.251E-01	1.106E+0	8.744E-01	5.172E-01	2.105E-01

Table B.18 Minimum total buffeting displacements at D5-windward

Cases	UX (m)	UY (m)	UZ (m)	ROTX (^{o})	ROTY (^{o})	ROTZ (^{o})
Case 1	-4.053E-02	-7.566E-01	-7.460E-01	-5.309E-01	-4.492E-01	-1.674E-01
Case 2	-4.023E-02	-7.488E-01	-7.743E-01	-5.407E-01	-4.344E-01	-1.655E-01
Case 3	-3.831E-02	-7.517E-01	-7.679E-01	-5.510E-01	-4.004E-01	-1.655E-01
Case 4	-7.894E-02	-4.615E-01	-1.284E+0	-6.294E-01	-7.190E-01	-1.287E-01
Case 5	-7.836E-02	-4.567E-01	-1.297E+0	-6.202E-01	-7.058E-01	-1.277E-01
Case 6	-7.541E-02	-4.596E-01	-1.254E+0	-6.111E-01	-6.586E-01	-1.272E-01

Table B.19 Maximum total buffeting displacements at D5-leeward

Cases	UX (m)	UY (m)	UZ (m)	ROTX (^{o})	ROTY (^{o})	ROTZ (^{o})
Case 1	3.297E-02	5.710E-01	6.300E-01	4.375E-01	2.767E-01	1.300E-01
Case 2	4.362E-02	1.688E-01	8.172E-01	3.757E-01	3.229E-01	6.408E-02
Case 3	4.323E-02	1.678E-01	7.868E-01	3.612E-01	3.263E-01	6.354E-02
Case 4	8.474E-02	9.037E-01	1.218E+0	7.703E-01	5.625E-01	2.196E-01
Case 5	8.411E-02	8.948E-01	1.192E+0	7.777E-01	5.625E-01	2.172E-01
Case 6	8.093E-02	8.997E-01	1.117E+0	7.851E-01	5.324E-01	2.172E-01

Table B.20 Minimum total buffeting displacements at D5-leeward

Cases	UX (m)	UY (m)	UZ (m)	ROTX (^{o})	ROTY (^{o})	ROTZ (^{o})
Case 1	-8.664E-02	-6.983E-01	-5.340E-01	-6.178E-01	-3.949E-01	-1.778E-01
Case 2	-8.581E-02	-6.912E-01	-5.495E-01	-6.313E-01	-3.834E-01	-1.757E-01
Case 3	-8.410E-02	-6.948E-01	-5.323E-01	-6.448E-01	-3.543E-01	-1.755E-01
Case 4	-1.141E-01	-4.265E-01	-1.001E+0	-7.489E-01	-6.314E-01	-1.364E-01
Case 5	-1.131E-01	-4.220E-01	-1.008E+0	-7.364E-01	-6.208E-01	-1.353E-01
Case 6	-1.103E-01	-4.247E-01	-9.605E-01	-7.238E-01	-5.796E-01	-1.348E-01

Table B.21 Maximum total buffeting displacements at D6-windward

Cases	UX (m)	UY (m)	UZ (m)	ROTX (^{o})	ROTY (^{o})	ROTZ (^{o})
Case 1	5.845E-02	7.825E-02	1.393E-01	2.209E-01	8.950E-02	2.274E-02
Case 2	5.733E-02	7.742E-02	1.352E-01	2.178E-01	9.221E-02	2.263E-02
Case 3	5.438E-02	7.659E-02	1.303E-01	2.143E-01	8.986E-02	2.242E-02
Case 4	8.345E-02	2.040E-01	2.345E-01	4.681E-01	1.576E-01	8.466E-02
Case 5	8.232E-02	2.031E-01	2.321E-01	4.686E-01	1.588E-01	8.335E-02
Case 6	7.800E-02	2.031E-01	2.264E-01	4.685E-01	1.518E-01	8.313E-02

Table B.22 Minimum total buffeting displacements at D6-windward

Cases	UX (m)	UY (m)	UZ (m)	ROTX (^{o})	ROTY (^{o})	ROTZ (^{o})
Case 1	-4.586E-02	-1.615E-01	-1.845E-01	-3.873E-01	-1.113E-01	-6.475E-02
Case 2	-4.587E-02	-1.615E-01	-1.870E-01	-3.887E-01	-1.063E-01	-6.364E-02
Case 3	-4.328E-02	-1.615E-01	-1.878E-01	-3.897E-01	-9.682E-02	-6.334E-02
Case 4	-8.182E-02	-1.615E-01	-2.748E-01	-4.505E-01	-1.756E-01	-4.730E-02
Case 5	-8.142E-02	-1.615E-01	-2.764E-01	-4.474E-01	-1.715E-01	-4.680E-02
Case 6	-7.695E-02	-1.606E-01	-2.748E-01	-4.438E-01	-1.592E-01	-4.670E-02
Case 7	-4.586E-02	-1.615E-01	-1.845E-01	-3.873E-01	-1.113E-01	-6.475E-02

Table B.23 Maximum total buffeting displacements at D6-leeward

Cases	UX (m)	UY (m)	UZ (m)	ROTX (^{o})	ROTY (^{o})	ROTZ (^{o})
Case 1	3.295E-02	1.195E-01	1.665E-01	2.968E-01	5.844E-02	3.576E-02
Case 2	4.399E-02	8.221E-02	2.202E-01	2.558E-01	6.859E-02	1.668E-02
Case 3	4.337E-02	8.221E-02	2.185E-01	2.523E-01	7.048E-02	1.653E-02
Case 4	7.672E-02	2.144E-01	3.145E-01	5.494E-01	1.247E-01	6.047E-02
Case 5	7.604E-02	2.144E-01	3.136E-01	5.498E-01	1.255E-01	5.954E-02
Case 6	7.144E-02	2.144E-01	3.092E-01	5.497E-01	1.194E-01	5.931E-02

Table B.24 Minimum total buffeting displacements at D6-leeward

Cases	UX (m)	UY (m)	UZ (m)	ROTX (^{o})	ROTY (^{o})	ROTZ (^{o})
Case 1	-6.125E-02	-1.583E-01	-1.253E-01	-4.137E-01	-1.199E-01	-5.964E-02
Case 2	-6.108E-02	-1.583E-01	-1.245E-01	-4.152E-01	-1.151E-01	-5.862E-02
Case 3	-5.866E-02	-1.583E-01	-1.237E-01	-4.161E-01	-1.057E-01	-5.834E-02
Case 4	-8.976E-02	-1.583E-01	-2.220E-01	-4.763E-01	-1.850E-01	-4.427E-02
Case 5	-8.940E-02	-1.574E-01	-2.220E-01	-4.732E-01	-1.811E-01	-4.380E-02
Case 6	-8.524E-02	-1.566E-01	-2.188E-01	-4.694E-01	-1.685E-01	-4.362E-02

Table B.25 Maximum total buffeting displacements at D7-windward

Cases	UX (m)	UY (m)	UZ (m)	ROTX (^{o})	ROTY (^{o})	ROTZ (^{o})
Case 1	4.550E-02	2.483E-02	3.708E-03	9.879E-03	3.599E-02	2.616E-02
Case 2	6.086E-02	3.254E-02	4.635E-03	9.147E-03	4.710E-02	2.031E-02
Case 3	5.967E-02	3.254E-02	4.635E-03	9.074E-03	4.601E-02	2.016E-02
Case 4	9.228E-02	5.138E-02	8.344E-03	1.866E-02	7.517E-02	4.789E-02
Case 5	9.118E-02	5.052E-02	8.344E-03	1.866E-02	7.416E-02	4.789E-02
Case 6	8.589E-02	5.052E-02	8.344E-03	1.859E-02	6.943E-02	4.782E-02

Table B.26 Minimum total buffeting displacements at D7-windward

Cases	UX (m)	UY (m)	UZ (m)	ROTX (^{o})	ROTY (^{o})	ROTZ (^{o})
Case 1	-3.830E-02	-2.704E-02	-4.713E-03	-6.472E-03	-2.918E-02	-1.827E-02
Case 2	-4.912E-02	-3.766E-02	-6.283E-03	-1.280E-02	-3.606E-02	-4.254E-02
Case 3	-4.942E-02	-3.766E-02	-5.498E-03	-1.280E-02	-3.622E-02	-4.245E-02
Case 4	-8.406E-02	-5.698E-02	-8.640E-03	-1.534E-02	-6.168E-02	-4.573E-02
Case 5	-8.399E-02	-5.601E-02	-8.640E-03	-1.527E-02	-6.160E-02	-4.554E-02
Case 6	-7.950E-02	-5.601E-02	-8.640E-03	-1.513E-02	-5.820E-02	-4.536E-02

Table B.27 Maximum total buffeting displacements at D7-leeward

Cases	UX (m)	UY (m)	UZ (m)	ROTX (^{o})	ROTY (^{o})	ROTZ (^{o})
Case 1	5.269E-02	3.527E-02	8.753E-03	8.899E-03	3.572E-02	2.948E-02
Case 2	5.142E-02	3.437E-02	8.753E-03	8.704E-03	3.476E-02	2.926E-02
Case 3	4.777E-02	3.437E-02	8.753E-03	8.509E-03	3.222E-02	2.905E-02
Case 4	8.500E-02	5.517E-02	1.353E-02	1.721E-02	5.784E-02	6.918E-02
Case 5	8.380E-02	5.517E-02	1.353E-02	1.721E-02	5.695E-02	6.918E-02

Table B.28 Minimum total buffeting displacements at D7-leeward

Cases	UX (m)	UY (m)	UZ (m)	ROTX (^{o})	ROTY (^{o})	ROTZ (^{o})
Case 1	-4.649E-02	-2.799E-02	-5.550E-03	-8.076E-03	-3.820E-02	-1.869E-02
Case 2	-5.912E-02	-3.998E-02	-7.135E-03	-1.523E-02	-4.684E-02	-4.325E-02
Case 3	-5.939E-02	-3.998E-02	-7.135E-03	-1.531E-02	-4.713E-02	-4.325E-02
Case 4	-9.313E-02	-5.998E-02	-1.189E-02	-1.901E-02	-7.849E-02	-4.667E-02
Case 5	-9.298E-02	-5.898E-02	-1.189E-02	-1.884E-02	-7.839E-02	-4.648E-02
Case 6	-8.864E-02	-5.898E-02	-1.189E-02	-1.851E-02	-7.430E-02	-4.629E-02

Table B.29 Maximum total buffeting displacements at T1

Cases	UX (m)	UY (m)	UZ (m)	ROTX (^{o})	ROTY (^{o})	ROTZ (^{o})
Case 1	2.964E-01	2.199E+0	8.928E-03	5.742E-01	1.314E-01	1.120E-02
Case 2	2.978E-01	1.780E+0	1.071E-02	4.732E-01	1.608E-01	8.860E-03
Case 3	3.077E-01	1.762E+0	9.821E-03	4.684E-01	1.557E-01	8.351E-03
Case 4	5.519E-01	4.037E+0	1.696E-02	1.057E+0	2.583E-01	1.864E-02
Case 5	5.560E-01	4.030E+0	1.607E-02	1.055E+0	2.536E-01	1.894E-02
Case 6	5.307E-01	4.019E+0	1.518E-02	1.052E+0	2.368E-01	1.925E-02

Table B.30 Minimum total buffeting displacements at T1

Cases	UX (m)	UY (m)	UZ (m)	ROTX (^{o})	ROTY (^{o})	ROTZ (^{o})
Case 1	-3.392E-01	-1.372E+0	-7.867E-03	-3.602E-01	-1.455E-01	-6.529E-03
Case 2	-4.138E-01	-3.141E+0	-6.993E-03	-8.109E-01	-1.630E-01	-1.306E-02
Case 3	-3.924E-01	-3.137E+0	-7.867E-03	-8.096E-01	-1.643E-01	-1.347E-02
Case 4	-6.490E-01	-3.409E+0	-1.399E-02	-8.902E-01	-2.828E-01	-1.544E-02
Case 5	-6.310E-01	-3.391E+0	-1.399E-02	-8.852E-01	-2.825E-01	-1.513E-02
Case 6	-5.844E-01	-3.366E+0	-1.399E-02	-8.787E-01	-2.676E-01	-1.472E-02

Table B.31 Maximum total buffeting displacements at T2

Cases	UX (m)	UY (m)	UZ (m)	ROTX (^{o})	ROTY (^{o})	ROTZ (^{o})
Case 1	3.172E-01	2.498E+0	8.991E-03	7.475E-01	1.523E-01	6.111E-03
Case 2	3.866E-01	2.013E+0	1.079E-02	6.135E-01	1.704E-01	1.203E-02
Case 3	3.666E-01	1.997E+0	9.891E-03	6.083E-01	1.718E-01	1.242E-02
Case 4	6.059E-01	4.592E+0	1.708E-02	1.378E+0	2.964E-01	1.435E-02
Case 5	5.892E-01	4.587E+0	1.618E-02	1.377E+0	2.960E-01	1.397E-02
Case 6	5.456E-01	4.578E+0	1.529E-02	1.373E+0	2.805E-01	1.368E-02

Table B.32 Minimum total buffeting displacements at T2

Cases	UX (m)	UY (m)	UZ (m)	ROTX (^{o})	ROTY (^{o})	ROTZ (^{o})
Case 1	-3.269E-01	-1.334E+0	-6.977E-03	-4.378E-01	-1.682E-01	-9.447E-03
Case 2	-3.279E-01	-3.008E+0	-6.202E-03	-9.712E-01	-2.057E-01	-7.453E-03
Case 3	-3.389E-01	-3.007E+0	-6.977E-03	-9.705E-01	-1.991E-01	-7.020E-03
Case 4	-6.089E-01	-3.303E+0	-1.240E-02	-1.078E+0	-3.301E-01	-1.569E-02
Case 5	-6.134E-01	-3.289E+0	-1.240E-02	-1.074E+0	-3.241E-01	-1.595E-02
Case 6	-5.855E-01	-3.269E+0	-1.240E-02	-1.067E+0	-3.026E-01	-1.621E-02

Table B. 33 Maximum longitudinal stresses SX (MPa)

Seg ment	Location	Case 1	Case 2	Case 3	Case 4	Case 5	Case 6
32	D-str1-w indward	6.80E+01	5.97E+01	7.21E+01	1.06E+02	1.05E+02	9.62E+01
32	D-str1-le eward	4.44E+01	5.91E+01	8.01E+01	8.82E+01	1.31E+02	1.28E+02
32	D-str2-w indward	4.86E+01	3.43E+01	3.17E+01	6.44E+01	6.36E+01	5.77E+01
32	D-str2-le eward	2.67E+01	3.46E+01	4.47E+01	5.74E+01	8.50E+01	8.31E+01
32	D-str3-w indward	3.23E+01	1.31E+01	-2.07E+0	2.93E+01	2.88E+01	2.57E+01
32	D-str3-le eward	1.19E+01	1.42E+01	1.51E+01	3.17E+01	4.64E+01	4.59E+01
32	D-str4-w indward	4.00E+01	3.19E+01	3.20E+01	4.79E+01	4.76E+01	4.82E+01
32	D-str4-le eward	1.68E+01	3.18E+01	6.94E+01	7.92E+01	7.23E+01	7.21E+01
32	D-str5-w indward	5.52E+0	-5.85E+0	-2.45E+01	-2.51E+01	-2.47E+01	-1.38E+01
32	D-str5-le eward	-1.64E+01	-4.99E+0	4.06E+01	5.44E+01	-3.49E+0	4.13E-02
17	D-str1-w indward	4.30E+01	5.97E+01	5.96E+01	9.31E+01	9.26E+01	8.27E+01
17	D-str1-le eward	4.45E+01	5.91E+01	4.01E+01	5.76E+01	8.86E+01	8.49E+01
17	D-str2-w indward	2.87E+01	3.00E+01	3.07E+01	5.83E+01	5.83E+01	5.20E+01
17	D-str2-le eward	2.96E+01	3.05E+01	2.01E+01	3.71E+01	5.54E+01	5.28E+01
17	D-str3-w indward	2.06E+01	1.31E+01	1.42E+01	3.85E+01	3.88E+01	3.45E+01
17	D-str3-le eward	2.11E+01	1.42E+01	8.70E+0	2.54E+01	3.65E+01	3.44E+01
17	D-str4-w indward	3.21E+01	4.41E+01	4.42E+01	6.91E+01	6.88E+01	6.42E+01
17	D-str4-le eward	3.35E+01	4.38E+01	3.74E+01	5.48E+01	6.52E+01	6.28E+01
17	D-str5-w indward	4.26E+0	-1.61E-01	6.66E-01	5.96E+0	6.27E+0	1.37E+01
17	D-str5-le eward	4.73E+0	5.33E-01	2.32E+01	4.02E+01	3.98E+0	4.47E+0

Table B. 34 Minimum longitudinal stresses SX (MPa)

Segment	Location	Case 1	Case 2	Case 3	Case 4	Case 5	Case 6
32	D-str1-windward	-8.37E+01	-7.46E+01	-8.65E+01	-1.39E+02	-1.38E+02	-1.30E+02
32	D-str1-leeward	3.20E+0	-1.17E+01	-3.19E+01	-8.02E+01	-1.23E+02	-1.19E+02
32	D-str2-windward	-8.18E+01	-6.75E+01	-6.55E+01	-8.44E+01	-8.36E+01	-7.79E+01
32	D-str2-leeward	9.00E-01	-7.00E+0	-1.65E+01	-3.40E+01	-6.16E+01	-5.93E+01
32	D-str3-windward	-8.01E+01	-6.15E+01	-4.77E+01	-3.83E+01	-3.75E+01	-3.43E+01
32	D-str3-leeward	-9.40E-01	-3.10E+0	-3.68E+0	4.70E+0	-1.04E+01	-9.50E+0
32	D-str4-windward	-5.96E+01	-5.16E+01	-5.22E+01	-7.57E+01	-7.60E+01	-7.76E+01
32	D-str4-leeward	2.70E+01	1.12E+01	-2.62E+01	-6.43E+01	-5.76E+01	-5.74E+01
32	D-str5-windward	-3.81E+01	-2.82E+01	-1.15E+01	9.32E+0	8.16E+0	-3.78E+0
32	D-str5-leeward	4.58E+01	3.32E+01	-1.28E+01	-2.52E+01	3.19E+01	2.80E+01
17	D-str1-windward	-4.54E+01	-6.03E+01	-5.84E+01	-1.06E+02	-1.04E+02	-9.20E+01
17	D-str1-leeward	-3.84E+01	-5.20E+01	-3.19E+01	-6.38E+01	-9.36E+01	-8.90E+01
17	D-str2-windward	-4.20E+01	-4.08E+01	-3.93E+01	-6.37E+01	-6.22E+01	-5.45E+01
17	D-str2--leeward	-3.36E+01	-3.30E+01	-2.13E+01	-3.62E+01	-5.37E+01	-5.02E+01
17	D-str3-windward	-4.00E+01	-2.97E+01	-2.83E+01	-3.97E+01	-3.87E+01	-3.32E+01
17	D-str3-leeward	-3.09E+01	-2.22E+01	-1.52E+01	-2.05E+01	-3.09E+01	-2.80E+01
17	D-str4-windward	-3.63E+01	-4.63E+01	-4.45E+01	-8.11E+01	-7.89E+01	-7.27E+01
17	D-str4-leeward	-2.89E+01	-3.80E+01	-3.05E+01	-6.01E+01	-6.94E+01	-6.59E+01
17	D-str5-windward	-1.66E+01	-9.66E+0	-8.23E+0	-1.31E+01	-1.17E+01	-1.76E+01
17	D-str5-leeward	-7.51E+0	-1.71E+0	-2.29E+01	-4.07E+01	-3.40E+0	-2.87E+0

APPENDIX C

TABLES OF BUFFETING FORCES OF TOWERS AND PIERS: MEAN WIND REPONSES

Table C.1 Mean wind forces of the towers and piers FX (kN)

Location	Case 1	Case 2	Case 3	Case 4	Case 5	Case 6
4WP1N	3.083E+01	-1.449E+01	-5.031E+01	5.100E+0	-2.472E+01	-5.550E+01
4WP2N	2.773E+01	-1.233E+01	-5.344E+01	7.249E+0	-2.584E+01	-5.118E+01
4EP1N	-2.463E+01	2.248E+01	5.820E+01	-2.025E+0	2.920E+01	6.112E+01
4EP2N	-2.588E+01	1.872E+01	6.421E+01	-3.584E+0	3.015E+01	5.402E+01
4WP1S	2.361E+02	2.072E+02	1.801E+02	2.027E+02	1.545E+02	1.216E+02
4WP2S	2.206E+02	1.925E+02	1.467E+02	1.910E+02	1.501E+02	1.355E+02
4EP1S	-2.252E+02	-2.111E+02	-1.819E+02	-1.825E+02	-1.494E+02	-1.382E+02
4EP2S	-2.406E+02	-1.824E+02	-1.477E+02	-1.910E+02	-1.433E+02	-1.390E+02
WT1I	-3.949E+02	-4.552E+02	-4.354E+02	-3.612E+02	-3.656E+02	-3.498E+02
WT1U	-6.143E+01	-6.218E+01	-6.186E+01	-5.091E+01	-5.540E+01	-4.957E+01
WT2I	-1.840E+03	-2.038E+03	-2.006E+03	-1.751E+03	-1.826E+03	-1.622E+03
WT2U	-1.808E+02	-1.850E+02	-1.923E+02	-1.523E+02	-1.609E+02	-1.578E+02
WT3	-2.226E+03	-2.136E+03	-2.422E+03	-1.870E+03	-1.756E+03	-1.865E+03
WT4	-6.449E+03	-6.468E+03	-6.520E+03	-4.857E+03	-5.058E+03	-5.138E+03
WT5	-5.695E+02	-4.282E+02	-2.336E+02	-4.427E+02	-3.168E+02	-1.605E+02
ET1I	-4.711E+02	-4.329E+02	-4.049E+02	-3.954E+02	-4.091E+02	-3.520E+02
ET1U	-5.736E+01	-5.730E+01	-5.603E+01	-5.480E+01	-4.916E+01	-5.462E+01
ET2I	-2.056E+03	-1.852E+03	-1.816E+03	-1.724E+03	-1.693E+03	-1.867E+03
ET2U	-1.604E+02	-1.730E+02	-1.651E+02	-1.524E+02	-1.619E+02	-1.528E+02
ET3	-2.079E+03	-2.075E+03	-2.304E+03	-1.751E+03	-2.044E+03	-1.866E+03
ET4	-5.790E+03	-6.655E+03	-6.867E+03	-4.930E+03	-4.438E+03	-4.572E+03
ET5	6.234E+02	4.608E+02	2.432E+02	4.614E+02	2.774E+02	1.635E+02

Table C.2 Mean wind forces of towers and piers FY (kN)

Location	Case 1	Case 2	Case 3	Case 4	Case 5	Case 6
4WP1N	1.656E+02	1.223E+02	1.012E+02	-9.750E+01	-7.799E+01	-6.728E+01
4WP2N	1.650E+02	1.361E+02	1.022E+02	-1.097E+02	-7.825E+01	-6.999E+01
4EP1N	1.063E+02	7.445E+01	4.327E+01	-6.374E+01	-3.750E+01	-2.267E+01
4EP2N	9.496E+01	7.440E+01	4.788E+01	-5.826E+01	-3.737E+01	-2.076E+01
4WP1S	2.292E+02	2.215E+02	2.258E+02	-1.571E+02	-1.363E+02	-1.401E+02
4WP2S	3.229E+01	5.854E+0	-1.285E+01	-3.230E+01	-1.287E+01	-1.338E+0
4EP1S	1.943E+02	1.873E+02	1.563E+02	-1.246E+02	-9.782E+01	-8.445E+01
4EP2S	-2.422E+01	-5.476E+01	-7.167E+01	1.161E+01	3.160E+01	4.250E+01
WT1I	-4.375E+01	-2.808E+01	-1.444E+01	2.778E+01	2.023E+01	1.038E+01
WT1U	-5.390E+0	-3.616E+0	-2.387E+0	3.733E+0	2.749E+0	1.503E+0
WT2I	5.394E+02	3.606E+02	2.038E+02	-3.474E+02	-2.364E+02	-1.299E+02
WT2U	4.958E+01	2.886E+01	1.744E+01	-3.298E+01	-2.318E+01	-1.376E+01
WT3	5.703E+02	3.775E+02	2.445E+02	-4.151E+02	-2.459E+02	-1.427E+02
WT4	6.339E+02	4.192E+02	2.519E+02	-4.247E+02	-2.556E+02	-1.632E+02
WT5	-2.225E+04	-2.211E+04	-2.203E+04	1.391E+04	1.405E+04	1.642E+04
ET1I	2.157E+01	1.004E+01	-1.393E+0	-1.234E+01	-3.487E+0	3.671E+0
ET1U	3.174E+0	1.360E+0	-1.724E-01	-1.686E+0	-5.389E-01	5.037E-01
ET2I	-5.116E+02	-3.626E+02	-2.074E+02	3.418E+02	2.274E+02	1.464E+02
ET2U	-4.118E+01	-3.059E+01	-1.670E+01	2.884E+01	1.925E+01	1.332E+01
ET3	-5.480E+02	-4.151E+02	-2.169E+02	4.047E+02	2.627E+02	1.647E+02
ET4	-6.104E+02	-4.478E+02	-2.290E+02	3.949E+02	2.586E+02	1.550E+02
ET5	-2.048E+04	-2.178E+04	-2.131E+04	1.458E+04	1.422E+04	1.464E+04

Table C.3 Mean wind forces of towers and piers FZ (kN)

Location	Case 1	Case 2	Case 3	Case 4	Case 5	Case 6
4WP1N	-1.419E+03	-1.751E+03	-1.902E+03	-1.366E+03	-1.491E+03	-1.819E+03
4WP2N	-1.531E+03	-1.815E+03	-2.022E+03	-1.362E+03	-1.488E+03	-1.873E+03
4EP1N	-1.131E+03	-1.367E+03	-1.588E+03	-1.174E+03	-1.253E+03	-1.505E+03
4EP2N	-1.014E+03	-1.465E+03	-1.571E+03	-1.060E+03	-1.206E+03	-1.353E+03
4WP1S	2.355E+03	2.544E+03	2.460E+03	2.045E+03	1.984E+03	2.198E+03
4WP2S	2.193E+03	2.300E+03	2.419E+03	2.258E+03	1.892E+03	2.148E+03
4EP1S	2.120E+03	2.121E+03	2.117E+03	1.646E+03	1.933E+03	1.701E+03
4EP2S	2.090E+03	2.301E+03	2.146E+03	1.983E+03	1.649E+03	1.792E+03
WT1I	-5.263E+02	-3.332E+02	-1.771E+02	-3.137E+02	-2.505E+02	-1.493E+02
WT1U	-7.259E+01	-4.550E+01	-2.695E+01	-4.934E+01	-3.225E+01	-2.027E+01
WT2I	-1.399E+04	-9.893E+03	-5.637E+03	-9.926E+03	-6.113E+03	-4.229E+03
WT2U	-1.405E+03	-8.724E+02	-5.013E+02	-9.379E+02	-6.046E+02	-3.629E+02
WT3	-1.422E+04	-1.110E+04	-6.489E+03	-1.037E+04	-7.693E+03	-4.303E+03
WT4	-1.499E+04	-1.038E+04	-6.664E+03	-1.092E+04	-7.779E+03	-4.381E+03
WT5	-1.664E+04	-1.054E+04	-5.949E+03	-1.133E+04	-7.411E+03	-4.128E+03
ET1I	-4.985E+02	-3.238E+02	-1.847E+02	-2.881E+02	-2.231E+02	-1.268E+02
ET1U	-6.847E+01	-4.869E+01	-2.337E+01	-4.172E+01	-3.312E+01	-1.725E+01
ET2I	-1.433E+04	-9.310E+03	-6.059E+03	-1.066E+04	-6.107E+03	-4.062E+03
ET2U	-1.260E+03	-9.560E+02	-4.891E+02	-9.314E+02	-5.981E+02	-3.524E+02
ET3	-1.664E+04	-1.104E+04	-6.313E+03	-1.007E+04	-6.661E+03	-4.001E+03
ET4	-1.415E+04	-1.149E+04	-6.037E+03	-1.043E+04	-6.880E+03	-4.291E+03
ET5	-1.601E+04	-9.551E+03	-6.584E+03	-9.833E+03	-7.648E+03	-4.194E+03

Table C.4 Mean wind forces of towers and piers MX (kN-m)

Location	Case 1	Case 2	Case 3	Case 4	Case 5	Case 6
4WP1N	5.150E+03	3.876E+03	3.240E+03	-3.495E+03	-2.825E+03	-2.348E+03
4WP2N	-4.820E+03	-3.594E+03	-2.880E+03	3.157E+03	2.096E+03	1.687E+03
4EP1N	3.321E+03	2.422E+03	1.722E+03	-2.322E+03	-1.457E+03	-1.062E+03
4EP2N	-3.058E+03	-1.902E+03	-9.564E+02	1.553E+03	7.460E+02	1.481E+02
4WP1S	5.729E+03	5.006E+03	4.480E+03	-3.391E+03	-3.371E+03	-2.635E+03
4WP2S	-2.662E+03	-1.633E+03	-8.868E+02	1.565E+03	1.003E+03	5.511E+02
4EP1S	3.733E+03	3.438E+03	2.605E+03	-2.428E+03	-1.820E+03	-1.505E+03
4EP2S	-8.541E+02	2.302E+02	9.159E+02	3.184E+02	-4.182E+02	-8.906E+02
WT1I	-3.318E+02	-2.448E+02	-1.229E+02	2.471E+02	1.550E+02	8.527E+01
WT1U	-6.886E+01	-4.515E+01	-2.518E+01	4.026E+01	2.964E+01	1.668E+01
WT2I	1.475E+04	9.198E+03	6.342E+03	-1.059E+04	-7.590E+03	-3.948E+03
WT2U	1.832E+03	1.190E+03	7.360E+02	-1.257E+03	-8.477E+02	-4.876E+02
WT3	2.553E+04	1.722E+04	1.009E+04	-1.612E+04	-1.168E+04	-6.645E+03
WT4	8.972E+04	6.336E+04	4.053E+04	-7.002E+04	-4.321E+04	-2.441E+04
WT5	-2.253E+06	-2.049E+06	-2.091E+06	1.820E+06	1.663E+06	1.844E+06
ET1I	3.144E+02	1.954E+02	1.208E+02	-2.107E+02	-1.337E+02	-8.019E+01
ET1U	5.323E+01	4.025E+01	1.847E+01	-4.250E+01	-2.340E+01	-1.433E+01
ET2I	-1.529E+04	-9.606E+03	-6.594E+03	1.117E+04	7.554E+03	4.508E+03
ET2U	-1.918E+03	-1.389E+03	-7.367E+02	1.308E+03	8.842E+02	5.714E+02
ET3	-2.481E+04	-1.610E+04	-1.081E+04	1.905E+04	1.199E+04	7.452E+03
ET4	-9.905E+04	-6.627E+04	-3.423E+04	6.498E+04	4.395E+04	2.661E+04
ET5	-2.357E+06	-2.260E+06	-2.404E+06	1.813E+06	1.661E+06	1.729E+06

Table C.5 Mean wind forces of towers and piers MY (kN-m)

Location	Case 1	Case 2	Case 3	Case 4	Case 5	Case 6
4WP1N	-1.076E+03	1.570E+02	1.462E+03	-4.093E+02	5.382E+02	1.287E+03
4WP2N	6.230E+02	-6.103E+02	-1.697E+03	2.119E+01	-8.632E+02	-1.691E+03
4EP1N	9.841E+02	-3.791E+02	-1.630E+03	3.283E+02	-6.129E+02	-1.644E+03
4EP2N	-6.017E+02	7.292E+02	1.998E+03	7.537E+01	1.039E+03	1.921E+03
4WP1S	-7.642E+03	-5.358E+03	-4.994E+03	-5.192E+03	-4.863E+03	-3.889E+03
4WP2S	7.654E+03	5.856E+03	5.220E+03	5.792E+03	4.473E+03	4.389E+03
4EP1S	7.667E+03	6.022E+03	4.506E+03	6.060E+03	4.523E+03	4.078E+03
4EP2S	-7.273E+03	-6.999E+03	-5.046E+03	-5.338E+03	-5.168E+03	-4.137E+03
WT1I	1.879E+03	1.935E+03	1.726E+03	1.703E+03	1.524E+03	1.838E+03
WT1U	3.879E+02	3.525E+02	3.800E+02	3.244E+02	3.604E+02	3.062E+02
WT2I	2.164E+05	2.146E+05	2.304E+05	1.886E+05	2.088E+05	1.826E+05
WT2U	2.927E+04	2.896E+04	2.564E+04	2.257E+04	2.424E+04	2.329E+04
WT3	2.656E+05	3.183E+05	2.777E+05	2.701E+05	2.436E+05	2.676E+05
WT4	7.275E+05	7.897E+05	7.780E+05	7.196E+05	6.641E+05	6.778E+05
WT5	1.392E+05	9.125E+04	6.158E+04	9.039E+04	6.691E+04	4.277E+04
ET1I	1.704E+03	1.720E+03	1.900E+03	1.783E+03	1.860E+03	1.711E+03
ET1U	3.856E+02	3.950E+02	3.365E+02	3.130E+02	3.577E+02	3.303E+02
ET2I	2.247E+05	2.292E+05	2.082E+05	2.167E+05	2.180E+05	2.035E+05
ET2U	2.700E+04	2.967E+04	2.931E+04	2.527E+04	2.497E+04	2.541E+04
ET3	3.103E+05	2.698E+05	2.975E+05	2.543E+05	2.564E+05	2.391E+05
ET4	8.114E+05	7.839E+05	7.659E+05	6.870E+05	7.245E+05	7.164E+05
ET5	-1.471E+05	-9.201E+04	-6.037E+04	-9.657E+04	-6.653E+04	-3.686E+04

Table C.6 Mean wind forces of towers and piers MZ (kN-m)

Location	Case 1	Case 2	Case 3	Case 4	Case 5	Case 6
4WP1N	-2.078E+03	-2.485E+03	-2.539E+03	1.847E+03	2.006E+03	1.784E+03
4WP2N	-2.245E+03	-2.485E+03	-2.530E+03	1.750E+03	1.979E+03	1.987E+03
4EP1N	2.292E+03	2.515E+03	2.659E+03	-1.887E+03	-2.135E+03	-1.861E+03
4EP2N	2.220E+03	2.387E+03	2.614E+03	-1.908E+03	-1.991E+03	-2.093E+03
4WP1S	-2.465E+03	-2.448E+03	-2.171E+03	1.961E+03	1.946E+03	2.051E+03
4WP2S	-2.228E+03	-2.261E+03	-2.257E+03	1.870E+03	1.768E+03	1.836E+03
4EP1S	2.663E+03	2.660E+03	2.339E+03	-2.099E+03	-1.856E+03	-2.038E+03
4EP2S	2.566E+03	2.231E+03	2.245E+03	-1.922E+03	-2.231E+03	-2.088E+03
WT1I	1.503E+02	1.882E+02	2.007E+02	-1.257E+02	-1.469E+02	-1.536E+02
WT1U	3.108E+01	3.510E+01	3.898E+01	-2.523E+01	-2.814E+01	-3.027E+01
WT2I	1.583E+03	1.904E+03	2.617E+03	-1.309E+03	-1.888E+03	-2.149E+03
WT2U	1.871E+02	2.353E+02	3.079E+02	-1.784E+02	-1.936E+02	-2.360E+02
WT3	1.720E+03	2.135E+03	2.824E+03	-1.658E+03	-1.816E+03	-2.498E+03
WT4	1.599E+03	2.189E+03	2.730E+03	-1.495E+03	-1.868E+03	-2.554E+03
WT5	1.795E+03	2.234E+03	2.860E+03	-1.388E+03	-2.102E+03	-2.502E+03
ET1I	-1.519E+02	-1.815E+02	-2.105E+02	1.382E+02	1.438E+02	1.614E+02
ET1U	-2.816E+01	-2.943E+01	-3.789E+01	2.567E+01	2.526E+01	2.772E+01
ET2I	-1.600E+03	-2.011E+03	-2.540E+03	1.465E+03	1.574E+03	2.149E+03
ET2U	-1.901E+02	-2.273E+02	-3.140E+02	1.459E+02	1.981E+02	2.320E+02
ET3	-1.629E+03	-2.113E+03	-2.883E+03	1.484E+03	1.847E+03	2.503E+03
ET4	-1.609E+03	-2.122E+03	-2.598E+03	1.530E+03	1.760E+03	2.355E+03
ET5	-1.698E+03	-2.074E+03	-2.804E+03	1.555E+03	1.869E+03	2.339E+03

APPENDIX D

TABLES OF BUFFETING FORCES OF TOWERS AND PIERS: TOTAL BUFFETING REPONSES

Table D.1 Maximum buffeting forces of towers and piers, Case 1

Location	FX (kN)	FY (kN)	FZ (kN)	MX (kN-m)	MY (kN-m)	MZ (kN-m)
4WP1N	1.459E+03	2.562E+03	1.195E+04	6.587E+04	4.348E+04	8.641E+03
4WP2N	1.750E+03	2.688E+03	1.196E+04	1.049E+05	5.472E+04	8.649E+03
4EP1N	1.552E+03	2.761E+03	1.154E+04	7.549E+04	4.690E+04	4.711E+03
4EP2N	1.864E+03	2.937E+03	1.155E+04	1.154E+05	5.112E+04	4.719E+03
4WP1S	1.562E+03	2.594E+03	1.415E+04	6.429E+04	4.602E+04	8.656E+03
4WP2S	1.857E+03	2.602E+03	1.417E+04	1.032E+05	4.732E+04	8.664E+03
4EP1S	1.273E+03	2.798E+03	1.308E+04	7.397E+04	3.941E+04	4.736E+03
4EP2S	1.604E+03	2.854E+03	1.309E+04	1.137E+05	5.439E+04	4.744E+03
WT1I	1.687E+03	2.332E+03	2.743E+03	6.186E+03	1.012E+04	2.657E+02
WT1U	2.355E+02	3.263E+02	3.916E+02	1.192E+03	1.934E+03	4.781E+01
WT2I	6.729E+03	4.692E+03	6.187E+04	3.539E+05	5.335E+05	6.560E+03
WT2U	6.058E+02	4.262E+02	5.746E+03	4.215E+04	6.457E+04	7.844E+02
WT3	8.528E+03	5.296E+03	6.764E+04	3.705E+05	7.212E+05	7.354E+03
WT4	5.161E+03	1.002E+04	6.779E+04	6.026E+05	1.953E+06	7.419E+03
WT5	1.168E+04	1.412E+04	6.783E+04	6.959E+06	1.242E+06	7.442E+03
ET1I	1.728E+03	2.339E+03	2.764E+03	5.890E+03	1.032E+04	5.576E+02
ET1U	2.413E+02	3.273E+02	3.946E+02	1.138E+03	1.972E+03	1.003E+02
ET2I	6.900E+03	4.445E+03	6.178E+04	3.644E+05	5.472E+05	1.043E+04
ET2U	6.213E+02	4.041E+02	5.737E+03	4.341E+04	6.622E+04	1.247E+03
ET3	8.733E+03	5.026E+03	6.753E+04	3.873E+05	7.395E+05	1.169E+04
ET4	5.133E+03	9.773E+03	6.768E+04	6.584E+05	2.000E+06	1.177E+04
ET5	1.214E+04	1.420E+04	6.773E+04	7.038E+06	1.325E+06	1.178E+04

Table D.2 Minimum buffeting forces of bridge deck, towers and piers, Case 1

Location	FX (kN)	FY (kN)	FZ (kN)	MX (kN-m)	MY (kN-m)	MZ (kN-m)
4WP1N	-1.477E+03	-2.405E+03	-1.521E+04	-7.372E+04	-4.899E+04	-5.057E+03
4WP2N	-1.748E+03	-2.531E+03	-1.522E+04	-1.059E+05	-5.482E+04	-5.065E+03
4EP1N	-1.353E+03	-2.686E+03	-1.430E+04	-8.110E+04	-4.678E+04	-8.881E+03
4EP2N	-1.652E+03	-2.860E+03	-1.431E+04	-1.200E+05	-5.820E+04	-8.889E+03
4WP1S	-1.230E+03	-2.321E+03	-1.012E+04	-7.322E+04	-4.163E+04	-5.080E+03
4WP2S	-1.513E+03	-2.565E+03	-1.013E+04	-1.063E+05	-5.831E+04	-5.088E+03
4EP1S	-1.448E+03	-2.604E+03	-9.536E+03	-8.070E+04	-4.938E+04	-8.899E+03
4EP2S	-1.754E+03	-2.900E+03	-9.550E+03	-1.206E+05	-4.973E+04	-8.907E+03
WT1I	-2.305E+03	-2.322E+03	-2.982E+03	-6.244E+03	-1.412E+04	-6.030E+02
WT1U	-3.217E+02	-3.249E+02	-4.257E+02	-1.205E+03	-2.719E+03	-1.085E+02
WT2I	-9.664E+03	-4.364E+03	-6.898E+04	-3.780E+05	-9.669E+05	-1.083E+04
WT2U	-8.689E+02	-3.967E+02	-6.406E+03	-4.503E+04	-1.169E+05	-1.295E+03
WT3	-1.178E+04	-4.934E+03	-7.541E+04	-4.015E+05	-1.291E+06	-1.214E+04
WT4	-1.382E+04	-9.582E+03	-7.556E+04	-6.848E+05	-3.419E+06	-1.219E+04
WT5	-1.135E+04	-4.288E+04	-7.560E+04	-3.363E+06	-1.401E+06	-1.223E+04
ET1I	-2.359E+03	-2.316E+03	-2.973E+03	-6.299E+03	-1.436E+04	-2.561E+02
ET1U	-3.292E+02	-3.240E+02	-4.244E+02	-1.215E+03	-2.765E+03	-4.607E+01
ET2I	-9.839E+03	-4.646E+03	-6.886E+04	-3.695E+05	-9.837E+05	-6.688E+03
ET2U	-8.846E+02	-4.221E+02	-6.395E+03	-4.401E+04	-1.190E+05	-7.997E+02
ET3	-1.199E+04	-5.246E+03	-7.527E+04	-3.872E+05	-1.314E+06	-7.497E+03
ET4	-1.372E+04	-9.956E+03	-7.542E+04	-6.292E+05	-3.473E+06	-7.563E+03
ET5	-1.113E+04	-4.291E+04	-7.546E+04	-3.432E+06	-1.332E+06	-7.588E+03

Table D.3 Maximum buffeting forces of towers and piers, Case 2

Location	FX (kN)	FY (kN)	FZ (kN)	MX (kN-m)	MY (kN-m)	MZ (kN-m)
4WP1N	1.794E+03	3.800E+03	1.724E+04	1.027E+05	6.210E+04	7.093E+03
4WP2N	2.191E+03	3.993E+03	1.725E+04	1.424E+05	7.409E+04	7.104E+03
4EP1N	1.699E+03	4.167E+03	1.639E+04	1.112E+05	6.002E+04	1.146E+04
4EP2N	2.132E+03	4.430E+03	1.640E+04	1.585E+05	7.456E+04	1.146E+04
4WP1S	1.878E+03	3.647E+03	1.876E+04	1.018E+05	6.444E+04	7.134E+03
4WP2S	2.284E+03	4.084E+03	1.877E+04	1.436E+05	6.380E+04	7.145E+03
4EP1S	1.368E+03	4.019E+03	1.721E+04	1.104E+05	4.962E+04	1.147E+04
4EP2S	1.827E+03	4.529E+03	1.723E+04	1.599E+05	7.827E+04	1.148E+04
WT1I	2.215E+03	3.294E+03	2.732E+03	8.358E+03	1.534E+04	6.979E+02
WT1U	3.092E+02	4.609E+02	3.900E+02	1.603E+03	2.934E+03	1.256E+02
WT2I	9.021E+03	5.947E+03	6.050E+04	4.760E+05	8.382E+05	1.202E+04
WT2U	8.122E+02	5.408E+02	5.619E+03	5.676E+04	1.014E+05	1.437E+03
WT3	1.138E+04	6.758E+03	6.614E+04	5.113E+05	1.132E+06	1.347E+04
WT4	6.260E+03	1.459E+04	6.633E+04	9.016E+05	3.055E+06	1.352E+04
WT5	1.455E+04	6.562E+04	6.637E+04	4.615E+06	1.696E+06	1.356E+04
ET1I	2.246E+03	3.223E+03	2.763E+03	8.882E+03	1.549E+04	3.453E+02
ET1U	3.136E+02	4.510E+02	3.944E+02	1.700E+03	2.963E+03	6.213E+01
ET2I	9.146E+03	7.088E+03	6.038E+04	4.459E+05	8.492E+05	8.929E+03
ET2U	8.235E+02	6.438E+02	5.608E+03	5.307E+04	1.028E+05	1.068E+03
ET3	1.153E+04	8.013E+03	6.601E+04	4.601E+05	1.147E+06	1.001E+04
ET4	6.179E+03	1.598E+04	6.619E+04	7.049E+05	3.090E+06	1.007E+04
ET5	1.583E+04	6.545E+04	6.624E+04	4.655E+06	1.993E+06	1.010E+04

Table D.4 Minimum buffeting forces of towers and piers, Case 2

Location	FX (kN)	FY (kN)	FZ (kN)	MX (kN-m)	MY (kN-m)	MZ (kN-m)
4WP1N	-2.001E+03	-4.003E+03	-2.025E+04	-9.201E+04	-6.305E+04	-1.165E+04
4WP2N	-2.454E+03	-4.189E+03	-2.027E+04	-1.517E+05	-7.966E+04	-1.166E+04
4EP1N	-2.004E+03	-4.244E+03	-1.877E+04	-1.035E+05	-6.557E+04	-6.743E+03
4EP2N	-2.504E+03	-4.497E+03	-1.878E+04	-1.640E+05	-7.747E+04	-6.754E+03
4WP1S	-1.638E+03	-4.060E+03	-1.419E+04	-8.974E+04	-5.276E+04	-1.167E+04
4WP2S	-2.114E+03	-4.014E+03	-1.421E+04	-1.484E+05	-8.323E+04	-1.168E+04
4EP1S	-2.108E+03	-4.311E+03	-1.320E+04	-1.013E+05	-6.821E+04	-6.787E+03
4EP2S	-2.625E+03	-4.329E+03	-1.322E+04	-1.608E+05	-6.599E+04	-6.797E+03
WT1I	-3.452E+03	-3.098E+03	-3.715E+03	-9.026E+03	-2.019E+04	-3.767E+02
WT1U	-4.818E+02	-4.335E+02	-5.303E+02	-1.728E+03	-3.885E+03	-6.778E+01
WT2I	-1.443E+04	-6.823E+03	-8.906E+04	-4.427E+05	-1.361E+06	-9.153E+03
WT2U	-1.297E+03	-6.197E+02	-8.271E+03	-5.269E+04	-1.646E+05	-1.094E+03
WT3	-1.765E+04	-7.713E+03	-9.736E+04	-4.564E+05	-1.820E+06	-1.026E+04
WT4	-2.087E+04	-1.535E+04	-9.755E+04	-6.997E+05	-4.853E+06	-1.032E+04
WT5	-1.803E+04	-2.022E+04	-9.759E+04	-9.361E+06	-2.089E+06	-1.035E+04
ET1I	-3.509E+03	-3.160E+03	-3.709E+03	-8.170E+03	-2.038E+04	-6.657E+02
ET1U	-4.898E+02	-4.422E+02	-5.294E+02	-1.569E+03	-3.924E+03	-1.198E+02
ET2I	-1.459E+04	-5.784E+03	-8.890E+04	-4.755E+05	-1.376E+06	-1.195E+04
ET2U	-1.312E+03	-5.260E+02	-8.256E+03	-5.670E+04	-1.664E+05	-1.429E+03
ET3	-1.783E+04	-6.573E+03	-9.718E+04	-5.110E+05	-1.839E+06	-1.339E+04
ET4	-2.067E+04	-1.419E+04	-9.736E+04	-8.981E+05	-4.896E+06	-1.347E+04
ET5	-1.689E+04	-2.014E+04	-9.741E+04	-9.416E+06	-1.803E+06	-1.348E+04

Table D.5 Maximum buffeting forces of towers and piers, Case 3

Location	FX (kN)	FY (kN)	FZ (kN)	MX (kN-m)	MY (kN-m)	MZ (kN-m)
4WP1N	1.790E+03	3.538E+03	1.845E+04	9.829E+04	5.726E+04	7.549E+03
4WP2N	2.198E+03	3.718E+03	1.847E+04	1.385E+05	7.116E+04	7.560E+03
4EP1N	1.778E+03	3.879E+03	1.752E+04	1.063E+05	5.791E+04	1.229E+04
4EP2N	2.222E+03	4.123E+03	1.754E+04	1.541E+05	6.904E+04	1.230E+04
4WP1S	1.883E+03	3.394E+03	2.056E+04	9.765E+04	5.967E+04	7.587E+03
4WP2S	2.301E+03	3.801E+03	2.058E+04	1.396E+05	6.141E+04	7.598E+03
4EP1S	1.437E+03	3.739E+03	1.887E+04	1.059E+05	4.804E+04	1.231E+04
4EP2S	1.908E+03	4.213E+03	1.889E+04	1.554E+05	7.273E+04	1.232E+04
WT1I	2.273E+03	3.024E+03	3.112E+03	8.175E+03	1.452E+04	7.675E+02
WT1U	3.173E+02	4.232E+02	4.442E+02	1.567E+03	2.777E+03	1.381E+02
WT2I	9.208E+03	5.635E+03	7.002E+04	4.538E+05	7.905E+05	1.339E+04
WT2U	8.290E+02	5.123E+02	6.503E+03	5.409E+04	9.568E+04	1.601E+03
WT3	1.163E+04	6.398E+03	7.655E+04	4.847E+05	1.068E+06	1.501E+04
WT4	6.449E+03	1.366E+04	7.675E+04	8.386E+05	2.881E+06	1.506E+04
WT5	1.509E+04	6.095E+04	7.680E+04	4.463E+06	1.642E+06	1.510E+04
ET1I	2.308E+03	2.984E+03	3.145E+03	8.469E+03	1.468E+04	3.485E+02
ET1U	3.223E+02	4.175E+02	4.489E+02	1.621E+03	2.808E+03	6.271E+01
ET2I	9.349E+03	6.374E+03	6.989E+04	4.338E+05	8.022E+05	9.016E+03
ET2U	8.417E+02	5.790E+02	6.491E+03	5.165E+04	9.708E+04	1.078E+03
ET3	1.179E+04	7.212E+03	7.641E+04	4.506E+05	1.083E+06	1.010E+04
ET4	6.372E+03	1.458E+04	7.660E+04	7.069E+05	2.919E+06	1.017E+04
ET5	1.604E+04	6.082E+04	7.666E+04	4.508E+06	1.842E+06	1.020E+04

Table D.6 Minimum buffeting forces of towers and piers, Case 3

Location	FX (kN)	FY (kN)	FZ (kN)	MX (kN-m)	MY (kN-m)	MZ (kN-m)
4WP1N	-2.053E+03	-3.754E+03	-2.065E+04	-8.323E+04	-5.396E+04	-1.105E+04
4WP2N	-2.509E+03	-3.931E+03	-2.066E+04	-1.351E+05	-6.557E+04	-1.106E+04
4EP1N	-1.959E+03	-3.979E+03	-1.916E+04	-9.356E+04	-5.362E+04	-6.364E+03
4EP2N	-2.465E+03	-4.220E+03	-1.918E+04	-1.460E+05	-6.615E+04	-6.374E+03
4WP1S	-1.687E+03	-3.817E+03	-1.437E+04	-8.111E+04	-4.529E+04	-1.107E+04
4WP2S	-2.166E+03	-3.772E+03	-1.439E+04	-1.323E+05	-6.877E+04	-1.108E+04
4EP1S	-2.071E+03	-4.051E+03	-1.338E+04	-9.153E+04	-5.598E+04	-6.400E+03
4EP2S	-2.593E+03	-4.067E+03	-1.340E+04	-1.433E+05	-5.647E+04	-6.410E+03
WT1I	-3.482E+03	-2.937E+03	-3.569E+03	-8.007E+03	-1.701E+04	-3.362E+02
WT1U	-4.859E+02	-4.110E+02	-5.094E+02	-1.533E+03	-3.273E+03	-6.050E+01
WT2I	-1.463E+04	-6.281E+03	-8.481E+04	-4.005E+05	-1.150E+06	-8.170E+03
WT2U	-1.315E+03	-5.706E+02	-7.876E+03	-4.769E+04	-1.391E+05	-9.768E+02
WT3	-1.789E+04	-7.106E+03	-9.271E+04	-4.157E+05	-1.538E+06	-9.155E+03
WT4	-2.106E+04	-1.434E+04	-9.290E+04	-6.527E+05	-4.105E+06	-9.218E+03
WT5	-1.794E+04	-1.927E+04	-9.294E+04	-8.461E+06	-1.715E+06	-9.240E+03
ET1I	-3.543E+03	-2.972E+03	-3.563E+03	-7.435E+03	-1.719E+04	-6.484E+02
ET1U	-4.945E+02	-4.158E+02	-5.085E+02	-1.427E+03	-3.309E+03	-1.167E+02
ET2I	-1.480E+04	-5.611E+03	-8.465E+04	-4.217E+05	-1.164E+06	-1.179E+04
ET2U	-1.331E+03	-5.101E+02	-7.861E+03	-5.026E+04	-1.408E+05	-1.410E+03
ET3	-1.809E+04	-6.371E+03	-9.253E+04	-4.506E+05	-1.556E+06	-1.321E+04
ET4	-2.087E+04	-1.361E+04	-9.271E+04	-7.771E+05	-4.145E+06	-1.329E+04
ET5	-1.718E+04	-1.922E+04	-9.276E+04	-8.518E+06	-1.551E+06	-1.330E+04

Table D.7 Maximum buffeting forces of towers and piers, Case 4

Location	FX (kN)	FY (kN)	FZ (kN)	MX (kN-m)	MY (kN-m)	MZ (kN-m)
4WP1N	2.819E+03	5.533E+03	2.499E+04	1.457E+05	1.006E+05	1.496E+04
4WP2N	3.458E+03	5.812E+03	2.501E+04	2.289E+05	1.213E+05	1.498E+04
4EP1N	2.755E+03	6.046E+03	2.394E+04	1.661E+05	1.006E+05	1.119E+04
4EP2N	3.452E+03	6.438E+03	2.396E+04	2.551E+05	1.204E+05	1.120E+04
4WP1S	2.836E+03	5.528E+03	2.523E+04	1.430E+05	1.008E+05	1.499E+04
4WP2S	3.489E+03	5.683E+03	2.526E+04	2.261E+05	1.110E+05	1.501E+04
4EP1S	2.417E+03	6.052E+03	2.341E+04	1.636E+05	8.967E+04	1.124E+04
4EP2S	3.147E+03	6.319E+03	2.344E+04	2.524E+05	1.213E+05	1.125E+04
WT1I	3.607E+03	4.874E+03	4.680E+03	1.463E+04	2.504E+04	6.414E+02
WT1U	5.036E+02	6.820E+02	6.680E+02	2.803E+03	4.797E+03	1.154E+02
WT2I	1.472E+04	9.996E+03	1.058E+05	7.600E+05	1.444E+06	1.400E+04
WT2U	1.324E+03	9.083E+02	9.829E+03	9.052E+04	1.748E+05	1.674E+03
WT3	1.841E+04	1.131E+04	1.157E+05	7.958E+05	1.945E+06	1.569E+04
WT4	1.416E+04	2.296E+04	1.160E+05	1.268E+06	5.237E+06	1.578E+04
WT5	2.376E+04	4.544E+04	1.161E+05	1.291E+07	2.916E+06	1.583E+04
ET1I	3.692E+03	4.911E+03	4.707E+03	1.385E+04	2.550E+04	8.440E+02
ET1U	5.155E+02	6.873E+02	6.719E+02	2.659E+03	4.885E+03	1.519E+02
ET2I	1.505E+04	9.357E+03	1.056E+05	7.855E+05	1.476E+06	1.630E+04
ET2U	1.355E+03	8.506E+02	9.810E+03	9.363E+04	1.786E+05	1.949E+03
ET3	1.881E+04	1.061E+04	1.155E+05	8.372E+05	1.988E+06	1.826E+04
ET4	1.406E+04	2.231E+04	1.157E+05	1.411E+06	5.346E+06	1.838E+04
ET5	2.478E+04	4.558E+04	1.158E+05	1.307E+07	3.138E+06	1.840E+04

Table D.8 Minimum buffeting forces of towers and piers, Case 4

Location	FX (kN)	FY (kN)	FZ (kN)	MX (kN-m)	MY (kN-m)	MZ (kN-m)
4WP1N	-2.772E+03	-5.057E+03	-3.016E+04	-1.306E+05	-8.742E+04	-1.339E+04
4WP2N	-3.399E+03	-5.322E+03	-3.019E+04	-1.902E+05	-1.064E+05	-1.341E+04
4EP1N	-2.721E+03	-5.623E+03	-2.847E+04	-1.459E+05	-8.880E+04	-1.723E+04
4EP2N	-3.411E+03	-5.995E+03	-2.850E+04	-2.151E+05	-1.057E+05	-1.725E+04
4WP1S	-2.463E+03	-4.948E+03	-2.363E+04	-1.288E+05	-7.870E+04	-1.344E+04
4WP2S	-3.113E+03	-5.333E+03	-2.366E+04	-1.900E+05	-1.074E+05	-1.346E+04
4EP1S	-2.726E+03	-5.521E+03	-2.213E+04	-1.443E+05	-8.860E+04	-1.727E+04
4EP2S	-3.440E+03	-6.016E+03	-2.216E+04	-2.151E+05	-9.587E+04	-1.729E+04
WT1I	-4.248E+03	-4.675E+03	-5.805E+03	-1.206E+04	-2.497E+04	-1.036E+03
WT1U	-5.930E+02	-6.542E+02	-8.287E+02	-2.314E+03	-4.801E+03	-1.864E+02
WT2I	-1.758E+04	-8.823E+03	-1.356E+05	-6.684E+05	-1.620E+06	-1.912E+04
WT2U	-1.581E+03	-8.021E+02	-1.260E+04	-7.967E+04	-1.959E+05	-2.286E+03
WT3	-2.161E+04	-1.000E+04	-1.483E+05	-7.120E+05	-2.168E+06	-2.142E+04
WT4	-2.259E+04	-2.101E+04	-1.486E+05	-1.203E+06	-5.772E+06	-2.152E+04
WT5	-2.420E+04	-7.210E+04	-1.486E+05	-7.723E+06	-2.730E+06	-2.158E+04
ET1I	-4.347E+03	-4.637E+03	-5.804E+03	-1.223E+04	-2.540E+04	-7.006E+02
ET1U	-6.068E+02	-6.487E+02	-8.285E+02	-2.344E+03	-4.884E+03	-1.261E+02
ET2I	-1.792E+04	-9.528E+03	-1.354E+05	-6.512E+05	-1.650E+06	-1.613E+04
ET2U	-1.612E+03	-8.657E+02	-1.257E+04	-7.756E+04	-1.996E+05	-1.928E+03
ET3	-2.202E+04	-1.078E+04	-1.480E+05	-6.824E+05	-2.208E+06	-1.807E+04
ET4	-2.243E+04	-2.193E+04	-1.483E+05	-1.086E+06	-5.872E+06	-1.820E+04
ET5	-2.368E+04	-7.217E+04	-1.483E+05	-7.851E+06	-2.577E+06	-1.823E+04

Table D.9 Maximum buffeting forces of towers and piers, Case 5

Location	FX (kN)	FY (kN)	FZ (kN)	MX (kN-m)	MY (kN-m)	MZ (kN-m)
4WP1N	2.923E+03	5.813E+03	2.690E+04	1.322E+05	8.731E+04	1.510E+04
4WP2N	3.595E+03	6.109E+03	2.693E+04	2.062E+05	1.072E+05	1.511E+04
4EP1N	2.916E+03	6.351E+03	2.576E+04	1.506E+05	8.910E+04	1.127E+04
4EP2N	3.648E+03	6.765E+03	2.579E+04	2.297E+05	1.048E+05	1.129E+04
4WP1S	2.947E+03	5.815E+03	2.754E+04	1.298E+05	8.772E+04	1.513E+04
4WP2S	3.634E+03	5.980E+03	2.757E+04	2.038E+05	9.819E+04	1.514E+04
4EP1S	2.561E+03	6.365E+03	2.556E+04	1.484E+05	7.948E+04	1.132E+04
4EP2S	3.329E+03	6.646E+03	2.559E+04	2.274E+05	1.058E+05	1.133E+04
WT1I	3.792E+03	5.151E+03	5.162E+03	1.317E+04	2.203E+04	6.323E+02
WT1U	5.295E+02	7.207E+02	7.368E+02	2.524E+03	4.220E+03	1.138E+02
WT2I	1.545E+04	1.042E+04	1.174E+05	6.899E+05	1.270E+06	1.377E+04
WT2U	1.390E+03	9.472E+02	1.090E+04	8.218E+04	1.536E+05	1.647E+03
WT3	1.933E+04	1.180E+04	1.283E+05	7.243E+05	1.710E+06	1.543E+04
WT4	1.491E+04	2.412E+04	1.286E+05	1.165E+06	4.605E+06	1.553E+04
WT5	2.506E+04	4.827E+04	1.287E+05	1.175E+07	2.586E+06	1.557E+04
ET1I	3.886E+03	5.173E+03	5.191E+03	1.261E+04	2.245E+04	8.631E+02
ET1U	5.426E+02	7.238E+02	7.410E+02	2.420E+03	4.302E+03	1.553E+02
ET2I	1.582E+04	9.975E+03	1.171E+05	7.069E+05	1.299E+06	1.675E+04
ET2U	1.423E+03	9.067E+02	1.088E+04	8.424E+04	1.572E+05	2.003E+03
ET3	1.977E+04	1.131E+04	1.281E+05	7.515E+05	1.749E+06	1.877E+04
ET4	1.482E+04	2.369E+04	1.284E+05	1.255E+06	4.705E+06	1.889E+04
ET5	2.588E+04	4.845E+04	1.284E+05	1.191E+07	2.728E+06	1.891E+04

Table D.10 Minimum buffeting forces of towers and piers, Case 5

Location	FX (kN)	FY (kN)	FZ (kN)	MX (kN-m)	MY (kN-m)	MZ (kN-m)
4WP1N	-2.811E+03	-5.444E+03	-2.880E+04	-1.488E+05	-1.039E+05	-1.393E+04
4WP2N	-3.443E+03	-5.730E+03	-2.883E+04	-2.185E+05	-1.243E+05	-1.395E+04
4EP1N	-2.703E+03	-6.051E+03	-2.719E+04	-1.662E+05	-1.035E+05	-1.800E+04
4EP2N	-3.399E+03	-6.451E+03	-2.722E+04	-2.470E+05	-1.256E+05	-1.802E+04
4WP1S	-2.501E+03	-5.326E+03	-2.257E+04	-1.471E+05	-9.367E+04	-1.398E+04
4WP2S	-3.156E+03	-5.743E+03	-2.260E+04	-2.183E+05	-1.258E+05	-1.400E+04
4EP1S	-2.713E+03	-5.941E+03	-2.115E+04	-1.647E+05	-1.034E+05	-1.804E+04
4EP2S	-3.433E+03	-6.474E+03	-2.118E+04	-2.470E+05	-1.140E+05	-1.806E+04
WT1I	-4.285E+03	-5.007E+03	-5.395E+03	-1.390E+04	-2.954E+04	-1.095E+03
WT1U	-5.981E+02	-7.006E+02	-7.701E+02	-2.666E+03	-5.679E+03	-1.970E+02
WT2I	-1.778E+04	-9.565E+03	-1.255E+05	-7.616E+05	-1.920E+06	-2.032E+04
WT2U	-1.599E+03	-8.695E+02	-1.165E+04	-9.076E+04	-2.323E+05	-2.429E+03
WT3	-2.186E+04	-1.084E+04	-1.372E+05	-8.092E+05	-2.570E+06	-2.276E+04
WT4	-2.279E+04	-2.270E+04	-1.375E+05	-1.355E+06	-6.846E+06	-2.287E+04
WT5	-2.424E+04	-7.780E+04	-1.375E+05	-8.886E+06	-3.188E+06	-2.293E+04
ET1I	-4.388E+03	-4.982E+03	-5.393E+03	-1.394E+04	-3.007E+04	-7.151E+02
ET1U	-6.125E+02	-6.971E+02	-7.699E+02	-2.673E+03	-5.782E+03	-1.287E+02
ET2I	-1.814E+04	-1.011E+04	-1.252E+05	-7.485E+05	-1.958E+06	-1.642E+04
ET2U	-1.632E+03	-9.182E+02	-1.163E+04	-8.917E+04	-2.368E+05	-1.963E+03
ET3	-2.229E+04	-1.144E+04	-1.369E+05	-7.864E+05	-2.620E+06	-1.840E+04
ET4	-2.264E+04	-2.343E+04	-1.372E+05	-1.263E+06	-6.969E+06	-1.853E+04
ET5	-2.394E+04	-7.791E+04	-1.372E+05	-9.042E+06	-3.069E+06	-1.857E+04

Table D.11 Maximum buffeting forces of towers and piers, Case 6

Location	FX (kN)	FY (kN)	FZ (kN)	MX (kN-m)	MY (kN-m)	MZ (kN-m)
4WP1N	2.806E+03	5.166E+03	2.516E+04	1.348E+05	9.437E+04	1.605E+04
4WP2N	3.456E+03	5.435E+03	2.519E+04	2.094E+05	1.179E+05	1.607E+04
4EP1N	2.861E+03	5.642E+03	2.407E+04	1.536E+05	9.827E+04	1.195E+04
4EP2N	3.568E+03	6.016E+03	2.409E+04	2.331E+05	1.133E+05	1.197E+04
4WP1S	2.837E+03	5.177E+03	2.618E+04	1.325E+05	9.502E+04	1.608E+04
4WP2S	3.501E+03	5.329E+03	2.621E+04	2.071E+05	1.075E+05	1.610E+04
4EP1S	2.496E+03	5.662E+03	2.433E+04	1.514E+05	8.717E+04	1.200E+04
4EP2S	3.240E+03	5.918E+03	2.436E+04	2.310E+05	1.147E+05	1.201E+04
WT1I	3.876E+03	4.337E+03	4.720E+03	1.259E+04	2.534E+04	6.577E+02
WT1U	5.411E+02	6.068E+02	6.738E+02	2.413E+03	4.854E+03	1.183E+02
WT2I	1.574E+04	8.678E+03	1.077E+05	6.645E+05	1.457E+06	1.432E+04
WT2U	1.417E+03	7.886E+02	1.001E+04	7.916E+04	1.763E+05	1.712E+03
WT3	1.971E+04	9.827E+03	1.178E+05	6.991E+05	1.962E+06	1.604E+04
WT4	1.532E+04	2.019E+04	1.181E+05	1.132E+06	5.284E+06	1.615E+04
WT5	2.434E+04	4.314E+04	1.181E+05	1.198E+07	2.838E+06	1.620E+04
ET1I	3.976E+03	4.341E+03	4.748E+03	1.217E+04	2.585E+04	9.332E+02
ET1U	5.551E+02	6.075E+02	6.778E+02	2.335E+03	4.952E+03	1.679E+02
ET2I	1.614E+04	8.461E+03	1.075E+05	6.759E+05	1.493E+06	1.820E+04
ET2U	1.452E+03	7.690E+02	9.986E+03	8.054E+04	1.806E+05	2.176E+03
ET3	2.018E+04	9.590E+03	1.176E+05	7.170E+05	2.009E+06	2.039E+04
ET4	1.523E+04	2.002E+04	1.178E+05	1.188E+06	5.406E+06	2.052E+04
ET5	2.493E+04	4.332E+04	1.179E+05	1.215E+07	2.943E+06	2.054E+04

Table D.12 Minimum buffeting forces of towers and piers, Case 6

Location	FX (kN)	FY (kN)	FZ (kN)	MX (kN-m)	MY (kN-m)	MZ (kN-m)
4WP1N	-2.897E+03	-5.490E+03	-3.262E+04	-1.292E+05	-9.638E+04	-1.287E+04
4WP2N	-3.538E+03	-5.783E+03	-3.265E+04	-1.908E+05	-1.133E+05	-1.289E+04
4EP1N	-2.727E+03	-6.100E+03	-3.079E+04	-1.442E+05	-9.411E+04	-1.671E+04
4EP2N	-3.435E+03	-6.508E+03	-3.082E+04	-2.155E+05	-1.163E+05	-1.673E+04
4WP1S	-2.563E+03	-5.374E+03	-2.561E+04	-1.280E+05	-8.647E+04	-1.291E+04
4WP2S	-3.230E+03	-5.799E+03	-2.565E+04	-1.906E+05	-1.149E+05	-1.293E+04
4EP1S	-2.743E+03	-5.992E+03	-2.404E+04	-1.432E+05	-9.419E+04	-1.675E+04
4EP2S	-3.476E+03	-6.534E+03	-2.407E+04	-2.155E+05	-1.051E+05	-1.676E+04
WT1I	-4.608E+03	-4.743E+03	-5.706E+03	-1.148E+04	-2.863E+04	-1.031E+03
WT1U	-6.432E+02	-6.637E+02	-8.144E+02	-2.200E+03	-5.503E+03	-1.855E+02
WT2I	-1.916E+04	-9.157E+03	-1.321E+05	-6.229E+05	-1.863E+06	-1.924E+04
WT2U	-1.723E+03	-8.323E+02	-1.227E+04	-7.422E+04	-2.253E+05	-2.301E+03
WT3	-2.355E+04	-1.038E+04	-1.444E+05	-6.603E+05	-2.494E+06	-2.156E+04
WT4	-2.468E+04	-2.164E+04	-1.447E+05	-1.097E+06	-6.643E+06	-2.166E+04
WT5	-2.455E+04	-7.865E+04	-1.448E+05	-7.719E+06	-2.895E+06	-2.172E+04
ET1I	-4.723E+03	-4.735E+03	-5.704E+03	-1.140E+04	-2.916E+04	-6.501E+02
ET1U	-6.592E+02	-6.624E+02	-8.142E+02	-2.186E+03	-5.607E+03	-1.170E+02
ET2I	-1.956E+04	-9.495E+03	-1.318E+05	-6.167E+05	-1.901E+06	-1.490E+04
ET2U	-1.759E+03	-8.627E+02	-1.224E+04	-7.347E+04	-2.299E+05	-1.782E+03
ET3	-2.403E+04	-1.075E+04	-1.441E+05	-6.493E+05	-2.544E+06	-1.670E+04
ET4	-2.452E+04	-2.214E+04	-1.444E+05	-1.050E+06	-6.768E+06	-1.682E+04
ET5	-2.444E+04	-7.879E+04	-1.445E+05	-7.861E+06	-2.834E+06	-1.686E+04

APPENDIX E

TABLES OF MEAN AND BUFFETING RORCES OF BRIDGE CABLES

Table E.1 Mean buffeting forces of bridge cables (kN), Cases 1-6

Location	Case 1	Case2	Case 3	Case 4	Case 5	Case 6
101N	-1.30E+02	1.27E+02	-6.17E+01	-5.41E+02	3.85E+01	-2.65E+01
108N	-3.43E+02	3.50E+02	8.50E+01	-8.28E+02	-1.41E+02	-2.31E+02
115N	-3.68E+02	2.73E+02	-6.50E+0	-8.84E+02	-1.72E+02	-2.79E+02
121N	-3.80E+02	2.24E+02	-6.59E+01	-9.16E+02	-1.86E+02	-3.02E+02
128N	-3.57E+02	2.00E+02	-8.53E+01	-8.75E+02	-1.68E+02	-2.80E+02
201N	-9.98E+01	7.45E+01	-1.70E+02	-6.40E+02	1.26E+02	4.35E+01
208N	-3.21E+01	-1.04E+02	-1.74E+02	-2.45E+02	2.52E+01	-3.35E+01
214N	-2.05E+01	-1.56E+02	-3.19E+02	-4.30E+02	1.19E+02	3.05E+01
221N	-1.33E+01	-2.37E+02	-4.34E+02	-5.18E+02	1.58E+02	4.85E+01
228N	1.98E+01	-2.52E+02	-4.81E+02	-5.42E+02	2.28E+02	1.21E+02
301N	-1.11E+02	6.77E+01	-9.26E+01	-4.67E+02	2.20E+01	-4.30E+01
308N	-8.85E+0	-1.11E+02	-3.50E+02	-5.77E+02	2.15E+02	1.19E+02
315N	-2.50E+0	-1.47E+02	-4.25E+02	-6.58E+02	2.54E+02	1.44E+02
321N	7.00E+0	-2.21E+02	-5.63E+02	-8.08E+02	3.26E+02	1.88E+02
328N	1.83E+01	-2.52E+02	-4.66E+02	-4.92E+02	2.01E+02	9.85E+01
401N	-1.39E+02	1.23E+02	-2.19E+01	-4.11E+02	-3.97E+01	-9.09E+01
408N	-3.51E+02	3.65E+02	-4.50E+0	-7.29E+02	-2.19E+02	-2.85E+02
415N	-3.67E+02	2.85E+02	-1.20E+02	-8.78E+02	-1.90E+02	-2.83E+02
421N	-3.77E+02	2.35E+02	-1.93E+02	-9.51E+02	-1.82E+02	-2.89E+02
428N	-3.16E+02	1.93E+02	-2.05E+02	-8.35E+02	-1.42E+02	-2.40E+02
101S	1.11E+02	-2.62E+02	-4.56E+02	-2.30E+02	2.73E+02	2.29E+02
108S	2.96E+02	-5.81E+02	-7.90E+02	-9.45E+01	4.73E+02	4.02E+02
115S	2.69E+02	-6.57E+02	-8.87E+02	-1.40E+02	4.33E+02	3.47E+02
121S	2.51E+02	-6.96E+02	-9.39E+02	-1.73E+02	4.09E+02	3.14E+02
128S	2.33E+02	-6.54E+02	-8.90E+02	-1.90E+02	3.91E+02	2.97E+02
201S	8.18E+01	-2.35E+02	-4.99E+02	-3.84E+02	3.02E+02	2.45E+02
208S	-3.82E+01	-1.39E+02	-2.60E+02	-1.74E+02	1.05E+01	-1.77E+01
214S	-5.80E+01	-1.50E+02	-3.75E+02	-3.88E+02	7.80E+01	2.65E+01
221S	-9.28E+01	-1.65E+02	-4.48E+02	-4.84E+02	5.85E+01	-6.50E+0
228S	-1.01E+02	-9.70E+01	-4.05E+02	-5.72E+02	9.00E+01	2.00E+01
301S	7.39E+01	-2.47E+02	-4.21E+02	-2.19E+02	2.09E+02	1.68E+02
308S	-3.14E+01	-1.25E+02	-4.25E+02	-5.12E+02	1.83E+02	1.21E+02
315S	-4.55E+01	-1.33E+02	-4.78E+02	-6.10E+02	2.03E+02	1.30E+02
321S	-7.30E+01	-1.50E+02	-5.75E+02	-7.83E+02	2.33E+02	1.37E+02
328S	-1.02E+02	-9.75E+01	-3.82E+02	-5.37E+02	7.25E+01	5.00E+0
401S	1.08E+02	-2.72E+02	-3.98E+02	-1.43E+02	2.25E+02	1.88E+02
408S	3.11E+02	-5.93E+02	-7.41E+02	-3.05E+02	6.07E+02	5.08E+02
415S	2.83E+02	-6.58E+02	-8.75E+02	-4.01E+02	5.89E+02	4.72E+02

421S	2.66E+02	-6.96E+02	-9.46E+02	-4.62E+02	5.79E+02	4.50E+02
428S	2.33E+02	-5.98E+02	-8.30E+02	-4.43E+02	5.22E+02	3.99E+02

Table E.2 Maximum buffeting forces of bridge cables (kN), Cases 1-6

Location	Case 1	Case2	Case 3	Case 4	Case 5	Case 6
101N	5.473E+02	1.189E+03	9.306E+02	1.138E+03	1.414E+03	1.461E+03
108N	4.426E+02	1.591E+03	1.221E+03	1.104E+03	1.477E+03	1.437E+03
115N	3.936E+02	1.427E+03	1.063E+03	1.005E+03	1.394E+03	1.334E+03
121N	3.733E+02	1.338E+03	9.752E+02	9.613E+02	1.362E+03	1.291E+03
128N	3.782E+02	1.313E+03	9.584E+02	9.506E+02	1.340E+03	1.274E+03
201N	8.144E+02	1.520E+03	1.193E+03	1.603E+03	1.976E+03	2.053E+03
208N	2.156E+02	2.035E+02	1.372E+02	3.215E+02	4.971E+02	4.550E+02
214N	5.637E+02	7.328E+02	5.518E+02	9.542E+02	1.268E+03	1.266E+03
221N	7.322E+02	7.853E+02	5.790E+02	1.180E+03	1.575E+03	1.567E+03
228N	9.508E+02	1.029E+03	7.804E+02	1.528E+03	1.967E+03	1.992E+03
301N	4.373E+02	9.482E+02	7.348E+02	8.708E+02	1.111E+03	1.133E+03
308N	9.833E+02	1.326E+03	1.035E+03	1.659E+03	2.074E+03	2.136E+03
315N	1.160E+03	1.512E+03	1.179E+03	1.918E+03	2.395E+03	2.470E+03
321N	1.467E+03	1.787E+03	1.384E+03	2.390E+03	2.993E+03	3.082E+03
328N	8.307E+02	9.234E+02	6.944E+02	1.324E+03	1.724E+03	1.736E+03
401N	2.622E+02	8.958E+02	6.934E+02	5.902E+02	7.586E+02	7.719E+02
408N	2.374E+02	2.323E+03	1.798E+03	6.756E+02	8.365E+02	8.796E+02
415N	4.304E+02	2.299E+03	1.753E+03	9.826E+02	1.236E+03	1.285E+03
421N	5.059E+02	2.292E+03	1.732E+03	1.100E+03	1.397E+03	1.446E+03
428N	4.790E+02	2.088E+03	1.573E+03	9.992E+02	1.277E+03	1.316E+03
101S	7.583E+02	8.368E+02	6.297E+02	1.325E+03	1.619E+03	1.681E+03
108S	1.037E+03	7.143E+02	5.177E+02	1.522E+03	1.976E+03	1.952E+03
115S	9.602E+02	5.992E+02	3.988E+02	1.373E+03	1.832E+03	1.785E+03
121S	9.182E+02	5.468E+02	3.415E+02	1.295E+03	1.759E+03	1.700E+03
128S	8.972E+02	5.546E+02	3.521E+02	1.285E+03	1.739E+03	1.685E+03
201S	9.628E+02	1.241E+03	9.430E+02	1.758E+03	2.129E+03	2.226E+03
208S	1.660E+02	2.208E+02	1.108E+02	3.029E+02	4.088E+02	4.003E+02
214S	5.110E+02	7.578E+02	5.204E+02	9.633E+02	1.197E+03	1.237E+03
221S	5.536E+02	9.793E+02	6.767E+02	1.042E+03	1.300E+03	1.347E+03
228S	7.556E+02	1.291E+03	9.409E+02	1.363E+03	1.670E+03	1.745E+03
301S	6.156E+02	6.171E+02	4.429E+02	1.074E+03	1.329E+03	1.368E+03
308S	8.884E+02	1.375E+03	1.031E+03	1.618E+03	1.955E+03	2.051E+03
315S	1.047E+03	1.583E+03	1.186E+03	1.875E+03	2.266E+03	2.378E+03
321S	1.295E+03	1.950E+03	1.458E+03	2.286E+03	2.771E+03	2.907E+03
328S	6.647E+02	1.129E+03	8.103E+02	1.221E+03	1.511E+03	1.569E+03
401S	5.834E+02	3.635E+02	2.509E+02	9.647E+02	1.213E+03	1.231E+03
408S	1.541E+03	2.735E+02	1.778E+02	2.410E+03	3.093E+03	3.082E+03
415S	1.581E+03	4.946E+02	3.290E+02	2.453E+03	3.160E+03	3.155E+03
421S	1.605E+03	5.707E+02	3.742E+02	2.485E+03	3.213E+03	3.207E+03
428S	1.463E+03	5.363E+02	3.499E+02	2.270E+03	2.945E+03	2.933E+03

Table E.3 Minimum buffeting forces of bridge cables (kN), Cases 1-6

Location	Case 1	Case2	Case 3	Case 4	Case 5	Case 6
101N	-8.073E+02	-9.359E+02	-1.054E+03	-2.219E+03	-1.337E+03	-1.514E+03
108N	-1.129E+03	-8.903E+02	-1.051E+03	-2.759E+03	-1.759E+03	-1.899E+03
115N	-1.130E+03	-8.811E+02	-1.076E+03	-2.773E+03	-1.738E+03	-1.891E+03
121N	-1.133E+03	-8.903E+02	-1.107E+03	-2.793E+03	-1.733E+03	-1.895E+03
128N	-1.092E+03	-9.131E+02	-1.129E+03	-2.700E+03	-1.675E+03	-1.833E+03
201N	-1.014E+03	-1.371E+03	-1.532E+03	-2.883E+03	-1.724E+03	-1.966E+03
208N	-2.798E+02	-4.118E+02	-4.843E+02	-8.118E+02	-4.468E+02	-5.220E+02
214N	-6.047E+02	-1.045E+03	-1.190E+03	-1.815E+03	-1.031E+03	-1.205E+03
221N	-7.587E+02	-1.259E+03	-1.446E+03	-2.216E+03	-1.260E+03	-1.470E+03
228N	-9.113E+02	-1.532E+03	-1.742E+03	-2.612E+03	-1.511E+03	-1.751E+03
301N	-6.597E+02	-8.128E+02	-9.199E+02	-1.805E+03	-1.067E+03	-1.219E+03
308N	-1.001E+03	-1.547E+03	-1.735E+03	-2.812E+03	-1.645E+03	-1.899E+03
315N	-1.165E+03	-1.806E+03	-2.028E+03	-3.233E+03	-1.888E+03	-2.183E+03
321N	-1.453E+03	-2.228E+03	-2.510E+03	-4.006E+03	-2.342E+03	-2.707E+03
328N	-7.942E+02	-1.427E+03	-1.626E+03	-2.308E+03	-1.323E+03	-1.539E+03
401N	-5.394E+02	-6.490E+02	-7.371E+02	-1.412E+03	-8.380E+02	-9.537E+02
408N	-9.403E+02	-1.593E+03	-1.807E+03	-2.134E+03	-1.275E+03	-1.449E+03
415N	-1.164E+03	-1.729E+03	-1.993E+03	-2.738E+03	-1.616E+03	-1.851E+03
421N	-1.260E+03	-1.823E+03	-2.117E+03	-3.002E+03	-1.761E+03	-2.024E+03
428N	-1.111E+03	-1.703E+03	-1.982E+03	-2.670E+03	-1.560E+03	-1.796E+03
101S	-5.354E+02	-1.360E+03	-1.541E+03	-1.785E+03	-1.073E+03	-1.223E+03
108S	-4.455E+02	-1.877E+03	-2.097E+03	-1.711E+03	-1.031E+03	-1.148E+03
115S	-4.228E+02	-1.913E+03	-2.172E+03	-1.653E+03	-9.654E+02	-1.091E+03
121S	-4.169E+02	-1.938E+03	-2.220E+03	-1.641E+03	-9.403E+02	-1.073E+03
128S	-4.322E+02	-1.863E+03	-2.133E+03	-1.665E+03	-9.562E+02	-1.091E+03
201S	-7.992E+02	-1.710E+03	-1.940E+03	-2.526E+03	-1.525E+03	-1.736E+03
208S	-2.424E+02	-4.980E+02	-6.311E+02	-6.516E+02	-3.879E+02	-4.356E+02
214S	-6.270E+02	-1.058E+03	-1.271E+03	-1.740E+03	-1.041E+03	-1.184E+03
221S	-7.391E+02	-1.310E+03	-1.573E+03	-2.010E+03	-1.183E+03	-1.360E+03
228S	-9.569E+02	-1.485E+03	-1.751E+03	-2.507E+03	-1.490E+03	-1.705E+03
301S	-4.678E+02	-1.112E+03	-1.285E+03	-1.511E+03	-9.115E+02	-1.033E+03
308S	-9.511E+02	-1.625E+03	-1.881E+03	-2.642E+03	-1.590E+03	-1.810E+03
315S	-1.138E+03	-1.848E+03	-2.142E+03	-3.094E+03	-1.860E+03	-2.119E+03
321S	-1.441E+03	-2.249E+03	-2.607E+03	-3.851E+03	-2.306E+03	-2.634E+03
328S	-8.687E+02	-1.324E+03	-1.574E+03	-2.295E+03	-1.366E+03	-1.559E+03
401S	-3.684E+02	-9.068E+02	-1.046E+03	-1.250E+03	-7.622E+02	-8.552E+02
408S	-9.194E+02	-1.460E+03	-1.659E+03	-3.019E+03	-1.880E+03	-2.067E+03
415S	-1.015E+03	-1.811E+03	-2.079E+03	-3.254E+03	-1.982E+03	-2.212E+03
421S	-1.073E+03	-1.963E+03	-2.267E+03	-3.408E+03	-2.055E+03	-2.308E+03
428S	-9.961E+02	-1.733E+03	-2.009E+03	-3.156E+03	-1.902E+03	-2.135E+03

REFERENCES

Abdel-Ghaffar, A.M. & Khalifa, M.A. (1991). Importance of cable vibration in dynamics of cable-stayed bridges, *Jounal of Engineering Mechanics, ASCE*, *117*, 2571-2589.

Agar, T.J.A. (1991). Dynamic instability of suspension bridges, *Computers & structures*, *41*(6), 1321-1328.

Argentini, T., Rocchi, D., Muggiasca, S., & Zasso, A. (2012). Cross-sectional distributions versus integrated coefficients of flutter derivatives and aerodynamic admittances identified with surface pressure measurement, *Journal of Wind Engineering and Industrial Aerodynamics*, *104-106*, 152-158.

Bartoli, G., & Mannini, C. (2008). A simplified approach to bridge deck flutter, *Journal of Wind Engineering and Industrial Aerodynamics*, *96*, 229–256.

Bearman, P.W. (1984). Vortex shedding from oscillating bluff bodies, *Annual Review of Fluid Mechanics*, *16*, 195-222.

Beith, J.G. (1998). A practical engineering method for the flutter analysis of long-span bridges, *Journal of Wind Engineering and Industrial Aerodynamics*, *77-78*, 357-366.

Blevin, R.D. (1990). *Flow Induced Vibration, 2nd Edition*, Van Nostrand Reinhold, New York.

Boonyapinyo, V., Yamada, H., & Miyata, T. (1994). Wind-induced non-linear lateral-torsional buckling of cable- stayed bridges, *Journal of Structural*

Engineering, ASCE, *120*(2), 486~506.

Box, G.E.P., & Draper, N.R. (2002). *Empirical Model Building and Response Surfaces*, Wiley, New York.

Brownjohn, J.M.W., & Xia, P. Q. (2000). Dynamic assessment of curved cable-stayed bridge by model updating, *Journal of Structural Engineering*, 126, 252-260.

Brownjohn, J.M.W., Xia, P., Hao, H. & Xia, Y. (2001). Civil structure condition assessment by FE model updating: methodology and case studies. *Finite Elements in Analysis and Design*, *37*(10), 761-775.

Brownjohn, J.M.W., Moyo, P., Omenzetter, P., & Lu, Y. (2003). Assessment of highway bridge upgrading by dynamic testing and finite-element model updating. *Journal of Bridge Engineering*, 8, 162-172.

Bucher, C.G., & Bourgund, U. (1990). "A fast and efficient response surface approach for structural reliability problems". *Structural safety*, *7*(1), 57-66.

Bucher, G.C., Lin, Y.K. (1988). Stochastic stability of bridges considering coupled modes, *Journal of Engineering Mechanics, ASCE*, *114*(12), 2055-2071.

Caetano, E., Cunha, A. & Taylor, C. (2000). Investigation of dynamic cable-deck interaction in a physical model of a cable-stayed bridge Part I: Modal analysis, *Earthquake Engineering and Structural Dynamics*, *29*, 481-498.

Cao, Y.D., Xiang, H.F. & Zhou, Y. (2000). Simulation of stochastic wind velocity field on long-span bridges, *Journal of Engineering Mechanics, ASCE*, *126*(1), 1-6.

Caracoglia, L., & Jones, N.P. (2003). Time domain vs. frequency domain characterization of aeroelastic forces for bridge deck sections, *Journal of Wind Engineering and Industrial Aerodynamics*, *91* (3), 371–402.

Catbas, F.N., & Aktan, A.E. (2002). Condition and damage assessment: issues and some promising indices. *Journal of Structural Engineering*, *128*(8), 1026-1036.

Catbas, F.N., Ciloglu, S.K., Hasancebi, O., Grimmelsman, K., & Aktan, A.E. (2007). "Limitations in structural identification of large constructed structures." *Journal of Structural Engineering, ASCE*, *133*(8), 1051-1066.

Chajes, M.J., Mertz, D.R., & Commander, B. (1997). Experimental load rating of a posted bridge. *Journal of Bridge Engineering*, *2*(1), 1-10.

Chan, T.H.T., Li, Z.X., Yu, Y., & Sun, Z.H. (2009). Concurrent multi-scale modelling of civil infrastructures for analyses on structural deteriorating—Part II: Model updating and verification. *Finite Elements in Analysis and Design*, *45*(11), 795-805.

Chan, T.H.T., Zhou, T.Q., Li, Z.X., & Guo, L. (2005). Hot spot stress approach for Tsing Ma Bridge fatigue evaluation under traffic using finite element method, *Structural Engineering and Mechanics*, *19*(3), 261-279.

Chang, C.C., & Poon, C.W. (2010). Nonlinear identification of lumped-mass buildings using empirical mode decomposition and incomplete measurement. *Journal of engineering mechanics*, *136*(3), 273-281.

Chang, P. C., Flatau, A., & Liu, S.C. (2003). Health monitoring of civil infrastructure, *Structural Health Monitoring*, *2*(3), 257–267.

Chen, J., & Xu, Y.L. (2004). *Wind Characteristics Study*, Report CSE-REP-04-01. (Hong Kong: Department of Civil and Structural Engineering, The Hong Kong Polytechnic University).

Chen, J., Hui, M.C., & Xu, Y.L. (2007). A comparative study of stationary and non-stationary wind models using field measurements. *Boundary-layer meteorology*, *122*(1), 105-121.

Chen, X., Matsumoto, M., & Kareem, A. (2000a). Aerodynamic coupling effects on flutter and buffeting of bridges. *Journal of engineering mechanics*, *126*(1), 17-26.

Chen, X., Matsumoto, M., & Kareem, A. (2000b). Time domain flutter and buffeting response analysis of bridges. *Journal of Engineering Mechanics*, *126*(1), 7-16.

Chen, X. Z., & Kareem, A., (2001). Nonlinear response analysis of long-span bridges under turbulent winds, *Journal of Wind Engineering and Industrial Aerodynamics*, *89* (14-15), 1335-1350.

Chen, X.Z., & Kareem, A. (2003). Aeroelastic analysis of bridges: Effects of turbulence and aerodynamic nonlinearities, *Journal of Engineering Mechanics*, *129*(8), 885-895.

Chen, Z.W., Xu, Y.L., & Wong, K.Y. (2011). Fatigue analysis of long-span suspension bridges under multiple loading: case study. *Engineering Structures*, *33*(12), 3246-3256.

Cheng, J., Jiang, J.J., Xiao, R.C., & Xiang, H.F. (2002). Nonlinear aerostatic stability analysis of Jiang Yin suspension bridge, *Engineering Structures*, *24*, 773 – 781.

Clough, R.W., & Penzien, J. (2003). *Dynamics of Structures*, 3rd ed., Berkeley, USA:

Computers and Structures.

Cigada, A., Diana, G., & Zappa, E. (2002). On the response of a bridge deck to turbulent wind: a new approach, *Journal of Wind Engineering and Industrial Aerodynamics*, 90, 1173－1182.

Costa, C., Borri, C., Flamand, O., & Grillaud, G. (2007). Time-domain buffeting simulations for wind-bridge interaction, *Journal of Wind Engineering and Industrial Aerodynamics*, *95*, 991-1006.

Craig, R.R., & Bampton, M.M.C. (1968). Coupling of substructures for dynamic analysis, *AIAA Journal*, *6*(7), 1313–1319.

Craig, R.R. (2000). Coupling of substructures for dynamic analysis: an overview, *Proceedings of the 41st AIAA/ASME/ASCE/ASC Structures*, Structural Dynamics and Materials Conference, Atlanta, GA, 171–179.

Davenport, A.G. (1961). The spectrum of horizontal gustiness near the ground in high winds. *Quarterly Journal of the Royal Meteorological Society*, *87*(372), 194-211.

Davenport, A.G. (1962). Buffeting of a suspension bridge by storm winds.*Journal of Structural Division, ASCE*, *88*(3), 233-268.

Deodatis, G. (1996). Simulation of ergodic multivariate stochastic processes. *Journal of Engineering Mechanics*, *122*(8), 778-787.

Diana, G., Bruni, S., Cigada, A., & Collina, A. (1993). Turbulence effect on flutter velocity in long span suspended bridges, *Journal of Wind Engineering and Industrial Aerodynamics*, *48*, 329–342.

Diana, G., Resta, F., Zasso, A., Belloli, M., & Rocchi, D. (2004). Forced motion and free motion aeroelastic tests on a new concept dynamometric section model of the Messina suspension bridge. *Journal of wind engineering and industrial aerodynamics*, *92*(6), 441-462.

Diana, G., Resta, F., & Rocchi, D. (2008). A new numerical approach to reproduce bridge aerodynamic non-linearities in time domain. *Journal of Wind Engineering and Industrial Aerodynamics*, *96*(10), 1871-1884.

Diana, G., Rocchi, D., Argentini, T., & Muggiasca, S. (2010). Aerodynamic instability of a bridge deck section model: Linear and nonlinear approach to force modeling. *Journal of Wind Engineering and Industrial Aerodynamics*, *98*(6), 363-374.

Ding, Q.S., Chen, A.R., & Xiang, H.F. (2001). A state space method for coupled flutter analysis of long span bridges, *Structural Engineering and Mechanics*, *14*(4), 491-504.

Ding, Q.S., & Xu, Y.L. (2004). *3-D finite element based flutter analysis of Stonecutters Bridge*, Report CSE-REP-03-01, (Hong Kong: Department of Civil and Structural Engineering, The Hong Kong Polytechnic University).

Ding, Y., Li, A., Du, D., & Liu, T. (2010). Multi-scale damage analysis for a steel box girder of a long-span cable-stayed bridge. *Structure and Infrastructure Engineering*, *6*(6), 725-739.

Doebling, S.W., Hemez, F.M., Schultze, J.F., & Cundy, A.L. (1999). A Metamodel-based Approach to Model Validation for Nonlinear Finite Element

Simulations. *Proceedings of the 20th international modal analysis conference*. International Society for Optical Engineering, *1*, 671-678.

Dowell, E.H. (1989). *A Modern Course in Aeroelasticity, Second Edition*, Dordrecht: Kluwer Academic Publishers.

Duan, Y.F., Xu, Y.L., Fei, Q.G., Wong, K.Y., Chan, W.Y., Ni, Y.Q., & Ng, C.L. (2011). Advanced finite element model of the Tsing Ma Bridge for structural health monitoring. *International Journal of Structural Stability and Dynamics*, *11*(2), 313-344.

Ehsan, F., & Scanlan, R.H. (1990). Vortex-induced vibrations of flexible bridges, *Journal of Engineering Mechanics*, *116*(6), 1392~1411.

Enevoldsen, I., Pedersen, C., Axhag, F., Johansson, Ö., & Töyrä, B. (2002). Assessment and measurement of the Forsmo Bridge, Sweden. *Structural engineering international*, *12*(4), 254-257.

Faravelli, L., & Casciati, S. (2004). Structural damage detection and localization by response change diagnosis. *Progress in Structural Engineering and Materials*, *6*(2), 104-115.

Farrar, C.R., Sohn, H., Hemez, F.M., Anderson, M.C., Bement, M.T., Cornwell, P.J., Doebling, S.W., Schultze, J.F., Lieven, N., & Robertson, A.N. (2004). *Damage prognosis: Current status and future needs. Report LA-14051-MS*. Los Alamos, NM, USA: Los Alamos National Laboratory, 123.

Fei, Q.G., Xu, Y.L., Ng, C.L., Wong, K.Y., Chan, W.Y., & Man, K.L. (2007). Structural health monitoring oriented finite element model of Tsing Ma Bridge tower. *International Journal of Structural Stability and Dynamics*, *7*(4), 647-668.

Franco, G., Betti, R., & Longman, R. W. (2006). On the uniqueness of solutions for the identification of linear structural systems. *Journal of applied mechanics*, *73*(1), 153-162.

Friswell, M.I., & Mottershead, J.E. (1995). *Finite Element Model Updating in Structural Dynamics*. *1st edition*, the Netherlands: Kluwer Academic Publishers.

Garvey, S.D., & Penny, J.E.T. (1994). Representing periodic structures efficiently as substructures, *Journal of Sound and Vibration*, *178*(1), 79–94.

Gu, M., Xu, Y.L., Chen, L.Z., & Xiang, H.F. (1999). Fatigue life estimation of steel girder of Yangpu cable-stayed bridge due to buffeting. *Journal of Wind Engineering and Industrial Aerodynamics*, *80*(3), 383-400.

Gu, M., Zhang, R.X., & Xiang, H.F. (2000). Identification of flutter derivatives of bridge decks, *Journal of Wind Engineering and Industrial Aerodynamics*, *84*(2), 151-162.

Guyan, R.J. (1965). Reduction of stiffness and mass matrices. *AIAA journal*,*3*(2), 380-380.

Hajela, P., & Soeiro, F.J. (1990). Structural damage detection based on static and modal analysis. *AIAA journal*, *28*(6), 1110-1115.

Haan Jr, F.L. (2000). *The effects of turbulence on the aerodynamics of long-span bridges*, Doctoral dissertation, University of Notre Dame.

Haan Jr, F.L., & Kareem, A. (2009). Anatomy of turbulence effects on the aerodynamics of an oscillating prism. *Journal of Engineering Mechanics*, *135*(9), 987-999.

Hatanaka, A., & Tanaka, H. (2002). New estimation method of aerodynamic admittance function. *Journal of Wind Engineering and Industrial Aerodynamics*, *90*, 2073-2086.

Heo, J.H., & Ehmann, K.F. (1991). A method for substructural sensitivity synthesis. *Journal of Vibration and Acoustics*, *113*(2), 201-208.

Hirai, A., Okauchi, I., Ito, M., & Miyata, T. (1967). Studies on the critical wind velocity for suspension bridges, *Proceedings of International Research Seminar on Wind Effects on Buildings and Structures*, University of Toronto Press, Ontario, Canada, 81~103.

Holmes, J.D. (1975). Prediction of the response of a cable-stayed bridge to turbulence, *Proceedings of 4th International Conference on Wind Effects on Buildings and Structures*, London, 187~197.

Holmes, J.D. (1996). Along-wind response of lattice towers part III: effective load distributions, *Engineering Structures*, *18*, 489-494.

Hong Kong Polytechnic University (2007). *Establishment of Bridge Rating System for Tsing Ma Bridge: 3D Finite Element Model of Global Bridge Structure, Report No.2*, Department of Civil and Structural Engineering, The Hong Kong Polytechnic University.

Hua, X.G., Chen, Z.Q., Ni, Y.Q., & Ko, J.M. (2007). Flutter analysis of long-span bridges using ANSYS. *Wind and Structures*, *10*(1), 61-82.

Hua, X.G., & Chen, Z.Q. (2008). Full-order and multimode flutter analysis using ANSYS. *Finite Elements in Analysis and Design*, *44*(9), 537-551.

Huang, N.E., Shen, Z., Long, S.R., Wu, M.C., Shih, H.H., Zheng, Q., ... & Liu, H.H. (1998). The empirical mode decomposition and the Hilbert spectrum for nonlinear and non-stationary time series analysis. *Proceedings of the Royal Society of London. Series A: Mathematical, Physical and Engineering Sciences*, *454*(1971), 903-995.

Hui, M.C.H. (2006). *Turbulent wind action on long span bridges with separated twin-girder decks*, Doctoral dissertation, Tongji University, China.

Hui, M.C.H., Ding, Q.S., & Xu, Y.L. (2006). Flutter analysis of Stonecutters Bridge. *Wind and Structures*, *9*(2), 125-146.

Hurty, W.C. (1965). Dynamic analysis of structural systems using component modes, *AIAA Journal*, *3*(4), 678–685.

Imregun, M., Visser, W.J., & Ewins, D.J. (1995). Finite element model updating using frequency response function data: I. Theory and initial investigation. *Mechanical Systems and Signal Processing*, *9*(2), 187-202.

Irwin, H.P.A.H. (1977). *Wind Tunnel and Analytical Investigations of the Response of Lions' Gate Bridge To Turbulent Wind. National Research Council of Canada*. NAE LTR-LA-210.

Jain. A., Jones. N.P., & Scanlan. R.H. (1996). Coupled flutter and buffeting analysis of long-span bridges. *Journal of Structural Engineering*, *122*(7), 716-725.

Jaishi, B., & Ren, W.X. (2005). Structural finite element model updating using ambient vibration test results, *Journal of Structural Engineering*, *131*, 617-628.

Jaishi, B., & Ren, W. X. (2007). Finite element model updating based on eigenvalue and strain energy residuals using multiobjective optimisation technique, *Mechanical Systems and Signal Processing*, *21*, 2295-2317.

Jancauskas, E.D., & Melbourne, W.H. (1986). The aerodynamic admittance of two-dimensional rectangular section cylinders in smooth flow. *Journal of Wind Engineering and Industrial Aerodynamics*, *23*, 395-408.

Jones, N.P., Scanlan, R.H., Jain, A., & Katsuchi, H. (1998). Advances (and challenges) in the prediction of long-span bridge response to wind, in: A. Larsen, S. Esdahl (Eds.), *Bridge Aerodynamics*, Balkema, Rotterdam, 59~85.

Jung, D.S., & Kim, C.Y. (2013). Finite element model updating of a simply supported skewed PSC I-girder Bridge using hybrid genetic algorithm. *KSCE Journal of Civil Engineering*, *17*(3), 518-529.

Kang, J., Park, S., Shin, S., & Lee, H. (2005). Structural system identification in time domain using measured acceleration. *Journal of Sound and Vibratio*n, *288*(1-2), 215-234.

Kareem, A. (2008). Numerical simulation of wind effects: a probabilistic perspective. *Journal of Wind Engineering and Industrial Aerodynamics*, *96*(10), 1472-1497.

Kasperski, M., & Niemann, H.J. (1992). The LRC (load-response-correlation) -method a general method of estimating unfavourable wind load distributions for linear and non-linear structural behaviour. *Journal of Wind Engineering and*

Industrial Aerodynamics, *43*(1), 1753-1763.

Katsuchi, H., Jones, N.P., & Scanlan, R.H. (1999). Multimode coupled flutter and buffeting analysis of the Akashi-Kaikyo Bridge. *Journal of Structural Engineering*, *125*(1), 60-70.

Kawatani, M., & Kim, H. (1992). Evaluation of aerodynamic admittance for buffeting analysis, *Journal of Wind Engineering and Industrial Aerodynamics*, *41-44*, 613–624.

Khuri, A. I., & Cornell, J. A. (1996). *Response surfaces: designs and analyses*, 2nd edition. CRC press.

Ko, J.M., & Ni. Y.Q. (2005). Technology developments in structural health monitoring of large-scale bridges, *Engineering Structures*, *27*(12), 1715-1725.

Kong, X., Wu, D.J., Cai, C.S., & Liu, Y.Q. (2012). New strategy of substructure method to model long-span hybrid cable-stayed bridges under vehicle-induced vibration. *Engineering Structures*, *34*, 421-435.

Kwok, K.C.S., Qin, X.R., Fok, C.H., & Hitchcock, P.A. (2012). Wind-induced pressures around a sectional twin-deck bridge model: Effects of gap-width on the aerodynamic forces and vortex shedding mechanisms. *Journal of Wind Engineering and Industrial Aerodynamics*, *110*, 50-61.

Larose, G.L. (1997). *The dynamic action of gusty winds on long-span bridges.* Ph.D. Thesis, Technical University of Denmark, Lyngby, Denmark.

Larose, G.L., & Mann, J. (1998). Gust loading on streamlined bridge decks. *Journal of Fluids and Structures*, *12*(5), 511-536.

Larose, G.L., Tanaka, H., Gimsing, N.J., & Dyrbye, C. (1998). Direct measurements of buffeting wind forces on bridge decks. *Journal of Wind Engineering and Industrial Aerodynamics*, *74*, 809-818.

Larose, G.L. (1999). Experimental determination of the aerodynamic admittance of a bridge deck segment. *Journal of Fluids and Structures*, *13*, 1029-1040.

Larsen, A. (1995). A generalized model for assessment of vortex-induced vibrations of flexible structures. *Journal of Wind Engineering and Industrial Aerodynamics*, *57*(2-3), 281~294.

Larsen, A., Savage, M., Lafrenière, A., Hui, M.C., & Larsen, S.V. (2008). Investigation of vortex response of a twin box bridge section at high and low Reynolds numbers. *Journal of Wind Engineering and Industrial Aerodynamics*,*96*(6), 934-944.

Lazzari, M., Vitaliani, R.V., & Saetta, A.V. (2004). Aeroelastic forces and dynamic response of long-span bridges. *International Journal for Numerical Methods in Engineering*, *60*, 1011–1048.

Lallemand, B., Level, P., Duveau, H., & Mahieux, B. (1999). Eigensolutions sensitivity analysis using a sub-structuring method. *Computers & structures*, *71*(3), 257-265.

Li, Y., & Kareem, A. (1990). ARMA systems in wind engineering. *Probabilistic Engineering Mechanics*, *5*(2), 49-59.

Li, Y., & Kareem, A. (1995). Stochastic decomposition and application to probabilistic dynamics. *Journal of engineering mechanics*, *121*(1), 162-174.

Li, Z.X., Chan, T.H.T., & Ko, J.M. (2001). Fatigue analysis and life prediction of bridges with structural health monitoring data Part I: Theory and strategy. *International Journal of Fatigue*, *23*(1), 45–53.

Li, Z.X., Chan, T.H.T., & Ko, J.M. (2001). Fatigue analysis and life prediction of bridges with structural health monitoring data Part II: Application, *International Journal of Fatigue*, *23*(1), 55–64.

Li, Z.X., Chan, T.H.T., & Ko, J.M. (2002). Evaluation of typhoon induced fatigue damage for Tsing Ma Bridge. *Engineering structures*, *24*(8), 1035-1047.

Li, Z.X., Zhou, T.Q., Chan, T.H.T., & Yu, Y. (2007). Multi-scale numerical analysis on dynamic response and local damage in long-span bridges, *Engineering Structures*, *29*(7), 1507-1524.

Li, Z.X., Chan, T.H.T., Yu, Y., & Sun, Z.H. (2009). Concurrent multi-scale modelling of civil infrastructures for analyses on structural deterioration—Part I: Modelling methodology and strategy. *Finite Elements in Analysis and Design*, *45*(11), 782-794.

Liepmann, H.W. (1952). On the application of statistical concepts to the buffeting problem. *Journal of the Aeronautical Sciences (Institute of the Aeronautical Sciences)*, *19*(12).

Lin, J.H. (1992). A fast CQC algorithm of PSD matrices for random seismic responses. *Computers & Structures*, *44*(3), 683-687.

Lin, R.M., & ZHU, J. (2006). Model updating of damped structures using FRF data, *Mechanical Systems and Signal Processing*, *20*, 2200-2218.

Lin, Y.K., & Yang, J.N. (1983). Multimode bridge response to wind excitations. *Journal of Engineering Mechanics, ASCE*, *109*(2), 586–603.

Liu, G., Xu, Y.L., & Zhu, L.D. (2004). Time domain buffeting analysis of long suspension bridges under skew winds, *Wind and Structures*, *7*(6), 421-447.

Liu, T.T., Xu, Y.L., Zhang, W.S., Wong, K.Y., Zhou, H.J., & Chan, K.W.Y. (2009). Buffeting-induced stresses in a long suspension bridge: Structural health monitoring oriented stress analysis, *Wind and Structures*, *12*(6), 479-504.

Lynch, J.P., Law, K.H., Kiremidjian, A.S., Carryer, E., Farrar, C.R., & Sohn, H. *(2004)* .Design and performance validation of a wireless sensing unit for structural monitoring applications, *Structural Engineering and Mechanics*, *17*(3–4), 393–408.

MacNeal, R.H. (1971). A hybrid method of component mode synthesis, *Computers and Structures*, *1*, 581–601.

McCune, R.W., Armstrong, C.G., & Robinson, D.J. (2000). Mixed-dimensional coupling in finite element models. *International Journal for Numerical Methods in Engineering*, *49*, 725-750.

Ministry of Transport of the People's Republic of China. (2004). *Wind resistant design specifications for highway bridges*, JTG/T D60-01-2004. (in Chinese)

Mottershead, J.E., & Friswell, M.I. (1993). Model updating in structural dynamics: a survey. *Journal of Sound and Vibration*, *167*(2), 347-375.

Myers, R.H., & Montgomery, D.C. (2002). *Response Surface Methodology: Process and Product Optimization Using Designed Experiments, 2nd Edition.*, Wiley, New York.

Nagai, M., Ishida, T., Xie, X., Yamaguchi, H., & Fujino, Y. (1998). Static and dynamic instability behaviors of long-span cable-stayed bridges under wind load, *Proceedings of Sixth East Asia-Pacific Conference on Structural Engineering & Construction*, Taiwan, *3*, 2281~2286.

Namini. A., Albrecht. P., & Bosch, H. (1992). Finite element-based flutter analysis of cable-suspended bridges, *Journal of Structural Engineering*, *118*(6), 1509-1526.

Novak, M., & Tanaka, H. (1975). Pressure correlations on a vibrating cylinder. *Proc. 4th Int. Conf. Wind Effects on Building and Structures, Heathrow*, 227-232.

Panda, S.S., & Manohar, C.S. (2009). Applications of meta-models in finite element based reliability analysis of engineering structures. *CMES-Computer Modeling in Engineering & Sciences*, *814*(1), 1-24.

Pandey, A.K., & Biswas, M. (1994). Damage detection in structures using changes in flexibility. *Journal of Sound and Vibration*, *169*(1), 3-17.

Perera, R., Marin, R., & Ruiz, A. (2012). Static–dynamic multi-scale structural damage identification in a multi-objective framework. *Journal of Sound and Vibration*, *332*(6), 1484-1500.

Perotti, F., Domaneschi, M., & De Grandis, S. (2013). The numerical computation of seismic fragility of base-isolated Nuclear Power Plants buildings. *Nuclear Engineering and Design*, *262*, 189-200.

Ren, W.X., Peng, X.L., & Lin, Y.Q. (2005). Experimental and analytical studies on dynamic characteristics of a large span cable-stayed bridge. *Engineering Structures*, *27*(4), 535-548.

Ren, W.X., & Chen, H.B. (2010). Finite element model updating in structural dynamics by using the response surface method. *Engineering Structures*, *32*, 2455-2465.

Ren, W.X., Fang, S.E., & Deng, M.Y. (2011). Response Surface–Based Finite-Element-Model Updating Using Structural Static Responses. *Journal of Engineering Mechanics, ASCE*, *137*, 248-257.

Reynders, E., Teughels, A., & Roeck, G.D. (2010). Finite element model updating and structural damage identification using OMAX data. *Mechanical Systems and Signal Processing*, *24*(5), 1306-1323.

Rutherford, A.C., Inman, D.J., Park, G., & Hemez, F.M. (2005). Use of response surface metamodels for identification of stiffness and damping coefficients in a simple dynamic system. *Shock and Vibration*, *12*(5), 317-331.

Samaras, E., Shinzuka, M., & Tsurui, A. (1985). ARMA representation of random processes. *Journal of Engineering Mechanics*, *111*(3), 449-461.

Sanayei, M., & Onipede, O. (1991). Damage assessment of structures using static test data. *AIAA Journal*, *29*(7), 1174-1179.

Sankaran, R., & Jancauskas, E.D. (1992). Direct measurement of the aerodynamic admittance of two-dimensional rectangular cylinders in smooth and turbulent flows. *Journal of Wind Engineering and Industrial Aerodynamics*,*41*(1), 601-611.

Sarpkaya, T. (1979). Vortex-induced oscillations: A selective review, *Journal of Applied Mechanics*, *46* (2), 241–258.

Sarpkaya, T. (2004). A critical review of the intrinsic nature of vortex-induced vibrations, *Journal of Fluids and Structures*, *19*(4), 389–447.

Scanlan, R.H., & Tomko, J.J. (1971). Airfoil and bridges deck flutter derivatives, *Journal of the Engineering Mechanics Division*, *97*(6), 1717-1737.

Scanlan, R.H., & Gade, R.H. (1977). Motion of suspension bridge spans under gusty wind, *Journal of the Structural Division, ASCE*, *103*, 1867-1883.

Scanlan, R.H. (1978). The action of flexible bridge under wind, II: buffeting theory, *Journal of Sound and Vibration*, *60*(2), 201-211.

Scanlan, R.H. (1984). Role of indicial functions in buffeting analysis of bridges. *Journal of Structural Engineering*, *110*(7), 1433-1446.

Scanlan, R.H. (1993). Problematics in formulation of wind-force models for bridge decks. *Journal of Engineering Mechanics*, *119*(7), 1353-1375.

Scanlan, R.H. (2000a). Motion related body-force functions in two-dimensional low-speed flow, *Journal of Fluids and Structures*, *14*, 49-63.

Scanlan, R.H. (2000b). Bridge deck aeroelastic admittance revisited, *Journal of Bridge Engineering*, *5*, 1–7.

Schlune, H., Plos, M., & Gylltoft, K. (2009). Improved bridge evaluation through finite element model updating using static and dynamic measurements. *Engineering Structures*, *31*(7), 1477-1485.

Shi, Y., & Chang, C.C. (2011). Substructural time-varying parameter identification using wavelet multiresolution approximation. *Journal of Engineering Mechanics*, *138*(1), 50-59.

Shinozuka, M., & Jan, C.M. (1972). Digital simulation of random processes and its applications. *Journal of sound and vibration*, *25*(1), 111-128.

Simiu, E., & Scanlan, R.H. (1996). *Wind Effects on Structures, 3rd edition*, USA: John Wiley & Sons.

Singh, L. (1997). *Experimental determination of aeroelastic and aerodynamic parameters of long-span bridges*, Doctoral dissertation, Johns Hopkins University, Baltimore.

Solari, G. (1989). Wind response spectrum, *Journal of engineering mechanics*, *115*, 2057-2073.

Spencer Jr, B.F., Ruiz-Sandoval, M.E., & Kurata, N. (2004). Smart sensory technology: opportunities and challenges, *Structural Control and Health Monitoring*, *11*(4), 349–368.

Sun, L.M., Sun, Z., Dan, D.H., & Zhang, Q.W. (2007). Large-span bridges and their health monitoring systems in China, *Proceedings of 2007 International Symposium on Integrated Life-cycle Design and Management of Infrastructure*, Shanghai, China, 79-95.

The Hong Kong Polytechnic University. (2004). *Stonecutters Bridge: 3-D Finite Element Based Buffeting Analysis, Report No. 2 Static and Dynamic Characteristics Study*, submitted to Highways Department, Hong Kong.

The Hong Kong Polytechnic University. (2004). *Stonecutters Bridge: 3-D Finite Element Based Buffeting Analysis, Report No. 5 Buffeting Response Analysis*, submitted to Highways Department, Hong Kong.

Theodorsen, T., & Mutchler, W. H. (1935). *General theory of aerodynamic instability and the mechanism of flutter*. NACA, R496, National Aeronautics and Space Administration, Washington DC.

Tubino, F. (2005). Relationships among aerodynamic admittance functions, flutter derivatives and static coefficients for long-span bridges, *Journal of Wind Engineering and Industrial Aerodynamics*, *93*, 929-950.

Tuladhar, R., Dilger, W. H., & Elbadry, M.M. (1995). Influence of cable vibration on seismic response of cable-stayed bridges, *Canadian Journal of Civil Engineering*, *22*, 1001-1020.

Van der Auweraer, H., & Peeters, B. (2003). International research projects on structural health monitoring: an overview, *Structural Health Monitoring*, *2*(4), 341–358.

Walshe, D.E., & Wyatt, T.A. (1983). Measurement and application of the aerodynamic admittance function for a boxgirder bridge, *Journal of Wind Engineering and Industrial Aerodynamics*, *14*, 211–222.

Wang, H., Tao, T., Zhou, R., Hua, X., & Kareem, A. (2014). Parameter sensitivity study on flutter stability of a long-span triple-tower suspension bridge. *Journal of Wind Engineering and Industrial Aerodynamics*, *128*, 12-21.

Wang, Y., Li, Z., Wang, C., & Wang, H. (2013). Concurrent multi-scale modelling and updating of long-span bridges using a multi-objective optimisation technique. *Structure and Infrastructure Engineering*, *9*(12), 1251-1266.

Walshe, D.E., & Wyatt, T.A. (1983). Measurement and application of the aerodynamic admittance function for a box-girder bridge. *Journal of Wind Engineering and Industrial Aerodynamics*, *14*(1), 211-222.

Weng, S., Xia, Y., Xu, Y.L., & Zhu, H.P. (2011). Substructure based approach to finite element model updating, *Computers and Structures*, *89*, 772-782.

Wilkinson, R.H. (1981). Fluctuating pressures on an oscillating square prism. Pt. 2: spanwise correlation and loading. *Aeronautical Quarterly*, *32*, 111-25.

Williamson, C.H.K., & Govardhan, R. (2004) Vortex-induced vibrations, *Annual Review of Fluid Mechanics*, *36*, 413–455.

Wilson, J.C., & Gravelle, W. (1991). Modelling of a cable-stayed bridge for dynamic analysis. *Earthquake Engineering & Structural Dynamics*, *20*(8), 707-721.

Wilson, J.C., & Liu, T. (1991) Ambient vibration measurements on a cable-stayed bridge, *Earthquake Engineering and Structural Dynamics*, *20*(8), 723-747.

Wong, K.Y. (2007). Design of a structural health monitoring system for long-span bridges. *Structure and Infrastructure Engineering*, *3*(2), 169-185.

Worden, K., & Dulieu-Barton, J.M. (2004). An overview of intelligent fault detection in systems and structures, *Structural Health Monitoring*, *3*(1), 85-98.

Wu, T., & Kareem, A. (2013a). Bridge aerodynamics and aeroelasticity: A comparison of modeling schemes. *Journal of Fluids and Structures*, *43*, 347-370.

Wu, T., & Kareem, A. (2013b). Aerodynamics and aeroelasticity of cable-supported bridges: identification of nonlinear features. *Journal of Engineering Mechanics*, *139*(12), 1886-1893.

Wu, T., Kareem, A., & Ge, Y. (2013). Linear and nonlinear aeroelastic analysis frameworks for cable-supported bridges. *Nonlinear Dynamics*, *74*(3), 487-516.

Xiang, H.F., Liu, C.H., & Gu, M. (1995). Time-domain analysis for coupled buffeting response of long span bridge, *Proceeding of the 9th ICWE*, New Delhi, 881-892.

Xiang, H.F., & Lin, Z.X. (1996) Wind resistance design guidebook for highway bridges, Beijing, China Communications Press. (in Chinese)

Xiang, H.F., & Ge, Y.J. (2003). On aerodynamic limit to suspension bridges. *Proceeding of Eleventh International Conference on Wind Engineering*, Lubbock, Texas, USA. *1*, 65-80.

Xu, Y.L. & Chen, J. (2004). Characterizing non-stationary wind speed using empirical mode decomposition. *Journal of Structural Engineering, ASCE*. *130*(6), 912-920.

Xu, Y.L., Liu, T.T., & Zhang, W.S. (2009). Buffeting-induced fatigue damage assessment of a long suspension bridge. *International Journal of Fatigue*, *31*(3), 575-586.

Xu, Y.L., Sun, D.K., Ko, J.M., & Lin, J.H. (1998) Buffeting analysis of long span bridges: a new algorithm, *Computers & structures*, *68*(4), 303-313.

Xu, Y.L., Sun, D.K., Ko, J.M., & Lin, J.H. (2000). Fully coupled buffeting analysis of Tsing Ma suspension bridge. *Journal of Wind Engineering and Industrial Aerodynamics*, *85*(1), 97-117.

Xu, Y.L., & Zhu, L.D. (2005). Buffeting response of long-span cable-supported bridges under skew winds, Part II: case study. *Journal of sound and Vibration*, *281*(3-5), 675-697.

Xu, Y.L. & Xia, Y. (2012). *Structural Health Monitoring of Long-span Suspension Bridges. 1st Edition*, London: Spon Press.

Xu, Y. L. (2013). *Wind Effects on Cable-supported Bridges*. John Wiley & Sons.

Yang, W.W., Chang, T.Y.P., & Chang, C.C. (1997). An efficient wind field simulation technique for bridges. *Journal of Wind Engineering and Industrial Aerodynamics*, *67*, 697-708.

Yeo, I., Shin, S., Lee, H.S., & Chang, S.P. (2000). Statistical damage assessment of framed structures from static response. *Journal of Engineering Mechanics, ASCE*, *126*(4), 414-421.

Zasso, A. (1996). Flutter derivatives: advantages of a new representation convention, *Journal of Wind Engineering and Industrial Aerodynamics*, *60*(1-3), 35-47.

Zaurin, R., & Catbas, F.N. (2010). Integration of computer imaging and sensor data for structural health monitoring of bridges. *Smart Materials and Structures*, *19*, 1-15.

Zhang, W., Cai, C.S., & Pan, F. (2013). Finite element modelling of bridges with equivalent orthotropic material method for multi-scale dynamic loads. *Engineering Structures*, *54*, 82-93.

Zhang, X., Xiang, H.F., & Sun, B. (2002) Nonlinear aerostatic and aerodynamic analysis of long-span suspension bridges considering wind-structure interactions, *Journal of Wind Engineering and Industrial Aerodynamics*, *90*, 1065-1080.

Zhang, X., & Brownjohn, J.M.W. (2003), Time domain formulation of self-excited forces on bridge deck for wind tunnel experiment, *Journal of Wind Engineering and Industrial Aerodynamics*, *91*, 723-736.

Zhao, J., & DeWolf, J.T. (1999). Sensitivity study for vibration parameters used in damage detection. *Journal of Structural Engineering, ASCE*, *125* (4), 410-416.

Zhu, L.D., & Xu, Y.L. (2005). Buffeting response of long-span cable-supported bridges under skew winds. Part 1: theory. *Journal of Sound and Vibration*, *281*(3), 647-673.

Zhu, L.D., Zhao C.L., Wen, S.B. & Ding, Q.S. (2009). Signature Turbulence Effect on Buffeting Responses of a Long-span Bridge with a Centrally-Slotted Box Deck, *Proceedings of the International Symposium on Computational Structural Engineering: Computational Structural Engineering*, Shanghai, China, June 22-24, 399-409.

Zhu, Q., & Xu, Y.L. (2014). Characteristics of distributed aerodynamic forces on a twin-box bridge deck. *Journal of Wind Engineering and Industrial Aerodynamics*, *131*, 31-45.

Zivanovic, S., Pavic, A., & Reynolds, P. (2007). Finite element modeling and updating of a lively footbridge: the complete process, *Journal of Sound and Vibration*, *301*, 126-145.